The Effects of Expansion Regions on the Turbulence Structure of a Supersonic Boundary Layer

M. Samimy, S. A. Arnette, and G. S. Elliott
Department of Mechanical Engineering
The Ohio State University
Columbus, Ohio 43210

Final Technical Report
(MSME-96-102)

for

for the Period of
January 1, 1994 to March 31, 1996

April 1996

The Effects of Expansion Regions on the Turbulence Structure of a Supersonic Boundary Layer

M. Samimy[1], S. A. Arnette[2], and G. S. Elliott[3]
Department of Mechanical Engineering
The Ohio State University
Columbus, Ohio 43210

---

[1] Principal Investigator, Professor
[2] Graduate Student; Currently, Aerodynamic Engineer, Sverdrup Technology
[3] Postdoctoral Researcher; Currently, Assistant Professor, Department of Mechanical
and Aerospace Engineering, Rutgers University

REPORT DOCUMENTATION PAGE

Form Approved
OMB No. 0704-0188

1. AGENCY USE ONLY (Leave blank)	2. REPORT DATE April 1996	3. REPORT TYPE AND DATES COVERED Final 01 JAN 94 – 31 Mar 96

4. TITLE AND SUBTITLE
The effects of Expansion Regions on The Turbulent Structure of a Supersonic Boundary Layer

5. FUNDING NUMBERS
F49620
94-1-0074

6. AUTHOR(S)
M. Samimy, S. Arnette, G. Elliott

7. PERFORMING ORGANIZATION NAME(S) AND ADDRESS(ES)
Ohio State University
Columbus OH 43210

AFOSR-TR-96
0354

9. SPONSORING / MONITORING AGENCY NAME(S) AND ADDRESS(ES)
Air Force Office Of Scientific Research
Aerospace & Materials Sciences Directorate
110 Duncan Avenue, Suite B-115
Bolling AFB DC 20332-0001

NA

10. SPONSORING / MONITORING AGENCY REPORT NUMBER
94-1-0074

11. SUPPLEMENTARY NOTES

12a. DISTRIBUTION / AVAILABILITY STATEMENT
APPROVED FOR PUBLIC RELEASE
DISTRIBUTION IS UNLIMITED

19960618 007

CODE

13. ABSTRACT (Maximum 200 words)

A fully-developed high Reynolds number Mach 3 turbulent boundary layer and the effects of four expansion regions (centered and gradual expansions of 7° and 14°) on the boundary layer were investigated by utilizing 1) multi-point instantaneous surface pressure measurements, 2) instantaneous single- and double-pulse flow visualizations based on Filtered Rayleigh Scattering (FRS), 3) two-component planar velocity measurements using Filtered Planar Velocimetry (FPV), and 4) detailed turbulence measurements using Laser Doppler Velocimetry (LDV). Flow visualization results indicate that the upper half of the fully developed turbulent boundary layer is populated with elongated longitudinal structures of considerable streamwise but very limited spanwise extent. These structures are randomly

14. SUBJECT TERMS.
Rayleigh Scattering, Supersonic

15. NUMBER OF PAGES
113

16. PRICE CODE

17. SECURITY CLASSIFICATION OF REPORT Unclassified	18. SECURITY CLASSIFICATION OF THIS PAGE Unclassified	19. SECURITY CLASSIFICATION OF ABSTRACT Unclassified	20. LIMITATION OF ABSTRACT U

NSN 7540-01-280-5500

Standard Form 298 (Rev. 2-89)

ABSTRACT

A fully-developed high Reynolds number Mach 3 turbulent boundary layer and the effects of four expansion regions (centered and gradual expansions of 7° and 14°) on the boundary layer were investigated by utilizing 1) multi-point instantaneous surface pressure measurements, 2) instantaneous single- and double-pulse flow visualizations based on Filtered Rayleigh Scattering (FRS), 3) two-component planar velocity measurements using Filtered Planar Velocimetry (FPV), and 4) detailed turbulence measurements using Laser Doppler Velocimetry (LDV). Flow visualization results indicate that the upper half of the fully developed turbulent boundary layer is populated with elongated longitudinal structures of considerable streamwise but very limited spanwise extent. These structures are randomly distributed in space and time and survive even the 14° centered expansion. The visualizations also show that large scale structures increase both in size and angle and small scale structures are quenched across the expansions. The angle of large scale structures return to the flat plat value further downstream of the expansions. The normalized power spectra of pressure fluctuations downstream of the expansions are more concentrated at lower frequencies than their upstream counterparts, confirming the small scale quenching shown by flow visualizations. Although essentially full recovery of the mean velocity profile is captured downstream of the expansions, the boundary layer turbulence remains far from equilibrium at the last measurement station ($s/\delta \approx 20$). Computations with the rotational method of characteristics indicate the evolution of the mean velocity profile downstream of the expansions is largely inviscid for approximately 10δ. Turbulence levels decrease across the expansion with the most significant reductions occurring near the surface. The reductions become less severe with increasing normal distance above the boundary. As expected, reductions are more severe for the 14° expansions. In fact, downstream of the two 14° expansions, reverse transition is indicated by sharp reductions in the turbulent kinetic energy levels and a change in sign of the Reynolds shear stress. Dimensionless turbulence parameters such as the anisotropy and shear stress correlation coefficient are also altered substantially, indicating the turbulence undergoes a complex evolution downstream of the

expansions. Four articles (three Journal papers and one conference papers) are included in the appendices of this report which detail the findings based on pressure measurements, flow visualizations, and velocity measurements based on FPV. This report focuses mainly on the detailed turbulence results obtained using LDV.

ACKNOWLEDGEMENTS

TABLE OF CONTENTS

NOMENCLATURES

n   Normal distance above the boundary.

s   Streamwise distance along model surface measured from beginning of expansions.

U   Mean streamwise velocity.

U_0 Mach 3 freestream velocity.

u Streamwise velocity fluctuations.

u_τ Friction velocity.

V   Mean normal velocity.

v Normal velocity fluctuations.

W   Mean spanwise velocity.

w Spanwise velocity fluctuations.

z   Spanwise direction.

δ_0 Flat plate boundary layer thickness at beginning of expansions (9.1 mm).

$\delta_{flatness}$ Boundary layer thickness indicated by the peak in the streamwise flatness profile.

θ Boundary layer momentum thickness; angle specifying flow direction.

ρ Density.

τ Particle residence time in measurement volume.

INTRODUCTION

The compressible turbulent boundary layer encountered in an application is likely not of the flat plate, zero pressure gradient, 'canonical' variety. More likely, it has been subjected to 'extra rates of strain' (as defined by Bradshaw [1974]) induced by effects such as pressure gradients, streamline curvature, and bulk compression or dilatation. Extra rates of strain are velocity gradients in addition to the usual normal gradient of streamwise velocity associated with boundary layers. The response of the compressible turbulent boundary layer to extra rates of strain is nonlinear [Smits and Wood, 1985]. Accordingly, turbulent shear flows subjected to such rates of strain have come to be known as complex turbulent flows. Not surprisingly, our knowledge of perturbed compressible turbulent boundary layers lags far behind our understanding of their 'canonical' counterparts.

Our lack of understanding of compressible turbulent boundary layers can be traced to both experimental and computational difficulties. The high Reynolds numbers associated with these flows will preclude direct numerical simulations for the foreseeable future. On the experimental side, current measurement techniques do not offer the spatial or temporal resolution required to fully resolve the boundary layer turbulence activity. An illustration of the spatial resolution required to resolve the near-wall region of the Mach 3 boundary layer studied here ($\delta \simeq 10$ mm) is provided by measurements acquired with Filtered Planar Velocimetry, where the velocity measured 0.4 mm above the surface is approximately 60% of the freestream velocity [Arnette, 1995 and Arnette et al., 1996]. As discussed by Spina and Smits [1987], fully resolving temporal near-wall variations requires a frequency response of at least $10\nu/u_\tau^2$ (ν = kinematic viscosity & u_τ = friction velocity). This is approximately 25 MHz for the current study, which is well beyond the capabilities of established measurement techniques.

Given this, further experimental investigations of compressible turbulent boundary layers, both canonical and perturbed, are needed. This is the motivation for the current research. A Mach 3, fully-developed, turbulent boundary layer ($Re_\theta = 24700$) is probed extensively and the effects of four different expansion regions on the turbulent boundary

1

layer are investigated. The expansion regions consist of centered (radius of the convex surface curvature is vanishingly small) and gradual expansions (radius of curvature for the convex surface curvature is approximately 50δ). For each radius of curvature, expansions with deflection angles of 7° and 14° were investigated.

This work is part of an extended investigation in which several nonintrusive optical diagnostics have been employed. In addition to the LDV results presented here, Filtered Rayleigh Scattering, double-pulsed Rayleigh scattering, Planar Laser-Induced Fluorescence, and two-component Filtered Planar Velocimetry have been employed and results presented elsewhere (Arnette et al. [1994, 1995, 1996], Samimy et al. [1994], and Arnette [1995]). On the computational side, the evolution of the incoming boundary layer's mean velocity profile through the centered expansions has been computed with the rotational method of characteristics. All of this work is presented by Arnette [1995]. In addition, measurements of fluctuating surface pressures in the boundary layers considered here have been presented by Dawson et al. [1994].

The passage of a two-dimensional, compressible, turbulent boundary layer through an expansion region is depicted in Fig. 1. Within the expansion, the boundary layer is subjected to a favorable streamwise pressure gradient ($\partial p/\partial s < 0$ where s is the streamwise coordinate), a normal pressure gradient ($\partial p/\partial n > 0$ where n is the coordinate normal to the surface and increases away from the surface), and bulk dilatation ($\nabla \cdot \underline{U} > 0$, i.e. the volume of a fluid element increases through the expansion region). Extra rates of strain are introduced by the expansion, namely $\partial U/\partial x$, $\partial V/\partial y$, and $\partial V/\partial x$ in the coordinate system of Fig. 1.

This flow field has been the subject of surprisingly little research, most work concerning viscid-inviscid interactions having been focussed on shock wave/boundary layer interactions. Excluding the present study, the work by Morkovin [1955], Thomann [1968], Narasimha and Viswanath [1975], Hampton and White [1983], Dussauge and Gaviglio [1987], Smith and Smits [1991], and Johnson [1993] represents most of the previous investigations.

Thomann [1968] isolated the effect of streamline curvature on the rate of heat transfer at the wall beneath a supersonic, turbulent boundary layer (M = 2.5) by placing

2

appropriately shaped bodies in the freestream above convex and concave surfaces to eliminate pressure gradients. When the boundary layer was subjected to 20° of convex curvature, the heat transfer rate at the wall decreased by approximately 20%. The decreased heat transfer rate is indicative of decreased turbulent mixing between the boundary layer and the freestream, confirming the general effects of the convex curvature to be stabilizing.

Dussauge and Gaviglio [1987] investigated the effect of a 12° centered expansion on a Mach 1.76 boundary layer (δ = 10 mm, Re_θ = 5000). In addition to mean and turbulence measurements, an analysis based on Rapid Distortion Theory isolated the effect of the bulk dilatation on the boundary layer. Mean velocity profiles downstream of the expansion initially displayed a thick sublayer region possessing a larger normal gradient of mean streamwise velocity ($\partial U/\partial n$ in the streamwise-normal coordinate system of Fig. 1) than the equilibrium profiles, with no apparent logarithmic region. After approximately $9\delta_0$, a logarithmic region reappeared. The calculations indicated the decreases in streamwise turbulence intensity sustained across the expansion were due primarily to bulk dilatation, but the decreases in turbulence level near the wall were not reproduced well by the calculations based solely on dilatation effects. After the expansion, the turbulence intensity near the wall (n/δ < 0.2) was initially very low relative to the incoming levels. For n/δ > 0.25, the turbulence intensity decreased slightly with increasing normal distance from the wall and the deviation between the pre- and post-expansion intensities decreased with increasing normal distance from the wall.

Downstream measurements showed the near-wall region to reestablish turbulence intensities comparable to the pre-expansion levels much more quickly than the outer portions of the boundary layer, where the evolution was very slow. This is a consequence of the confinement of the turbulence production to the near-wall region where there are significant mean gradients. The outer portions of the boundary layer are void of production and governed by diffusion and dissipative processes. Another line of reasoning arises from the relative scales which populate the near-wall and outer portions of the boundary layer. Small scale turbulence of the near-wall region is more susceptible to 'quenching' by bulk dilatation than the large scale motions of the outer region (i.e. if a small scale motion is

3

idealized as a small vortex and viscous effects are neglected, conservation of angular momentum dictates that an increase in vortex size will decrease the motion's vorticity).

The rapid recovery of the region near the wall led Dussauge and Gaviglio [1987] to propose that a new internal layer formed downstream of the expansion, and that the incoming boundary layer had been relaminarized. Investigations of incompressible boundary layers led Narasimha and Sreenivasan [1973] to define a relaminarized boundary layer as one in which "the Reynolds stresses have become of negligible importance to the mean flow". Relaminarization can occur when a turbulent boundary layer is subjected to a large, favorable pressure gradient. For compressible turbulent boundary layers that pass through an expansion fan, Narasimha and Viswanath [1975] suggest relaminarization occurs for $\Delta p / \tau_0$ greater than approximately 70, where Δp is the pressure difference across the expansion and τ_0 is the wall shear stress just upstream of the expansion.

Smith and Smits [1991] investigated the passage of a Mach 2.84 ($\delta_0 = 26$ mm, $Re_\theta = 77600$) turbulent boundary layer through a 20° centered expansion region. Mean and turbulence profiles were measured $1\delta_0$ ahead of and $3.5\delta_0$ downstream of the expansion corner. Similar to the results of Dussauge and Gaviglio [1987], the mean velocity profile did not possess a logarithmic region at the downstream survey location. Turbulence measurements indicate caution should be used in using the term "relaminarization" to describe these flows, as the profiles of mass flux fluctuations were essentially unchanged between the two survey locations. However, the streamwise velocity fluctuations and longitudinal normal Reynolds stress were significantly decreased across the expansion. Calculations based on Rapid Distortion Theory, similar to those of Dussauge and Gaviglio [1987], were performed and dilatation was again found to be mainly responsible for the decreased turbulence levels.

In light of the evidence that such effects are important when present, Bradshaw [1974] developed a method of incorporating corrections for mean compression or dilatation in turbulence computations. As cited by Bradshaw over 20 years ago, a lack of fundamental understanding of these effects remains a problem. However, such effects are intuitively connected to the principle of conservation of angular momentum. When a fluid element

4

passes through a two-dimensional expansion fan, its cross-sectional area in the X-Y, X-Z, and Y-Z planes increases due to the positive $\partial U/\partial x$ and negative $\partial V/\partial y$ (referenced to the x-y coordinate system of Fig. 1). As a result, all three components of vorticity are damped, resulting in an overall stabilization.

Dawson et al.[1994] used high frequency-response, miniature pressure transducers to acquire multi-point measurements of the fluctuating surface pressures in the same incoming Mach 3 turbulent boundary layer and four expanded boundary layers studied here. Normalized power spectra showed the pressure fluctuations to be much more concentrated at low frequencies just downstream of the expansions relative to upstream of the expansions. The elevated low frequency levels were accompanied by sharp decreases in the levels at high frequencies. This led to the conclusion that small scale motions are quenched almost immediately by the expansion region (presumably due to dilatational effects). This agrees with the sharp reductions in turbulence level near the wall observed by Dussauge and Gaviglio [1987] and Smith and Smits [1991].

EXPERIMENTAL PROCEDURES

1. Flow Facility

The experiments were performed at the Aeronautical and Astronautical Research Laboratory at The Ohio State University. Two four-stage compressors supply air to the system, which has a storage capacity of 42.5 m^3 at pressures up to 16.4 MPa. Supply air is introduced to the stagnation chamber through an array of radial inlet holes. The stagnation chamber pressure is maintained to within $\pm 1\%$ of the set point. For these experiments, the stagnation pressure was 0.82 MPa (8.2 atm), and the stagnation temperature was nominally 280 K.

The employed supersonic blow-down tunnel has been employed previously in a dual-stream configuration to investigate the compressible mixing layer. For the current investigation, only the supersonic stream is utilized. The boundary layer develops on a flat plate (which serves as a splitter plate to separate the two streams of the compressible mixing layer) and the expansion models are fixed to a flat plate section which replaces the removable splitter plate tip. The two-dimensional, converging-diverging nozzle profile is opposite the flat plate on the top wall of the tunnel. As a result, the boundary layer develops on a flat plate from the stagnation chamber to the test section. The top surface of the flat plate is at the lateral center of the test section, so that the incoming supersonic flow occupies a passage 152.4 mm wide by 76.2 mm high. After the expansion regions, the model surfaces diverge away from the expansion corner toward the bottom of the test section, which has a total cross section of 152.4 mm wide by 152.4 mm high. Thus only half of the available test section is utilized at the onset of the expansion region. Inviscid calculations indicate the expansion waves reflected when the primary expansion waves intersect the top of the test section impact the surface of the 7° centered expansion model near the very end of the model, intersect the 7° gradual expansion model surface at $s/\delta_0 \cong$ 43, and do not intersect the two 14° expansion models. All measurements were acquired upstream of these locations.

In addition to the four expansion models, a flat plate model was constructed to allow detailed investigations of the non-perturbed boundary layer. With the expansion models

6

installed, optical access is available for only 3 cm of the incoming boundary layer. The flat plate model allows the equilibrium boundary layer to be extended through the length of the test section.

Optical access to the test section is provided by a window in each bounding surface. Each side wall has an interchangeable window and blank panel which give a total possible viewing area 450 mm long in the streamwise direction and 80 mm high in the normal direction.

The employed coordinate system is presented in Fig. 1. The streamwise coordinate, s, is measured along the surface of the expansion models. The origin (s = 0) occurs at the beginning of the expansion regions. The normal coordinate, n, is zero at the surface and everywhere normal to the surface. As depicted in Fig. 1b, the radius of curvature for both gradual expansion models is 450 mm, giving $R/\delta_0 \simeq 50$ for the Mach 3 incoming flow.

A Mach 3.0 incoming flow was utilized in all of the experiments. LDV measurements, which are discussed further below, show the freestream turbulence intensities in the streamwise and normal directions to be less than 1.5% and 1.0%, respectively. The freestream velocity is nominally 600 m/s, but varies slightly from run to run with the stagnation temperature, which is monitored. At the onset of the convex surface curvature associated with the expansion models, the boundary layer thickness ($\delta_{99\%}$) is 9.1 mm and the momentum thickness (θ) is 0.37 mm. The Reynolds number based on momentum thickness (Re_θ) is 24700. The unit Reynolds number is $6.7 \times 10^5/m$.

Upon installing a model, schlieren photography was used to insure no non-uniformities were present. Spanwise and streamwise static pressure distributions at the model surfaces monitored via static pressure taps have been presented elsewhere [Dawson et al., 1994, Arnette, 1995].

2. Laser Doppler Velocimetry System

A TSI Model 9100-7 LDV system was used in conjunction with the blue (λ = 488 nm) and green (λ = 514.5 nm) beams of a Model 2020 Spectra Physics 5-watt Argon-ion laser to measure streamwise and normal velocities. The beam pairs propagated through the test section in the spanwise direction and were oriented at an angle of 45° with both the

7

normal direction and streamwise directions. The measurements were acquired in the spanwise center of the test section. No frequency shifting was used. A 3.75X beam expander was used to reduce the size of the measurement volume, thereby improving the signal-to-noise ratio, and also the spatial resolution. Forward scattering was collected at an angle of $10°$ with the spanwise-aligned beam axis. The scattering was collected off-axis to help reduce the amount of stray laser light seen by the photomultiplier tubes and to reduce the spanwise length of the measurement volume. The ellipsoid measurement volume was calculated to be 0.33 mm long in the spanwise direction and 0.13 mm in diameter at the e^{-2} intensity level. The fringe spacings were calculated to be 7.3 μm and 7.7 μm for the green and blue beams, respectively.

The data was collected with TSI FIND software on a 486 DX personal computer. The photomultiplier tube outputs were filtered and processed with a Model IFA-750 digital burst correlator. For each point, 8192 measurements were collected at typical data rates of 5 to 10 kHz. The digital burst correlator performs an autocorrelation on a collected burst. Since the autocorrelation of a time-varying signal is by definition the Fourier transform of the signal's frequency spectrum, performing a Fourier transform on the autocorrelation gives the frequency at which the particle encounters the fringes in the measurement volume. The time for the particle to travel between adjacent fringes is simply the period of the resulting frequency. Combining this with the fringe spacing yields a velocity measurement. Further details concerning the LDV system are presented by Arnette [1995].

The flow was seeded with silicone oil particles less than 1 μm in diameter generated with a TSI Model 9306 six-jet atomizer. The particle-laden air stream was injected through the back wall of the stagnation chamber through an array of spanwise-aligned ports located approximately 10 mm above the flat plate on which the boundary layer formed. In order to operate the atomizer at pressures sufficiently high to inject the particle-laden airstream into the stagnation chamber, the atomizer was placed within a pressure vessel, which was maintained at the stagnation pressure. The pressure within the atomizing unit was maintained 414 kPa above the stagnation pressure. The seeded output of the atomizer was directed through the end of the holding pressure vessel to the back wall of the stagnation chamber with flexible hosing. A ball valve allowed the seeding to be turned off while

8

maintaining the system pressure and a needle valve allowed the seeded air flow to be throttled.

The LDV system was located on an optical table capable of motion in the streamwise and normal directions. The motion is achieved through gearing used in conjunction with Ampro Inc. stepper motors. In order to enable closed-loop motion control, the table was equipped with linear encoders possessing a resolution of 8000 steps/inch. Table-mounted linear encoders were chosen over motor-mounted rotary encoders to ensure that any 'slop' in the drive system would not cause positioning errors. Data was collected only when the measurement volume was located within ±0.001 mm of the desired position in the streamwise and normal directions. The FIND software made it possible to incorporate the motion control with the data acquisition. As a result, data could be collected at approximately 20 points in a single run.

Data was collected in the coincident mode, which is to say that for a data point to be considered valid, a burst had to be detected in both the green and blue beams. The coincident window width was set to 1.0 μs.

Corrections for velocity bias were incorporated in the computations of all turbulence statistics. The employed correction requires that the 'particle residence time' or temporal duration of each burst be used as a weighting function in the summations used to calculate the various velocity statistics. For example, mean velocities were calculated as $U = (\sum U_i \tau_i)/\sum \tau_i$ where U is the corrected mean velocity, U_i is the ith instantaneous velocity measurement, and τ_I is the particle residence time associated with the ith velocity measurement.

Because the transmitted beams converge to form the measurement volume and the measurements were acquired in the spanwise center of the test section, measurements could only be acquired to within about 2 mm of the surface. The same beam orientation of $\pm\ 45°$ to the flat plate streamwise direction was maintained downstream of the expansion regions. The measured velocities were projected onto the streamwise and normal directions in post processing.

Since data were collected during runs of several minutes duration, variations of the stagnation temperature (and hence the freestream velocity) were taken into account. Freestream velocity measurements were acquired during a lengthy run while measuring the

9

stagnation temperature so that the relationship of freestream velocity to stagnation temperature was known. Since the stagnation temperature was measured with an RTD to within $\pm$ 0.1 K throughout each run, establishing this relationship allowed velocities acquired at different points in the boundary layer to be normalized by the proper freestream velocity, i.e. the freestream velocity at the time of the measurement.

RESULTS AND DISCUSSIONS

1. Mean Static Pressures and Flow Visualizations

Instantaneous schlieren images of the flat plate boundary layer, the passage of the boundary layer through the 7° centered expansion, and the passage of the boundary layer through the 14° centered expansion are presented in Figs. 2a, 2b, and 2c, respectively. The boundary layer thickens across the expansions, which is not surprising given the sustained decreases in density. Average schlieren images suggest the boundary layer thickness increases by factors of approximately 1.5 and 2.0 across the 7° and 14° expansions, respectively. The criterion of Narasimha and Viswanath [1975] that relaminarization occurs for $\Delta p / \tau_0 > 75$ was examined. As discussed by Arnette et al. [1995], using the correlation of Tetervin [1967] (presented by Narasimha and Viswanath [1975]) to estimate the skin friction coefficient for the incoming boundary layer gives $\Delta p / \tau_0$ estimates of 48 and 76 for the 7° and 14° centered expansion cases, respectively. This suggests the boundary layers downstream of the 14° expansions might be relaminarized. Although $\Delta p / \tau_0$ is the same for the two 14° cases, relaminarization should be sensitive to the magnitude of the favorable pressure gradient, not the pressure difference across the expansion region (the ratio $\Delta p / \tau_0$ was formed with centered expansions in mind). Accordingly, the 14° gradual case should not be close to relaminarization based on this criterion.

Confirmation of relaminarization for supersonic turbulent boundary layers is scarce. For the boundary layers of this study, Dawson et al. [1994] found the RMS pressure fluctuations at the surface (as a fraction of the mean static pressure) did not decrease across the four expansions. In fact, the ratio initially increases across the centered expansions, indicating significant turbulence activity exists downstream of the expansions. This does not give an indication of relaminarization. Despite satisfying the $\Delta p / \tau_0 > 75$ criterion for relaminarization with the 20° centered expansion of their Mach 2.84 turbulent boundary layer, Smith and Smits [1991] caution against the term "relaminarization". Although streamwise turbulence intensities 3.5δ downstream of the corner were significantly lower than incoming levels, mass flux fluctuation levels were essentially unchanged.

11

Though one naturally associates a cessation of turbulence activity with the term "relaminarization", the definition offered by Narasimha and Viswanath [1973] specifies only that the Reynolds stresses cease to be important to the mean flow. Within the context of this definition it is difficult to comment on the existence of relaminarization.

In the course of this investigation, Filtered Rayleigh Scattering (FRS) was employed to obtain extensive flow visualizations of the equilibrium Mach 3 boundary layer and the boundary layer downstream of the various expansion regions. Details of the FRS implementation and complete visualization results are presented elsewhere [Arnette et al., 1995]. A light sheet formed with the beam of a pulsed Nd:YAG laser, which has a duration of approximately 10 ns, permits instantaneous visualizations to be acquired. The 10 Hz pulse repetition rate results in successive images being totally uncorrelated. Scattering from condensed water particles formed from the trace water vapor in the dry tunnel supply air is collected with an intensified CCD camera. The characteristic particle dimension has been estimated to be no more than 50 nm. Because of its higher static temperature, the condensation is not formed within the boundary layer. Thus the condensation/no-condensation interface provides a means of nominally visualizing the outer edge of the boundary layer. Because of the trace presence of the water vapor and the small size of the condensation particles, the scattered signal levels are very small relative to the stray light formed by the intersection of the laser sheet with the solid boundary. In the FRS technique, a transparent cell containing diatomic iodine vapor is placed in front of the camera lens and serves as an optical filter. Diatomic iodine possesses electronic transitions which correspond to the frequency of a properly-tuned, injection-seeded Nd:YAG laser (the laser frequency is tuned by applying a bias voltage to a temperature circuit within the injection seeder). The laser frequency is tuned to coincide with an iodine transition, therefore the stray laser light is absorbed by the filter before it reaches the camera. Scattering from the condensed particles in the flow is not absorbed since it is Doppler shifted to a different frequency by virtue of the large freestream velocity. This provides a means of imaging *only* the scattering from the condensation in the flow.

Instantaneous visualizations of the Mach 3 flat plate boundary layer acquired in this manner are presented in Figure 3. Although the boundary layer itself is dark in the images

12

because of the lack of condensation within the boundary layer, the presence of large scale turbulent structures is clearly indicated in the outer portions of the boundary layer. The structures cause the top edge of the layer to assume a very intermittent appearance. The presence of smaller scale turbulent motions around the periphery of the large structures is also indicated. It is now widely held that these large structures are major contributors to the Reynolds shear stresses through the entrainment of potential fluid. Accordingly, they are extremely important to the turbulence dynamics.

The passage of the boundary layer through the 7° centered (Fig. 4a) and 7° gradual (Fig. 4b) expansions are presented in Fig. 4. Similar instantaneous images of the boundary layer passage through the 14° centered (Fig. 5a) and 14° gradual (Fig. 5b) expansions are presented in Fig. 5. The bright condensation above the boundary layer downstream of the 14° centered expansions is the result of CO_2 condensation. For all cases, the large scale structures of the outer layer survive the expansion. Comparison of post-expansion and pre-expansion visualizations indicates the large scale motions increase in scale and undergo an increase in angular orientation (relative to the solid boundary downstream of the structure) across the expansions. If a structure remains coherent across an expansion, the sustained decrease in density mandates an increase in scale. The increase in structure angle is likely a kinematic effect associated with the fact that the bottom of the structure is accelerated through the inclined expansion region before the top of the structure.

The survival of the large scale structures downstream of the expansions is not perpetual. The presence of the large scale structures is much less prominent in visualizations acquired further downstream of the expansions suggest the structures are much less prominent further downstream [Arnette et al., 1995 and Arnette, 1995]. It is likely that the large scale structures are at least weakened downstream of the expansions. The visualizations give little indication of the large scale structures further downstream of the 14° centered expansion ($11 < s/\delta_0 < 25$) and 14° gradual expansion ($28 < s/\delta_0 < 42$). Physically, this is similar to the rapid quenching of small scale turbulence discussed earlier. It seems the large scale motions are simply slower to respond than small scale turbulent motions.

2. Computational Results

It is somewhat surprising that a computational method for *inviscid* supersonic flows would be of any use in studying supersonic turbulent boundary layers. The important point to note is that viscous effects in the turbulent boundary layer are most significant in the near-wall region and the method of characteristics is used here to calculate the evolution of the outer layer through the expansion regions. Further justification comes from the fact that, during the rapid expansion, pressure forces (which are included in the analysis) are larger than those due to viscous and Reynolds stresses (which are not included in the analysis).

Since there is a velocity gradient normal to the surface, the mean boundary layer flow is rotational. Accordingly, the rotational method of characteristics must be employed. Similar approaches have been adopted by Dussauge and Gaviglio [1987], Smith and Smits [1991], and Johnson [1993]. The outer layer is modeled as a steady, two-dimensional, inviscid, adiabatic, rotational flow. The entropy is allowed to vary across streamlines, but is assumed constant along streamlines. Though not strictly true, the stagnation enthalpy was assumed constant throughout the entire field. This was deemed acceptable because, for the assumed static temperature profile, the stagnation enthalpy in the boundary layer deviated no more than 1.2% from the freestream value. With this assumption, the computational procedure presented by Shapiro [1953] can be employed.

To begin the computation, a curve along which the velocity, flow direction, and entropy are known must be established. The leading edge of the expansion fan, which is inclined at the Mach angle of the incoming flow, was constructed with the incoming boundary layer profiles. The velocity profiles were those measured with LDV in the flat plate boundary layer. The incoming entropy profile is also required. Unfortunately, temperature profiles were not measured. The normalized temperature profile measured by Smits [1990] in a Mach 2.84 turbulent boundary layer was employed in conjunction with the measured stagnation temperature to obtain the temperature profile, which was combined with the static pressure to compute the entropy.

Since the computations are valid only for supersonic flow, an 'artificial' sonic line was specified at the surface. This sonic line was assumed to follow the surface. Marching

14

through the expansion consisted of turning the surface point through some $\Delta\theta$ and calculating the intersection of the I-characteristic emanating from the surface point with the characteristic from the first point above the surface on the previous I-characteristic, and on. Since the entropy is required at each point, it is necessary to keep track of the streamlines.

The main objectives for the computations were to see if the evolution of the mean velocity field through the expansions was largely inviscid and to see if the results might give an indication as to whether or not serious problems with LDV particle lag were encountered. Since these objectives were met with the centered expansion calculations, the computations were not pursued for the gradual expansion regions. It is also noteworthy that if particle lag were a problem, it would be most substantial for the centered expansions since the flow acceleration is more rapid than for the gradual expansions.

Mean velocity profiles obtained from the method of characteristics computations downstream of the 7° centered expansion corner are plotted alongside the mean velocity profiles measured with LDV in Fig. 6. Results are presented for $s/\delta_0 = 1.5, 2.8, 8.4, 14.0$, and 19.3 (δ_0 = 9.1 mm). To aid the viewer, the results for successive axial locations have been staggered horizontally in the figure.

At $s/\delta_0 = 1.5$, the two profiles display excellent agreement. In fact, the largest deviation between the two is only about 1% of the freestream velocity. As is done throughout this study, the normal coordinate (n) is measured normal to the surface. Since the surface point is downstream of the expansion corner, the normal axis for the velocity profile is oriented 7° away from the normal axis for the flat plate boundary layer (as illustrated in Fig. 1). In the velocity profile extracted from the computed velocity field, the expansion region is confined between n $\approx$ 6 mm and n $\approx$ 9 mm. As would be expected from the inviscid computation, sharp changes in velocity are present at these locations. The measured profile serves as a testament to the 'smoothing' effect of viscosity. The actual flow does not display the sharp changes in velocity, but instead displays a smooth change in velocity between the top and bottom of the expansion region.

That the normalized velocity above the expansion region is not unity is a result of the normalization. The Mach 3 freestream velocity above the flat plate, U_0, is used as the normalizing velocity, but the measured velocity is oriented 7° away from the streamwise direction of the incoming flow. As a result, the freestream above the expansion fan should have a normalized velocity of $U_0 \cos 7°/U_0$, which equals 0.993. This is the case for the computed profile. The agreement between the computed and measured profiles is good. The small deviation is probably related to the uncertainty associated with the stagnation temperature measurement, which was used to obtain the proper freestream velocity for the normalization.

At $s/\delta_0 = 2.8$ downstream of the 7° centered expansion corner the agreement between the measured and computed profiles is again quite good. In fact, the profiles are essentially identical in shape and it appears that the deviation between the two is caused mainly by the normal displacement of the computed profile below the measured profile. The 'knee' which appears in the velocity profiles is a result of the acceleration encountered within the expansion region. In addition to the increase in velocity magnitude across the expansion, the velocity vector is redirected in a direction more in line with the streamwise direction (which is parallel to the 7° inclined surface downstream of the expansion corner).

One might wonder why the 'knee' in the velocity profile at $s/\delta_0 = 2.8$ was not present at $s/\delta_0 = 1.5$. There are two relevant observations. Both stem from the fact that at $s/\delta_0 = 1.5$ the expansion region falls within the boundary layer. The first is a result of the sizeable normal gradients of streamwise velocity within the boundary layer. Consider the bottom edge of the expansion region - although fluid beneath the expansion has been accelerated, fluid within the expansion enters the expansion with a larger streamwise velocity since it is higher in the boundary layer. In fact, referring to Fig. 6, the computed profile does possess a small 'knee' discontinuity at n = 6 mm. It is smaller than the one in the computed profile at $s/\delta_0 = 2.8$ for this reason. The other factor is viscous effects or viscous-like effects induced by the outward turbulent transport of near wall fluid, both of which become more significant closer to the boundary. Even though the computed profile contains a small knee at $s/\delta_0 = 1.5$, none is present in the measured profile because of these effects. At $s/\delta_0 = 2.8$, the knee in the computed profile occurs near the top of the boundary layer where these effects are less significant.

Measured and computed profiles obtained at $s/\delta_0 = 8.4$, 14.0, and 19.3 (s = 76.2 mm, 125.0 mm, and 175.3 mm) downstream of the 7° centered expansion corner are also presented in Fig. 6. The computed and measured profiles display good agreement at $s/\delta_0 = 8.4$ and 14.0. At $s/\delta_0 = 8.4$, the expansion region is confined between n ≈ 25 mm and n ≈ 40 mm, while at $s/\delta_0 = 14.0$ the bottom of the expansion region is evident at n ≈ 40 mm. Of all the measurement locations, the measured and computed profiles at $s/\delta_0 = 19.3$ exhibit the worst agreement. The measured velocities are consistently less than the computed velocities at the same normal elevation.

It should be recalled that the computations do not include viscous effects. Viscous effects, which diffuse the retardation associated with the no-slip condition away from the surface, would tend to cause the measured velocities to be less than those computed with the inviscid method of characteristics. Similarly, the outward turbulent transport of low speed, near-wall fluid would result in a retardation of the velocity profile. Effects such as these are the very reason the method of characteristics cannot be used to compute general boundary layer flows. If an equilibrium, turbulent boundary layer is to be reestablished downstream of the expansion, the observed retardation of the velocity profile relative to the computed, inviscid profile must occur.

Mean velocity profiles obtained from the method of characteristics computations downstream of the 14° centered expansion corner are plotted alongside the mean velocity profiles measured with LDV in Fig. 7. Results are presented for $s/\delta_0 = 0.3, 1.5, 2.8, 8.4$, and 14.0.

The measured and computed profiles obtained at $s/\delta_0 = 0.3$ (s = 2.5 mm) exhibit good agreement everywhere except n < 3 mm. Since the flat plate freestream velocity is used to normalize the velocity parallel to the inclined surface, the freestream above the expansion has a normalized velocity of $U_0 \cos 14°/U_0$, which equals 0.970. Both profiles exhibit good agreement with this value.

A few comments concerning the deviation near the surface at $s/\delta_0 = 0.3$ between the measured and computed profiles are in order. First, the computations have difficulties near the wall. This is partly due to the fact that near the wall viscous effects are non-negligible and, as a result, the computations do not model the flow as well. Difficulties also arise because LDV measurements were possible only for n ≥ 2 mm. This caused the incoming profile information to be incomplete. Beneath n = 2 mm, a linear interpolation between

17

the lowest measured point and the surface (where a Mach number of unity was assumed, as discussed earlier) was used to complete the incoming profile. This may have given rise to inaccuracies. These two lines of thought suggest the computed profile is the source of the discrepancy.

Because of the rapid nature of the expansion near the surface, it is also likely that the seed particles near the surface have not fully responded to the rapid expansion at s/δ_0 = 0.3. If a Mach number of 1.5 and stagnation temperature of 280 K are taken as representative values for n < 2 mm, Prandtl-Meyer theory indicates a 14° expansion will result in an acceleration from 420 m/s to 500 m/s. This change in velocity is larger than that encountered further from the boundary. At a stagnation temperature of 280 K, a Mach 3 freestream is accelerated from 600 m/s to 650 m/s. In addition to the flow acceleration, the particles must respond to the change in flow direction. Because of the diverging geometry of the centered expansions, the particles near the surface have less time to respond to the expansion. These facts suggest that problems with particle response, if incurred, would most likely appear near the surface close to the expansion region.

The computed and measured profiles obtained at s/δ_0 = 1.5 (s = 13.7 mm) downstream of the 14° centered expansion corner display significant disagreement between n = 3 mm and n = 10 mm, which corresponds roughly to the portion of the profile within the expansion region. This may indicate the seed particles were not able to respond rapidly enough to the expansion. The agreement between the computed and measured profile at s/δ_0 = 2.8 (s = 25.4 mm) is quite good, suggesting any particle lag encountered further upstream is no longer present. As with the profiles for the 7° centered expansion, a 'knee' is present in the profile due to the acceleration through the expansion.

The computed and measured profiles obtained at s/δ_0 = 14.0 (s =127.0 mm) downstream of the 14° centered expansion corner display maximum deviations of about 5% of the normalizing velocity. Similar agreement was obtained at s/δ_0 = 8.4 (s = 76.2 mm). Despite the deviations, the measured profiles at s/δ_0 = 8.4 and 14.0 are very similar in shape to the computed profiles at both locations. As was the case downstream of the 7° centered expansion, it seems that viscous effects and/or turbulent activity are causing the measured profile to fall below the computed profile.

18

In general, the computed velocity profiles exhibit good agreement with the profiles measured with LDV, indicating the evolution of the mean velocity profile in the outer layer is essentially inviscid. However, this situation is not perpetual. It appears that at approximately $s/\delta_0 \simeq 10$, viscous and/or turbulent effects cause the velocity profile to be retarded relative to the profile obtained with the inviscid computation. The good general agreement between the computed and measured velocity profiles downstream of the centered expansions also indicates that particle lag should not be a concern downstream of the two gradual expansions where the acceleration is less rapid.

3. Laser Doppler Velocimetry Measurements

Flat Plate Boundary Layer

Profiles of normalized mean streamwise velocity obtained in the flat plate boundary layer at locations separated by 127.0 mm in the streamwise direction are presented in Fig. 8. The upstream location is 12.7 mm of the beginning of the convex surface curvature for the four expansion models ($s = -12.7$ mm $= -1.4\delta_0$). The downstream measurements were obtained 127.0 mm further downstream with the flat plate extension installed in the test section ($s = 114.3$ mm $= 12.6\delta_0$). The normal coordinate is plotted in units of millimeters. At $s = 127.0$ mm, the velocity at a given normal elevation is noticeably less than that of the upstream profile.

As shown in Fig. 9, if the normal coordinate is normalized by the local boundary layer thickness (point at which the streamwise velocity is 99% of the freestream velocity, $\delta_{99\%}$), the profiles collapse. At $s = -12.7$ mm, $\delta_{99\%} = 9.1$ mm and at $s = 127.0$ mm, $\delta_{99\%} = 12.3$ mm. This shows the flat plate boundary layer thickness grows at a rate of 1 mm per every 46 mm of streamwise distance. The good collapse of the profiles confirms the boundary layer is fully-developed.

Streamwise and normal turbulence profiles obtained in the flat plate boundary layer at the same two streamwise locations are presented in Figs. 10 and 11, respectively. The standard deviation of the velocity fluctuations normalized by the freestream velocity is plotted on the horizontal axis. As with the mean velocities, the profiles collapse quite well when the normal coordinate is normalized by the local boundary layer thickness ($\delta_{99\%}$). In

19

these and all other turbulence profiles, the turbulence quantities (in this case the standard deviation of the velocity fluctuations) are normalized using the freestream velocity. Figs. 10 and 11 show σ_u is much larger than σ_v. In fact, plots of anisotropy (σ_u/σ_v) show σ_u is approximately twice σ_v for $n/\delta_0 < 0.7$. As expected, the anisotropy decreases at larger normal elevations until the freestream is reached, where the fluctuations are isotropic.

Reynolds shear stress ($\overline{u\,v}/U_0^2$) profiles for the flat plate boundary layer are presented in Fig. 12. As with the standard deviation of the streamwise and normal velocity fluctuations (which are the square root of the longitudinal and normal Reynolds stresses), the Reynolds shear stress decreases with increasing normal distance. This is a result of the confinement of the turbulence production to the near-wall region where there are large mean velocity gradients.

The shear stress correlation coefficient or turbulence structure parameter, $\overline{u\,v}/(\sigma_u\sigma_v)$, is also of interest. If streamwise and normal velocity fluctuations were perfectly negatively correlated, this quantity would assume a value of -1. The profile of Fig. 13 shows that for $n/\delta_0 < 0.7$, the correlation coefficient is approximately -0.4, which agrees quite well with the results obtained by Smits et al. [1989] in a Mach 2.8 equilibrium, turbulent boundary layer. The correlation coefficient is less meaningful in the freestream because $\overline{u\,v}$, σ_u, and σ_v are very small.

Though only two velocity components were measured, it is still insightful to look at the 'two-component' turbulent kinetic energy. The normalized turbulent kinetic energy per unit mass $[\overline{u^2+v^2}/U_0^2]$ in the flat plate boundary layer at the two streamwise locations is presented in Fig. 14. Given the confinement of the turbulence production to the near-wall region, it is not surprising that the turbulent kinetic energy decreases with increasing normal distance.

The streamwise evolution of other turbulence parameters such as the streamwise turbulent transport of turbulent kinetic energy $[\overline{u(u^2+v^2)}/U_0^3]$, the normal turbulent transport of turbulent kinetic energy $[\overline{v(u^2+v^2)}/U_0^3]$, streamwise skewness ($\overline{u^3}/\sigma_u^3$), normal

skewness ($\overline{v^3}/\sigma_v^3$), streamwise flatness ($\overline{u^4}/\sigma_u^4$), and normal flatness ($\overline{v^4}/\sigma_v^4$) are presented by Arnette [1995]. Consistent with the results presented here, the profiles of these turbulence quantities exhibit good collapse between the two streamwise locations, giving further indication that the incoming boundary layer is fully-developed. Profiles of these quantities obtained at s = -12.7 mm are presented in conjunction with the measurements obtained downstream of the expansion regions.

The streamwise and normal turbulent transport of the two-component turbulent kinetic energy are negative and positive, respectively, within the boundary layer. Not surprisingly, this shows the turbulent transport to be dominated by the outward displacement of fluid closer to the boundary (which would possess a smaller streamwise velocity). Higher transport levels near the wall reflect the concentration of the turbulent kinetic energy near the surface.

Boundary Layer Downstream of the 7° Centered Expansion

The evolution of the mean velocity profiles downstream of the 7° centered expansion corner, which were previously compared to the results obtained with the method of characteristics, are presented in Fig. 15. Although the plot is crowded, the different stages in the evolution of the mean velocity profile are illustrated. At $s/\delta_0 = 1.5$, the flow has passed through the expansion region beneath $n/\delta_0 = 0.7$ and been accelerated. Above the expansion, the profile is simply that of the incoming flow. It is worth noting that the top of the boundary layer at $s/\delta_0 = 1.5$ occurs at about $n/\delta_0 = 1.5$. Although the boundary layer is far from equilibrium at this point, the 'boundary layer thickness' has increased by approximately 50% over a streamwise distance of only $1.5\delta_0$.

At $s/\delta_0 = 2.8$, most of the boundary layer has passed through the expansion region. Beneath $n/\delta_0 = 0.7$, the profiles at $s/\delta_0 = 1.5$ and 2.8 are essentially identical. Above $n/\delta_0 = 0.7$, the downstream profile has been accelerated through the expansion. Between $s/\delta_0 = 2.8$ and 8.4, more flow above $n/\delta_0 = 1.5$ enters the expansion and is accelerated. Beneath the expansion, the profile remains unchanged between $s/\delta_0 = 1.5$ and 8.4. At $s/\delta_0 = 14.0$, the velocity profile has begun to show the first signs of retardation due to viscous effects and

21

the normal outward turbulent transport of near-wall fluid. The retardation is most noticeable for $n/\delta_0 < 0.5$. Further downstream of the corner at $s/\delta_0 = 19.3$, the retardation of the velocity profile has diffused outward to approximately $n/\delta_0 = 2$. At this location, the velocity profile again appears similar to that of an equilibrium, turbulent boundary layer.

It is interesting to note that the 'retardation' of the velocity profile which occurs between the two most downstream locations in Fig. 15 is similar to that encountered during normal boundary layer growth. In the flat plate boundary layer velocity profiles of Fig. 8, where the normal coordinate is not nondimensionalized with a local length scale, the downstream profile is also 'retarded' relative to the upstream profile. This indicates that between $s/\delta_0 = 14.0$ and 19.3 downstream of the 7° centered expansion, the boundary layer experiences something similar to normal growth.

In order to determine whether or not the boundary layer has recovered the equilibrium velocity profile of the incoming boundary layer, local length and velocity scales must be used to nondimensionalize the profiles. This is addressed further below after an introductory consideration of the expansions' effects on the turbulence.

The downstream evolution of the standard deviation of the streamwise velocity fluctuations (normalized by the incoming freestream velocity), where the normal coordinate is nondimensionalized with the incoming boundary layer thickness, is presented in Fig. 16. Because of the large changes in local boundary layer thickness, it is difficult to draw solid conclusions. Given the dilatation encountered across the expansion region, it would be nominally expected that all turbulence measures would be lower than in the incoming boundary layer. At $s/\delta_0 = 1.5$, the streamwise turbulence levels near the surface are lower than the levels encountered near the surface in the incoming boundary layer.

Further decreases are sustained near the surface between $s/\delta_0 = 1.5$ and 2.8 and between $s/\delta_0 = 2.8$ and 8.4. The turbulence levels near the surface finally begin to recover between $s/\delta_0 = 8.4$ and 14.0. Further recovery is evident between $s/\delta_0 = 14.0$ and 19.3, but the turbulence levels remain far below those measured in the incoming boundary layer. If the profiles were normalized with a local reference velocity instead of the incoming

freestream velocity, they would be even smaller since any reference velocity would increase across the expansion region.

Seemingly puzzling results are obtained away from the surface in Fig. 16, where the turbulence levels are higher downstream of the expansion than in the incoming boundary layer at the same n/δ_0. This is a result of the normalization methodology. Since the boundary layer increases in thickness across the expansion and the normal coordinate is not nondimensionalized with *local* length scales, points deeper in the boundary layer (where there is more turbulent activity) occur at larger n/δ_0 values with increasing downstream distance. This can be remedied by nondimensionalizing the normal coordinate with a local length scale. The obvious choice is the boundary layer thickness, which is normally derived from the point where the velocity is a certain percentage of the freestream velocity. Unfortunately, at some locations the distortion of the mean velocity profile caused by the expansion region makes it impossible to locate the boundary layer thickness in this way (e.g. the profile at $s/\delta_0 = 2.8$ has a knee near the top of the boundary layer).

It was decided to use the normal elevation at which the peak in the streamwise flatness ($\overline{u^4}/\sigma_u^4$) occurs as the local length scale (denoted by δ_{flatness}). Several alternative quantities exist, such as the normal elevation at which the standard deviation of the velocity fluctuations or the Reynolds shear stress decrease to freestream levels. The flatness method was chosen for two main reasons: 1) the streamwise flatness profile is altered very little by the various expansion regions and 2) the streamwise flatness profile displayed an easily identified, sharp peak indicating the top of the boundary layer turbulence at all of the measurement locations. These observations do not hold for the other turbulence quantities. Profiles of most turbulence quantities are altered dramatically by the expansion regions and, further, most quantities exhibit gradually decreasing levels at the top of the boundary layer (e.g. the Reynolds shear stress).

In the incoming boundary layer, the flatness peak occurs at $n/\delta_0 = 1.0$. Since the flatness is commonly used to calculate intermittency with the relation $I = 3/(\overline{u^4}/\sigma_u^4)$, it is not surprising that it is a good indicator of boundary layer thickness.

23

The velocity profiles are replotted in Fig. 17 with the normal coordinate nondimensionalized by $\delta_{flatness}$. As expected, the top of the boundary layer occurs at $n/\delta_{flatness} \cong 1.0$ at all measurement locations where the velocity profile resembles that of an equilibrium boundary layer. The $\delta_{flatness}$ values obtained at the various measurement locations give a good reading of the how much the boundary layer thickness increases across the expansion region. At $s/\delta_0 = 1.5, 2.8, 8.4, 14.0$, and 19.3, $\delta_{flatness} / \delta_0 = 1.2, 1.7, 1.5, 1.9$, and 2.0. These results suggest $\delta_{flatness}$ undergoes a complex evolution downstream of the expansion. It increases across the expansion, decreases between $s/\delta_0 = 2.8$ and 8.4, and then increases downstream of $s/\delta_0 = 8.4$. As would be expected, $\delta_{flatness}$ increases monotonically downstream of the other three expansion regions. The unique behavior for the 7° centered expansion is probably the result of a questionable $\delta_{flatness}$ value at $s/\delta_0 = 2.8$. Two observations are relevant. At $s/\delta_0 = 2.8$, the top of the boundary layer falls within the expansion region (as indicated by the mean velocity profile of Fig. 15). As a result, the seed particles may not be faithfully tracking the flow at this location. Secondly, $\delta_{flatness}$ is based on the fourth order moment of the streamwise velocity fluctuations and higher order moments like this are sensitive to even slightly imperfect particle response. In average schlieren images, the boundary layer thickness appears to increase by a factor of about 1.5 across the expansion region, which exhibits fairly good agreement with the increases in $\delta_{flatness}$ sustained at $s/\delta_0 = 1.5$ and 8.4. It is also interesting to note that the maximum velocity of $1.04U_0$ measured downstream of the expansion at $s/\delta_0 = 14.0$ is identical to the value obtained from Prandtl-Meyer theory (see Table 1).

Having established a suitable normal length scale, whether or not the mean velocity profile is fully recovered at the last measurement station can be addressed. The velocity profiles obtained at the three most downstream locations, nondimensionalized such that the value at $n/\delta_{flatness} = 1.0$ matches the flat plate profile (which is normalized by the incoming freestream velocity), are presented in Fig. 18. The profiles obtained at $s/\delta_0 = 1.5$ and 2.8 have not been included because of obvious deviations from the equilibrium profile. All three of the profiles in Fig. 18 are similar to the incoming profile. In fact, the profile at $s/\delta_0 = 19.3$ matches the incoming profile to within about 1% of the reference value, indicating the velocity profile is essentially recovered.

Recovery of the mean velocity profile is not enough to declare the boundary layer fully recovered from the expansion. The streamwise turbulence profiles are replotted in Fig. 19 with the normal coordinate nondimensionalized by $\delta_{flatness}$. When plotted in this manner, the evolution of the turbulence profiles is more easily understood. At $s/\delta_0 = 1.5$, the turbulence level drops below the incoming boundary layer profile for $n/\delta_{flatness} < 0.8$. As expected, the portion of the boundary layer that has encountered the expansion sustains decreases in turbulence levels. Between $s/\delta_0 = 1.5$ and 2.8, further decreases are sustained across the entire thickness of the boundary layer. Between $s/\delta_0 = 2.8$ and 8.4, substantial decreases occur in the bottom half of the boundary layer, while the reductions in the top half of the boundary layer are less severe. Although the reductions are caused by the expansion region, the large streamwise extent of the reductions shows that the boundary layer does not respond instantaneously to the perturbation. Between $s/\delta_0 = 8.4$ and 14.0 no significant reductions occur and the levels nearest the surface have begun to increase. The recovery continues between $s/\delta_0 = 14.0$ and 19.3. The increases occupy more of the boundary layer at the downstream location, suggesting the recovery 'grows outward' from the surface. Nevertheless, the turbulence levels at $s/\delta_0 = 19.3$ remain far below those of the incoming boundary layer.

Measurements further downstream of the expansion corner would be desirable. Unfortunately, optical access to the test section was a limiting factor. Even had there been uninhibited optical access, the size of the test section limited the inclined models to lengths far shorter than it appears would be required for full recovery.

The evolution of the standard deviation of the normal velocity fluctuations normalized by the incoming freestream velocity is presented in Fig. 20. The main trends are the same as encountered with the streamwise fluctuations; 1) large decreases are sustained deeper in the boundary layer and less significant reductions are encountered higher in the boundary layer and 2) the turbulence levels begin to recover at the last two measurement locations.

Sharp reductions near the surface were also observed by Dussauge and Gaviglio [1987] in their investigation of the 12° expansion of a Mach 1.76 turbulent boundary layer and Smith and Smits [1991] in their investigation of the 20° expansion of a Mach 2.8

turbulent boundary layer. Since the region near the surface is associated with small scale, high frequency turbulence; and small scale turbulence is usually associated with fluctuating vorticity, it is not surprising that the turbulence near the wall is significantly damped by the expansion region. The dilatation encountered across the expansion dictates that vortical elements will increase in scale. When this occurs, conservation of angular momentum dictates the vorticity associated with these motions will be reduced.

The decreases sustained in the outer portions of the boundary layer in Figs. 19 and 20 are much less severe than those sustained near the surface. This is testament to the fact that the outer layer turbulence is dominated by large scale turbulent motions, which are much more coherent than the small scale turbulent motions near the surface and possess a much larger response time scale. Although the turbulence associated with the large scale motions of the outer layer appears to be weakened by the expansion, the turbulent structures are not totally eliminated. These trends fit quite well with the observations made in conjunction with FRS visualizations (Fig. 4), where the large scale structures were seen to maintain their identity across the expansion [Arnette et al., 1995]. Idealizing the large scale motions as spanwise vortices, the observed decreases are not surprising since the structures increase in scale.

The more significant reductions in σ_v than σ_u just downstream of the expansion results in increased anisotropy values at $s/\delta_0 = 1.5$. Further downstream the anisotropy falls below that of the incoming boundary layer, showing that the boundary layer does not recover the equilibrium turbulence structure of the incoming boundary layer in a monotonic fashion. As with the turbulence levels, the recovery of the profile towards the equilibrium profile first appears near the surface and progressively fills more of the boundary layer thickness with increasing downstream distance.

The evolution of the normalized Reynolds shear stress ($\overline{uv}/U_0^2$) downstream of the 7° centered expansion is presented in Fig. 21. Although the reductions in streamwise and normal turbulence levels become much less severe with increasing normal distance above the surface, the Reynolds shear stress is reduced dramatically across the entire boundary layer thickness. This may indicate the large scale motions sustain a significant decrease in

26

coherence across the expansion. In fact, in the profile at $s/\delta_0 = 1.5$ the Reynolds shear stress in part of the top half of the boundary actually changes sign. This indicates the turbulence has ceased to extract energy from the mean flow and is instead losing energy to the mean flow. As with the other turbulence quantities, sharp, rapid reductions are sustained near the surface. The Reynolds shear stress undergoes a significant amount of recovery in the top half of the boundary layer between $s/\delta_0 = 1.5$ and 2.8, while no hint of recovery occurs in the bottom half of the boundary layer. This also indicates the idea of a monotonic recovery which grows outward from the surface is not entirely correct. Downstream of $s/\delta_0 = 2.8$, the recovery does appear to grow outward from the surface, with significant increases near the surface which diffuse outward through the rest of the boundary layer.

The evolution of the shear correlation coefficient $[\overline{uv}/(\sigma_u \sigma_v)]$ is presented in Fig. 22. Similar to the results for the flat plate boundary layer, the correlation coefficient is less meaningful in the freestream because $\overline{u\,v}$, σ_u, and σ_v are small. If the turbulence structure of the boundary layer remained unchanged during its passage through the expansion and the turbulent fluctuations were simply reduced in magnitude, one would expect the correlation coefficient to remain essentially unchanged. This is certainly not the case in Fig. 22, indicating the boundary layer structure undergoes a complex alteration across the expansion. However, the profile at $s/\delta_0 = 19.3$ is more similar to that of the incoming boundary layer, suggesting the boundary layer is recovering the turbulence structure of the incoming boundary layer.

The evolution of the normalized two-component turbulent kinetic energy per unit mass $[\overline{(u^2 + v^2)}/U_0^2]$ is presented in Fig. 23. As with the streamwise and normal turbulence intensities, sharp reductions are incurred near the surface and less substantial reductions are encountered in the top half of the boundary layer. Initial indications of recovery are evident near the surface at $s/\delta_0 = 8.4$. Although substantial recovery occurs near the surface at $s/\delta_0 = 14.0$ and 19.3, the turbulent kinetic energy at $s/\delta_0 = 19.3$ remains well below that found in the incoming boundary layer.

The streamwise and normal turbulent transport of the two-component turbulent kinetic energy [$\overline{u(u^2+v^2)}/U_0^3$ and $\overline{v(u^2+v^2)}/U_0^3$, respectively] downstream of the 7° centered expansion are presented in Figs. 24 and 25. As for the profile obtained in the flat plate boundary layer, the streamwise transport is negative and the normal transport is positive, indicating the transport of turbulent kinetic energy can be associated mainly with the outward displacement of turbulence originally located closer to the boundary. The streamwise transport near the surface vanishes almost immediately downstream of the expansion and does not begin to increase again until downstream of $s/\delta_0 = 8.4$. However, the reductions in the streamwise transport further from the surface occur much more slowly, with no sign of recovery at $s/\delta_0 = 19.3$. This offers further evidence that the large scale structures survive the expansion. The normal transport (Fig. 25) undergoes a very different evolution. Reductions in the normal transport are essentially complete at $s/\delta_0 = 1.5$ across the entire boundary layer thickness.

The evolution of the streamwise ($\overline{u^3}/\sigma_u^3$) and normal skewness ($\overline{v^3}/\sigma_v^3$) is presented in Figs. 26 and 27, respectively. Within the incoming boundary layer ($s/\delta_0 = -1.4$), the streamwise skewness is negative and the normal skewness is positive. This is again consistent with the observation that the largest velocity fluctuations tend to be negative in the streamwise direction and positive in the normal direction. The skewness magnitudes in the freestream are inflated because σ_u and σ_v are small. Downstream of the expansion, the streamwise skewness profile remains essentially unchanged from that of the incoming boundary layer. However, the normal skewness is altered dramatically across the expansion and remains significantly different than the incoming profile at $s/\delta_0 = 19.3$. The normal skewness becomes less positive across the boundary layer, which is consistent with less significant positive v fluctuations.

Streamwise and normal flatness profiles [$\overline{u^4}/\sigma_u^4$ and $\overline{v^4}/\sigma_v^4$ respectively] are presented in Figs. 28 and 29. For the incoming boundary layer, the streamwise and normal flatness profiles are very similar in shape, but the streamwise flatness undergoes a larger change across the boundary layer than the normal flatness. As cited previously, intermittency is

28

often computed from the streamwise flatness with the relation $I \approx 3 / (\overline{u^4} / \sigma_u^4)$. Using this relation, the profiles of Fig. 28 at $s/\delta_0 = -1.4$ and all measurement locations downstream of the 7° centered expansion indicate the boundary layer is always turbulent below $n/\delta_0 = 0.5$. As expected, the intermittency decreases with increasing normal elevation.

Given the nondimensionalization of the normal coordinate with $\delta_{flatness}$, the streamwise flatness profiles must necessarily exhibit good collapse at all of the measurement locations in both the incoming and perturbed boundary layers. This was the case for all four of the expansions.

Downstream of the 7° centered expansion, the normal flatness (Fig. 29) is reduced within the boundary layer, again suggesting that positive v fluctuations become less prominent downstream of the expansion. The large alteration of the normal skewness and flatness profiles relative to their streamwise counterparts coupled with the more severe reductions of the normal turbulence intensity than the streamwise turbulence intensity all seem to indicate that normal velocity fluctuations are more severely affected by the expansion than streamwise velocity fluctuations.

Boundary Layer Downstream of the 14° Centered Expansion

Not surprisingly, the evolution of the boundary layer downstream of the 14° centered expansion displays strong similarities to that downstream of the 7° centered expansion. Inviscid theory gives density ratios across the 7° and 14° expansions of 0.66 and 0.42, respectively (Table 1). Given the more severe bulk dilatation associated with the larger expansion, one would expect more severe reductions in the various turbulence measures.

The evolution of the mean velocity profile downstream of the 14° centered expansion is presented in Fig. 30, where the velocities are nondimensionalized by the freestream velocity of the Mach 3 incoming flow and the normal coordinate is nondimensionalized with the local $\delta_{flatness}$. The profiles clearly illustrate the acceleration encountered across the expansion. The largest measured velocity of $1.06U_0$, which occurs at $s/\delta_0 = 14.0$, is slightly smaller than the value of $1.08U_0$ obtained from Prandtl-Meyer theory (see Table 1). In order to see if the mean velocity profiles had fully recovered by the last measurement

station, the two most downstream profiles are replotted with the incoming velocity profile in Fig. 31. In this figure, the velocities have been nondimensionalized with a local reference velocity so that the profiles coincide at $n/\delta_{\text{flatness}} = 1.0$. The recovery is quite slow, at $s/\delta_0 = 14.0$ the profile remains far from equilibrium. Unfortunately, measurements further downstream were not possible.

At $s/\delta_0 = 0.3$, 1.5, 2.8, 8.4, and 14.0, $\delta_{\text{flatness}} / \delta_0 = 1.1$, 1.3, 1.6, 2.1, and 2.5. As expected, the boundary layer 'flatness thickness' monotonically increases downstream of the 14° centered expansion. In average schlieren images, the boundary layer thickness increases by a factor of about 2.0, which compares well to the increase in δ_{flatness} at $s/\delta_0 = 2.8$.

The evolution of the standard deviations of the streamwise and normal velocity fluctuations are presented in Figs. 32 and 33, which can be compared directly to the results of Figs. 19 and 20 for the 7° centered expansion. The general evolution of the streamwise turbulence levels is very similar for the two cases, but the reductions are more prolonged and more severe for the larger expansion angle. For instance, the streamwise turbulence near the surface at $s/\delta_0 = 8.4$ downstream of the 7° centered expansion is about 4% and the levels have begun to increase again. However, at $s/\delta_0 = 8.4$ downstream of the 14° centered expansion, the turbulence levels are about 3% and the levels have still not begun to increase. The same trends hold for the normal turbulence levels, where the reductions downstream of the 14° centered expansion are more severe than those encountered downstream of the 7° centered expansion. Similar to the 7° centered expansion, the anisotropy (σ_u/σ_v) is reduced downstream of the 14° centered expansion as a result of the more significant reductions for the streamwise turbulence levels than for the normal turbulence levels.

The measurements obtained at the two points nearest the surface at $s/\delta_0 = 0.3$ in Figs. 32 and 33 appear to be of questionable merit, which is undoubtedly related to the questionable seed particle response very near the expansion region. Accordingly, these points have been eliminated from the plots of the other turbulence quantities downstream of the 14° centered expansion.

The evolution of the Reynolds shear stress ($\overline{uv}/U_0^2$) is presented in Fig. 34. The shear stress undergoes large reductions very rapidly. As expected, the reductions are more

30

severe than those encountered downstream of the 7° centered expansion (Fig. 21). The Reynolds shear stress actually changes sign across the entire boundary layer thickness, indicating the turbulence has ceased to extract energy from the mean flow. In fact, the shear stress does not again become negative until near the surface at $s/\delta_0 = 8.4$. These results indicate the 14° centered expansion has caused what might be termed 'reverse transition', as evidenced by the destruction of all evidence of coherent turbulent activity.

Though not presented here, the evolution of the shear correlation coefficient $[\overline{uv}/(\sigma_u \sigma_v)]$ downstream of the 14° centered expansion is consistent with other results in that the profiles are altered more significantly downstream of the stronger expansion. The same holds true for evolution of the two-component turbulent kinetic energy per unit mass $[\overline{(u^2 + v^2)}/U_0^2]$, which is presented in Fig. 35. The turbulent kinetic energy decreases essentially monotonically all the way to the last measurement station ($s/\delta_0 = 14.0$). Initial signs of recovery are apparent near the surface at $s/\delta_0 = 14.0$. The 14° centered expansion represents the strongest 'perturbation' since it represents the large expansion angle of the two rapid (centered) expansions. Almost all of the turbulent kinetic energy has been destroyed at $s/\delta_0 = 8.4$. This also supports the notion that a reverse transition has occurred. As would be expected, the destruction of the turbulent kinetic energy occurs much more gradually than the sign change of the Reynolds shear stress.

Given the strong reductions in the Reynolds shear stress in Fig. 34, the boundary layer downstream of the 14° centered expansion would probably meet the criterion for relaminarization put forth by Narasimha and Sreenivasan [1975] for incompressible boundary layers subjected to favorable pressure gradients which states that a relaminarized boundary layer is one in which the Reynolds stresses have ceased to be important to the evolution of the mean flow. Although the collapse of the Reynolds shear stress suggests the turbulence is rendered essentially incoherent by the expansion, the turbulent velocity fluctuations are not destroyed immediately downstream of the expansion (witness Figs. 32 and 33). Accordingly, the term reverse transition is adopted here instead of relaminarization. The occurrence of reverse transition is taken to be indicated by a change in sign of the Reynolds

shear stress (which indicates that the mean flow is extracting energy from the turbulence) and a sharp reduction in the turbulent kinetic energy levels.

Though not presented here, the evolution of the streamwise and normal turbulent transport of the two-component turbulent kinetic energy (per unit mass) $[\overline{u(u^2+v^2)}/U_0^3$ and

$\overline{v(u^2+v^2)}/U_0^3$, respectively] were examined. The streamwise transport term is reduced at each successive measurement location. In fact, the magnitudes of the reductions sustained downstream of the 7° (Fig. 24) and 14° centered expansions at similar s/δ_0 locations are approximately equal. The rapid destruction of the normal transport of turbulent kinetic energy downstream of the 14° centered expansion also compares very favorably to that incurred downstream of the 7° centered expansion, though indications of near-surface recovery are delayed until further downstream for the 14° case.

Similar to the 7° centered expansion, the streamwise skewness $(\overline{u^3}/\sigma_u^3)$ and flatness $(\overline{u^4}/\sigma_u^4)$ profiles are essentially unchanged at all of the measurement locations and the normal skewness $(\overline{v^3}/\sigma_v^3)$ and flatness $(\overline{v^4}/\sigma_v^4)$ profiles are altered significantly. While the normal skewness became less positive downstream of the 7° expansion (Fig. 27), it actually changes sign through most of the boundary layer thickness downstream of the 14° expansion.

An overall comparison of the results obtained downstream of the 7° and 14° centered expansions yields several interesting observations. As expected, measures of turbulence activity like turbulence intensities, turbulent kinetic energy, and Reynolds shear stress are reduced more significantly for the stronger expansion. In addition, it takes longer for the mean velocity profile to recover the incoming, equilibrium profile downstream of the 14° centered expansion. The 14° centered expansion causes a reverse transition in which the Reynolds shear stress changes sign very quickly after the expansion, but the 7° centered expansion is apparently not strong enough to cause a similar reversion. However, the evolution of the correlation coefficient, the normal and streamwise turbulent transport of turbulent kinetic energy, the normal and streamwise skewness, and the normal and

streamwise flatness are very similar downstream of the two expansions. These results suggest the alteration of the turbulence structure is similar for the two centered expansions.

Boundary Layer Downstream of the 7° Gradual Expansion

The evolution of the mean velocity profile downstream of the 7° gradual expansion, where the velocities have been normalized with the incoming Mach 3 freestream velocity, is presented in Fig. 36. For the 7° gradual expansion, the convex surface curvature has a duration of 55 mm ($6.0\delta_0$) measured along the surface. The freestream is accelerated to about $1.03U_0$ at $s/\delta_0 = 14.4$ and 19.2, which compares quite well to the value of 1.04 obtained from simple Prandtl-Meyer theory for a 7° expansion (see Table 1). To investigate the recovery of the mean velocity profile, the measurements are replotted in Fig. 37 with the velocities normalized such that the profiles downstream of the expansion match the incoming profile at $n = \delta_{flatness}$. Although none of the profiles exactly match that of the incoming boundary layer, the velocity profile is converging on the equilibrium profile with increasing downstream distance. At $s/\delta_0 = 14.4$ and 19.2, the velocity profiles' largest deviation from the incoming profile is only about 3%, which is about the same degree of agreement obtained at $s/\delta_0 = 14.0$ and 19.3 downstream of the 7° centered expansion (Fig. 18). This is true even though the gradual convex curvature does not end until $s/\delta_0 = 6.0$. Thus, the evolution of the mean velocity profile suggests the rate of imposition of the perturbation (radius of curvature for the convex surface) is not significant to the flow development downstream of the expansion.

At $s/\delta_0 = 6.0$, 8.3, 14.4, and 19.2, $\delta_{flatness}/\delta_0 = 1.4$, 1.5, 1.9, and 1.9. Similar to the boundary layer downstream of the 14° centered expansion, the boundary layer thickness downstream of the 7° gradual expansion increases monotonically. In average schlieren images, the boundary layer thickness appears to increase by a factor of about 1.5, which is in good agreement with the increase in $\delta_{flatness}$ obtained at the end of the convex curvature ($s/\delta_0 = 6.0$).

The standard deviations of the streamwise and normal velocity fluctuations are presented in Figs. 38 and 39, respectively. The evolution of the profiles downstream of the 7° gradual expansion is strikingly similar to that downstream of the 7° centered expansion.

33

In fact, both the streamwise and normal turbulence profiles obtained downstream of the $7°$ gradual expansion at $s/\delta_0 = 6.0$ (which corresponds to the end of the convex curvature) are essentially identical to those obtained downstream of the centered expansion at $s/\delta_0 = 2.8$. This shows that substantial turbulence reductions occur within the gradual expansion region. The profiles obtained at $s/\delta_0 = 19.3$ downstream of the centered and gradual expansions are essentially identical. These results suggest the differences in the evolution downstream of the $7°$ centered and gradual expansions are significant only for a short streamwise distance downstream of the expansions. Given these observations, it is not surprising that the anisotropy profile at $s/\delta_0 = 6.0$ downstream of the $7°$ gradual expansion is essentially identical to that obtained at $s/\delta_0 = 2.8$ downstream of the $7°$ centered expansion. As with the turbulence profiles, the anisotropy profile at $s/\delta_0 = 19.3$ downstream of the $7°$ centered and gradual expansions are essentially identical.

The evolution of the Reynolds shear stress in Fig. 40 is also very similar to that obtained downstream of the $7°$ centered expansion. The profile obtained at $s/\delta_0 = 6.0$ downstream of the gradual expansion compares most favorably with the profile obtained downstream of the centered expansion at $s/\delta_0 = 8.4$ (Fig. 21). This is quite different than the comparisons of the standard deviations of the velocity fluctuations, where the profile at $s/\delta_0 = 6.0$ downstream of the gradual expansion compared most favorably to the profile obtained at $s/\delta_0 = 2.8$ downstream of the centered expansion. Since the Reynolds shear stress is associated mainly with the large scale structures, this shows the structures respond differently to the centered and gradual expansions. The profiles at $s/\delta_0 = 19.3$ downstream of the centered and gradual expansions are essentially identical. The evolution of the shear stress correlation coefficient downstream of the $7°$ gradual expansion is equally similar to that obtained downstream of the $7°$ centered expansion.

The evolution of the two-component turbulent kinetic energy per unit mass is presented in Fig. 41. Since the anisotropy is not altered severely downstream of either the $7°$ centered or gradual expansions, it is not surprising that the evolution of the turbulent kinetic energy is similar to the evolution of the streamwise and normal turbulence intensities. Near the expansion regions, profiles obtained at a given streamwise distance downstream of the beginning of the gradual expansion region compare most favorably to

34

those obtained at a larger streamwise distance downstream of the centered expansion corner. Further downstream, there are no significant differences between profiles at the same distances downstream of the centered and gradual expansions. Similar remarks hold for the streamwise and normal turbulent transport of turbulent kinetic energy.

The evolution of the streamwise and normal skewness downstream of the 7° gradual expansion is essentially identical to that downstream of the 7° centered expansion. The streamwise skewness is not changed appreciably and the normal skewness becomes less positive. Similar to the other expansions, streamwise flatness profiles are similar at every measurement location. Also similar to the other cases, the normal flatness is reduced significantly.

Taken in their entirety, the measurements clearly indicate the boundary layer remains far from recovery at $s/\delta_0 = 19.3$, even though the mean velocity profile has essentially recovered the equilibrium profile of the incoming boundary layer. Similar to the 7° centered expansion, the 7° gradual expansion is not strong enough to induce the reverse transition observed for the 14° centered expansion.

Boundary Layer Downstream of the 14° Gradual Expansion

Given the strong agreement between the results obtained downstream of the 7° centered and gradual expansions, one might expect the results downstream of the 14° centered and gradual expansions to be essentially identical. Although this is the case for the most part, differences exist which serve to illustrate the nonlinear nature of the interaction of the turbulent boundary layer with the expansion regions.

The evolution of the mean velocity profile downstream of the 14° gradual expansion is presented in Fig. 42. The maximum velocity downstream of the expansion is about $1.06U_0$, which compares favorably to the value of $1.08U_0$ obtained from Prandtl-Meyer theory (see Table 1).   At $s/\delta_0 = 2.8$ ($\Delta\theta = 3.3°$), 8.6 ($\Delta\theta = 9.7°$), 12.1 ($\Delta\theta = 14.0°$), 13.5, 17.0, and 19.9,
$\delta_{flatness} / \delta_0 = 1.2, 1.6, 2.0, 2.1, 2.5$, and 2.8. Similar to the boundary layer downstream of the 14° centered expansion, the boundary layer thickness downstream of the 14° gradual expansion increases monotonically. In average schlieren images, the boundary layer

35

thickness appears to increase by a factor of about 2.0 across the expansion region, which exhibits very good agreement with the factor of 2.0 increase in δ_{flatness} at the end of the gradual surface curvature ($s/\delta_0 = 12.1$).

The velocity profiles are replotted in Fig. 43 where the velocities have been nondimensionalized to achieve agreement with the incoming profile at $n = \delta_{\text{flatness}}$. Although the profiles appear to be asymptotically approaching the incoming profile with increasing downstream distance similar to the other expansions, the velocity profile is still not fully recovered at the last measurement station ($s/\delta_0 = 19.9$).

The evolution of the standard deviation of the streamwise velocity fluctuations downstream of the 14° gradual expansion is presented in Fig. 44. Not surprisingly, strong similarities exist between the results obtained downstream of the 14° centered and gradual expansions. The profile obtained at $s/\delta_0 = 8.6$ downstream of the gradual expansion compares very favorably to that obtained at $s/\delta_0 = 2.8$ downstream of the centered expansion. This is true even though the flow at the surface has turned through only 10.0° of the 14° gradual expansion at $s/\delta_0 = 8.6$. The profiles obtained at $s/\delta_0 = 13.5$ and 16.8 downstream of the gradual expansion compare quite favorably with that obtained at $s/\delta_0 = 8.4$ downstream of the 14° centered expansion. The profile obtained at $s/\delta_0 = 19.9$ downstream of the gradual expansion is very similar to that obtained at $s/\delta_0 = 14.0$ downstream of the centered expansion. Unlike the 7° expansions where the turbulence profiles far downstream of the expansions were the same for the centered and gradual expansions at similar s/δ_0 locations, significant differences remain between the 14° centered and gradual expansions at the last measurement location. In addition, indications of recovery near the surface do not appear until $s/\delta_0 = 19.9$ for the gradual expansion, but are clearly present at $s/\delta_0 = 14.0$ for the centered expansion.

The standard deviation of the normal velocity fluctuations are presented in Fig. 45. As with the streamwise fluctuations, the best agreement between the profiles for the 14° centered and gradual expansions is achieved when the profiles downstream of the gradual expansion are compared to profiles located closer to the centered expansion corner. Similar observations hold for the anisotropy.

36

The evolution of the Reynolds shear stress downstream of the 14° gradual expansion is presented in Fig. 46. In general, the reductions (meaning less negative in Fig. 46) in the Reynolds shear stress are less severe downstream of the 14° gradual expansion than downstream of the 14° centered expansion. This is highlighted by the fact that while the sign of the Reynolds shear stress changes across the entire boundary layer thickness downstream of the centered expansion, it appears there is always a region downstream of the gradual expansion for which $\overline{uv} < 0$. Nevertheless, given the large reductions in the Reynolds shear stress levels, reverse transition is indicated.

It is interesting to note that the decreases in the Reynolds shear stress magnitudes downstream of the expansion occur much more rapidly than the decreases in the standard deviations of the streamwise and normal velocity fluctuations (σ_u and σ_v). Since the Reynolds shear stresses can be mainly associated with large scale structures, it is clear the large structures are much less coherent downstream of the expansion regions. The less rapid decay of the turbulence levels indicates the energy concentrated in large scales cascades into smaller scale, less coherent turbulence downstream of the expansion.

Though not shown here, the evolution of the shear correlation coefficient downstream of the gradual expansion is similar to the other turbulence quantities in that the closest match for a given profile downstream of the gradual expansion is found closer to the centered expansion corner.

The evolution of the two-component turbulent kinetic energy per unit mass is presented in Fig. 47. The disparity in the s/δ_0 location for matching profiles downstream of the centered and gradual expansions is clearly present. Accordingly, the streamwise location at which the turbulent kinetic energy displays an obvious increase near the surface occurs further downstream of the beginning of the gradual expansion than the centered expansion ($s/\delta_0 = 19.9$ for the gradual expansion versus $s/\delta_0 = 14.0$ for the centered expansion). This trend, which appears consistently in the evolution of the various turbulence profiles, almost suggests it would be most proper to define s = 0 for the gradual expansion near the center of the convex surface curvature. This was not the case, however, for the 7° expansions where the most closely matching profiles for the centered and gradual expansions occurred

37

at similar s/δ_0 locations (except very near the expansion regions). It is also significant in Fig. 47 that the lowest values of the turbulent kinetic energy are the same for the two 14° expansions, suggesting the overall reduction is sensitive mainly to total deflection angle.

Downstream of the 14° centered expansion, the streamwise transport undergoes a gradual reduction relative to the normal transport, which is destroyed almost immediately. Downstream of the 14° gradual expansion, reduction of the normal transport is less rapid. In fact, for the 14° gradual expansion, the reductions of the streamwise and normal transport quantities appear to proceed at roughly the same rate. The cited streamwise displacement between the most closely matched profiles downstream of the centered and gradual expansions is also present.

Similar to the other expansion cases, the streamwise skewness profiles exhibit fairly good collapse at all of the measurement locations. Also consistent with the results from the other expansions, the normal skewness is altered drastically and shows no sign of recovery at the last measurement location. In fact, the normal skewness actually changes sign, suggesting the most significant normal velocity fluctuations downstream of the expansion are towards the boundary. The evolution of the streamwise and normal flatness profiles is also similar to the other expansions. The streamwise flatness profiles collapse at all measurement locations, while the normal flatness levels are reduced.

The LDV measurements provide a large amount of quantitative information about the evolution of the boundary layer downstream of the four expansion regions. As a result, they offer a solid foundation from which to compare the effects of the various expansion regions.

Several expected results were obtained. Schlieren visualizations indicate that the boundary layer thickness increases by factors of approximately 1.5 and 2.0 across the 7° and 14° expansions, respectively. Taking the thickness defined by the peak in the streamwise flatness profile as a measure of the boundary layer thickness, the sustained increases compare favorably to the results from the schlieren visualizations. It was expected that the mean velocity profile would recover the equilibrium profile more quickly than the turbulence profiles, which was borne out by the results. Measures of turbulence activity decrease across the expansions and the severity of the reductions increases with expansion angle. In

38

addition, indications of recovery appear sooner (nearer the expansion regions) for the $7°$ expansions than for the $14°$ expansions.

Confirmation of the small scale quenching and large scale survival suggested by the fluctuating pressure measurements of Dawson et al. [1994] and the flow visualizations of Arnette et al. [1995] can be found in the results presented here. Just downstream of the expansion regions, Dawson et al. [1994] found that the fluctuation energy is much more heavily concentrated at low frequencies (associated with large scale structures) than in the incoming boundary layer. In the current study, large reductions in turbulence levels were sustained near the surface (where the turbulence activity is associated mainly with small scale motions) and less severe reductions were sustained further from the surface (where the turbulence activity is dominated by the large scale structures of the outer layer).

In designing the experiments, it was hoped that the downstream limit for the LDV measurements of $s/\delta_0 = 20$ would be far enough downstream to capture most of the boundary layer recovery. Although the mean velocity profile came close to full recovery for all of the expansions, the turbulence profiles remained far from full-recovery at the most downstream measurement locations. The general evolution of the boundary layer downstream of the four expansions might be best described as a rapid reduction of the incoming boundary layer turbulence levels followed by a slow recovery towards the equilibrium state. For all cases, it appeared the expansions have a more significant effect on normal velocity fluctuations than streamwise fluctuations. This is suggested by the fact that the streamwise skewness and flatness profiles were not altered significantly downstream of the expansions, but the normal skewness consistently became less positive (actually changing sign at some locations) and the normal flatness was decreased.

Interesting comparisons can be drawn between the four expansion cases. Perhaps the most interesting result is the apparent reverse transition of the boundary layer downstream of the two $14°$ expansions. Reverse transition is indicated by the change in sign of the Reynolds shear stresses (which implies that the normal transfer of energy from the mean flow to the turbulence has been reversed) and a substantial reduction of the turbulent kinetic energy levels. Although the two $7°$ expansions also seem to push the boundary layer

39

in the direction of reverse transition, it appears the smaller expansions are not strong enough to cause complete reversion.

For the 7° centered and gradual expansions, differences in the boundary layer evolution downstream of the expansion region induced by the different radii of curvature were fleeting. Profiles of the turbulence intensities obtained just downstream of the gradual expansion region compare most favorably to those obtained at smaller s/δ_0 values downstream of the centered expansion. However, at the most downstream measurement locations, profiles obtained downstream of the gradual expansion compare most favorably to the profiles obtained at similar s/δ_0 values downstream of the centered expansion. This was not true for the Reynolds shear stress, where the most favorable agreement between the centered and gradual expansion results was *always* obtained at similar s/δ_0 values.

For the 14° centered and gradual expansions, the differences in the boundary layer evolution resulting from the different radii of curvature had not disappeared at the most downstream measurement locations. Profiles downstream of the gradual expansion compare most favorably to profiles obtained at smaller s/δ_0 values downstream of the centered expansion corner. Defining $s = 0$ at the center of the gradual expansion corner would cause the most closely matched turbulence profiles downstream of the centered and gradual expansions to occur at similar s/δ_0 values. Unfortunately, this simple adjustment would not work for the 7° expansions. These observations suggest that radius of curvature effects are more long-lasting for the larger expansion angle.

CONCLUSIONS

The effects of four expansion regions [centered and gradual ($R/\delta_0 = 50$) expansions of $7°$ and $14°$] on a fully-developed, Mach 3 turbulent boundary layer were investigated. The incoming Mach 3 boundary layer was also studied extensively.

Measurements of streamwise and normal velocities obtained with Laser Doppler Velocimetry (LDV) show the boundary layer is altered dramatically across the expansion regions. Although essentially full recovery of the mean velocity profile was captured with the LDV measurements, the turbulence structure of the expanded boundary layers remains vastly different from that of the incoming boundary layer at the most downstream measurement locations ($s/\delta_0 \simeq 20$).

As expected, measures of turbulence activity such as turbulence intensities, Reynolds shear stress, and turbulent kinetic energy decreased across the expansion regions with more significant reductions for the stronger expansions. Although the sustained reductions in turbulence levels might be interpreted as a simple 'weakening' of the boundary layer turbulence due to the encountered dilatation, dimensionless turbulence quantities such as the anisotropy and shear stress correlation coefficient are also altered substantially. These changes show the turbulence structure of the boundary layer is altered across the expansions. Again, the changes were more substantial for the stronger expansions. It also appears that the turbulent fluctuations normal to the surface are affected more strongly by the expansions than the streamwise fluctuations. This was indicated by the fact that the streamwise skewness and flatness profiles were not altered significantly by the expansions, but the normal skewness consistently became less positive (actually changing sign at some locations) and the normal flatness was decreased downstream of the expansion regions.

The evolution of the boundary layer downstream of the four expansion regions might be best described as a rapid damping of the turbulence followed by a slow recovery towards the equilibrium state. The $14°$ centered and gradual expansions induce what is probably best described as reverse transition, which is characterized by a change in sign of the Reynolds shear stress and sharp reductions of the turbulent kinetic energy levels.

41

Although the 7° expansions also induce reductions in the Reynolds shear stress and turbulent kinetic energy levels, they are not strong enough to cause complete reversion.

For all of the expansions, recovery of the boundary layer turbulence initially appears near the surface. Given the confinement of turbulence production to the near-wall region where there are significant mean gradients, this is not surprising. Similar behavior was observed by Dussauge and Gaviglio [1987]. The initial appearance of the turbulence recovery displayed the expected dependence on expansion angle, appearing further downstream for stronger expansions.

There was another notable difference in the boundary layer evolution downstream of the 7° and 14° expansions. Comparisons of the turbulence profiles downstream of the 7° centered and gradual expansions suggest differences in boundary layer evolution attributable to the different radii of curvature were small, i.e. profiles obtained downstream of the gradual expansion compare most favorably to those obtained at similar distances downstream of the centered expansion. This convergence of the profiles at similar streamwise locations was not observed for the 14° expansions within the streamwise region where measurements could be acquired, giving some indication of nonlinear boundary layer response.

REFERENCES

Arnette, S.A., 1995, "The Effects of Expansion Regions of Supersonic Turbulent Boundary Layers," Ph.D. Dissertation, Dept. of Mechanical Engr.., The Ohio State University.

Arnette, S.A., Samimy, M., and Elliott, G.S., 1994, "The Effect of Expansion on Large Scale Structure Evolution in a Compressible Turbulent Boundary Layer," AIAA-94-2228.

Arnette, S.A., Samimy, M., and Elliott, G.S., 1995, "Structure of Supersonic Turbulent Boundary Layer After Expansion Regions," AIAA J., 33: 430-438.

Arnette, S.A., Samimy, M., and Elliott, G.S., 1996, "Two-Component Filtered Planar Velocimetry Measurements in the Compressible Turbulent Boundary Layer," AIAA-96-0305.

Bradshaw, P., 1974, "The Effect of Mean Compression or Dilatation on the Turbulence Structure of Supersonic Boundary Layers," J. of Fluid Mech., 63: 449-464.

Dawson, J.D., Samimy, M., and Arnette, S.A., 1994, "The Effects of Expansion on a Supersonic Boundary Layer: Surface Pressure Measurements ", AIAA J., 32: 2169-2177.

Dussauge, J.P. and Gaviglio, J., 1987, "The Rapid Expansion of a Supersonic Turbulent Flow: Role of Bulk Dilatation," J. of Fluid Mech., 174: 81-112.

Hampton, L.P. and White, R.A., 1983, "The Effect of Sudden Expansions and Compressions on Turbulent Boundary Layer Momentum Thickness in Supersonic Flow," University of Illinois, Dept. of Mechanical and Industrial Engineering, Report UILU ENG-83-4004.

Johnson, A.W., 1993, "Laminarization and Retransition of Turbulent Boundary Layers in Supersonic Flow", Ph.D. Dissertation, Yale University, New Haven, CT.

Morkovin, M.V., 1955, "Effects of High Acceleration on a Turbulent Supersonic Shear Layer," Heat Transfer and Fluid Mechanics Institute, Stanford University.

Narasimha, R. and Sreenivasan, K.R., 1973, "Relaminarization in Highly Accelerated Turbulent Boundary Layers," J. of Fluid Mech., 61: 417-447.

Narasimha, R. and Viswanath, P.R., 1975, "Reverse Transition at an Expansion Corner in Supersonic Flow," AIAA J., 13: 693-695.

Samimy, M., Arnette, S.A., and Elliott, G.S., 1994, "Streamwise Structures in a High Reynolds Number Supersonic Boundary Layer," Physics of Fluids, 6: 1081-1083.

Shapiro, A.H., 1953, The Dynamics and Thermodynamics of Compressible Flow, 2 Vols., The Ronald Press Company, New York, NY.

Smith, D.R. and Smits, A.J., 1991, "The Rapid Expansion of a Turbulent Boundary Layer in a Supersonic Flow," Theoret. Comput. Fl. Dyn., 2:319-328.

Smits, A.J. and Wood, D.H., 1985, "The Response of Turbulent Boundary Layers to Sudden Perturbations," Annual Review of Fluid Mechanics, 17: 321-358.

Smits, A.J., Spina, E.F., Alving, A.E., Smith, R.W., Fernando, E.M. and Donovan, J.F., 1989, "A Comparison of the Turbulence Structure of Subsonic and Supersonic Boundary Layers," Physics of Fluids A, 1: 1865-1875.

Smits, A.J., 1990, "New Developments in Understanding Supersonic Turbulent Boundary Layers," 12th Symposium on Turbulence, Rolla, Missouri.

Spina, E.F. and Smits, A.J., 1987, "Organized Structures in a Compressible Turbulent Boundary Layer," J. of Fluid Mech., 182: 85-109.

Tetervin, N., 1967, "An Analytical Investigation of the Flat Plate Turbulent Boundary Layer in Compressible Flow," NOLTR 67-39, Aerodynamics Research Report 286, Naval Ordnance Lab, Silver Springs, MD.

Thomann, H., 1968, "Effect of Streamwise Wall Curvature on Heat Transfer in a Turbulent Boundary Layer," J. of Fluid Mech., 33: 283-292.

Table 1. Flow quantity ratios across expansion derived from Prandtl-Meyer theory.

M_1	3.0	
Deflection	7°	14°
M_2	3.40	3.86
p_2/p_1	0.56	0.30
ρ_2/ρ_1	0.66	0.42
T_2/T_1	0.85	0.71
U_2/U_1	1.04	1.08
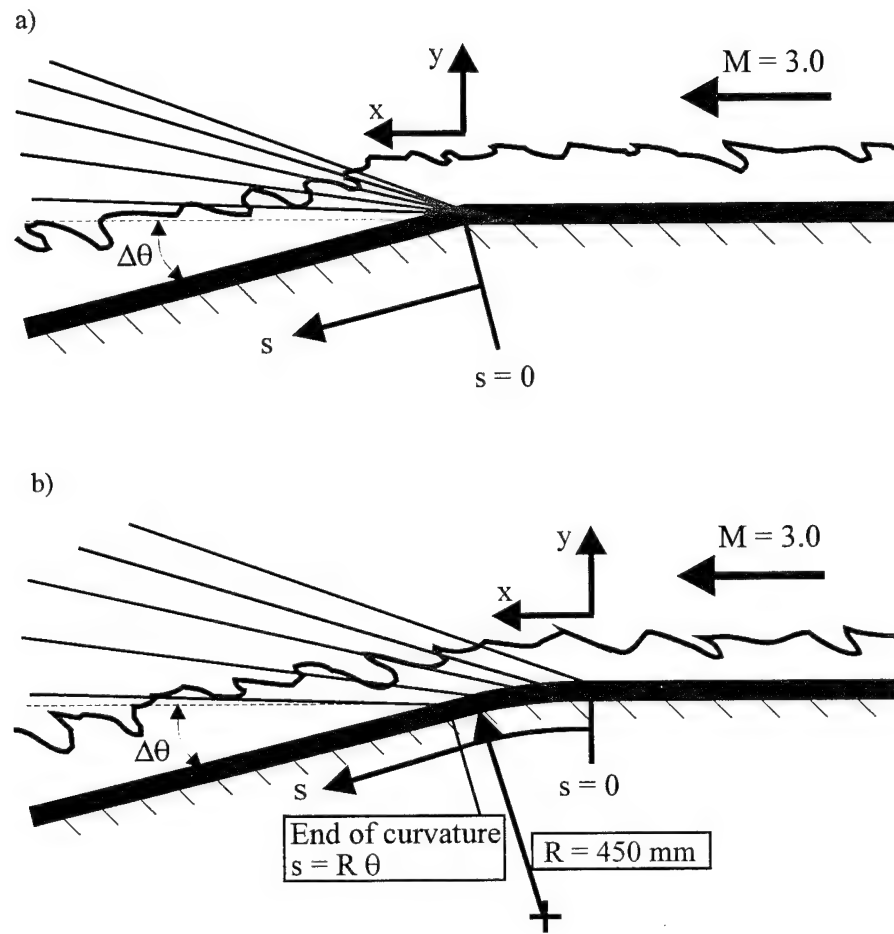
Figure 1. Schematics of the a) centered and b) gradual expansion models. There are two centered expansion and two gradual expansion models ($\Delta\theta = 7°$ and $14°$ for both). The (x,y) origin is on the surface at the onset of curvature. The n coordinate is zero at the surface and everywhere normal to the surface.

a)

x = 150 mm   x = 0 mm

b)

x = 125 mm   x = 0 mm

c)

x = 125 mm   x = 0 mm
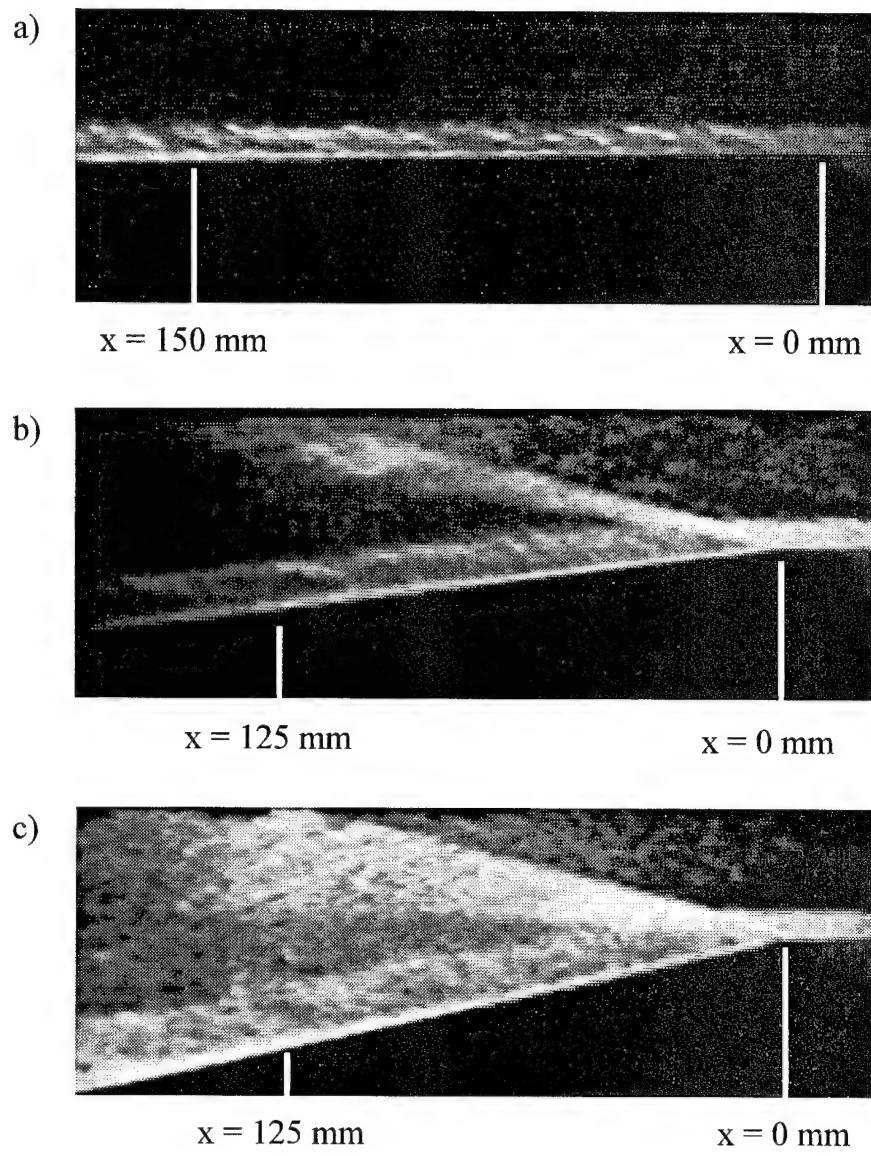
Figure 2. Instantaneous schlieren images of the flat plate boundary layer (a),
7°centered expansion (b), and 14°centered expansion (c).

a)
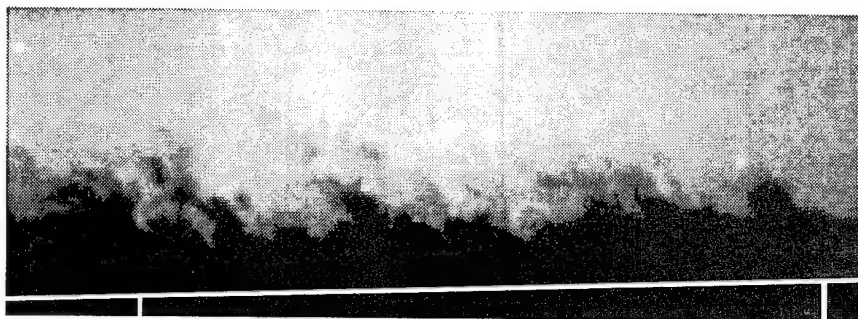
b)
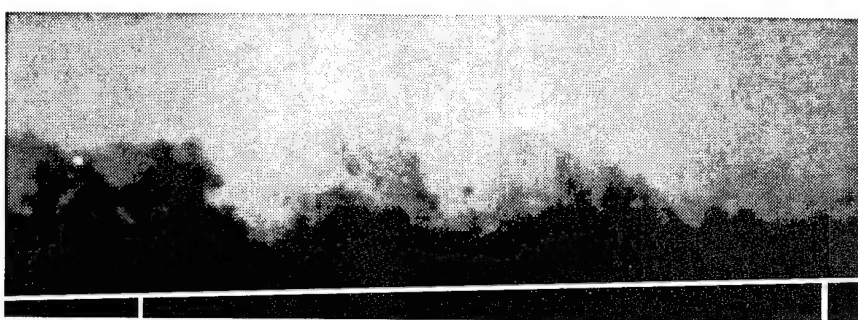
c)
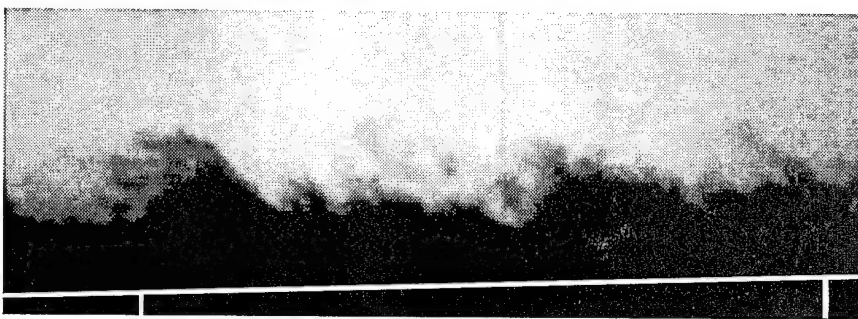
s = 135 mm   s = 75 mm

Figure 3. Instantaneous FRS streamwise views of the flat plate boundary layer. The added white lines indicate the position of the model surface.

a)

$s / \delta_o = 8.8$ $s / \delta_o = 0$

b)

$s / \delta_o = 8.8$ $s / \delta_o = 0$
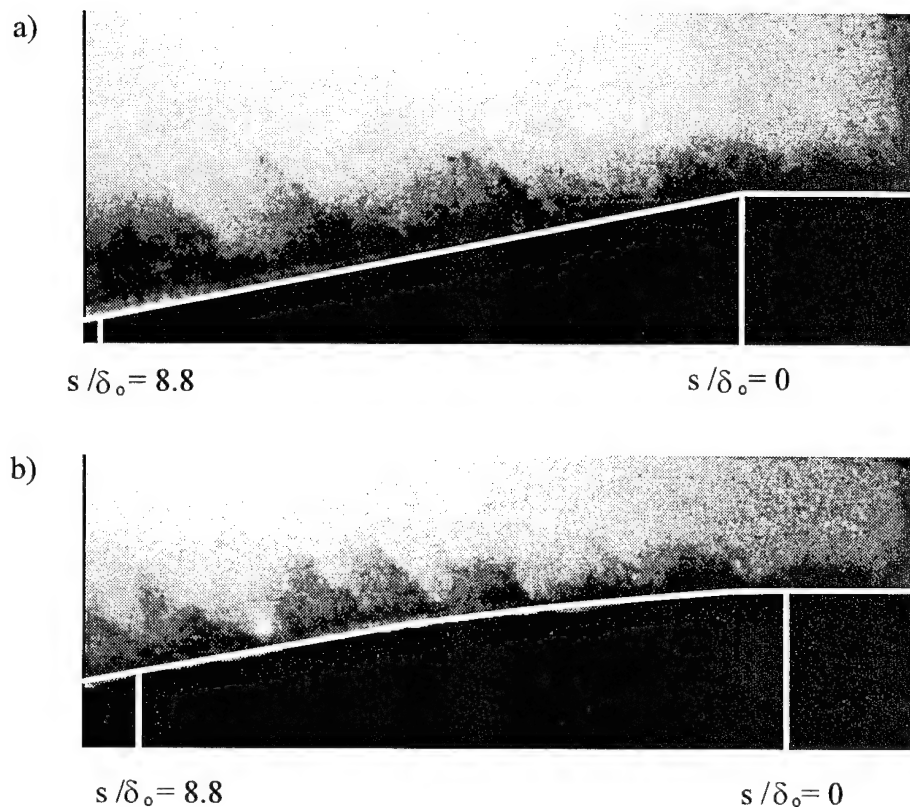
Figure 4. Instantaneous FRS visualizations of the 7° centered (a) and gradual (b) expansion regions. The white lines indicate the position of the model surface.

49

a)

$s/\delta_o = 8.7$ $s/\delta_o = 0$

b)

$s/\delta_o = 8.2$ $s/\delta_o = 0$
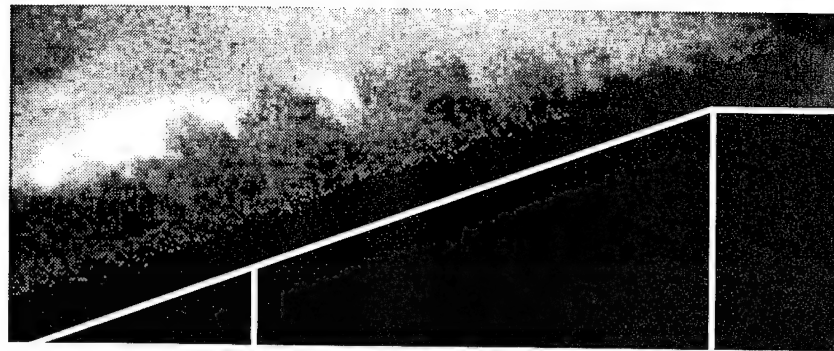
Figure 5. Instantaneous FRS visualizations of the $14°$ centered (a) and gradual (b) expansion regions. The white lines indicate the position of the model surface.

50
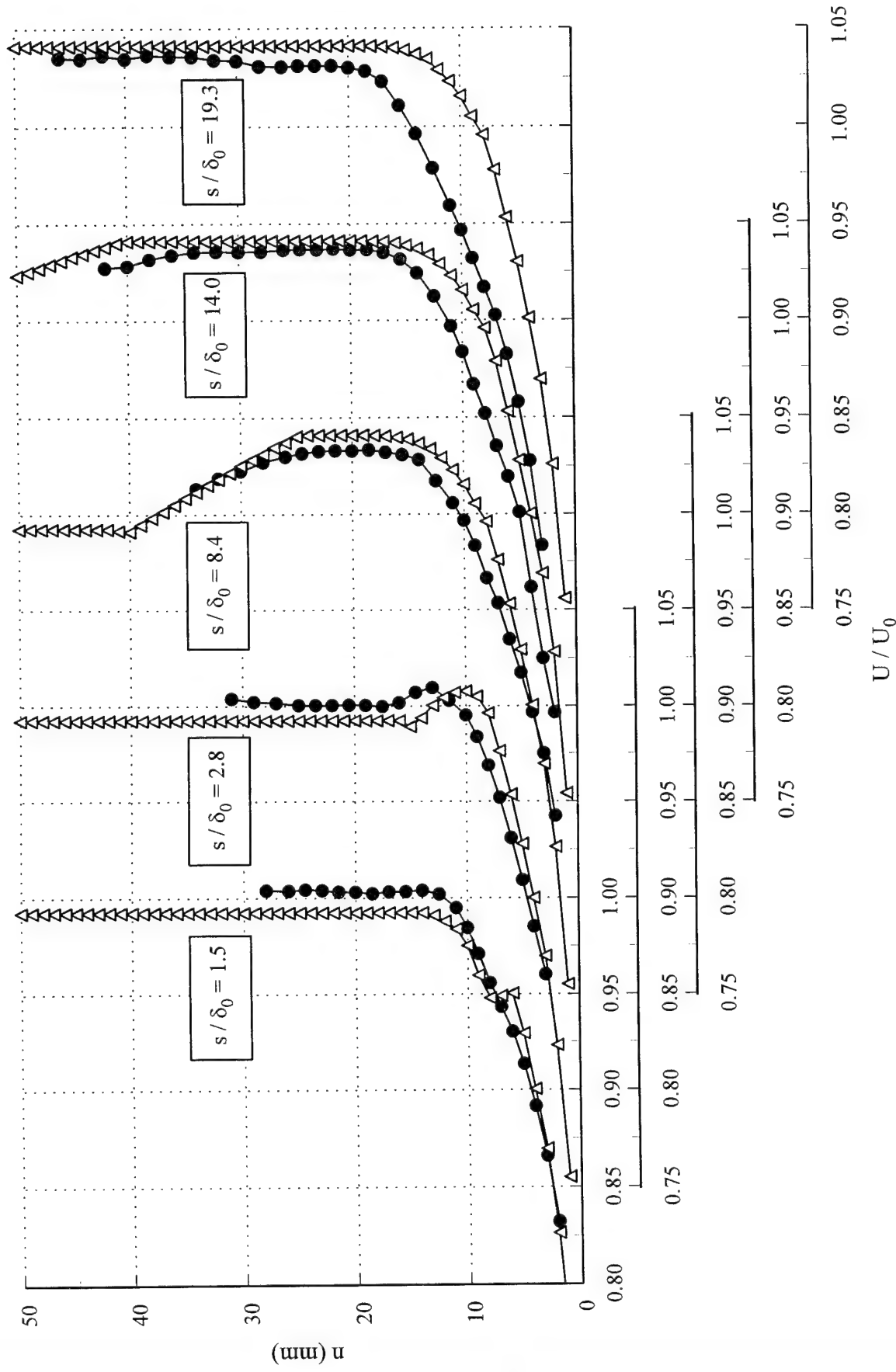
Figure 6. Mean velocity profiles measured with LDV (solid symbols) and computed with the method of characteristics (empty symbols) downstream of the 7 degree centered expansion at $s/\delta_0 = 1.5$, 2.8, 8.4, 14.0, and 19.3. Axes for successive locations are staggered.

51
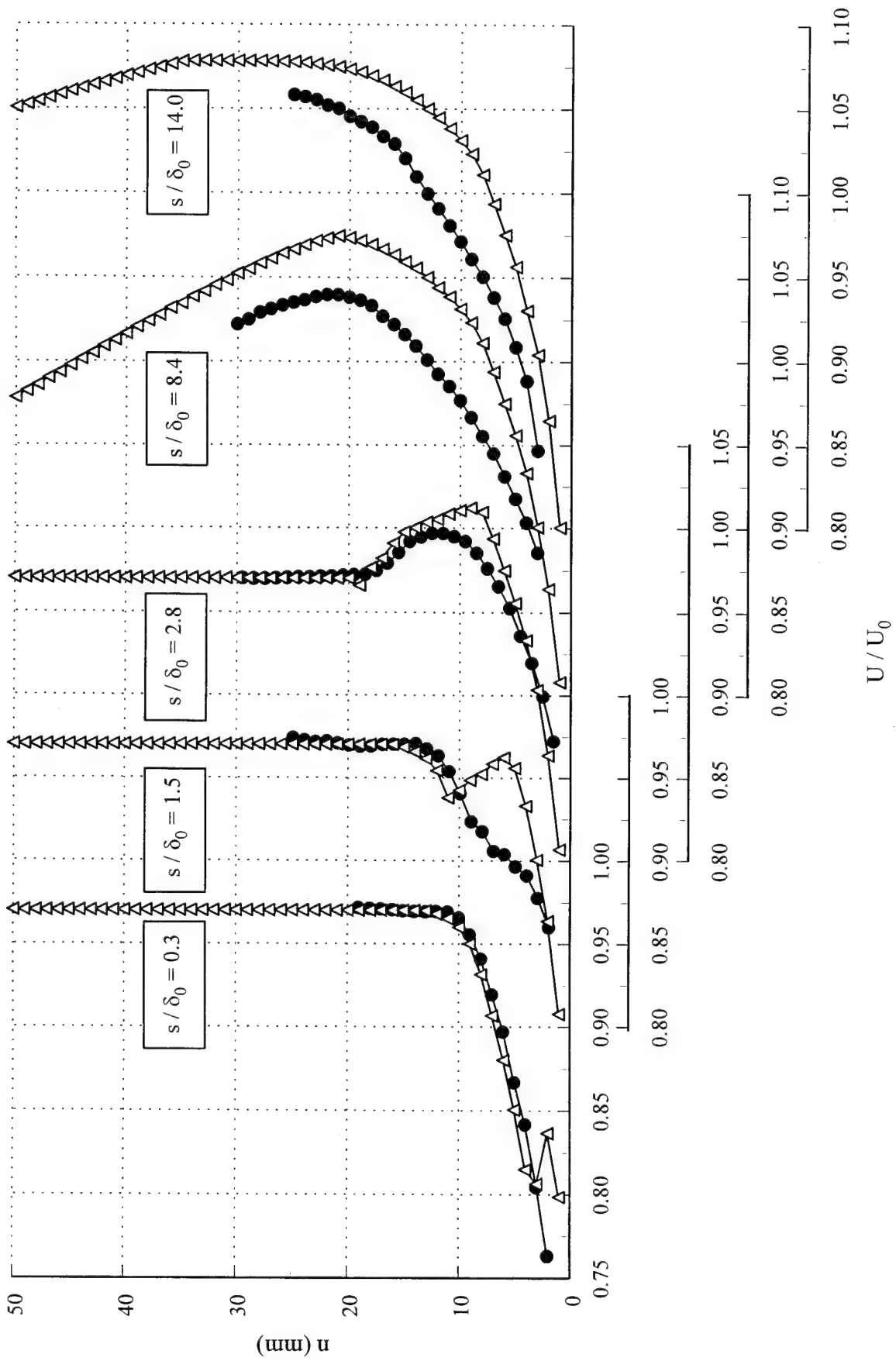
Figure 7. Mean velocity profiles measured with LDV (solid symbols) and computed with the method of characteristics (empty symbols) downstream of the 14 degree centered expansion at $s/\delta_0 = 0.3$, 1.5, 2.8, 8.4, and 14.0. Axes for successive locations are staggered.

52
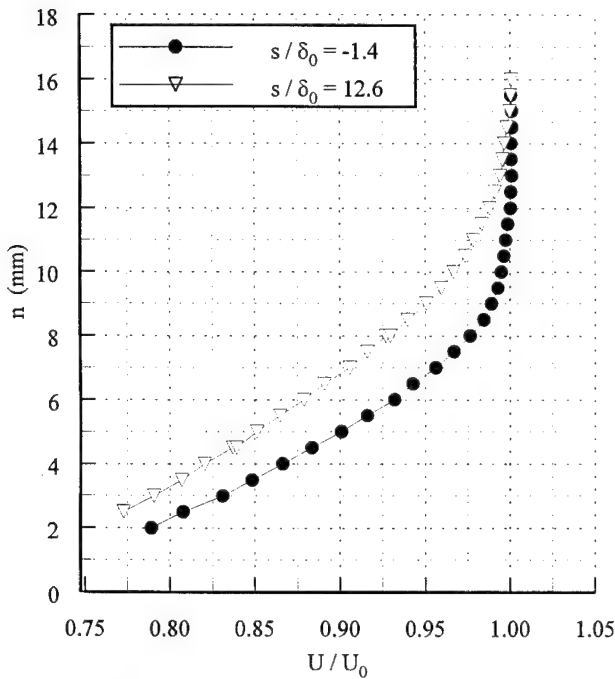
Figure 8. Streamwise velocity profiles in the flat plate boundary layer. The normal coordinate is plotted in units of millimeters.
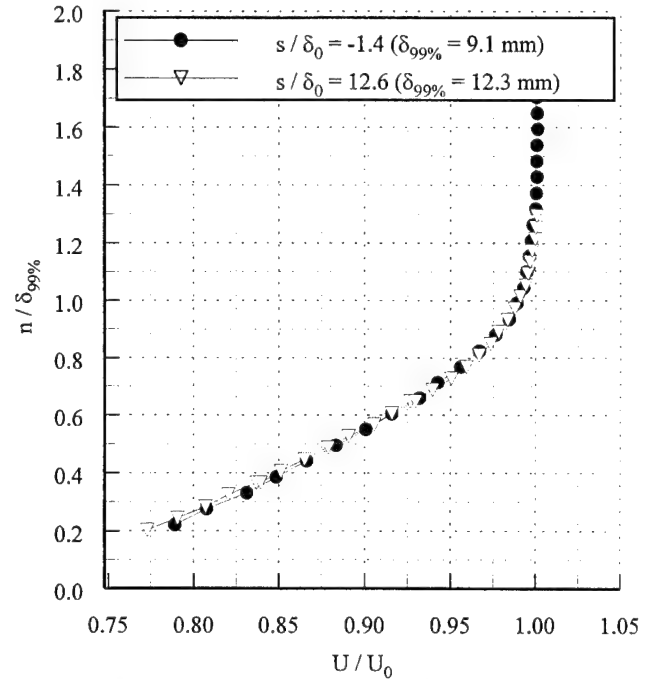
Figure 9. Streamwise velocity profiles in the flat plate boundary layer. The normal coordinate is nondimensionalized by the local boundary layer thickness.
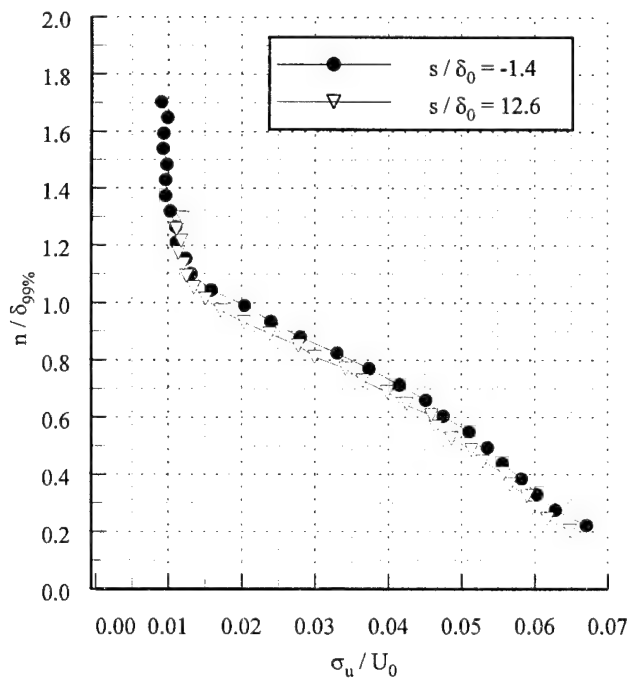
Figure 10. Streamwise turbulence profiles in the flat plate boundary layer.
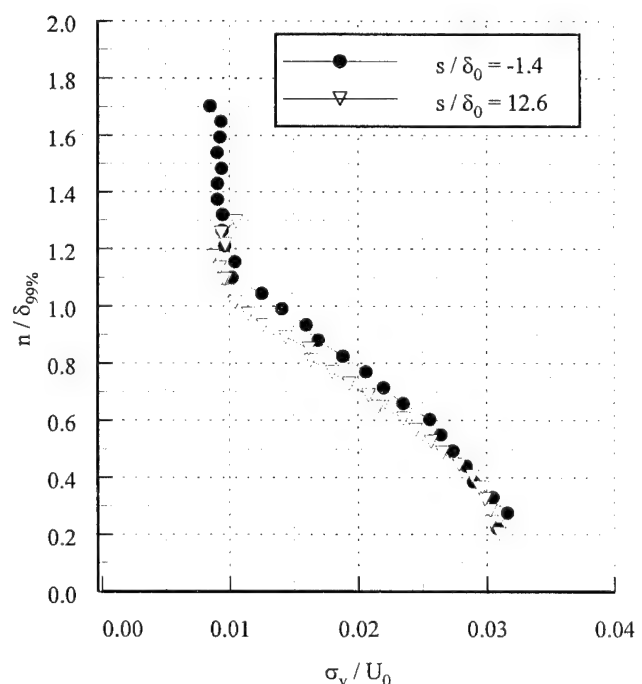
Figure 11. Normal turbulence profiles in the flat plate boundary layer.

53
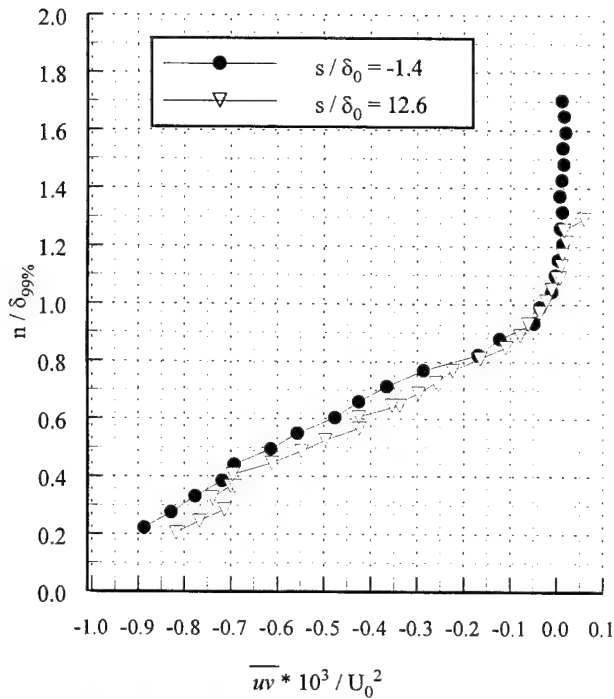
Figure 12. Reynolds shear stress profiles in the flat plate boundary layer. The normal coordinate is nondimensionalized by the local boundary layer thickness.
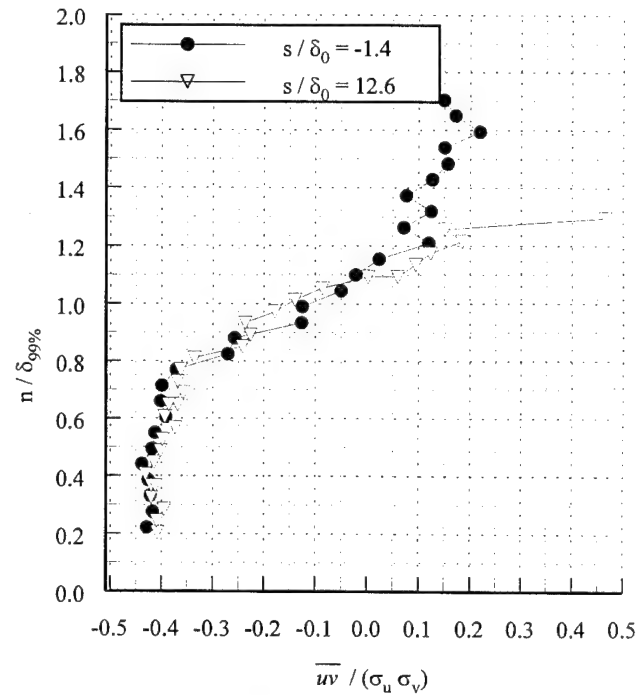
Figure 13. Correlation coefficient profiles in the flat plate boundary layer. The normal coordinate is nondimensionalized by the local boundary layer thickness.
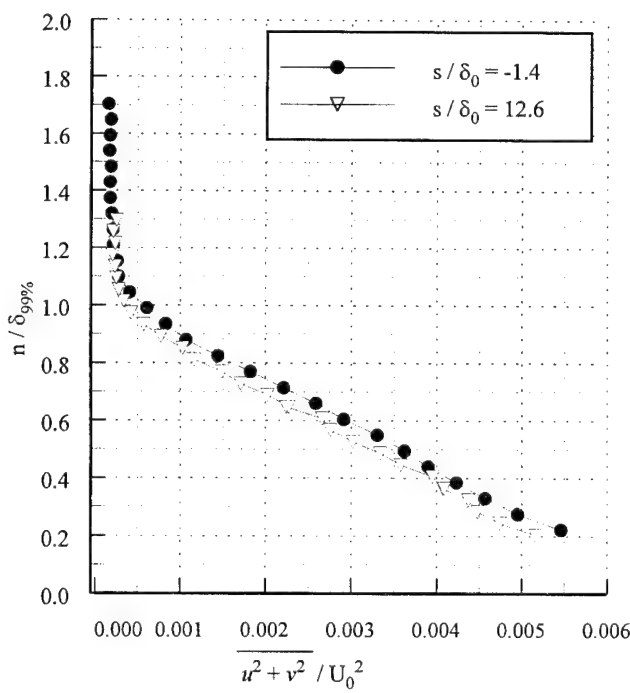
Figure 14. Turbulent kinetic energy profiles in the flat plate boundary layer. The normal coordinate is nondimensionalized by the local boundary layer thickness.
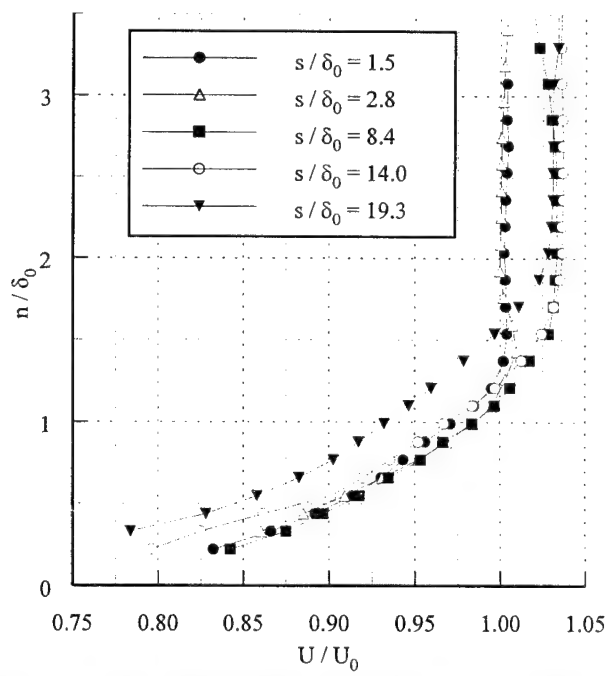
Figure 15. Mean velocity profiles downstream of the 7 degree centered expansion. Velocities are nondimensionalized by the Mach 3 freestream velocity and the normal coordinate is nondimensionalized by the incoming boundary layer thickness.

54
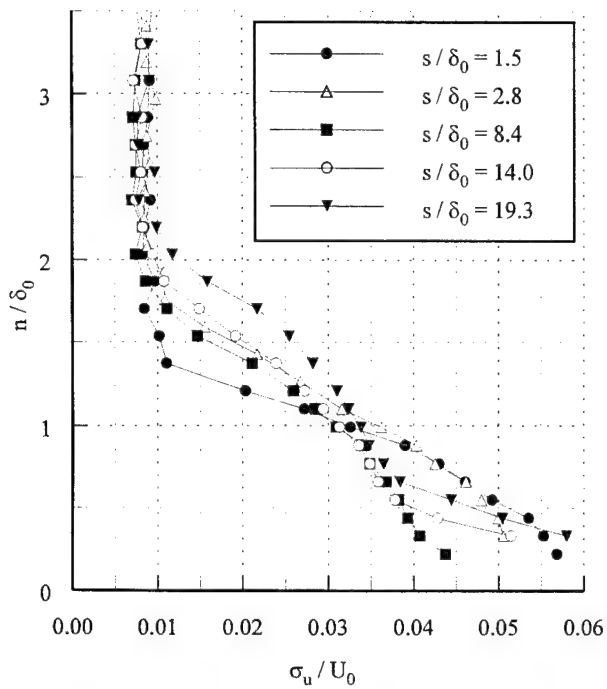
Figure 16. Streamwise turbulence profiles downstream of the 7 degree centered expansion. The incoming boundary layer thickness and Mach 3 freestream velocity are used for the normalization.
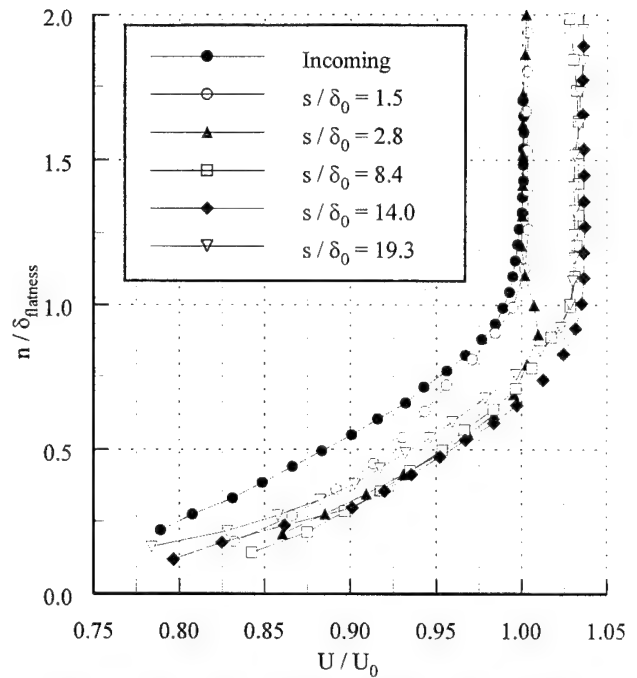
Figure 17. Mean velocity profiles downstream of the 7 degree centered expansion. The normal coordinate is nondimensionalized by the local thickness obtained from the flatness profile. Velocities are nondimensionalized by the Mach 3 freestream velocity.
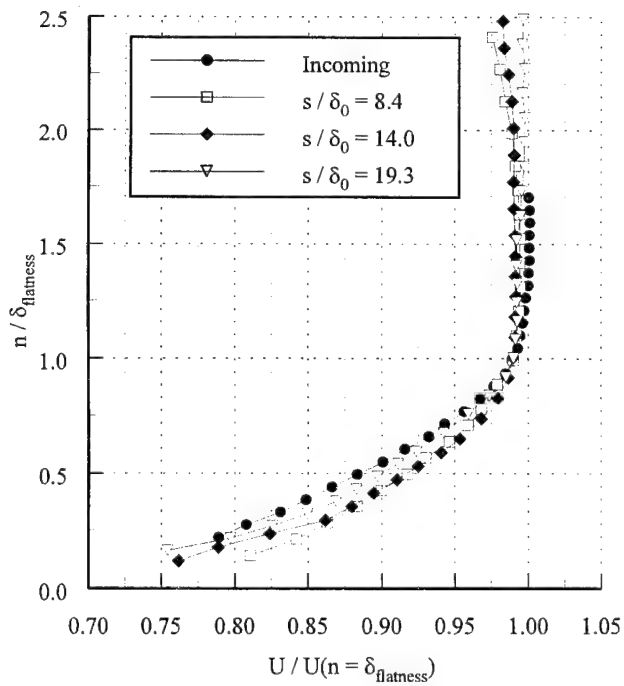
Figure 18. Mean velocity profiles downstream of the 7 degree centered expansion. Velocities are nondimensionalized by the local velocity at $n = \delta_{flatness}$.
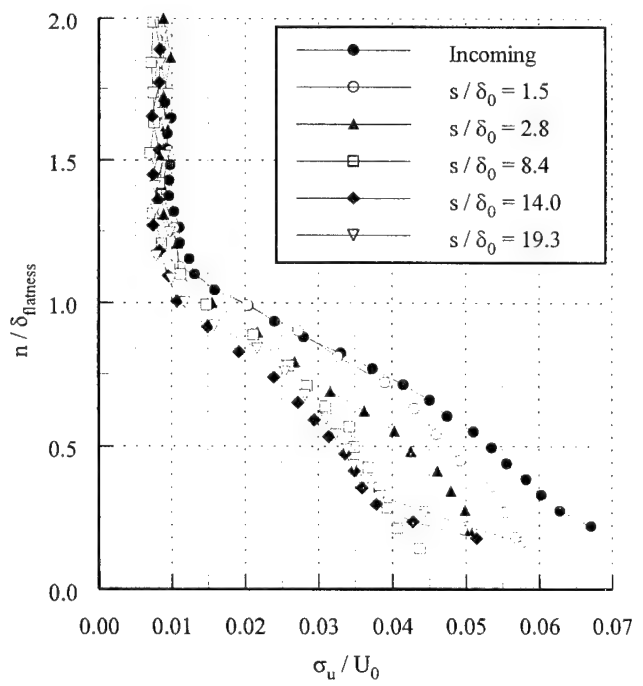
Figure 19. Streamwise turbulence profiles downstream of the 7 degree centered expansion.

55
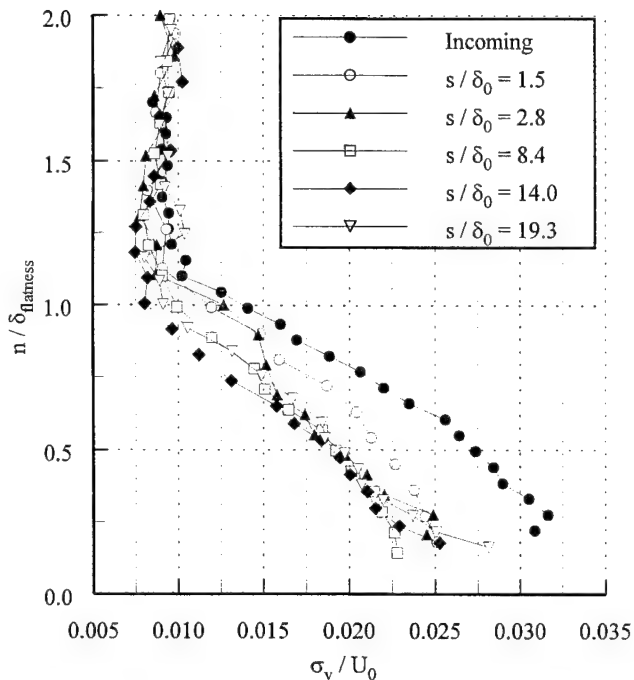
Figure 20. Normal turbulence profiles downstream of the 7 degree centered expansion.
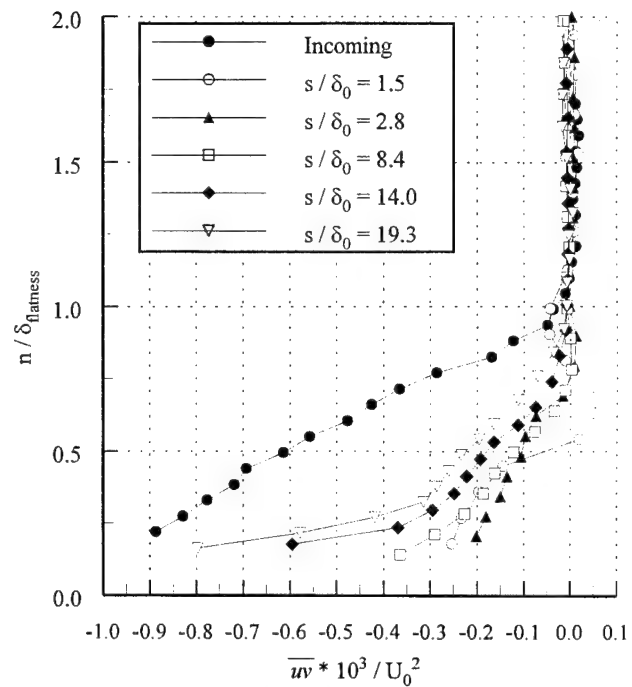
Figure 21. Reynolds shear stress profiles downstream of 7 degree centered expansion.
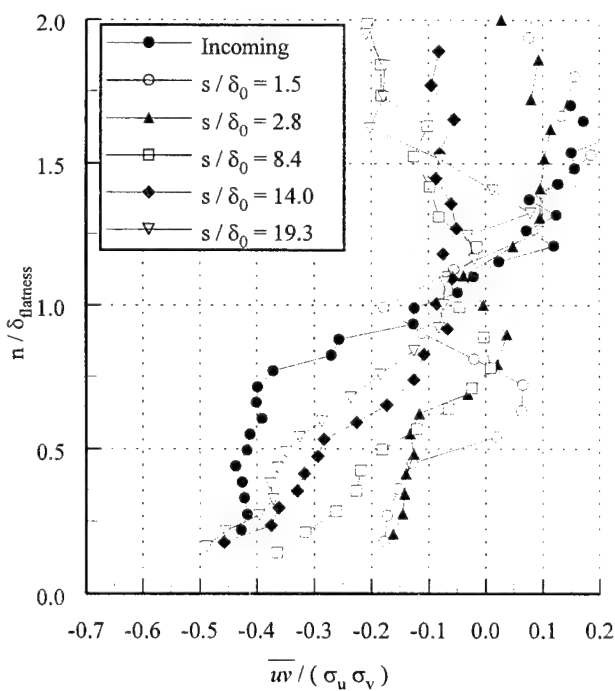
Figure 22. Shear correlation coefficient profiles downstream of the 7 degree centered expansion.
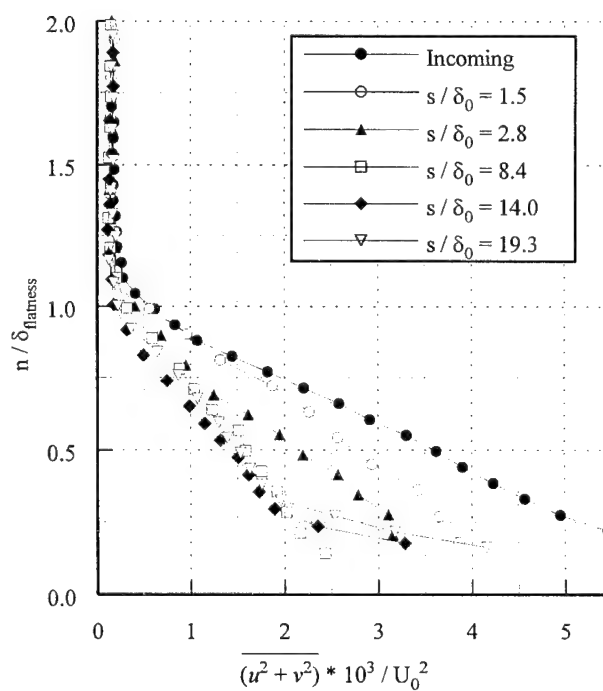
Figure 23. Turbulent kinetic energy profiles downstream of the 7 degree centered expansion.
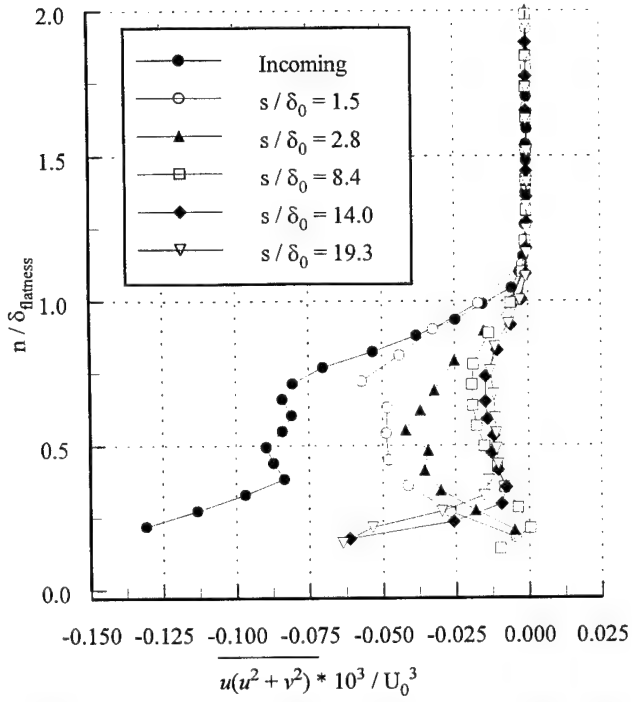
Figure 24. Streamwise turbulent transport of turbulent kinetic energy downstream of the 7 degree centered expansion.
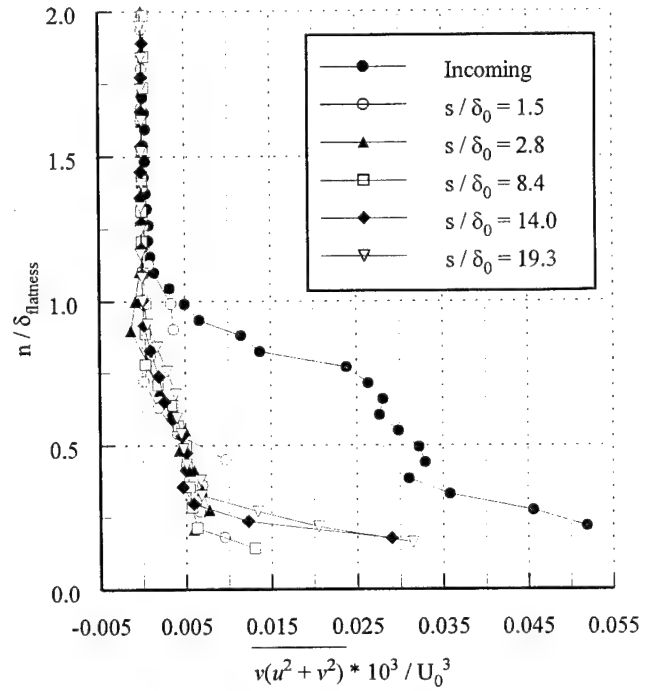
Figure 25. Normal turbulent transport of turbulent kinetic energy downstream of the 7 degree centered expansion.
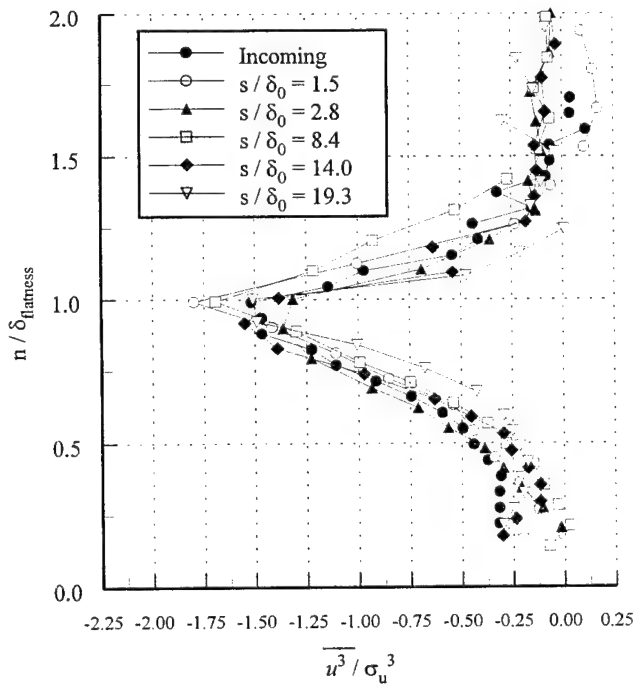
Figure 26. Streamwise skewness profiles downstream of the 7 degree centered expansion.
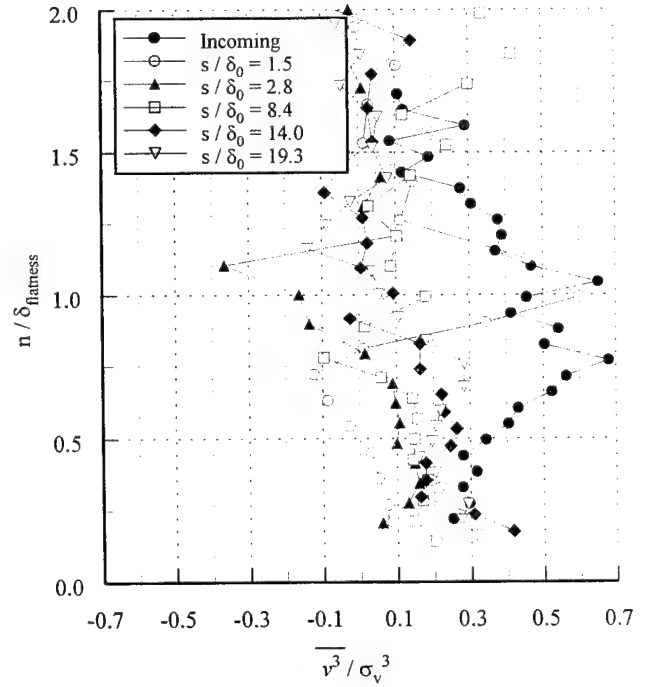
Figure 27. Normal skewness profiles downstream of the 7 degree centered expansion.

57
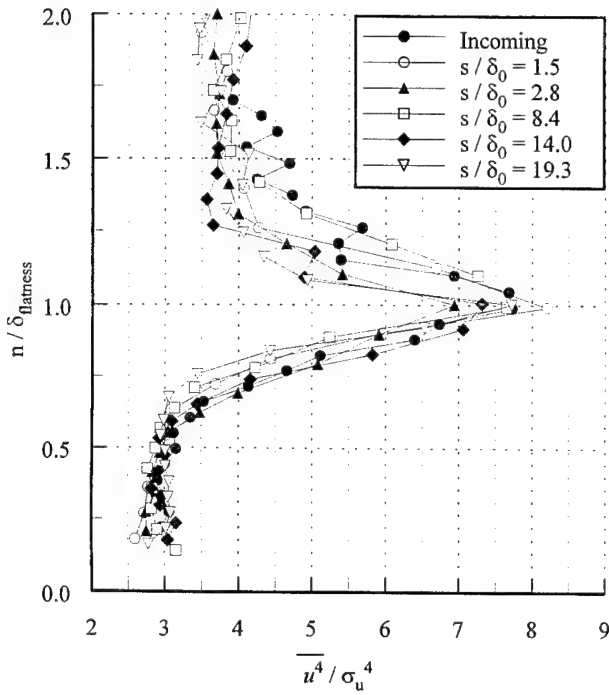
Figure 28. Streamwise flatness profiles downstream of the 7 degree centered expansion.
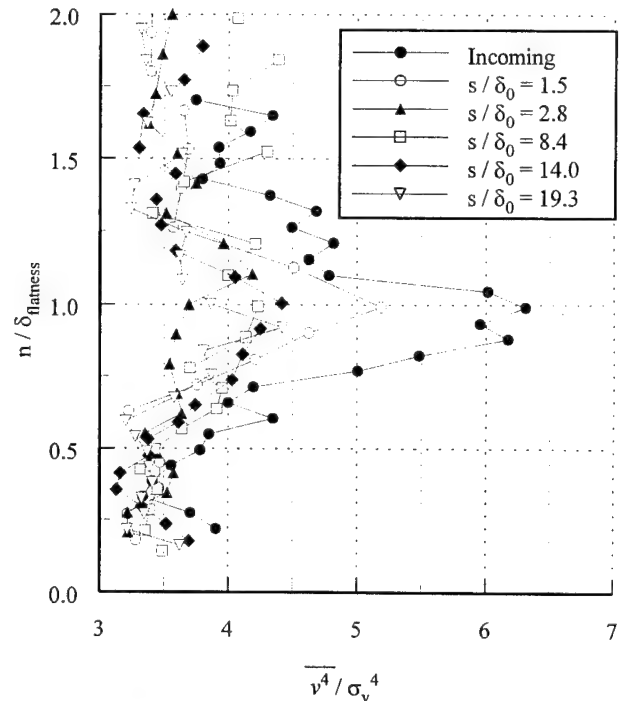
Figure 29. Normal flatness profiles downstream of the 7 degree centered expansion.
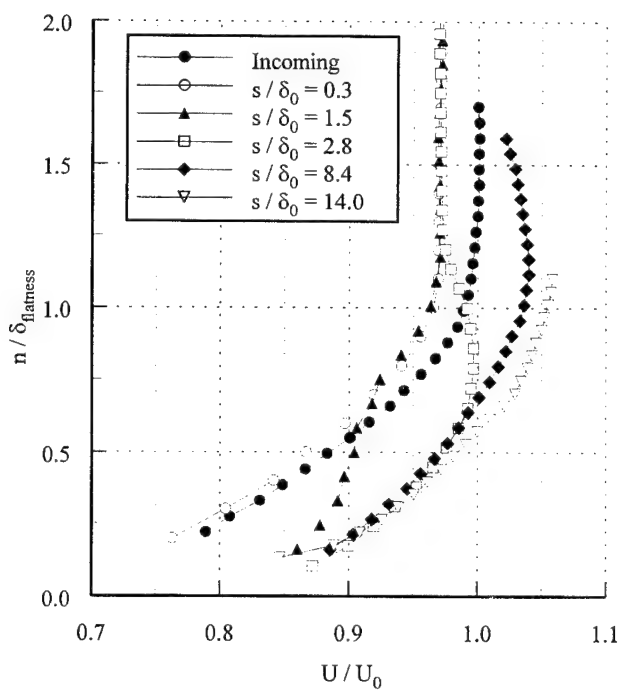
Figure 30. Mean velocity profiles downstream of the 14 degree centered expansion.
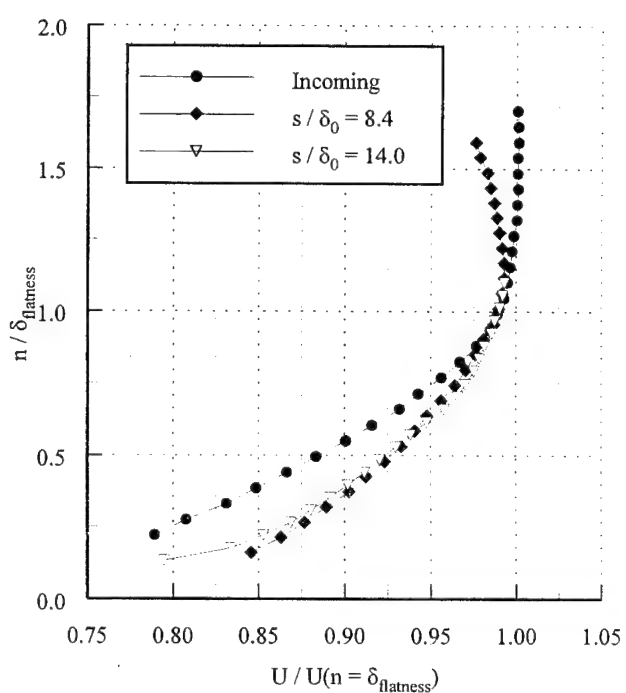
Figure 31. Mean velocity profiles downstream of the 14 degree centered expansion. Velocities are normalized by the local velocity at $n = \delta_{flatness}$.
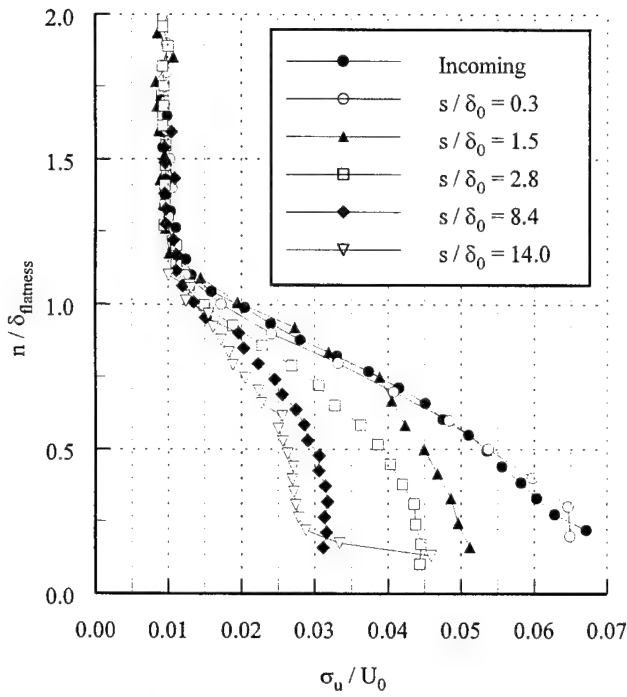
Figure 32. Streamwise turbulence profiles downstream of the 14 degree centered expansion.
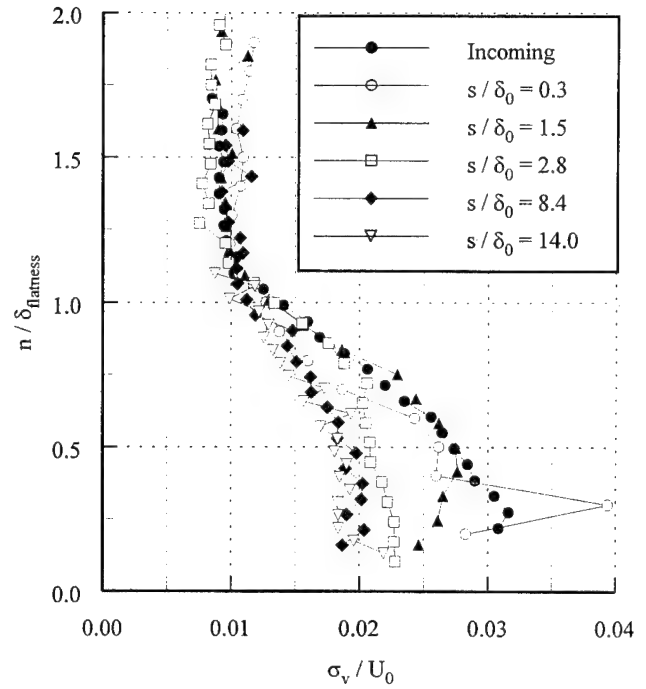

Figure 33. Normal turbulence profiles downstream of the 14 degree centered expansion.
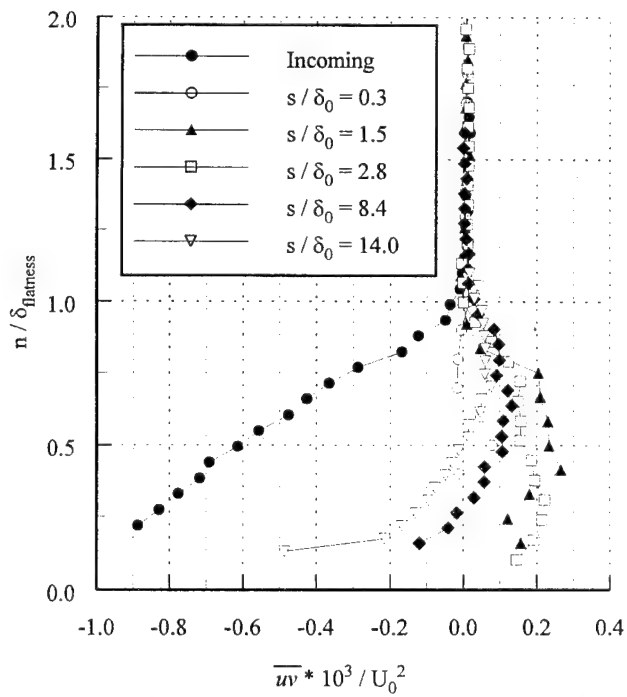

Figure 34. Reynolds shear stress profiles downstream of the 14 degree centered expansion.
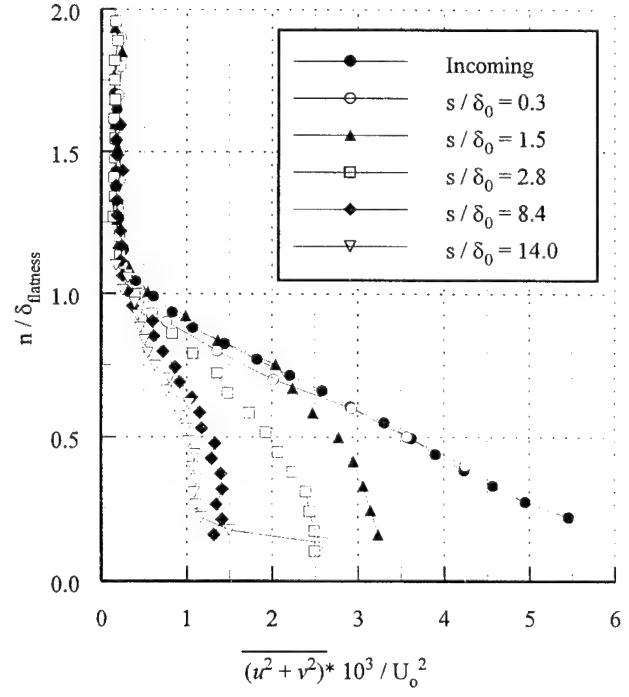

Figure 35. Turbulent kinetic energy profiles downstream of the 14 degree centered expansion.

59
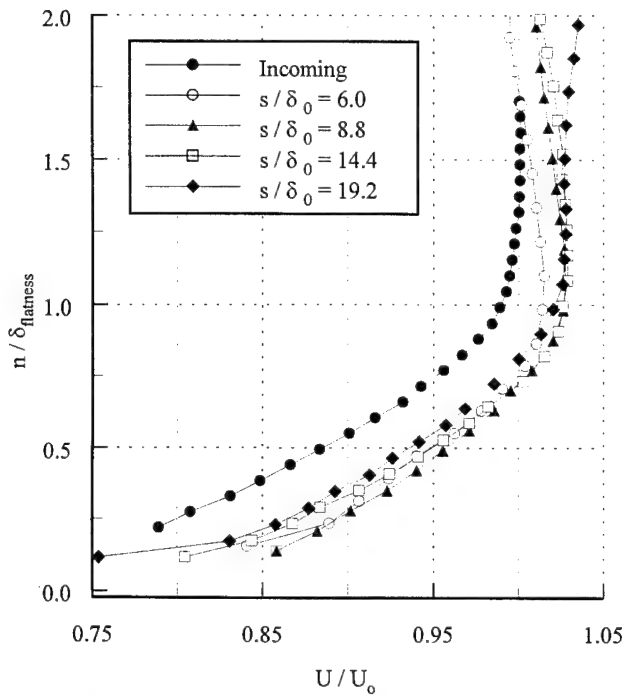
Figure 36. Mean velocity profiles downstream of the 7 degree gradual expansion.
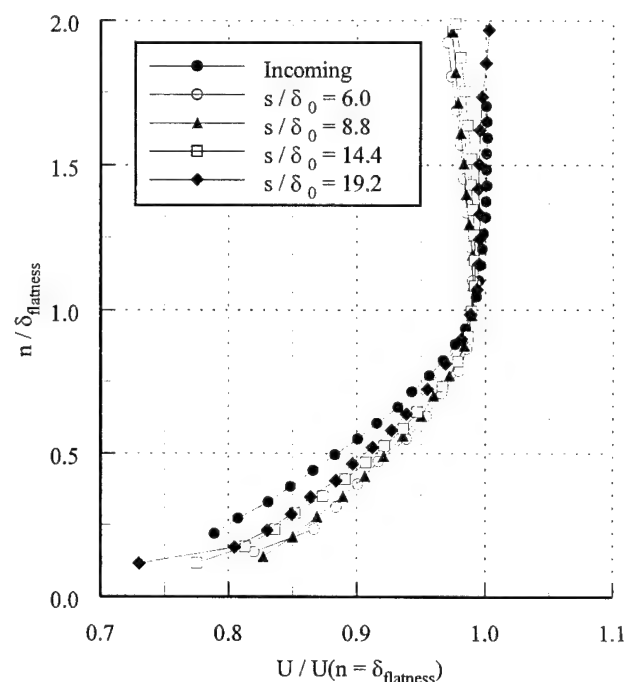


Figure 37. Mean velocity profiles downstream of the 7 degree gradual expansion. Velocities are nondimensionalized by the velocity at $n = \delta_{flatness}$.
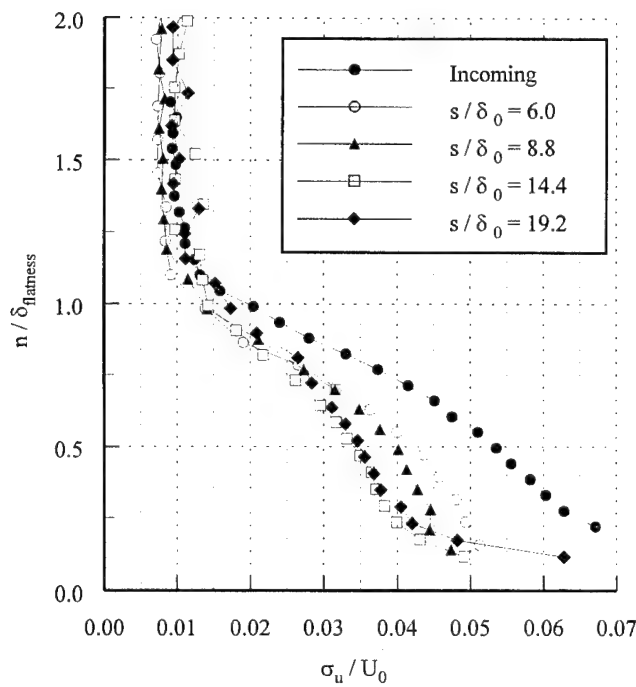

Figure 38. Streamwise turbulence profiles downstream of the 7 degree gradual expansion.
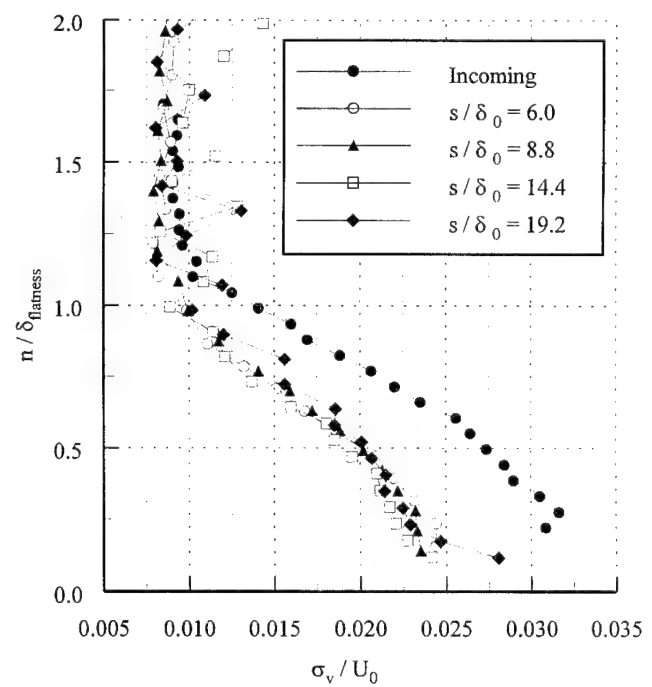
Figure 39. Normal turbulence profiles downstream of the 7 degree gradual expansion.

60
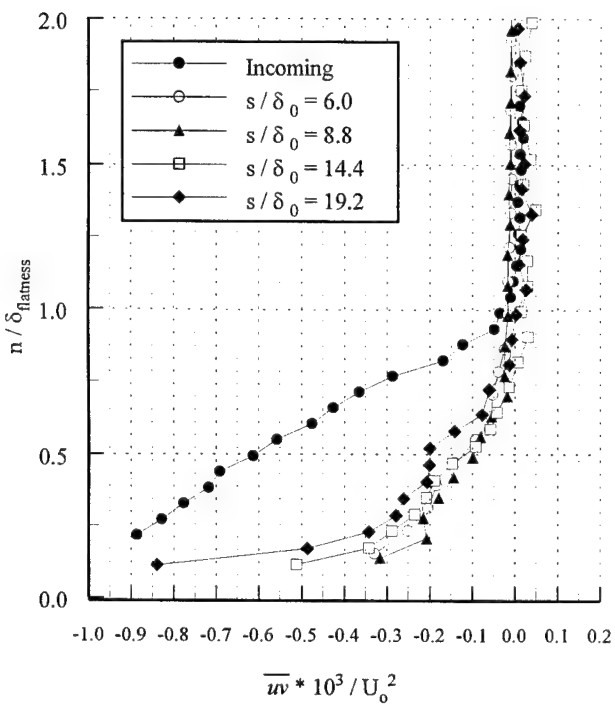
Figure 40. Reynolds shear stress profiles downstream of the 7 degree gradual expansion.
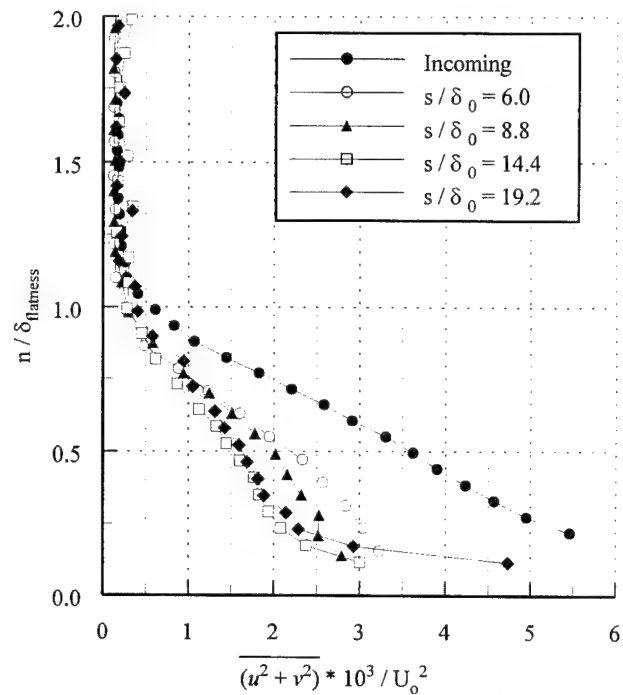
Figure 41. Turbulent kinetic energy profiles downstream of the 7 degree gradual expansion.
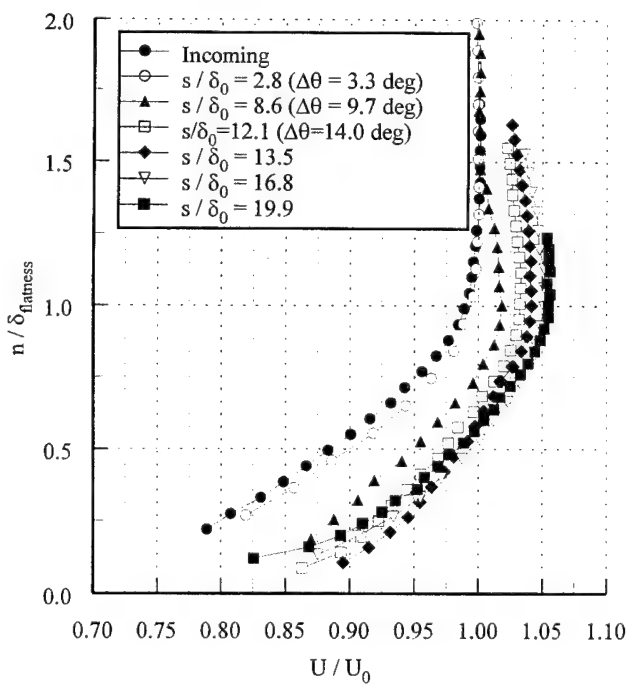
Figure 42. Mean velocity profiles downstream of the 14 degree gradual expansion.
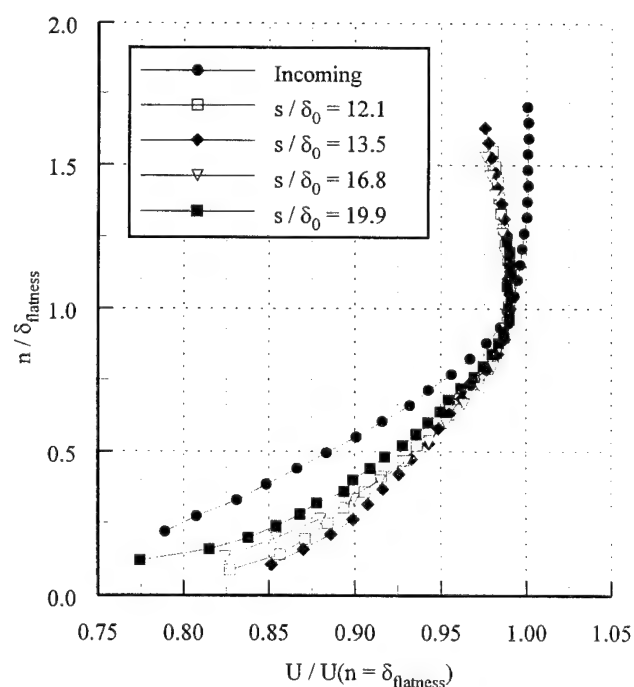
Figure 43. Mean velocity profiles downstream of the 14 degree gradual expansion. Velocities are nondimensionalized by the velocity at $n = \delta_{flatness}$.

61
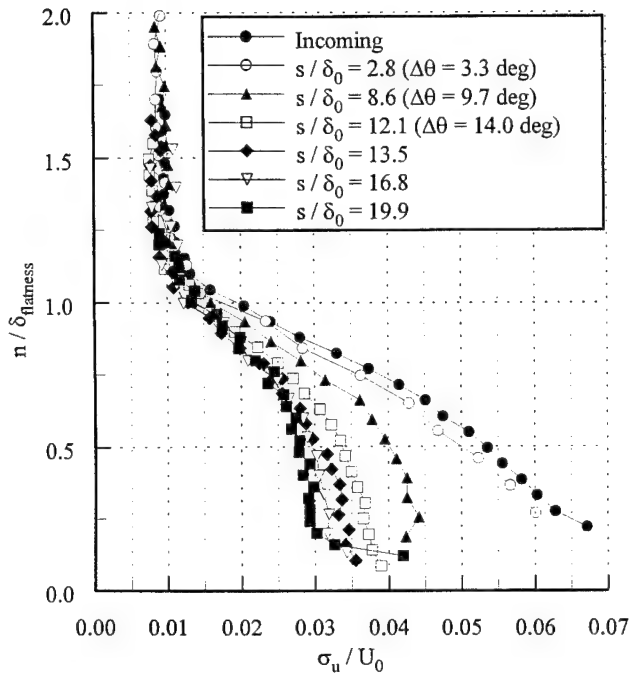
Figure 44. Streamwise turbulence profiles downstream of the 14 degree gradual expansion.
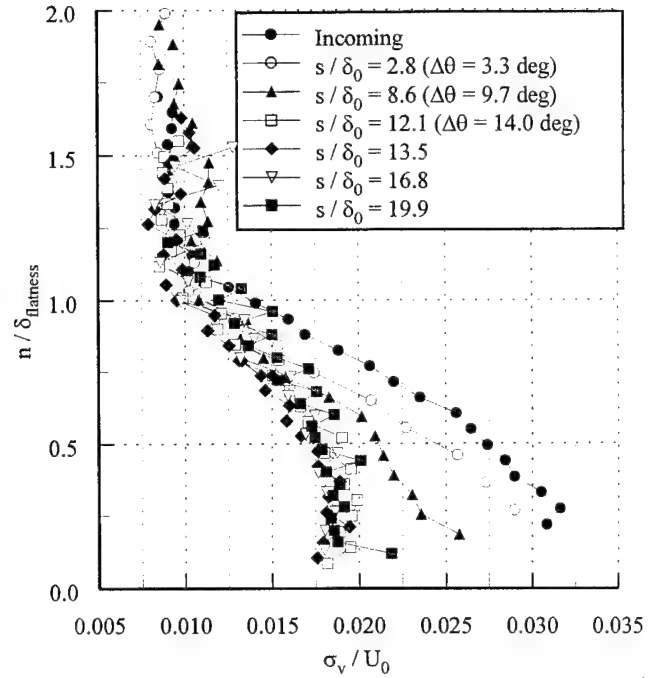
Figure 45. Normal turbulence profiles downstream of the 14 degree gradual expansion.
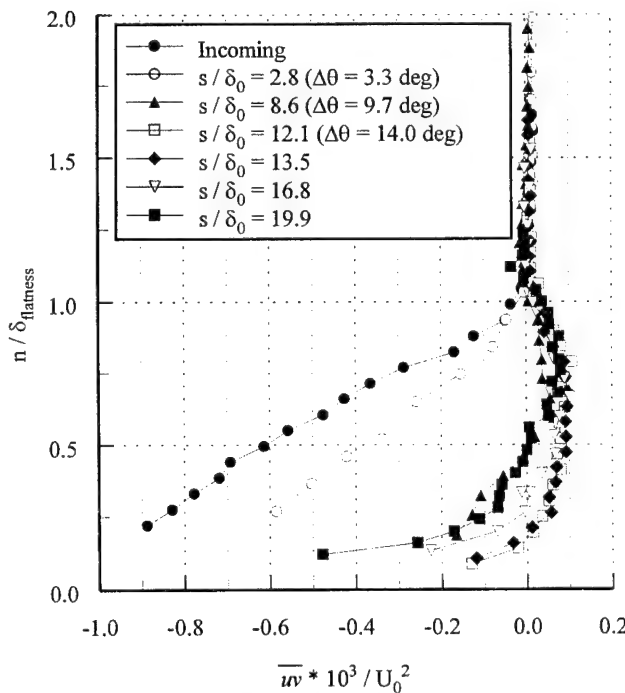

Figure 46. Reynolds shear stress profiles downstream of the 14 degree gradual expansion.
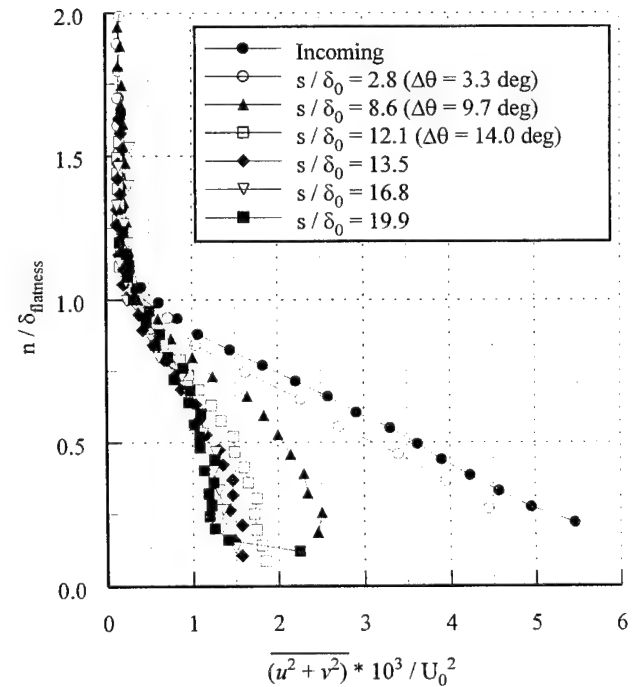
Figure 47. Turbulent kinetic energy profiles downstream of the 14 degree gradual expansion.

62

APPENDICES

Appendix I   Samimy, M., Arnette, S.A., and Elliott, G.S., 1994, "Streamwise Structures in a High Reynolds Number Supersonic Boundary Layer," <u>Physics of Fluids</u>, 6: 1081-1083.

Streamwise structures in a turbulent supersonic boundary layer

M. Samimy, S. A. Arnette, and G. S. Elliott
Department of Mechanical Engineering, The Ohio State University, Columbus, Ohio 43210

Flow visualizations in a high Reynolds number, Mach 3, fully developed turbulent boundary layer indicate that the upper half of the boundary layer is populated with elongated longitudinal structures. These structures are robust with considerable streamwise but very limited spanwise extent, and are randomly distributed in space and time. Possible mechanisms for the generation of these structures are discussed.

Over three decades ago, Morkovin[1] hypothesized that the structure of supersonic shear layers should not be much different than that of incompressible shear layers, as long as the root-mean-square density fluctuations normalized by the mean density remain relatively small. Bradshaw[2] suggested a Mach number of 5 as the upper limit for such similarity in boundary layers and wakes, and 1.5 for jets and free shear layers. The disparity in the limiting Mach number for similarity is a result of the highly three-dimensional nature of structures in boundary layers, which are much less sensitive to the Mach number difference across the layer than the more organized energetic structures in jets and free shear layers.[3] While the free stream Mach number characterizes the compressibility level in boundary layers and wakes, the convective Mach number is a more appropriate parameter in jets and mixing layers.[4] The upper limit of the convective Mach number for similarity of the structure of compressible and incompressible free shear layers is on the order of 0.5.[5] Bradshaw stressed that by structure he meant properties such as correlation coefficients and spectrum shape which are normalized by appropriate turbulent quantities rather than properties such as skin friction coefficient and Reynolds stresses which are normalized by the mean flow quantities. One would infer from this definition that large-scale structures, which are major contributors to turbulence properties such as the correlation coefficient, will also remain similar within the Mach number ranges mentioned above.

Unfortunately, information on the structure of supersonic boundary layers is very scarce, and therefore the extent to which Morkovin's hypothesis applies and the upper Mach number limit for the similarity of compressible and incompressible boundary layers have not been rigorously tested. Smits et al.[6] compared turbulence data for subsonic and Mach 3 boundary layers and found many similarities but also some subtle differences. This suggests that Morkovin's hypothesis might not hold in boundary layers at Mach numbers even as low as 3. Since the Reynolds numbers based on the momentum thickness in these comparisons were quite different (80 000 versus 5000), one must be cautious in drawing concrete conclusions from these comparisons. However, our limited results in a Mach 3 boundary layer with a Reynolds number of 25 000 confirm some of these differences (e.g., much lower correlation coefficient in the upper half of the boundary layer relative to the subsonic case or even a Mach 2 case), and point out that the differences are most probably due to compressibility rather than Reynolds number effects.[5]

The most prevalent structures observed in the incompressible boundary layers are the low speed streamwise streaks that dominate the wall region (the viscous sublayer, the buffer region, and a part of the logarithmic region) and the horseshoe (low Reynolds number) or hairpin (high Reynolds number) structures which dominate part of the logarithmic region and the outer part of the boundary layer.[7] In the outer part of supersonic boundary layers, large structures having inclination angles somewhat larger than those of the outer layer structures in subsonic boundary layers have been observed.[8] Also, the correlation measurements of Smits et al.[6] show that in the outer region the average spanwise scale of the structures is similar, however, the average streamwise scale for the supersonic case is twice that of the subsonic case. There does not seem to be a general agreement on the mechanisms behind the formation of the streaks. As the Reynolds number increases, the extent of the wall-region significantly decreases. Thus in supersonic and hypersonic boundary layers, the breadth of the wall layer is so small that it is beyond the reach of current experimental and simulation capabilities. Therefore, while the wall region of low Reynolds number incompressible boundary layers has been probed extensively, that of high speed flows, and as a result the similarity of structure of compressible and incompressible flows in this region, has been investigated very little. In this Letter, we present some new results in the outer region of a Mach 3 boundary layer which highlight another major difference between the structures in compressible and incompressible boundary layers.

The experiments were conducted at the Aeronautical and Astronautical Research Laboratory of the Ohio State University. The wind tunnel has a test section 152.4 mm wide and 76.2 mm high. The incoming boundary layer develops on a flat plate of nearly 670 mm in length upstream of the test section. The boundary layer and momentum thicknesses of the Mach 3.01 fully developed turbulent boundary layer are 9.2 and 0.37 mm, and the unit Reynolds number is 6.68×10^7/m.[5]

The filtered Rayleigh scattering technique was used for flow visualizations. A thin light sheet was created using a Quanta Ray GCR-4 frequency-doubled (532 nm) Nd:YAG laser, which is injection seeded to provide a narrow linewidth and approximately 50 GHz tuning capa-
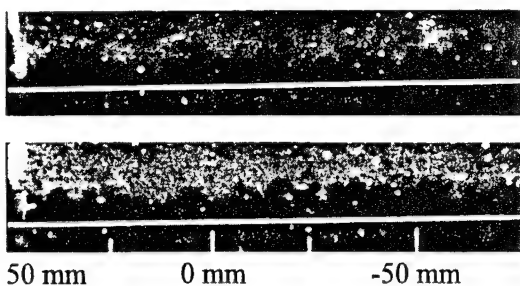
FIG. 1. Spanwise (y-z plane) images of the boundary layer.

FIG. 2. Streamwise (x-y plane) images of the boundary layer.

bility. The pulse duration of the laser is 9 ns, effectively freezing the flow while an image is taken. Images are collected with a Princeton Instruments ICCD camera with 14-bit output and stored on a computer. The scattering medium for these visualizations is the small amount of water vapor that remains in the tunnel supply air after passing through the system's desiccant driers. Upon expanding through the supersonic nozzle, the water vapor condenses from a supersaturated state to form small particles in the supersonic free stream. The higher temperature due to viscous dissipation prevents condensation within the boundary layer, thus providing a means of visualizing the interface between boundary layer and free-stream fluid. The formation of condensed water particles in supersonic flows has been used in visualizations of compressible boundary layers[9,10] and mixing layers.[11] The scattered light from these particles is in the Rayleigh regime indicating that the particles have a diameter less than approximately 50 nm. Therefore, they should faithfully follow the large-scale structures of the boundary layer. The time scale for the formation and destruction of these particles is very small, but very difficult to measure accurately. All indications from high speed mixing layer experiments in this facility are that the particles should have sufficient response time to mark the changes in the large-scale structures. The strong reflections near the solid surface dominate the weak Rayleigh scattering signal from the condensed water particles within the boundary layer. The filtered Rayleigh scattering technique introduced by Miles et al.[12] was used to eliminate this background scattering. We have extensively employed this technique in supersonic flows.[5,10,11,13]

Figure 1 shows two typical spanwise images (y-z plane) of the boundary layer. Since the laser has a repeition rate of 10 Hz and was operating in the single pulse mode, all of the presented images are uncorrelated. The images in Fig. 1 portray a typical supersonic boundary layer with the outer layer large-scale structures that have limited spanwise extent and give rise to a highly intermittent interface region. Figure 2 shows two streamwise (x-y plane) images of the boundary layer. The image on the top shows a large-scale structure, with an angle of about 35° to the streamwise direction, that extends significantly into the free stream. This is the kind of structure perceived to dominate the supersonic boundary layer.[14] The intermittency of the boundary layer would be much higher if the boundary
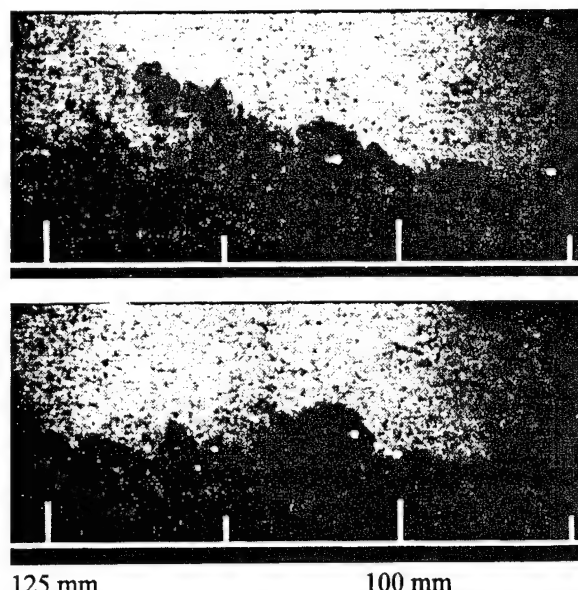
layer were dominated by this type of structures. The magnitude and extent of intermittency for supersonic boundary layers are much smaller than for subsonic boundary layers.[6,8] The second image is a similar view (more images presented in Ref. 10) which indicates how much the outer layer structures change with time and space. This might shed some light on the reduced intermittency of supersonic boundary layers.

Figure 3 shows plan views (x-z plane) of the boundary layer at $y/\delta = 0.49$ and 0.65 (similar images were acquired at $y/\delta = 0.87$); the flow direction is from upper right to lower left in the images. The camera was located 35° above the x-z plane and 45° from the spanwise direction. One observes the strong presence of structures which are parallel to the wall and aligned with the streamwise direction. The Rayleigh scattering signal from the condensation in the free stream dominates the signal when the laser sheet is located above y/δ of about 0.9 and there is no signal when the sheet is located below y/δ of about 0.5 due to the lack of condensation particles. Therefore, one could say with certainty that the upper half of the boundary layer is populated with these structures. However, the question of how close to the wall these structures exist cannot be answered at this point. These structures have a large streamwise, but limited spanwise extent. In comparison with the streamwise streaks in the wall region of subsonic boundary layers, these structures seem to have larger aspect ratio (spanwise to streamwise extent) and also do not change substantially with y, in contrast to dramatic changes in the subsonic case.[15] Note that the structures shown in Fig. 3 indicate high speed fluid in contrast to the low speed streaks visualized in the subsonic case. These structures are very robust, as evidenced by the fact that removing all the flow conditioning elements from the settling chamber did not significantly affect their presence and nature. These structures disappear when several images are averaged, signifying that the structures are randomly distributed in space
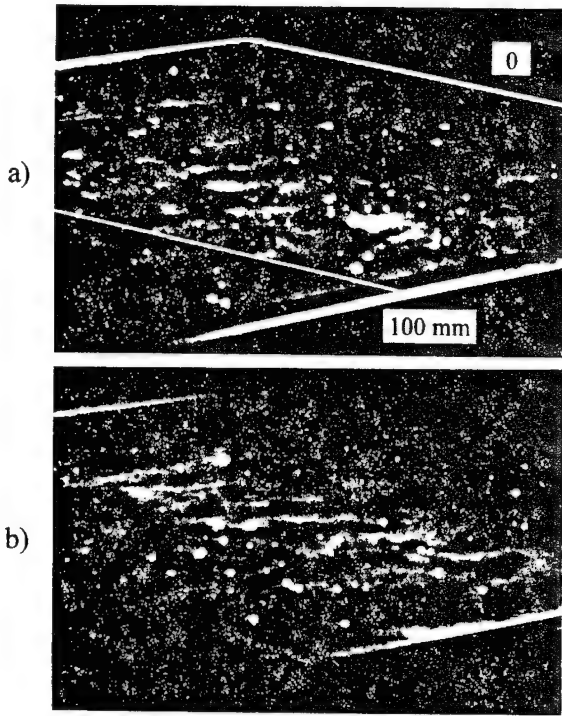
FIG. 3. Plan (x-z plane) images of the boundary layer at y/δ of (a) 0.49 and (b) 0.65.

and time. Space–time correlation measurements using hot wires[16] indicate strong correlations for a large streamwise distance in the outer part of the boundary layer, suggesting the existence of persistent large structures in incompressible boundary layers. However, conditional measurements in the outer region[17,18] have shown the structures are inclined approximately 30° to the streamwise direction, in contrast to the structures shown in Fig. 3 that appear to be aligned with the streamwise direction. Smith et $al.$[19] used UV Rayleigh scattering in a very small-scale tunnel with a Reynolds number based on momentum thickness of 14 000 at $y/\delta=0.6$ and did not find any streamwise structures. Their flow marking method was similar to that used here and it is not clear why they did not observe these structures. The scale/Reynolds number differences might be responsible. It should also be noted that without eliminating scattering from the surfaces with the molecular filter, we would not be able to observe the structures shown in Fig. 3.

The results shown in Fig. 3 raise two questions: What is the significance of these structures? Also, what is the mechanism behind their generation? There is no concrete answer to either question and one can only speculate at this time. Since these structures dominate at least the upper half of the boundary layer, they should play an important role in the dynamics of the boundary layer. Recent simulation[20] and experimental[21] results show that the mechanism behind the generation of longitudinal streaks in incompressible cases is more closely related to the local shear rate than the no-slip boundary condition. One mechanism that would generate high shear rate in the upper part

of a supersonic boundary layer is a shocklet. A shocklet is generated if the convective velocity of an individual structure is supersonic. For this Mach 3 flow, this would require the presence of structures in the upper part of the boundary layer with a convective velocity smaller than $0.7U_\infty$. The broadband convective velocity for supersonic flows is about $0.9U_\infty$,[8] which perhaps makes the existence of shocklets an unlikely event.

[1]M. V. Morkovin, "Effects of compressibility on turbulent flows," in $Mechanique$ de la $Turbulence,$ edited by A. Favre (CNRS, Paris, 1961).

[2]P. Bradshaw, "Compressible turbulent shear layers," Annu. Rev. Fluid Mech. **9**, 33 (1977).

[3]M. V. Morkovin, "Mach number effects on free and wall turbulent structures in light of instability flow interactions," in $Studies$ in $Turbulence,$ edited by T. B. Gatski, S. Sarkar, and C. G. Speziale (Springer-Verlag, Berlin, 1991).

[4]D. Papamoschou and A. Roshko, "The compressible turbulent mixing layer: an experimental study," J. Fluid Mech. **197**, 453 (1988).

[5]M. Samimy, G. S. Elliott, D. D. Glawe, M. F. Reeder, and S. A. Arnette, "Compressible mixing layers with and without particles," Tech. Report No. MEMS-92-101, Ohio State University, 1992.

[6]A. J. Smits, E. F. Spina, A. E. Alving, R. W. Smith, E. M. Fernando, and J. F. Donovan, "A comparison of the turbulence structure of subsonic and supersonic boundary layers," Phys. Fluids A **11**, 1865 (1989).

[7]S. K. Robinson, "Coherent motions in the turbulent boundary layers," Annu. Rev. Fluid Mech. **23**, 601 (1991).

[8]E. S. Spina, A. J. Smits, and S. K. Robinson, "The physics of supersonic turbulent boundary layers," to appear in Annu. Rev. Fluid Mech. (1994).

[9]D. R. Smith, J. Poggie, W. Konrad, and A. J. Smits, "Visualization of the structure of shock wave turbulent boundary layer interactions using Rayleigh scattering," AIAA Paper No. AIAA-91-0651 (1991).

[10]S. A. Arnette, M. Samimy, and G. E. Elliott, "The effect of expansion on the large scale structure of a compressible turbulent boundary layer," AIAA Paper No. AIAA-93-2991 (1993).

[11]G. S. Elliott, M. Samimy, and S. A. Arnette, "A study of compressible mixing layers using filtered Rayleigh scattering based visualizations," AIAA J. **30**, 2567 (1992).

[12]R. B. Miles, W. R. Lempert, and J. Forkey, "Instantaneous velocity fields and background suppression by filtered Rayleigh scattering," AIAA Paper No. AIAA-91-0357 (1991).

[13]S. A. Arnette, M. Samimy, and G. S. Elliott, "On streamwise vortices in high Reynolds number supersonic axisymmetric jets," Phys. Fluids A **5**, 187 (1993).

[14]E. F. Spina, J. F. Donovan, and A. J. Smits, "On the structure of high-Reynolds-number supersonic turbulent boundary layers," J. Fluid Mech. **222**, 293 (1991).

[15]S. J. Kline, W. C. Reynolds, F. A. Schraub, and P. W. Runstadler, "The structure of turbulent boundary layers," J. Fluid Mech. **30**, 741 (1967).

[16]R. F. Blackwelder and S. G. Kovasznay, "Time scale and correlations in a turbulent boundary layer," Phys. Fluids **15**, 1545 (1972).

[17]N. Trigui, "Detailed documentation of the direct effects of large eddy break-up devices on the turbulence structure in turbulent boundary layers," Ph.D. Dissertation, Ohio State University, 1991.

[18]C. E. Wark and H. M. Nagib, "Experimental investigation of coherent structures in turbulent boundary layers," J. Fluid Mech. **230**, 183 (1991).

[19]M. Smith, A. J. Smits, and R. B. Miles, "Compressible boundary-layer density cross section by UV Rayleigh scattering," Opt. Lett. **14**, 916 (1989).

[20]M. J. Lee, J. Kim, and P. Moin, "Structure of turbulence at high shear rate," J. Fluid Mech. **216**, 561 (1990).

[21]M. Rashidi and S. Banerjee, "The effect of boundary conditions and shear rate on streak formation and breakdown in turbulent channel flows," Phys. Fluids A **2**, 1827 (1990).

Phys. Fluids, Vol. 6, No. 3, March 1994

Letters   1083

Appendix II   Dawson, J.D., Samimy, M., and Arnette, S.A., 1994, The Effects
of Expansion on a Supersonic Boundary Layer: Surface Pressure
Measurements ", <u>AIAA J.</u>, 32: 2169-2177.

Effects of Expansions on a Supersonic Boundary Layer: Surface Pressure Measurements

J. A. Dawson, M. Samimy, S. A. Arnette

Effects of Expansions on a Supersonic Boundary Layer: Surface Pressure Measurements

Jonathan A. Dawson,* Mo Samimy,† and Stephen A. Arnette‡
Ohio State University, Columbus, Ohio 43210

Multipoint wall pressure measurements are used to investigate the response of a Mach 3, fully developed, compressible, turbulent boundary layer ($Re\theta = 25,000$) to centered and gradual ($R/\delta \approx 50$) expansions, both of 7- and 14-deg deflection. Although rms fluctuation levels decrease across the expansions, the rms normalized by the local static pressure remains nominally constant. Just downstream of the expansions, normalized power spectra are more concentrated at low frequencies ($f < 10$–15 kHz) than upstream, suggesting small-scale turbulence is quenched. This spectra alteration is more prominent for centered expansions and larger deflections. The spectra evolve very quickly after the centered expansions and very slowly after the gradual expansions. Downstream of the expansions, space-time correlations do not lend themselves to the derivation of convection velocities, signifying a severe distortion of the boundary layers. Measurements immediately after the gradual expansions compare well with those further downstream of the centered expansions of the same deflection, suggesting the distance from the beginning of the expansions is the appropriate length scale for characterizing the boundary-layer evolution. After the expansions, a band of elevated spanwise coherence (around 15–30 kHz) and elevated spanwise correlation levels emerge. Increases in streamwise coherence and correlation are less pronounced. At the last measurement stations, the boundary layers remain far from equilibrium.

Nomenclature

P = mean static pressure
R = radius of curvature of gradual expansion
U = mean velocities in the streamwise direction
V = mean velocities in the normal direction
x = streamwise direction
y = normal direction
z = spanwise direction
Δx = streamwise transducer spacing
Δz = spanwise transducer spacing
δ = boundary-layer thickness
ρ = density
σ_P = rms pressure fluctuations

Subscripts

L = local value
0, 1 = value before the expansion
2 = value after the expansion
θ = based on momentum thickness

I. Introduction

FLAT plate, compressible, turbulent boundary layers have been studied for decades. However, in practical situations, compressible boundary layers are typically influenced by streamline curvature, bulk dilatation or compression, pressure gradients, and other complexities. These effects define a larger class of complex turbulent flows that possess "extra rates of strain." Extra rates of strain are defined as velocity gradients that exist in addition to the dominant $\partial U/\partial y$ boundary-layer gradient.[1] A summary of the current knowledge of perturbed, compressible turbulent boundary layers is given by Spina et al.[2]

In passing through an expansion, the compressible turbulent boundary layer is subjected to a favorable pressure gradient (and

the associated bulk dilatation) and convex streamline curvature. There have been several investigations of compressible turbulent boundary layers subjected to favorable pressure gradients in the absence of convex streamline curvature[2]. Bradshaw[1] found the effects of pressure gradients on supersonic flows to be significantly underestimated by an order-of-magnitude analysis of the turbulence equations. Morkovin[3] found longitudinal turbulence intensities to be decreased significantly by a favorable pressure gradient. It has also been demonstrated that the induced bulk dilatation serves to decrease the wall shear stress and increase the boundary-layer thickness. Although preceded by a region of adverse pressure gradient, the outer edge of the Mach 2.5 turbulent boundary layer of Lewis et al.[4] subjected to a favorable pressure gradient corresponded approximately to a streamline, signifying a suspension of freestream fluid entrainment into the boundary layer. These observations show the favorable pressure gradient to be stabilizing; i.e., the turbulence's ability to transport momentum to the wall or entrain fresh fluid is decreased.

Convex streamline curvature in a compressible flow is normally accompanied by a favorable pressure gradient (as in this study). However, convex curvature can be isolated from the associated pressure gradients by introducing appropriate concave streamline curvature on an opposing solid boundary. Such an investigation was performed by Thomann[5] in studying the effect of streamline curvature on wall heat transfer for an incoming Mach 2.5 turbulent boundary layer. Gradual convex curvature of 20 deg resulted in a decrease in the wall heat transfer of approximately 15–20% relative to the flat plate levels. Gradual concave curvature of 20 deg resulted in a similar percent increase. This shows convex curvature to also be stabilizing; i.e., the turbulence's ability to transport low-temperature, freestream fluid into the near-wall region is reduced.

As mentioned, the compressible turbulent boundary layer is subjected to both convex streamline curvature and a favorable pressure gradient in negotiating an expansion region. Given the nonlinear response of the turbulent boundary layer to extra rates of strain, there is no reason to expect the boundary-layer response to represent a simple superposition of the effects induced individually by streamline curvature and pressure gradients.

Dussauge and Gaviglio[6] investigated a 12-deg centered expansion of a Mach 1.8 equilibrium turbulent boundary layer ($\delta = 10$ mm, $Re_\theta = 5000$). Hot-wire measurement of longitudinal velocity and temperature fluctuations were acquired. Across the expansion,

boundary-layer thickness. The reductions were small for $y/\delta > 0.7$ but became more substantial closer to the boundary. Calculations based on rapid distortion theory that accounted for the effect of bulk dilatation reproduced the reductions in longitudinal turbulence intensity very well in the outer portions of the boundary layer. However, the more significant reductions near the wall were not fully captured by the calculations. The evolution of the mean velocity profile downstream of the expansion is very similar to that of Lewis et al.[4] for a flat plate boundary layer subjected to a favorable pressure gradient. The logarithmic region of the mean velocity profile was destroyed across the 12-deg expansion and did not reappear until approximately 10δ downstream of the expansion corner. At this location, longitudinal Reynolds stress profiles remained well below equilibrium levels. The turbulence recovery originated near the wall, progressively occupying more of the boundary-layer thickness. Thus it was concluded that a new wall layer was formed and that the boundary layer had relaminarized. Dussauge[7] proposed a description for the relaminarization process and identified two zones of influence: an outer zone where slow variations occur and an inner zone where turbulence is re-formed.

For incompressible turbulent boundary layers, it has been shown that a sufficiently favorable pressure gradient can cause relaminarization.[8] Reversion of the mean flow is said to be completed when the net effect of the Reynolds stresses is negligible. Narasimha and Viswanath[9] suggest relaminarization occurs after an expansion corner if $\Delta P/\tau_0 > 70$–75, where ΔP is the pressure drop across the expansion and τ_0 is the surface shear stress before the expansion.

Smith and Smits[10] studied a 20-deg centered expansion of a Mach 2.84 boundary layer ($\delta = 26$ mm, $Re_\theta = 77{,}600$). Measurements 3.5δ downstream of the expansion corner compared favorably with those of Dussauge and Gaviglio.[6] No logarithmic region was evident in the mean velocity profile, and both the longitudinal turbulence intensity and Reynolds stress were significantly reduced. Calculations similar to those of Dussauge and Gaviglio[6] were performed with similar success. Interestingly, the mass-flux fluctuation profile was not altered significantly through the expansion. Thus, although the published criterion for relaminarization had been met, caution was urged in using the term.

As highlighted by Spina et al.,[2] these studies of expanded compressible turbulent boundary layers demonstrate the effects of bulk dilatation more than those of surface curvature since, for these two-dimensional flows, $\partial U/\partial x + \partial V/\partial y \gg \partial V/\partial x$. This disparity should be enhanced with increasing Mach number.

Using the same expansion models and tunnel as in this study, Arnette et al.[11] used filtered Rayleigh scattering to investigate the effects of expansions on the Mach 3 turbulent boundary layer. Streamwise-elongated structures were found to populate the upper half of the boundary layer before and after the expansion regions. The planar visualizations, in which the freestream was marked with a condensation tracer, did not permit visualizations deeper in the boundary layer. A discussion of these structures in the flat plate boundary layer is given by Samimy et al.[12] Arnette et al.[11] found the large-scale structures of the outer layer maintained their identity and increased in scale across the expansions and the structure angle also appeared to increase. The visual prominence of the large-scale structures was enhanced across the expansions due to more significant penetrations of marked potential fluid into the boundary layer, suggesting small-scale motions were quenched. This observation seems to agree with the results of Dussauge and Gaviglio[6] and Smith and Smits,[10] where sharp reductions in near-wall turbulence were encountered across the expansions.

The present work studies the effect of varying degrees and rates of expansion on a Mach 3 turbulent boundary layer. The four expansion cases consist of centered expansions of 7 and 14 deg and gradual expansions ($R/\delta = 50$) of 7 and 14 deg.

II. Experimental Setup

The experiments were performed at the Ohio State University Aeronautical and Astronautical Research Laboratory. Compressed dry air is provided by two four-stage compressors and stored in tanks with a capacity of 42.5 m³ at pressures up to 16.4 MPa. Air is delivered to the tunnel through an array of radial inlet holes, and the stagnation pressure is adjusted with a pneumatically controlled ball valve. The stagnation pressure was 1.14 MPa, and the stagnation temperature was nominally 280 K. The incoming supersonic flow occupies a passage 152.4 mm wide and 76.2 mm tall at the beginning of the expansion regions, after which the cross-sectional area of the passage increases. The boundary layer develops on a flat plate from the stagnation chamber to the beginning of the expansions (67 cm from the nozzle throat to the beginning of the expansions), and transition is natural. The one-sided nozzle contour is opposite the flat plate surface. Previous laser Doppler velocimetry (LDV) measurements have shown the streamwise and normal freestream turbulence intensities are less than 3%.[13] At the location of the beginning of the expansion regions, the LDV results showed $M_\infty = 3.01$, $\theta = 0.37$ mm, $Re_\theta = 24{,}700$, and $\delta_0 = 9.2$ mm.

Schematics of the expansion models are shown in Fig. 1. For the centered expansion models (Fig. 1a), the flat plate boundary layer experiences a 7- or a 14-deg expansion corner. For the gradual expansion models (Fig. 1b), the flat plate boundary layer experiences 7 or 14 deg of gradual convex surface curvature ($R = 450$ mm). It has been shown for gradual concave curvature that the effects on the boundary layer vary with R/δ.[14,15] Given this, a large value of R/δ (≈ 50) was used with expectations that differences would arise between the centered and gradual expansions of the same total deflection. The regions of gradual surface curvature have a streamwise extent of 55 mm ($6\delta_0$) and 110 mm ($12\delta_0$) for the 7- and 14-deg gradual expansions, respectively. As in Fig. 1, the streamwise coordinate x is measured along the model surface with the origin at the beginning of the expansions. The previously measured δ_0 is used to normalize the streamwise coordinate. Pertinent ratios across the expansions obtained from an inviscid analysis are given in Table 1.

Static pressure information was acquired from static taps in the models with a 12-port Scanivalve. Measurements were made in both the spanwise and streamwise directions with a distance between static taps of 12.7 mm ($1.4\delta_0$). The streamwise static taps were offset from the model centers by 19.1 mm ($2.1\delta_0$) so as to not interfere with the centered transducers.

Table 1 Ratio across expansions from inviscid analysis

| Total deflection, deg	7	14
Mach number, M_2	3.40	3.86
Velocity ratio, U_2/U_1	1.05	1.08
Pressure ratio, P_2/P_1	0.56	0.30
Density ratio, ρ_2/ρ_1	0.66	0.42
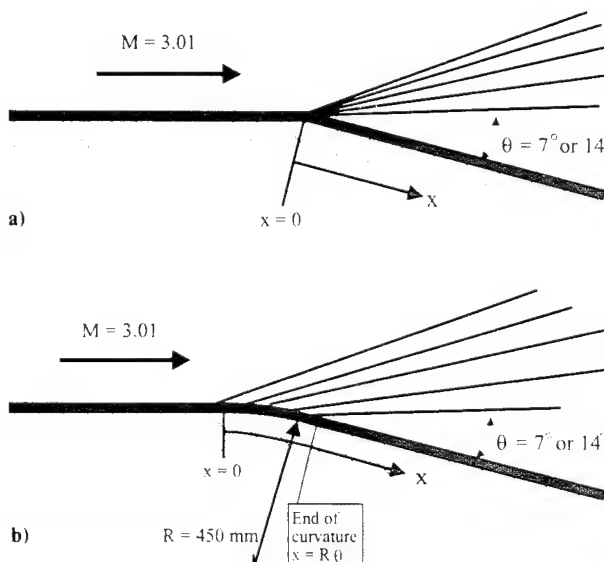
Fig. 1 Schematics of the a) centered and b) gradual expansion models.
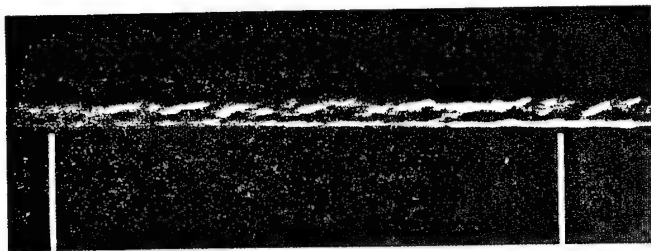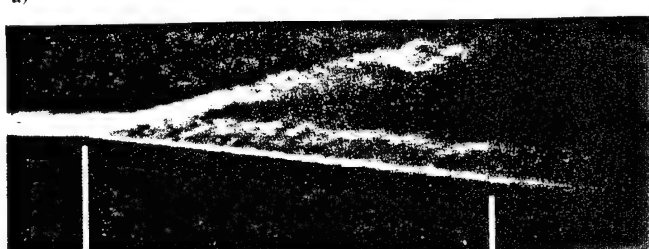
Fig. 2 Instantaneous schlieren images of the a) flat plate, b) 7-deg centered, and c) 14-deg centered expansion boundary layers.
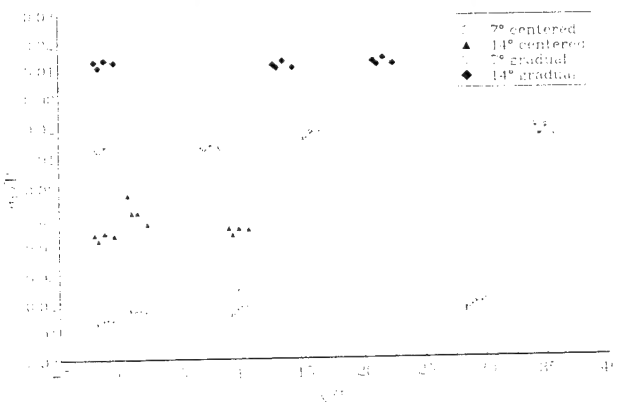

Fig. 3 Normalized rms pressure fluctuations for all four expansion models and the incoming boundary layer (the results for different models are staggered vertically).

Fig. 4 Streamwise distribution of static pressure at the model surfaces, $P_1 = 22$ kPa.

Fig. 5 Normalized power spectra downstream of the 7-deg centered expansion: a) immediately after the expansion and b) downstream evolution.

The instantaneous pressure data were acquired with four fast-response Endevco pressure transducers (Model 8514-10) powered by an Ectron model 563F signal conditioner. The transducers were statically calibrated against a mercury manometer. Previous work has shown the difference between the static and dynamic calibrations is only a few percent for these types of transducers (see, for example, Tan et al.[16] or Fernholz et al.[17]). The gain was set so as to match the output of the transducers under maximum pressure differential to the ±10 V range of the analog-to-digital (A/D) converter.

The transducer diaphragm (diameter of approximately 1 mm) is recessed below a cover containing pinholes. Corcos[18] demonstrated that the response of a transducer is valid up to a nondimensional frequency of $2\pi f r/U_c \approx 1.0$, where f is the maximum valid frequency, r is the diaphragm radius, and U_c is the measured convection velocity. If the convection velocity of the structures is approximately 90% of the freestream value (as found by Spina et al.[19]) of about 600 m/s obtained previously in this tunnel with LDV,[13] $f \approx 168$ kHz. However, the resonation of the transducer cavity appeared to corrupt the data above about 70 kHz. As a result, the data were low-pass filtered at 60 kHz. To eliminate low-frequency noise, a high-pass filter was applied at 1 kHz. The transducers were mounted in an aluminum plug that fit into holes located on the model centerlines. Since the plug is circular, the transducers can be skewed at any angle to the flow direction. For this work, only streamwise and spanwise orientations were employed.

The data were acquired using a Datel PC414-A2 12-bit A/D converter board and accompanying software (PC414-SET). The A/D converter was equipped with a simultaneous sample and hold

module that allowed data on all four channels to be sampled at the same time, thereby negating any phase difference between the signals. Data were collected simultaneously at the four locations at a sampling rate of 250 kHz per channel. Subjecting the four transducers to identical pressure signals confirmed that no artificial phase shifts between different channels were present in the system. A data set contained 51,200 data points per channel. This system has a mean sensitivity of approximately 60 Pa per bit with A/D fluctuations of approximately ±1 bit at constant pressure. All data were stored and subsequently processed on a 486 PC. Data filtering and analysis were performed with MATLAB software and the accompanying Signal Processing Toolbox. The power spectral analyses were performed with 100 sets of 1024 data points, and correlations were performed with 50 sets of 1024 data points. Full details of the data analysis are given by Dawson.[20]

Flow visualization was performed using a standard schlieren setup. Images were collected with an ICCD camera and recorded on Super-VHS. The photographs were used both to check for freestream uniformity and to obtain measurements of the boundary layer thickness.

III.　Results and Discussion

As can be seen in Fig. 2, where instantaneous (light pulse duration of 10 ns) schlieren images of the flat plate and centered expansion cases are shown, the boundary layer thickens substantially across the expansion regions. Measurements from average schlieren images indicate the boundary-layer thickness increases approximately 150% across the 7-deg expansions and 200% across the 14-deg expansions. Calculations based on the expansion of an incoming power-law velocity profile to the inviscid density ratios in which zero entrainment through the expansion is assumed (as suggested by the measurements of Lewis et al.[4]) indicate a boundary-layer thickening of 12–14% less than that estimated from the schlieren images. Given the increase in boundary-layer thickness across the expansions, the use of δ_0 as a global length scale is less than ideal.

Using the method of Narasimha and Viswanath,[9] $\Delta P/\tau_0$ is estimated to be 48 and 76 for the 7- and 14-deg expansions, respectively. Since the favorable pressure gradient is less severe for the the gradual expansion, the 14-deg centered expansion is the only one considered close to relaminarization. Figure 3 gives the normalized rms pressure fluctuations for the incoming and four expansion boundary-layer cases. The rms values are normalized by the average of the mean pressures recorded by the four adjacent transducers at each measurement station. The σ_P/P of 0.013 in the incoming boundary layer compares very favorably to the value of 0.014 obtained by Muck et al.[21] in a Mach 2.9 high-Reynolds-number, turbulent boundary layer. The normalized levels increase initially across the centered expansions. Further downstream the levels compare well with those of the flat plate boundary layer. This shows significant turbulent fluctuations to persist downstream of the expansions, which does not give an indication of relaminarization (even for the 14-deg centered expansion). The fact that the streamwise mass-flux fluctuations in a Mach 2.84 boundary layer did not change appreciably across a 20-deg expansion led Smith and Smits[10] to caution against the term relaminarization. The variations for adjacent transducers far downstream of the expansions are probably due to the slightly different dynamic responses of individual transducers since the static transducer calibration was repeated several times during the data collection to insure reliable results.

The streamwise distribution of mean static pressure at the model surfaces (both upstream and downstream of the four expansions) is shown in Fig. 4. Nonuniformities in the streamwise (Fig. 4) and spanwise (given by Dawson[20]) distributions in the incoming boundary layer correspond to a peak-to-peak Mach number variation of only 0.03. Spanwise distributions downstream of the four expansions were collected at a distance of $3.65\delta_0$ downstream of the end of the surface curvature (given by Dawson[20]). Downstream of the 14-deg expansions ($M_\infty \approx 3.86$, see Table 1), variation magnitudes at these locations are similar to those found in the incoming boundary layer. Downstream of the 7-deg expansions ($M_\infty \approx$

3.40), the spanwise variations correspond to a peak-to-peak Mach number variation of 0.18.

The measured pressure ratios (P_2/P_1) across the 7-deg expansion models are very close to those obtained from an inviscid Prandtl-Meyer analysis (Table 1), but the measured ratios for both 14-deg models are higher than the inviscid ratios. Smith and Smits[10] also measured a higher pressure ratio than the inviscid ratio for a 20-deg centered expansion in a Mach 2.84 flow. Pressure ratios calculated using the hypersonic similarity parameter[22] are 0.33 for the 14-deg and 0.59 for the 7-deg expansions, which are slightly lower than those of Fig. 4. For the centered expansions, the pressure reaches a minimum in $5–10\delta_0$ and then gradually increases.

A.　7-Deg Centered Expansion

Significant development of the power spectrum (normalized by $\sigma_P^2/125,000$) of the pressure fluctuations occurs over a short streamwise distance immediately after the 7-deg centered expansion. Figure 5a shows that the first stage consists of a shift of the spectral density to low frequencies ($f < 15$ kHz) and a corresponding decrease at higher frequencies (recall that the normalized spectra reflect only the spectral distribution of the fluctuation "energy"). The elevated low-frequency levels then begin to decrease, whereas the broad range of higher frequencies recovers more slowly. At these same positions, streamwise coherence levels in the low-frequency range drop from above to below those of the incoming boundary layer as the transducer spacing increases from $0.33\delta_0$ to $1.63\delta_0$, whereas little change occurs for higher frequencies. This again suggests that rapid development occurs just after the expansion.

The downstream power spectra show the pressure spectra to approach and then to begin to move away from the flat plate distribution (Fig. 5b). Since there is a distance of about $20\delta_0$ between the two downstream measurement locations, it is quite possible that the low-frequency levels drop below those of the flat plate boundary layer between these two stations. Whether or not this is true, there is clearly not a monotonic recovery to the flat plate spectrum.

An interesting observation arises downstream. The last two measurement stations in Fig. 6 show bands of elevated spanwise coherence relative to the flat plate boundary layer centered near 20 kHz. This might indicate organized structures in the flow that were not present before the expansion. If this were the case, the significant increase in coherence level between $x/\delta_0 = 9.52$ and 28.8 would signify increasing spanwise extent and/or organization with downstream distance. Interestingly, the streamwise coherence at these locations shows only slight increases.

The correlation results show a slight increase in the peak streamwise correlation downstream (Fig. 7a) but a significant increase in the peak spanwise correlation (Fig. 7b). The increases in coherence and correlation levels seem to suggest these new structures have larger spanwise extent and greater spanwise organization than in the incoming boundary layer. It is again noted that in the presented graphs, the transducer spacings are normalized by the incoming boundary-layer thickness. Although the increase in
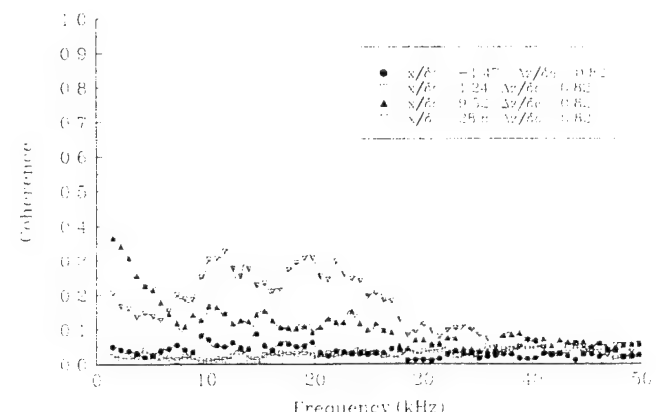

Fig. 6　Spanwise coherence downstream of the 7-deg centered expansion.
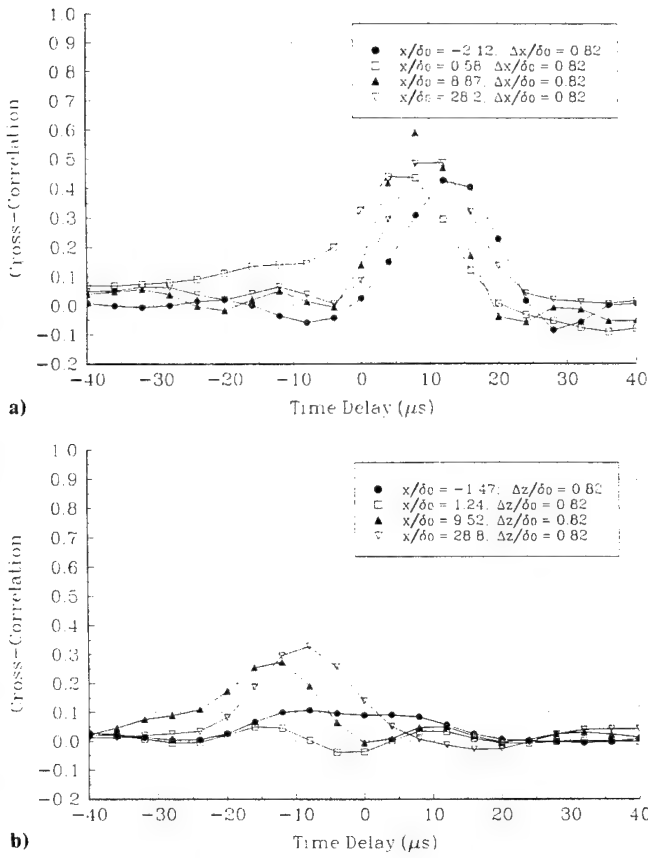
Fig. 7 Space-time correlations downstream of the 7-deg centered expansion: a) streamwise and b) spanwise.

boundary-layer thickness across the expansion might partially account for the higher coherence and correlation levels after the expansion, it is shown later that this is not the primary explanation.

The most common use of the space-time correlation is in the identification of a convection velocity U_c. If it is assumed that the turbulence is not rapidly changing (Taylor's frozen field hypothesis), then the time delay at peak correlation level is a measure of the average time it takes for coherent motions to traverse the probe separation. In Fig. 7, the time resolution of the four-channel measurements (4 µs) is not sufficient for an accurate measurement of the convection velocity. For the incoming boundary layer only, two-channel data were acquired at 500 kHz per channel to increase the time resolution from 4 to 2 µs. With those data, convection velocities of 80–90% of the freestream velocity measured by Samimy et al.[12] were obtained, in agreement with the current literature.[19] A value of $0.9U_\infty$ is obtained by interpolating a peak at $\Delta t = 14$ µs in Fig. 7. Furthermore, as expected in the two-dimensional flat plate boundary layer, the spanwise space-time correlations were symmetric about $\Delta t = 0$ for $\Delta z/\delta_0 = 0.33$ and displayed negligible correlation for $\Delta z/\delta_0 = 0.82$ (Fig. 7b) and 1.63. In addition to these results, other tests confirmed that no artificial phase delays existed between the transducers (e.g., switching the transducer order did not affect the results).

The convection velocities indicated by the streamwise correlations after the expansion regions are unreasonably high. The spatial simulation of supersonic turbulence by Lee et al.[23] showed that if one performed a space-time correlation of dilatation fluctuations (which are closely related to pressure fluctuations), convection velocities greater than the actual propagation velocities would be obtained. This is due to the propagation of acoustic disturbances with the acoustic velocity relative to the local velocity. It should also be noted that Arnette et al.[24] have obtained large ensembles of double-pulse, instantaneous visualizations downstream of this 7-deg centered expansion and performed two-dimensional space/time correlations for the purpose of obtaining convection velocities. The results show that the visual features commonly identified as large scale eddies convect at a velocity slightly less than the
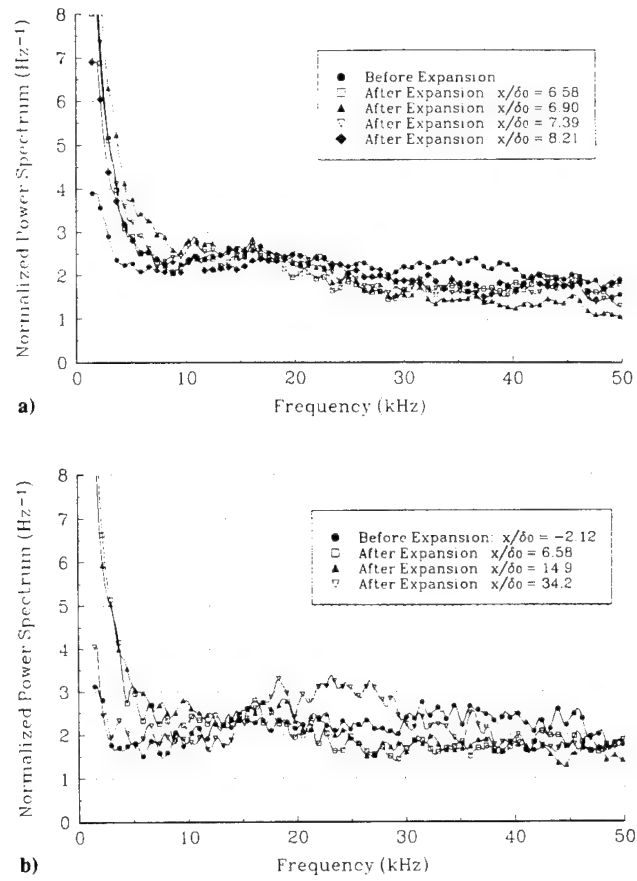
Fig. 8 Normalized power spectra downstream of the 7-deg gradual expansion: a) immediately after the expansion and b) downstream evolution.
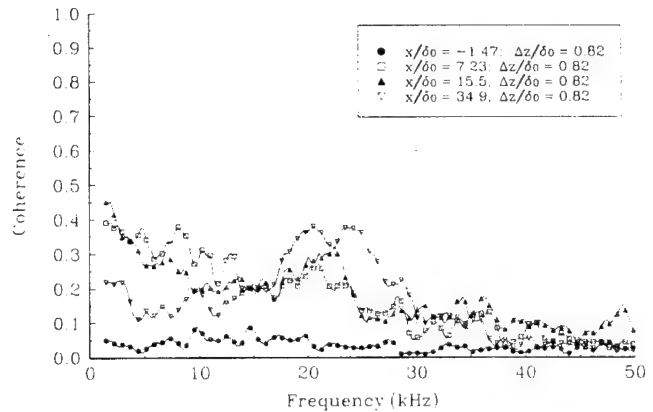
Fig. 9 Spanwise coherence downstream of the 7-deg gradual expansion.

freestream velocity downstream of the expansion (obtained from an inviscid analysis assuming the flat plate freestream velocity measured by Samimy et al.[13]). Thus it appears that space-time correlations of fluctuating surface pressures are not a suitable technique for determining convection velocities in these severely distorted boundary layers.

For the spanwise space-time correlations, there are notable shifts to negative time delays downstream of the expansions, which is very puzzling. Although one might conceive of some type of acoustically propagating disturbance giving rise to nonzero time shifts at maximum correlation, the lack of symmetry about $\Delta t = 0$ is very perplexing. Further downstream, the peak time delays move towards those of the incoming boundary layer for both streamwise and spanwise correlations, but the delays are still far off at the last measurement locations.

B. 7-Deg Gradual Expansion

The results of the 7-deg gradual expansion model demonstrate that just downstream of the end of the expansion region ($x/\delta_0 \approx 7$) no rapid spectral development is occurring as for the 7-deg centered expansion but that a small shift to low-frequencies is still noticeable (Fig. 8a). This suggests the gradual curvature has allowed the boundary layer to adjust within the expansion. The low frequency spectral levels increase between $x/\delta_0 = 6.58$ and 6.90 and then progressively decrease at $x/\delta_0 = 7.39$ and 8.21, signifying a nonmonotonic spectral evolution. No measurements were made within the gradual expansion regions. Streamwise coherence results also demonstrate that the evolution after the gradual expansion is not rapid.

The 7-deg gradual expansion exhibits not only elevated spanwise coherence for $f = 15$–30 kHz but also elevated spectral densities at $x/\delta_0 = 34.2$ (Fig. 8b). None of the other postexpansion spectra displayed elevated spectral levels at these frequencies. Clearly, the feature giving rise to elevated coherence at 15–30 kHz is more prominent here than at any other measurement location for any other expansion. The broad spanwise coherence peak at 15–30 kHz in Fig. 9 offers further support. If some type of new "structural" feature is responsible, they are much more energetic than in the centered expansion cases. The correlations in Figs. 9a and 9b demonstrate again that although the spanwise extent is increased significantly, little identifiable increase has occurred in the streamwise direction.

Again, the space-time correlations (Fig. 10a) exhibit small time delays that produce unreasonable convection velocities. The spanwise correlations (Fig. 10b) are again nonsymmetric with large peaks at nonzero time delays. It appears that as the flow progresses downstream the correlation is beginning to evolve towards that of the flat plate boundary layer, although drastic differences are still present at the last measurement location. The time delays at peak correlation for the streamwise separations do not appear to approach those of the flat plate boundary layer with increasing down-


a)
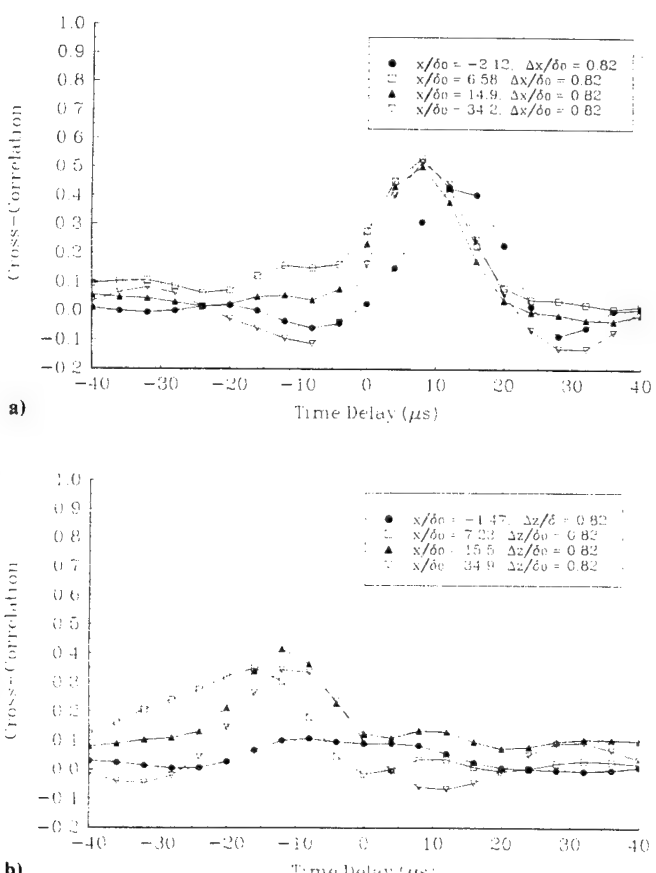
b)
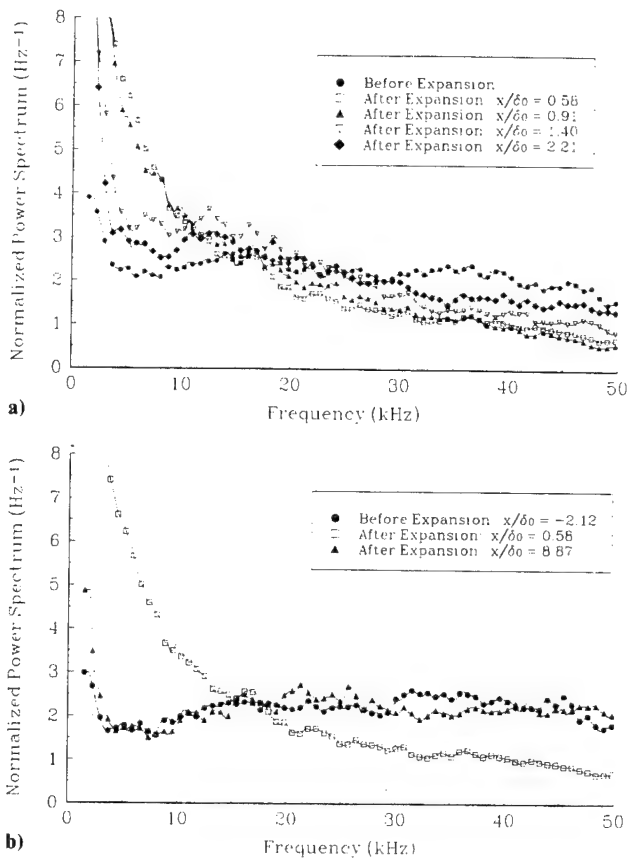
Fig. 11 Normalized power spectra downstream of the 14-deg centered expansion: a) immediately after the expansion and b) downstream evolution.

stream distance. Clearly, the state of the boundary layer at $x/\delta_0 = 34.2$ is very different than that of the flat plate boundary layer.

A fair comparison can be made between the pressure spectra (Figs. 5 and 8) and the spanwise coherence (Figs. 6 and 9) at $x/\delta_0 = 6.58$ for the 7-deg gradual model and $x/\delta_0 = 8.87$ for the 7-deg centered model, and likewise between $x/\delta_0 = 14.9$ for the 7-deg gradual model and $x/\delta_0 = 28.2$ for the 7-deg centered model. The spectra and spanwise coherence for the 7-deg gradual expansion at $x/\delta_0 = 34.2$ display higher levels at $f = 10$–30 kHz than are found at $x/\delta_0 = 28.2$ for the 7-deg centered expansion. The favorable comparison at the cited locations suggests the new features would emerge further downstream of the centered expansion. The earlier appearance of these features in the gradual case seems to indicate that the gradual curvature allows the turbulence to rearrange itself more efficiently through the expansion. Whether or not the overall length required for emergence (measured from the beginning of the expansion) changes cannot be commented on due to the limited model lengths.

C. 14-Deg Centered Expansion

The pressure fluctuation spectrum immediately after the 14-deg centered expansion demonstrates rapid evolution. Figure 11a shows the spectral shift to low frequencies ($f < 15$ kHz). The initial amplification at low frequencies followed by marked attenuation appears very similar to the 7-deg centered expansion (Fig. 5a). The streamwise coherence results just after the expansion display rapid development similar to the 7-deg centered expansion.

The similarity of the power spectra at $x/\delta_0 = 8.87$ (Fig. 11b) to that of the flat plate boundary layer is very misleading. Looking at the last measurement station in Figs. 12a and 12b, a substantial increase in the streamwise coherence across the entire frequency range is seen, whereas for the spanwise coherence an increase is observed at low frequencies. This indicates strong differences from the flat plate boundary layer are present, but there is no clear emergence of a band of new "structures" as for the 7-deg centered expansion. The streamwise and spanwise correlations, however,

a)

b)

Fig. 10 Space-time correlations downstream of the 7-deg gradual expansion: a) streamwise and b) spanwise.

a)
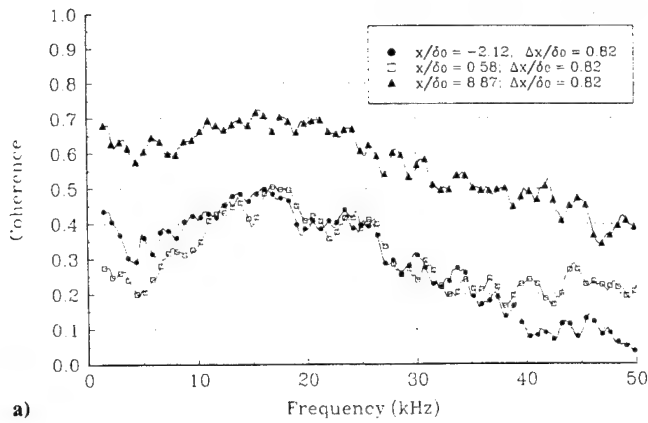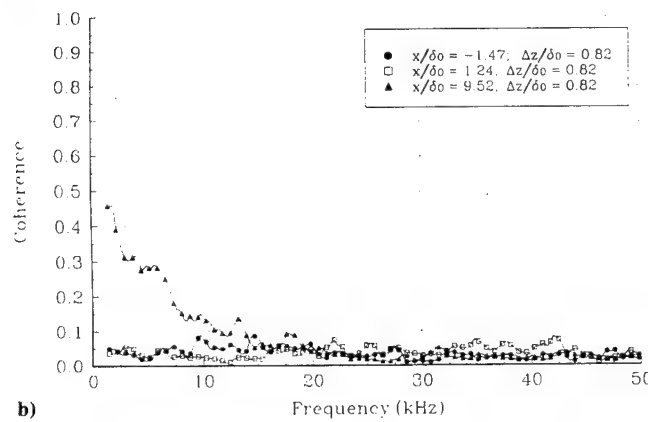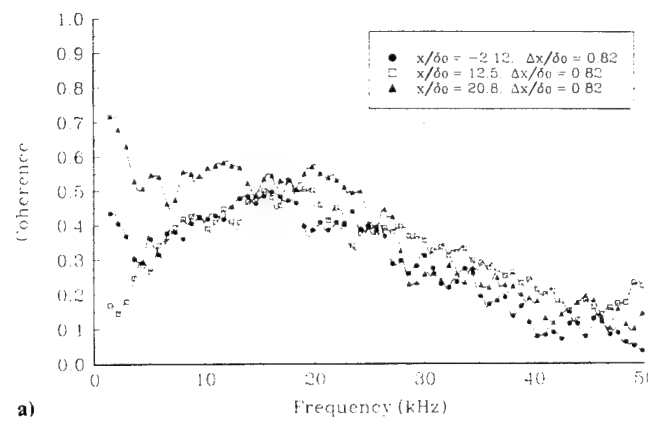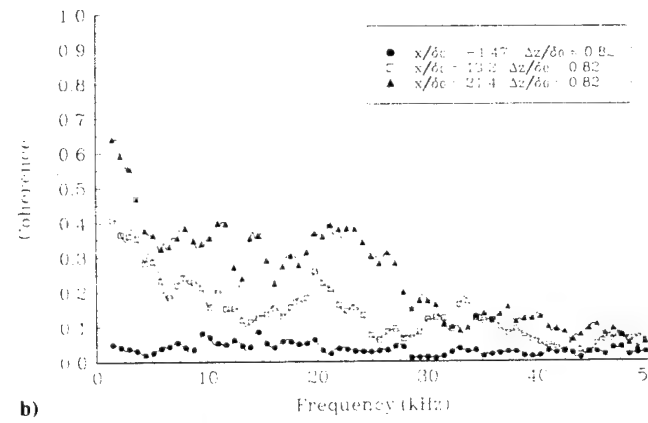
Fig. 12   Coherence downstream of the 14-deg centered expansion:
a) streamwise and b) spanwise.
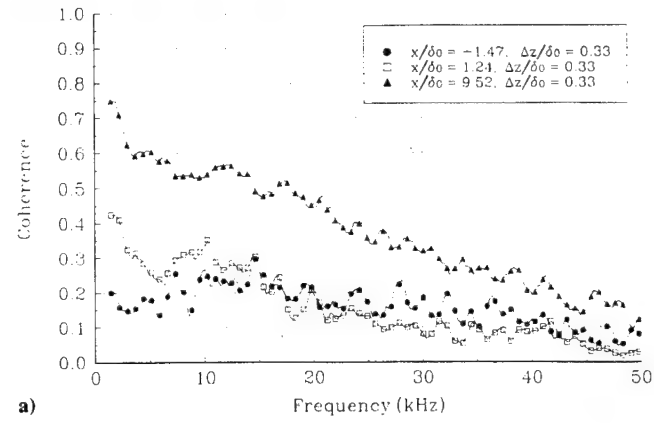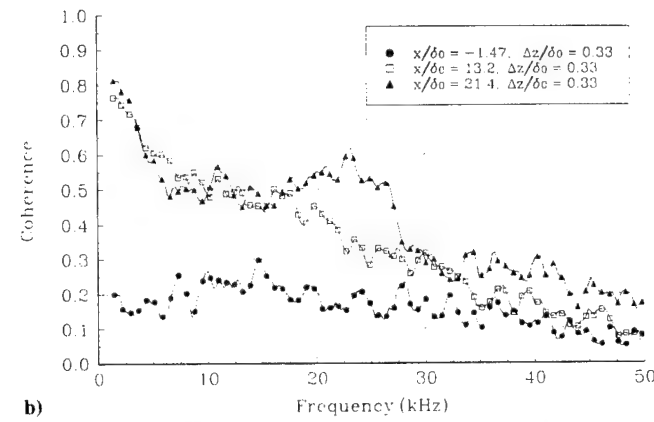
Fig. 14   Spanwise coherence downstream of 14-deg expansions:
a) centered and b) gradual.


Fig. 13   Coherence downstream of the 14-deg gradual expansion: a)
streamwise and b) spanwise.
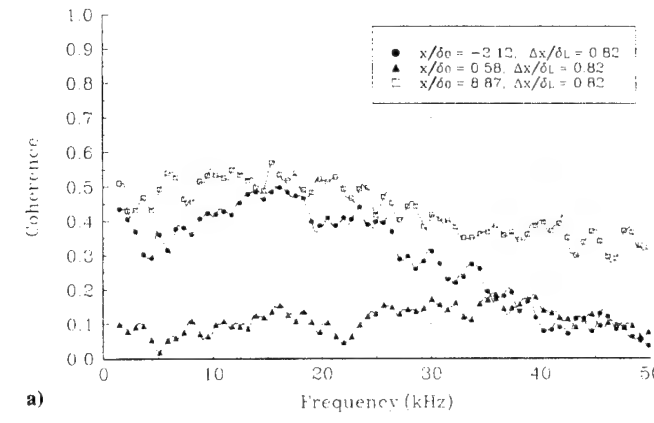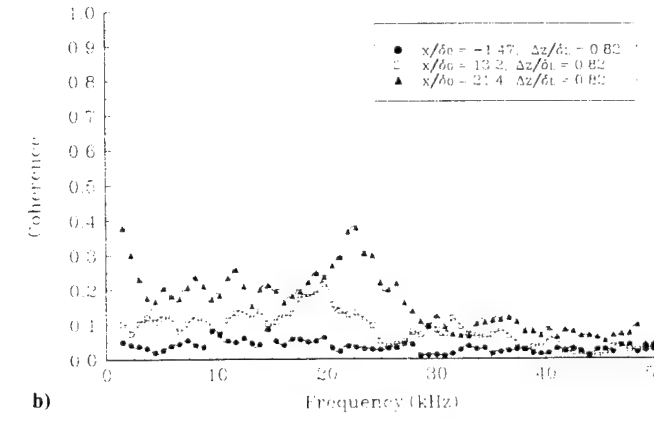
Fig. 15   Coherence downstream of 14-deg expansions with a trans-
ducer spacing of Δx(or z)/δ_L = 0.82 (normalized by local boundary-
layer thickness): a) streamwise coherence, 14-deg centered expansion
and b) spanwise coherence, 14-deg gradual expansion.

display a deviation from the flat plate correlations similar to the other expansions. The peak time delays in the space-time correlations again approach those of the incoming boundary layer with increasing downstream distance but remain far from the flat plate values at the last measurement location ($x/\delta_0 \simeq 9$). This again emphasizes that the boundary layer is quite different from the incoming boundary layer.

The emergence of the new features downstream of the 7-deg centered expansion is first apparent at $x/\delta_0 \simeq 10$ and is very noticeable at $x/\delta_0 \simeq 30$. The results indicate that the larger perturbation causes a more significant redistribution of the pressure fluctuations. As one would expect a longer period of adjustment for stronger perturbations, it may be expected that the emergence of any new structures would take longer for the 14-deg centered expansion. Since the last measurement station is at $x/\delta_0 = 9$, it may be that the 14-deg centered expansion model is too short for the new structures to emerge. Merit for this idea is presented later.

D. 14-Deg Gradual Expansion

Similar to the 7-deg gradual expansion, the results for the 14-deg gradual expansion demonstrate that development just after the end of the expansion is not very rapid. However, the shift to low frequencies is much more noticeable than for the 7-deg gradual expansion as expected. Coherence results also display relatively slow development after the expansion.

As in both 7-deg expansions, the emergence of new structures is evident for the 14-deg gradual model. The downstream locations of Figs. 13a and 13b display a band of elevated coherence relative to the flat plate boundary layer. Again, the band is centered nominally at 20 kHz, suggesting that features similar to those of the 7-deg expansions have emerged.

Similar to the other expansions, coherence and space-time correlation levels at the last measurement location ($x/\delta_0 = 20.8$) are significantly larger than those of the incoming boundary layer. The peak time delays again evolve towards those of the flat plate boundary layer with increasing downstream distance, but very substantial differences are still present at $x/\delta_0 = 20.8$.

The coherence results for the 14-deg expansion models indicate the length of the 14-deg centered expansion model is too short for the development of the new structures. Comparing the farthest downstream measurement locations for these two models (Figs. 14a and 14b), it is obvious that the trends are the same, except that a peak around 15–30 kHz is superimposed on the spanwise coherence for the gradual case. Similar comparisons exist for the streamwise coherence at these locations. This shows that the development of the spanwise coherence is consistent for both 14-deg perturbations, but the extra length of the gradual expansion model allows the new features to emerge, whereas the centered model is too short.

Since the boundary-layer thickness increases across the expansion, using the pre-expansion value δ_0 as a global scale to normalize the transducer spacings might be questioned. Given the fixed transducer separations, one might wonder if the substantial increases in coherence and correlation levels sustained downstream of the expansions is not due mainly to the increase in boundary layer thickness. Figure 15 shows coherence results for $\Delta(x \text{ or } z)/\delta_L$ = 0.82 where δ_L is the local boundary-layer thickness. Substantial increases in coherence with increasing downstream distance are still present, showing the increases in coherence and correlation levels are not simply a result of the δ_0 normalization. Similar trends are present for the correlation levels. Results are not given for the 7-deg cases because the fixed transducer separations did not afford similar δ_L-normalized separations at different locations.

IV.   Conclusions

The results of this work indicate that the passing of a high-Reynolds-number Mach 3 turbulent boundary layer through centered or gradual ($R/\delta_0 \simeq 50$) expansions of 7 and 14 deg causes marked, long-lasting changes in the boundary-layer structure. The rms pressure fluctuations normalized by the local mean wall pressure remain nearly constant across all of the expansion regions. Normalized pressure spectra exhibit a shift to lower frequencies across

the expansion, which is thought to reflect the quenching of small-scale, high-frequency motions by the dilatation associated with the expansion regions. This distortion of the spectra across the expansions is more significant for the 7-deg centered expansion than for the 14-deg gradual expansion but increases with total deflection for constant radius of surface curvature. The power spectra and spanwise coherence exhibit extremely fast development immediately after the centered expansions and relatively slow development immediately after the gradual expansions. For both the 7- and 14-deg cases, respectively, the structure of the boundary layer immediately after the gradual expansion region compares well with the structure of the boundary layer several boundary-layer thicknesses downstream of the centered expansion case, suggesting that the shorter "time of flight" through the centered expansions allows less boundary-layer adjustment. Streamwise space-time correlations in the perturbed boundary layers do not lend themselves to the derivation of convection velocities (although reasonable values are obtained in the flat plate boundary layer). New features appear at 15–30 kHz downstream of the expansions that are characterized by high levels of spanwise coherence and appear to give rise to spanwise correlation levels much higher than those of the flat plate boundary layer. Associated increases in streamwise coherence and correlation are not as pronounced. No strong evidence of a specific structural feature has been linked to these observations. The boundary-layer structure remained vastly different from that of the flat plate boundary layer at the last measurement locations, $x/\delta_0 \simeq$ 34 (28) for the 7-deg gradual (centered) expansion and $x/\delta_0 = 20$ (10) for the 14-deg gradual (centered) expansion.

References

[1]Bradshaw, P., "The Effect of Mean Compression or Dilatation on the Turbulence Structure of Supersonic Boundary Layers," *Journal of Fluid Mechanics*, Vol. 63, Pt. 3, 1974, pp. 449–464.

[2]Spina, E. F., Smits, A. J., and Robinson, S. K., "The Physics of Supersonic Turbulent Boundary Layers," *Annual Review of Fluid Mechanics*, Vol. 26, 1994, pp. 287–319.

[3]Morkovin, M. V., "Effects of High Acceleration on a Turbulent Supersonic Shear Layer," Heat Transfer and Fluid Mechanics Inst., Stanford Univ., Stanford, CA, 1955.

[4]Lewis, J. E., Gran, R. L., and Kubota, T., "An Experiment on the Adiabatic Compressible Turbulent Boundary Layer in Adverse and Favorable Pressure Gradients," *Journal of Fluid Mechanics*, Vol. 51, Pt. 4, 1972, pp. 657–672.

[5]Thomann, H., "Effects of Streamwise Wall Curvature on Heat Transfer in a Turbulent Boundary Layer," *Journal of Fluid Mechanics*, Vol. 33, Pt. 2, 1968, pp. 283–292.

[6]Dussauge, J. P., and Gaviglio, J., "The Rapid Expansion of a Supersonic Turbulent Flow: Role of Bulk Dilatation," *Journal of Fluid Mechanics*, Vol. 174, 1987, pp. 81–112.

[7]Dussauge, J. P., "The Relaxation of a 'Relaminarized' Turbulent Boundary-Layer, in Supersonic– Flow," *Proceedings of the Fifth Symposium on Turbulent Shear Flows*, Cornell Univ., Ithaca, NY, 1985, pp. 2.27–2.31.

[8]Narasimha, R., and Sreenivasan, K. R., "Relaminarization in Highly Accelerated Turbulent Boundary Layers," *Journal of Fluid Mechanics*, Vol. 61, Pt. 3, 1973, pp. 417–447.

[9]Narasimha, R., and Viswanath, P. R., "Reverse Transition at an Expansion Corner in Supersonic Flow," *AIAA Journal*, Vol. 13, No. 5, 1975, pp. 693–695.

[10]Smith, D. R., and Smits, A. J., "The Rapid Expansion of a Turbulent Boundary Layer in a Supersonic Flow," *Theoretical and Computational Fluid Dynamics*, Vol. 2, 1991, pp. 319–328.

[11]Arnette, S. A., Samimy, M., and Elliott, G. S., "The Effect of Expansion on the Large Scale Structure of a Compressible Turbulent Boundary Layer," AIAA Paper 93-2991, July 1993.

[12]Samimy, M., Arnette, S. A., and Elliott, G. S., "Streamwise Structures in a Turbulent Supersonic Boundary Layer," *Physics of Fluids*, Vol. 6, No. 3, 1994, pp. 1081–1083.

[13]Samimy, M., Elliott, G. S., Glawe, D. D., Reeder, M. F., and Arnette, S. A., "Compressible Mixing Layers with and without Particles," Ohio

State Univ. TR MEMS-92-101, Columbus, OH, Aug. 1992.

[14]Jayaram, M., Taylor, M. W., and Smits, A.J., "The Response of a Compressible Turbulent Boundary Layer to Short Regions of Concave Surface Curvature," *Journal of Fluid Mechanics*, Vol. 175, 1985, pp. 343–362.

[15]Degani, D., and Smits, A. J., "Response of a Compressible, Turbulent Boundary Layer to a Short Region of Surface Curvature," *AIAA Journal*, Vol. 27, No. 1, 1989, pp. 23–28.

[16]Tan, D. K. M., Tran, T. T., and Bogdonoff, S. M., "Surface Pressure Fluctuations in a Three-Dimensional Shock Wave/Boundary Layer Interaction," AIAA Paper 85-0125, Jan. 1985.

[17]Fernholz, H. H., Finley, P. J., Dussauge, J. P., and Smits, A. J., "A Survey of Measurements and Measuring Techniques in Rapidly Distorted Compressible Turbulent Boundary Layers," AGARDograph No. 315, 1989.

[18]Corcos, G. M., "Resolution of Pressure in Turbulence," *Journal of the Acoustical Society of America*, Vol. 35, No. 2, 1963, pp. 192–199.

[19]Spina, E. F., Donovan, J. F., and Smits, A. J., "On the Structure of High-Reynolds-Number Supersonic Turbulent Boundary Layers," *Journal of Fluid Mechanics*, Vol. 222, 1991, pp. 293–327.

[20]Dawson, J. A., "An Experimental Investigation of Supersonic Turbulent Boundary Layers After an Expansion via Wall Pressure Measurements," M.S. Thesis, Dept. of Mechanical Engineering, Ohio State Univ., Columbus, OH, 1993.

[21]Muck, K. C., Dussauge, J., and Bogdonoff, S. M., "Structure of the Wall Pressure Fluctuations in a Shock-Induced Separated Turbulent Flow," AIAA Paper 85-0179, Jan. 1985.

[22]Lu, F. K., and Chung K., "Downstream Influence Scaling of Turbulent Flow Past Expansion Corners," *AIAA Journal*, Vol. 30, No. 12, 1992, pp. 2976, 2977.

[23]Lee, S., Lele, S. K., and Moin, P., "Simulation of Spatially Evolving Turbulence and the Applicability of Taylor's Hypothesis in Compressible Flow," *Physics of Fluids A*, Vol. 4, No. 7, 1992, pp. 1521–1530.

[24]Arnette, S. A., Samimy, M., and Elliott, G. S., "The Effect of Expansion on Large Scale Structure Evolution in a Compressible Turbulent Boundary Layer," AIAA Paper 94-2228, June 1994.

Appendix III Arnette, S.A., Samimy, M., and Elliott, G.S., 1995, "Structure of Supersonic Turbulent Boundary Layer After Expansion Regions," <u>AIAA J.</u>, 33: 430-438.

Structure of Supersonic Turbulent Boundary Layer After Expansion Regions

S. A. Arnette, M. Samimy, G. S. Elliott

Structure of Supersonic Turbulent Boundary Layer After Expansion Regions

S. A. Arnette,* M. Samimy,† and G. S. Elliott‡
Ohio State University, Columbus, Ohio 43210

The effects of four expansion regions [centered and gradual ($R/\delta_0 \simeq 50$) expansions of both 7 and 14 deg] on a fully developed Mach 3 turbulent boundary layer were investigated. Instantaneous visualizations were made possible by the presence of scalar water condensation in the freestream and its absence in the higher temperature boundary layer. The elongated longitudinal structures previously found in the flat plate boundary layer are present downstream of the expansions. Large-scale structures increase in scale across the expansions. Structure angles also initially increase but are found to return to the flat plate value $10\delta_0$ downstream of the 7-deg centered expansion. The rapid quenching of small-scale turbulence by the expansions results in a more intermittent boundary layer visually dominated by large-scale structures. Convection velocities derived from double-pulse correlations are reasonable in the flat plate and 7-deg centered expansion boundary layers. Excess condensation downstream of the 14-deg expansions (probably CO_2) made the 14-deg expansion results more difficult to interpret.

Nomenclature

n	= normal distance above the surface
R	= radius of curvature for the gradual expansions, correlation coefficient
Re_θ	= Reynolds number based on boundary layer momentum thickness
s	= streamwise distance along the surface measured from the start of the convex curvature
U	= mean velocity vector
U	= mean streamwise velocity
u_τ	= friction velocity
V	= mean normal velocity
x	= horizontal distance measured from $(s, n) = (0, 0)$
y	= vertical distance measured from $(s, n) = (0, 0)$
Δp	= pressure difference across the expansion region
δ_0	= boundary layer thickness at $s = 0$ mm
δ_{vis}	= boundary layer thickness defined by 99% of the freestream intensity
δ_{RMS}	= normal distance above the boundary where the peak in the rms profile occurs
θ	= boundary layer momentum thickness
ν	= kinematic viscosity
τ_0	= surface shear stress ahead of the expansion region

Introduction

IMPROVED understanding of compressible turbulent boundary layers will always offer the potential for significant advances in high-speed flight applications as boundary layers are of such central importance to issues of drag and heat transfer. Although an increasingly detailed characterization of two-dimensional, flat plate, zero pressure gradient, compressible turbulent boundary layers continues to emerge,[1] it is rare that such canonical flows occur in applications. Instead, the boundary layer likely experiences several extra rates of strain caused by effects such as pressure gradients and streamline curvature.[2] Boundary-layer response to such perturbations is nonlinear, so that the effect of multiple perturbations cannot be predicted even if their individual effects are known.[3] Thus,

studies of boundary layers subjected to multiple perturbations are needed.

Although our understanding of the effects of mean compression or dilatation on supersonic turbulent boundary layers is not very advanced, such effects are intuitively connected to the principle of conservation of angular momentum in the presence of the distortion of a mass element.[2] The passage of a two-dimensional, compressible turbulent boundary layer through an expansion is depicted in Fig. 1. In the expansion, the boundary layer encounters stabilizing convex streamline curvature, a favorable streamwise pressure gradient ($\partial p/\partial s < 0$), a normal pressure gradient ($\partial p/\partial n > 0$), and bulk dilatation ($\nabla \cdot U > 0$). The mean velocity divergence within the expansion region ($\partial U/\partial x > 0$, $\partial V/\partial y > 0$ in the coordinate system of Fig. 1) and streamline curvature ($\partial V/\partial x < 0$) cause fluid elements' cross-sectional area to increase in the x–y, x–z, and y–z planes. As a result, all vorticity components are damped, resulting in an overall stabilization. References 4–12 are most of the relevant studies known to the authors. As discussed by Spina et al.,[1] past work illustrates the effects of dilatation over those of streamline curvature, i.e., $\nabla \cdot U \gg \partial V/\partial x$ (a disparity that is enhanced with increasing Mach number).

Thomann[5] isolated the effects of 20 deg of gradual convex curvature on the heat transfer beneath a supersonic, turbulent boundary layer ($M_\infty = 2.5$) by eliminating pressure gradients with an appropriately shaped body in the freestream. The heat transfer rate decreased by approximately 20%, suggesting a significant reduction in turbulent mixing.

Dussauge and Gaviglio[6] investigated the 12-deg centered expansion of an $M_\infty = 1.76$ boundary layer ($\delta_0 = 10$ mm, $Re_\theta = 5 \times 10^3$). In addition to mean and turbulence measurements, an analysis based on Rapid Distortion Theory isolated the effect of bulk dilatation. Mean velocity profiles downstream of the expansion region initially displayed a thick sublayer region possessing a larger streamwise velocity gradient than that found in the incoming profile, with no apparent logarithmic region. After approximately $9\delta_0$, a logarithmic region reappeared. The calculations indicated the decreases in streamwise turbulence intensity sustained through the expansion were due primarily to bulk dilatation, although the reductions near the wall were not reproduced well by the calculations including only dilatation effects. After the expansion, the turbulence intensity near the wall ($n/\delta < 0.2$) was initially very low relative to incoming levels. For $n/\delta > 0.25$, the drop in turbulence intensity decreased with increasing normal distance. The near-wall region established turbulence intensities comparable to incoming levels more quickly than the outer portions of the boundary layer, where the evolution was slow. This is a consequence of the turbulence production being confined to the near-wall region that possesses significant mean

a)

b)
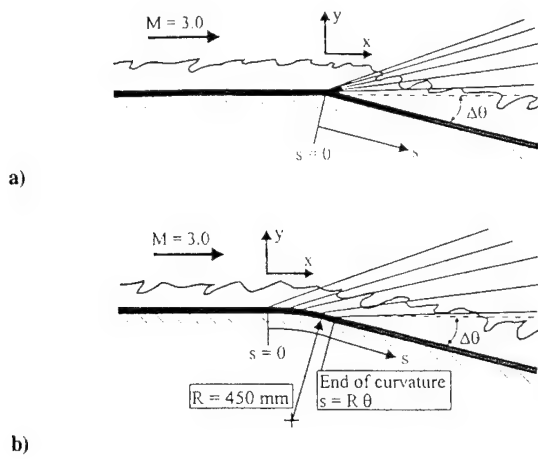
**Fig. 1 Schematics of the a) centered and b) gradual expansion models ($\Delta\theta$ = 7 and 14 deg for both). The (x, y) origin is at the curvature onset at the surface. The n coordinate is zero at the surface and everywhere normal to the surface.**

gradients. The rapid recovery of the near-wall region led to the proposal that a new internal layer had been formed after the expansion and that the boundary layer had been relaminarized.

A relaminarized boundary layer is defined as one in which the effects of the Reynolds stresses on the mean flow have become negligible.[13] It can occur when a turbulent boundary layer is subjected to a large, favorable pressure gradient. For expanded compressible turbulent boundary layers, Narasimha and Viswanath[12] suggest that relaminarization occurs for $\Delta p/\tau_0$ greater than approximately 70.

Smith and Smits[7] investigated the 20-deg centered expansion of an $M_\infty = 2.84$ ($\delta_0 = 26$ mm, $Re_\theta = 7.76 \times 10^4$) turbulent boundary. Mean and turbulence profiles were measured $1\delta_0$ upstream and $3.5\delta_0$ downstream of the corner. Again, the mean velocity profile did not possess a logarithmic region at $s/\delta_0 = 3.5$. The streamwise turbulence intensity and normal Reynolds stress were significantly decreased across the expansion, but the streamwise mass-flux fluctuation profile was essentially unchanged, suggesting more significant density fluctuations after the expansion. Calculations similar to those of Ref. 6 again showed the decreases in turbulence levels across the expansion were due mainly to dilatation.

Dawson et al.[10] acquired multipoint measurements of the fluctuating surface pressures in the expanded supersonic turbulent boundary layers of this study. Normalized power spectral densities were much more concentrated at low frequencies just downstream of the expansions relative to upstream, with accompanying sharp decreases at high frequencies. This suggested small-scale motions are quenched almost immediately by the expansion regions. Streamwise space–time correlations in the flat plate boundary layer showed the convection velocity to be 0.80–0.90 U_∞, which agrees well with other studies.[14] However, convection velocities were unreasonably high downstream of the expansions. These results suggest the relationship between the pressure field and the large-scale structures is severely altered by the expansions, which might be related to the wave propagation of acoustic disturbances relative to the mean flow velocity.[10] Such an effect has been demonstrated in a spatially simulated, turbulent, supersonic flow.[15]

It has become increasingly clear that turbulent boundary layers contain nonrandom, coherent structure. Impetus for investigating these structures comes from the discovery that they are of major importance to the dynamics of the turbulence. Our knowledge of coherent structures in compressible boundary layers is limited to the δ-scale motions of the outer layer.[1,16] This is in sharp contrast to the incompressible case, where several structural features have been investigated.[16] The reason is a lack of both spatial and temporal resolution.[17] Discussions of coherent structure in supersonic turbulent boundary layers are given elsewhere.[1,9,11,14,17]

Plan view visualizations in the Mach 3 flat plate boundary layer of this study reveal structures of a very large streamwise, and

limited spanwise, extent.[9,11,18] As such, these elongated longitudinal structures are somewhat similar to those near the wall of incompressible boundary layers. However, these structures were found well above the inner layer, nominally at $n/\delta = 0.5$–1.0, and have a larger spanwise extent than near-wall streaks of incompressible cases. Although the structures are possibly present deeper in the boundary layer, the visualization technique precluded visualizations closer to the wall. The removal of the flow conditioning assembly had little or no effect on the presence of the elongated structures. These facts suggest the structures may be a robust feature of the compressible boundary layer, although no comment could be made on their importance. Their apparent absence in incompressible boundary layers calls to question longstanding ideas concerning the similarity of the turbulence structure of incompressible and compressible boundary layers.[18]

This work is part of an ongoing study of the effects of expansion regions on supersonic turbulent boundary layers. A more complete presentation of the results appears elsewhere.[11]

Experimental Procedure

The experiments were performed at the Aeronautical and Astronautical Research Laboratory at the Ohio State University. The boundary layer develops on a flat plate from the stagnation chamber to the beginning of the convex surface curvature (67 cm from the throat to the beginning of the surface curvature). The incoming Mach 3 flow occupies a passage 152.4 mm wide by 76.2 mm high. After the expansion regions, the model surfaces diverge away from the expansion corner towards the bottom of the test section, which has a total cross section of 152.4 mm wide by 152.4 mm high. This configuration and the employed coordinate system is illustrated in Fig. 1. Optical access is provided by windows in the top and side walls. The system has a storage capacity of 42.5 m^3 at pressures up to 16.4 MPa. The stagnation pressure was 1.14 MPa (11.2 atm) $\pm 1\%$, and the stagnation temperature was nominally 280 K. The stagnation chamber is equipped with a removable flow conditioning section consisting of a perforated plate, a 10-cm honeycomb section, and a screen. Previous laser Doppler velocimetry (LDV) measurements by Samimy et al.[19] showed the freestream streamwise and normal turbulence intensities to be less than 3%. At the location corresponding to the start of the four expansion regions the results were $M_\infty = 3.01$, $\delta_0 = 9.2$ mm, $\theta = 0.37$ mm, and $Re_\theta = 2.47 \times 10^4$.

The centered and gradual expansion geometries are depicted in Fig. 1. The radius of curvature for both gradual expansion models is 450 mm, giving $R/\delta_0 \simeq 50$. In addition to the four expansion models, a flat plate model was used to extend the incoming boundary layer through the length of the test section. It includes a flush-mounted window (20 mm by 310 mm) along its centerline to reduce surface reflections.

Schlieren photography was used to ensure no freestream nonuniformities were present. Spanwise and streamwise distributions of mean static pressures at the model surfaces were monitored via static taps in the models. Schlieren images[9-11] and mean pressure measurements[9,10] are presented elsewhere.

Small particles of condensed water form in the nozzle during the expansion to Mach 3, creating a scalar marker in the freestream. The condensate comes from the small amount of water vapor left in the supply air after passing through the system's desiccant dryers, which reduce the compressed air's water content to very low levels. Condensate is not formed in the higher temperature boundary layer. This provides an approximate indicator for visually differentiating the turbulent boundary layer from the freestream. The high sensitivity of the collected signal to the incident polarization direction suggests the scattering falls near the Rayleigh regime, giving an effective particle diameter on the order of 50 nm for the employed 532-nm illumination. This suggests the particles are sufficiently small to accurately follow the marked fluid. Similar condensation visualizations of compressible turbulent boundary layers have been obtained with uv Rayleigh scattering.[20]

Most visualizations were acquired with the filtered Rayleigh scattering (FRS) technique, originally proposed by Miles et al.[21]
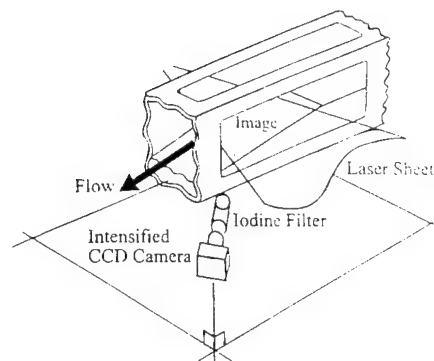
Fig. 2 Schematic of the laser sheet and camera/filter configuration for the global plan views.

FRS has been successfully applied in supersonic jets,[22] mixing layers,[23] and boundary layers[9,11,18] and has been discussed in detail elsewhere.[21,24-26] An optical cell containing diatomic iodine vapor is used as a frequency discriminator. Diatomic iodine possesses electronic transitions that absorb the frequency-doubled 532-nm radiation of the Nd:YAG laser.[21] The cumulative absorption of the iodine molecules forms a notch filter. The absorption profile can be modified by changing the thermodynamic state of the iodine vapor[21] or the gas composition.[26] Scattering from the condensed particles in the flow is positively Doppler shifted for appropriate optical configurations. Assuming the particles insensitive to molecular motions, the line width of the scattering is simply that of the interrogating laser. By using an injection-seeded Nd:YAG laser, the laser line width is narrow enough that, when the laser frequency is properly tuned, the filter will absorb background reflections (at the laser frequency) while passing Doppler shifted scattering from the condensate.

Several sheet orientations were employed for the FRS visualizations. For streamwise views the sheet entered the test section from the top, and for spanwise views it entered from the side. For both, the camera was rotated 45 deg downstream from the spanwise direction to obtain a positive frequency shift. For the acquisition of global plan views, obtaining a frequency shift that sufficiently separated the condensed particle scattering and the background reflections required that the camera/filter be rotated downstream approximately 45 deg from the spanwise-aligned axis of the laser sheet (which entered from the side). To view the laser sheet, the camera/filter was elevated. For the flat plate, the camera was elevated approximately 35 deg above the plane of the laser sheet. For the expansion models, this angle was increased by approximately the expansion angle, i.e., the sheet was kept parallel to the surface and the camera was placed in nominally the same position in the laboratory frame. This configuration is illustrated in Fig. 2. The pulse duration of the Nd:YAG laser is 9 ns, which effectively freezes the flow. The frequency-doubled Nd:YAG laser is capable of 660 mJ/pulse.

Double-pulse streamwise images of the flat plate and two centered expansion boundary layers were acquired with standard laser sheet lighting of the condensation. The Nd:YAG laser can provide two pulses for each lamp excitation by multiple Q-switching. The delay between the initial and delayed light pulses, which can be set between 15 and 200 μs, was measured with an oscilloscope. To reduce reflections at the boundaries, the centered expansion models were equipped with centered, flush-mounted windows approximately 20 mm wide.

Images were collected with Princeton Instruments 14-bit intensified charge-coupled device (CCD) cameras and stored on 486DX personal computers. Two of these systems were used in the double-pulse experiments. The framing rates (2–3 Hz) result in consecutive images being uncorrelated. The laser provides outputs for camera synchronization, one in single-pulse mode and two in double-pulse mode. The camera controllers possess circuitry such that each will wait until the other is ready to acquire an image (finished storing the previous image) before acquiring an image at the appropriate pulse of the laser's next double pulse. Double-pulsed Nd:YAG lasers have been used in other studies of compressible boundary layers[27,28] and mixing layers.[29]

Results and Discussion

The boundary-layer thickness increases across the expansions, which is expected given the sustained decrease in density. Schlieren images suggest the boundary-layer thickness increases by factors of approximately 1.5 and 2.0 for the 7- and 14-deg expansions, respectively.[10] A standard inviscid analysis gives pressure ratios (p_2/p_1) of 0.56 for the 7-deg expansions and 0.30 for the 14-deg expansions. The measured ratios were 0.53 (0.60) for the 7-deg centered (gradual) case and 0.36 (0.41) for the 14-deg centered (gradual) case.[10,11]

The method of Narasimha and Viswanath[12] was used to estimate the incoming skin friction coefficient in examining the criterion that relaminarization occurs for $\Delta p/\tau_0 > 75$. For the 7- and 14-deg centered expansions, this method gives $\Delta p/\tau_0$ estimates of 48 and 76, respectively. Since relaminarization is sensitive to the magnitude of the favorable pressure gradient, the 14-deg gradual expansion is not considered close to relaminarization. Despite satisfying the criterion, Smith and Smits[7] caution against the term relaminarization based on their cited mass flux fluctuation measurements in a Mach 3 boundary layer subjected to a 20-deg centered expansion. In the flows of this study, the ratio of rms surface fluctuation to local static surface pressure never drops below the flat plate value, which does not give an indication of relaminarization.[10]

Instantaneous streamwise FRS visualizations of the flat plate boundary layer are presented in Fig. 3. In the images, the flow is from right to left. In these and all other visualizations, added white lines indicate the position of the solid surface. The outer portions of the boundary layer are dominated by the presence of large-scale structures that display the presence of smaller scale motions at their outer edges. However, these smaller motions are too large to be identified with Falco's[30] typical eddies at the current Reynolds number ($Re_\theta \simeq 2.5 \times 10^4$). Motions of this scale in compressible boundary layers must be considered to scale on outer layer variables.[14] Similar to Smith and Smits,[31] instantaneous schlieren images of the boundary layer display downstream-inclined structures that span the entire boundary layer thickness.

Spanwise visualizations of the incoming boundary layer 25 mm upstream of the beginning of the expansion regions ($s = -25$ mm) are presented in Fig. 4. The large δ-scale structures of the outer layer are of limited spanwise extent, giving the top edge of the boundary layer a highly intermittent appearance.

Streamwise views of the boundary layer evolution through the 7-deg centered expansion are presented in Fig. 5. As in Figs. 5a and 5b, most large-scale structures increase in scale across the expansion. Recognizing a large-scale structure as a correlated mass of fluid, the sustained decrease in density would necessitate an increase in scale. Further, most structures just downstream of the expansion display a structure angle (relative to the downstream boundary) markedly


s – 135 mm   s – 75 mm
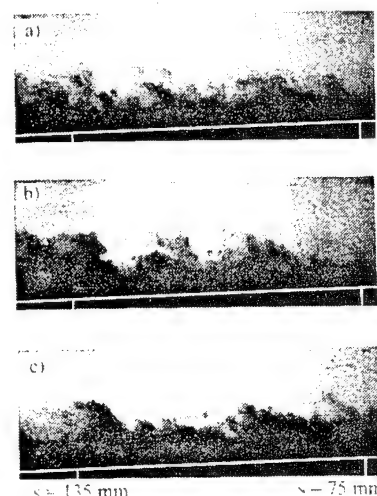
Fig. 3 Instantaneous FRS streamwise views of the flat plate boundary layer. The added white lines indicate the model surface. Indicated distances are relative to $s = 0$ mm (onset of expansion regions with expansion model installed).
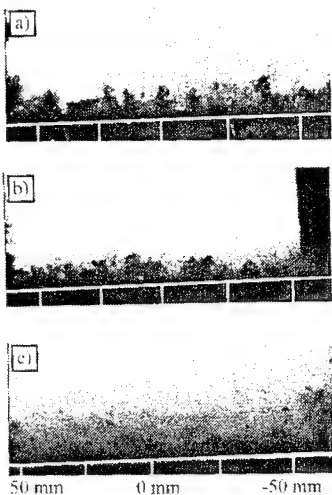
Fig. 7 Instantaneous FRS spanwise views of the boundary layer downstream of the 7-deg centered expansion at s/δ_0 of a) 4.2, b) 13.9, and c) 24.3 (δ_0 = 9.2 mm). Horizontal lines indicate the model surface.

Fig. 8 Average intensity profile and rms intensity fluctuation profile for the flat plate and 7-deg centered expansion (s/δ_0 = 11.4) boundary layers.

the wells of fluid containing condensation penetrate deeper into the boundary layer than upstream of the expansion. Although the increase in vertical extent of the large-scale structures alone would cause these fluid wells to represent a larger fraction of the boundary-layer thickness, the quenching of smaller scale motions has given rise to more substantial penetrations. At $s/\delta_0 = 13.9$ (Fig. 7b) and 24.3 (Fig. 7c), the boundary layer is more full, suggesting a recovery of smaller scale motions. Spanwise views downstream of the other three expansions undergo the same progression. Results for the other expansions are given elsewhere.[11]

It seems that soon after the beginning of the expansion, small-scale motions are quenched. In fact, small-scale quenching was evident for the gradual expansion cases well before the end of the convex surface curvature. Qualitatively, the usual association of small scales with fluctuating vorticity seems appropriate. The conservation of angular momentum dictates that, given the encountered dilatation, small-scale fluctuating vorticity is damped (strictly true only in the absence of viscous effects). This, along with the usual association of small scales with the near-wall region, may help explain the sharp reductions in near-wall turbulence measured previously across centered expansions.[6,7] The survival of the larger scale motions through the expansions (which dominate the outer portions of the boundary layer) may explain the decreasing severity of reductions in turbulence intensity across expansions with increasing normal distance.[6,7]

Ensembles of streamwise views (200–250 images) were obtained of the flat plate (Fig. 3), 7-deg centered, and 14-deg centered expanded boundary layers. FRS was employed in the first two cases but was not needed for the latter case due to the CO_2 condensation. At the surveyed locations, the ensemble averages show the growth rate of the flat plate boundary layer is greater than that downstream of the 7-deg centered expansion, which in turn is greater than that downstream of the 14-deg centered expansion.[11]

Average intensity profiles and rms fluctuation profiles (normalized by the corresponding average profiles) for the flat plate and 7-deg centered expansion ($s/\delta_0 = 11.4$) boundary layers are presented in Fig. 8 (average profiles of 5 adjacent pixel columns). Normalizing with the elevation at peak rms (δ_{RMS}) is fairly effective in collapsing the average profiles. Further, δ_{RMS} represents a locally pertinent, obtainable parameter on which to base comparisons. It was chosen over δ_{vis} because of the difficulty encountered in accurately defining the elevation at which a certain percentage of the freestream intensity occurs. The average profiles suggest the boundary-layer thickness is approximately $3\delta_{RMS}$.

The rms profiles in Fig. 8 are reminiscent of rms temperature fluctuation profiles (normalized by local mean value) of supersonic turbulent boundary layers[34,35] in that a peak is present in the central portion of the boundary layer. This is very different from distributions of rms streamwise and normal velocity fluctuations, which
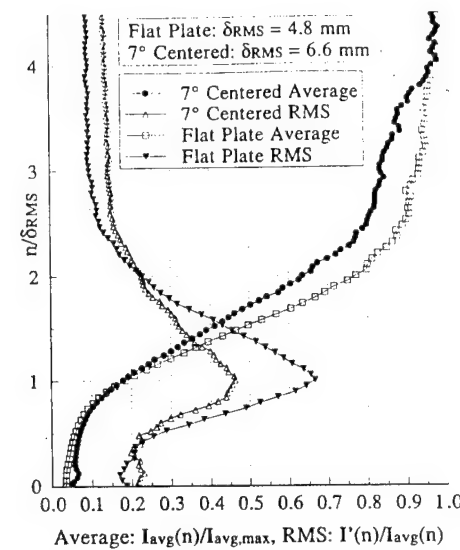
monotonically decrease with increasing normal distance when normalized by local mean values.[34,35] Not surprisingly, this shows the condensation visualizations are most closely related to temperature. The mean temperature decreases from the surface to the top of the boundary layer, just the opposite of the average intensity. If the flat plate rms fluctuations are normalized by $[1 - I_{avg}(y)/I_{avg,max}]$, which is more representative of the mean temperature profile, the peak rms level is reduced by a factor of 4.3, giving a maximum of approximately 0.16 at $n/\delta_{vis} \simeq 0.3$. This compares fairly well to the maximum value of 0.08 found at $y/\delta \simeq 0.5$ in a Mach 3 boundary-layer temperature profile.[35] The remaining discrepancy may be partially due to the on-off nature of the condensation. Although mixed fluid at a given elevation in the boundary layer would be expected to occasionally possess the local mean temperature, fluid is either on or off in the visualizations depending on whether entrained condensation has been destroyed. The mean is determined mainly by the proportion of time condensation that is present and likely falls between the on and off extremes. Thus, higher rms levels are expected.

The rms peak downstream of the 7-deg centered expansion is only two-thirds of the flat plate rms peak (Fig. 8). The freestream rms, due mainly to fluctuations in laser intensity, is 0.10–0.15 for both cases, suggesting a direct comparison is valid. This reduction in peak rms is almost certainly related to the previously cited reduction of visual intermittency caused by the re-establishment of small-scale turbulence. If the outer layer were occupied only by large-scale structures, the fluid containing condensation upstream and downstream of the structures would give rise to large fluctuations about the mean, as in the flat plate boundary layer. However, the decreased growth rate downstream of the 7-deg centered expansion also suggests the large structures are weakened by the expansion, i.e., less able to entrain fluid, which might also be relevant to the reduced rms. Average and rms profiles for the boundary layer downstream of the 14-deg centered expansion were very different than those of Fig. 8 due to the CO_2 condensation and are presented elsewhere.[11]

Spatial correlations were calculated for the ensembles of instantaneous, streamwise visualizations. The correlations are unconditional in that a reference point is defined in the image space, the correlation field surrounding that point is calculated for each image, and the resulting correlation fields are then averaged over the ensemble. If an effective means of locating the reference point in a given image in a similar location relative to, or within, large-scale structures was derived, the average correlations would be a direct reflection of large-scale structure geometry and orientation. Since this is not done, a region of high correlation is not necessarily a result of large-scale structures (for example, if a reference point near the boundary-layer edge fell between the outer portions of adjacent large-scale structures). For this reason, the reference points were
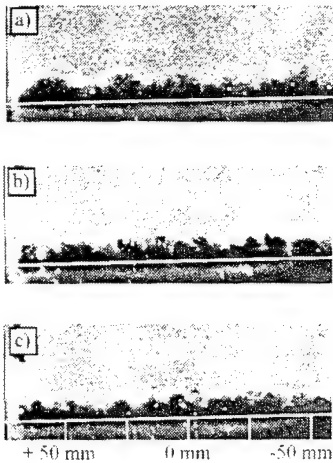
Fig. 4 Instantaneous FRS spanwise views of the flat plate boundary layer 25 mm upstream of the expansion regions. White lines indicate the model surface.
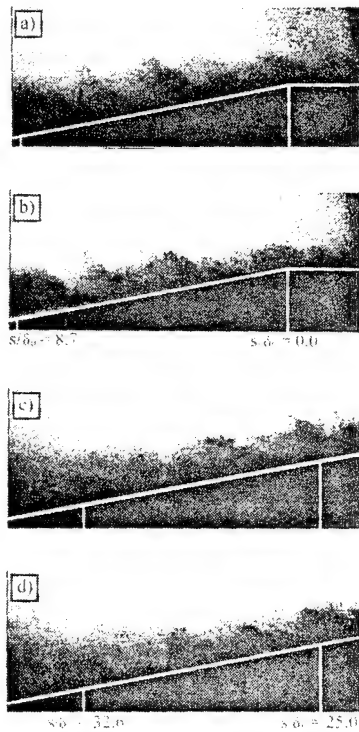

Fig. 5 Instantaneous FRS streamwise views downstream of the 7-deg centered expansion. Added white lines indicate the model surface.

greater than the flat plate value. A consideration of the kinematics of the passage of a large-scale structure through an expansion gives the probable explanation. Previous studies[14,17,32] have shown the large-scale structures are inclined to the wall at approximately 45 deg. The forward boundary of an expansion is inclined at 19.5 deg for a Mach 3 incoming flow. Although the forward boundary is inclined at larger angles closer to the surface because of the boundary-layer Mach number distribution, Mach angles close to 45 deg (which corresponds to $M = 1.41$) are confined very close to the surface. Thus the bottom of a structure will encounter the expansion region before the top. In addition, the diverging geometry of the expansion fan will cause the bottom of a structure to be accelerated through the expansion before the top. These two effects would result in an increased structure angle. Streamwise images acquired further downstream of the 7-deg centered expansion are presented in Figs. 5c and 5d. The boundary layer has a fuller appearance than it did just downstream of the expansion corner. Although large-scale structures corrugate the top edge of the boundary layer, the presence of smaller scales within the boundary layer makes their presence less obvious.
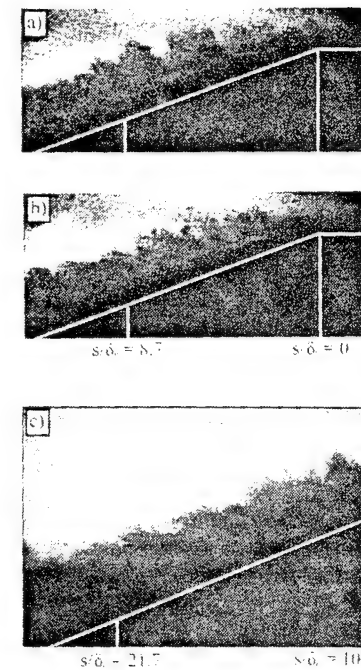

Fig. 6 Instantaneous FRS streamwise views downstream of the 14-deg centered expansion. Added white lines indicate the model surface.

Streamwise views of the 14-deg centered expansion region are presented in Figs. 6a and 6b. Again, the structures sustain an increase in both scale and angle through the expansion. Several structures downstream of the corner in Figs. 6a and 6b are essentially perpendicular to the surface. In general, the increases in scale and angle were more significant for the 14-deg centered or gradual expansion than for the corresponding 7-deg expansion, as would be expected if the explanations cited earlier were responsible. Near the downstream edge of the images, condensation more intense than that in the freestream is found just above the "no-condensation" layer. This new condensate is believed to be CO_2. The CO_2 in the tunnel air is well beyond saturation at the freestream conditions downstream of the 14-deg expansions.[34]

Since the excess condensation provided such a stronger signal than the condensed water particles, the relative amounts of CO_2 and H_2O in the flow were examined. The fact that the existing H_2O vapor does not condense in this facility with a Mach 2 nozzle installed was utilized. The condensation of H_2O vapor in supersonic expansions occurs as a rapid collapse from a supersaturated state. The data compiled by Wegener and Mack[33] suggest that for this tunnel operated at Mach 2, approximately 70 K of supercooling should be expected for very low water vapor content. The static temperature drops 77 K in the Mach 2 nozzle between the throat and exit. Therefore, if the H_2O vapor in the flow became saturated at the Mach 2 nozzle throat, condensation similar to that in the Mach 3 flow would be expected. Thus, an upper bound estimate for the H_2O content of the dried supply air can be obtained by assuming saturation at the Mach 2 nozzle throat. If this is done, an H_2O content of 2.9×10^{-5} kg H_2O/kg air is obtained. For the standard atmosphere there are 4.6×10^{-4} kg CO_2/kg air. This shows that CO_2, if condensed, could give signal levels much higher than the H_2O condensation. In fact, condensed H_2O particles may serve as CO_2 condensation sites.

The CO_2 condensation was not encountered downstream of the 7-deg expansions. Further downstream of the 14-deg centered expansion (Fig. 6c), the CO_2 condensation fills a progressively larger region above the boundary layer. The boundary layer has a very nonintermittent appearance with little evidence of large-scale structures. The boundary layer assumed this appearance whenever the CO_2 condensation was present. It is not clear if this is due to the CO_2 condensation or due to a sharp decrease in the boundary layer's ability to entrain fluid condensation containing.

Spanwise views downstream of the 7-deg centered expansion are presented in Fig. 7. At $s/\delta_0 = 4.2$ (Fig. 7a), the large-scale structures have increased in vertical scale relative to the flat plate case. Also,
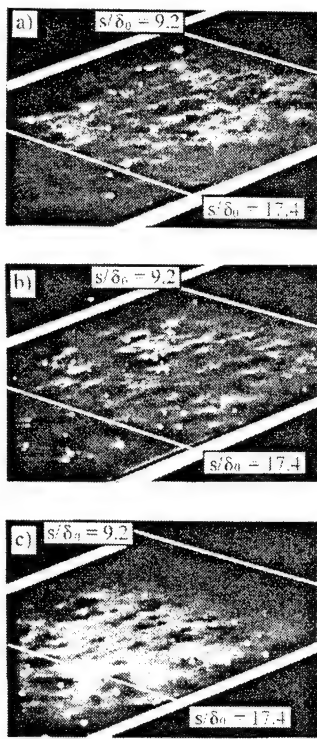
Fig. 11   Instantaneous FRS plan views of the boundary layer downstream of the 14-deg gradual expansion. The sheet is parallel to the surface at $n = 10.0$ mm (a and b) and $n = 13.5$ mm (c).


Fig. 12   Double-pulse streamwise views of the flat plate boundary layer. The bottom images were acquired 25.0 μs after the top images. The horizontal lines indicate the model surface.

occurred at specific spanwise locations, which might suggest a facility disturbance was responsible for the formation of the structures. However, all of the averaged images were uniform across the span. Results for all of the expansion cases are presented elsewhere.[11]

Figure 11 presents instantaneous plan views of the boundary layer downstream of the 14-deg gradual expansion at elevations of $n = 10.0$ mm (Figs. 11a and 11b) and 13.5 mm (Fig. 11c). The CO_2 condensation is present above the boundary layer, but the small amount of condensation present within the layer (probably H_2O) is imaged here. The appearance of the structures at greater normal elevations than in Fig. 10 is not surprising given the increase in boundary-layer thickness across the expansion. The elongated structures are clearly present at the lower elevation. Again, their presence is less clear with increasing normal distance.

Double-pulse visualizations of the flat plate boundary layer acquired with a time delay of 25.0 μs are presented in Fig. 12. The large-scale structures can be easily tracked from the initial to the delayed images. In many of the acquired image pairs the process of fluid entrainment is captured. As in Fig. 12, the entrainment process appears to typically consist of a forward rotation of the top of a large-scale structure. The rotation captures some fluid containing condensation and isolates it from the freestream. Such an occurrence would probably constitute a significant quadrant IV $\overline{uv}$ event. Entrainment into the boundary layer is indicated by the destruction of condensation originally present in the entrained fluid.

Quantitative information concerning large-scale structure convection can be gained from double-pulse images. Some have adopted the approach of identifying the centroids of large-scale structures, measuring the translation between the initial and delayed images, and calculating a velocity from the known time delay.[27,28] For the small time delays employed, the difficult task of identifying structure centroids gives rise to high uncertainties in structure velocities. Further, delineating rotation and convection is difficult. A second approach is to perform space–time correlations on ensembles of image pairs.[29] The presented correlations are based on 150 pairs of initial and delayed images. Formulas are given elsewhere.[11]

Average images are generated for both the 150 initial images and the 150 delayed images. The appropriate average is subtracted from each of the initial and delayed images, so that the correlations are of the fluctuations from the local mean. A two-dimensional region, denoted by (s_{ref}, n_{ref}), is defined in the initial fluctuation image. The signal at each pixel in this region is then correlated with the signals at various streamwise displacements $(s_{ref} + ds, n_{ref})$ in the delayed image. The correlation for each pixel in (s_{ref}, n_{ref}) is averaged with those of pixels falling on the same horizontal line in (s_{ref}, n_{ref}), so that the correlation at a point (ds, n_{ref}) reflects the cumulative correlation of a horizontal line at vertical position n_{ref} shifted a streamwise distance ds in the delayed image. This process is repeated for each horizontal line in (s_{ref}, n_{ref}). The resulting correlations are then averaged over the 150 image pairs and normalized by the maximum resulting coefficient for convenience. Thus, a correlation coefficient of 1.0 does not imply perfect correlation.
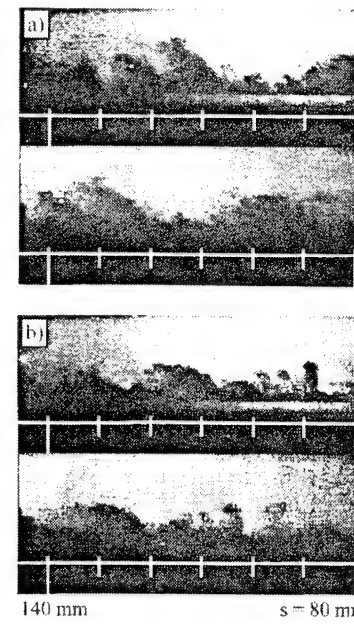
Correlation contours obtained in the flat plate boundary layer with a time delay of 25.0 μs are presented in Fig. 13a. For all of the double-pulse correlation fields, the streamwise direction is from left to right. In performing the correlations, δ_{vis} at the center of the ensemble images (11.8 mm in this case) was adopted as a length scale. The two-dimensional region was defined with a streamwise width of $\delta_{vis}/2$ as greater widths produced negligible differences in the correlation fields despite the added computation time. The point corresponding to maximum correlation in Fig. 13a occurs at $n/\delta_{vis} = 0.58$ and corresponds to a velocity of 610 m/s. For the given spatial magnification and time delay, a pixel element corresponds to a velocity difference of 9.4 m/s. This quantity is adopted as the uncertainty, resulting in 610 ± 10 m/s.

The presence of significant correlation levels at displacements corresponding to velocities greater than the freestream value is not surprising. If a convecting thin vertical line were correlated, the correlation would quickly peak at the optimal displacement and then quickly return to negligible levels. However, for structures of significant streamwise extent, the transition from negligible levels to the peak and back is more gradual. Another possible reason comes from the cited entrainment of freestream fluid at the front of the structures. The apparent increase in structure size caused by the condensation destruction may be interpreted in the correlation as an additional displacement. Further, the correlation is unconditional. If freestream fluid occupies the correlated region, the optimal displacement will correspond to the freestream velocity.

Spina and Smits[17] showed that large-scale structures maintain their identity for at least 1.5δ by analyzing streamwise-separated patterns of conditionally sampled mass-flux fluctuations and wall pressure fluctuations. For the 50.0 μs delay, a structure would convect 30 mm at 600 m/s. Despite traveling approximately 3δ_{vis}, almost all structures are easily tracked from initial to delayed image. The correlation field for a 50.0 μs delay ensemble is presented in

a)

b)
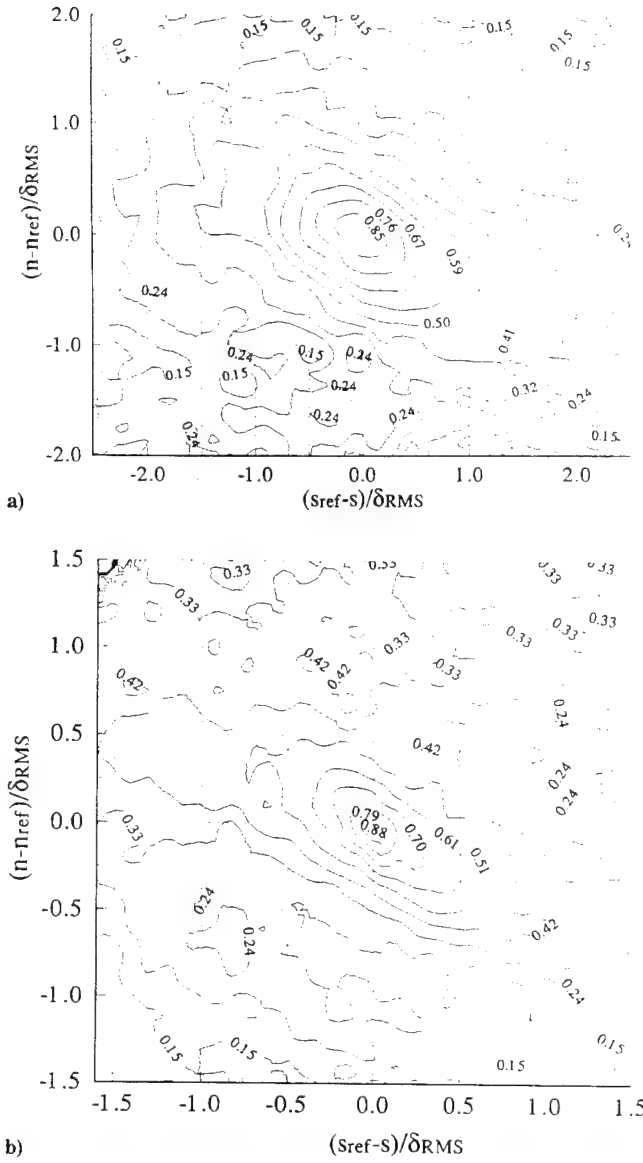
Fig. 9 Spatial correlations centered at n_{ref}/δ_{RMS} = 2.00 for a) the flat plate and b) the 7-deg centered expansion (s_{ref}/δ_0 = 9.2) boundary layers.

defined well within the boundary layer as defined by the average intensity profile. The employed formulas are presented elsewhere.[11,20] With this formulation, the correlation at the reference point is 1.00.

To draw relevant comparisons between the different cases, the normal length scale δ_{RMS} was used to locate the reference point. An ensemble correlation field for the flat plate boundary-layer streamwise views is presented in Fig. 9a. The reference point is located at $(s_{ref}, n_{ref}) = (13.0\delta_0, 2.0\delta_{RMS})$ where $\delta_0 = 9.2$ mm and $\delta_{RMS} = 4.2$ mm. For the spatial correlation fields, the streamwise direction is horizontal right to left. Normal and streamwise displacements have been normalized by δ_{RMS}. Thus, $(n - n_{ref})/\delta_{RMS} = -2.0$ corresponds to the surface. Recall. δ_{vis} is approximately equal to $3\delta_{RMS}$. Accordingly, this reference point is located well within the no-condensation region. As a result, correlations at higher elevations would be expected to occur only when large-scale structures are present. The contours slope downstream at approximately 45 deg. which is a result of the inclination of the large-scale structures. Similarly inclined contours were obtained by Smith et al.[20] Contours of significant correlation extend out to $n/\delta_{RMS} = 3.0$ and beyond, essentially to the top of the boundary layer as defined by the average intensity profile.

Ensemble spatial correlation fields obtained downstream of the 7-deg centered expansion, centered at $(s_{ref}, n_{ref}) = (9.2\delta_0, 2.0\delta_{RMS})$ where $\delta_{RMS} = 6.4$ mm. are presented in Fig. 9b. The correlation
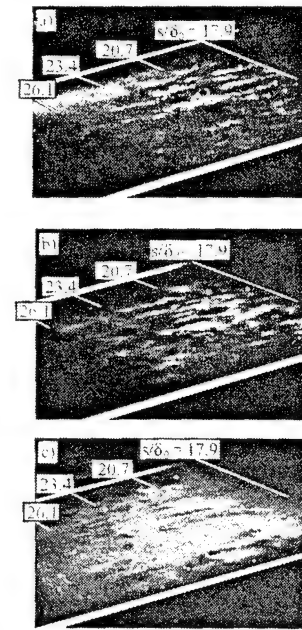

Fig. 10 Instantaneous FRS plan views of the boundary layer downstream of the 7-deg centered expansion (flow straighteners removed). The sheet is parallel to the surface at a) n = 4.5 mm, b) 6.5 mm, and c) 10.5 mm.

field is very similar to that of the flat plate case, with the regions of significant correlation having approximately the same dimensionless extent. Given the disparity in δ_{RMS} between the cases, the large scale structures are larger downstream of the expansion. Since δ_{RMS} is a similar fraction of δ_{vis} for the two cases, the increase in structure size nominally scales with the increase in δ_{vis} across the expansion. Similar to the flat plate case, the correlation contours are inclined at approximately 45 deg. Thus no increase in structure angle is apparent at this location. Although the structure angle appears larger just downstream of the expansion region (Fig. 5), it appears that the increase may not be long lasting. Spatial correlations downstream of the 14-deg centered expansion, given elsewhere,[11] bear no resemblance to those of Fig. 9. The dimensionless extent of significant correlation levels is significantly smaller than in Fig. 9, and the contours exhibit no downstream inclination. Again, this is probably related to the CO_2 condensation.

Figure 10 presents global plan views of the boundary layer at $n = 4.5, 6.5$, and 10.5 mm downstream of the 7-deg centered expansion. Recalling that the average intensity profile of Fig. 8 gives a δ_{vis} value of approximately 18 mm at $s/\delta_0 = 11.4$, these elevations are well within the boundary layer. The flow direction is from upper right to lower left. The spanwise extent of the test section is indicated by the lines aligned in the streamwise direction. Lines aligned in the spanwise direction have been added to give a sense of scale. The bright regions again indicate the presence of water condensation. Given the strong, negative correlation between temperature and streamwise velocity fluctuations in compressible turbulent boundary layers[1,6] and the fact that the condensation forms in the freestream, regions of condensation may be nominally considered high-speed fluid. Similar to plan views of the flat plate boundary layer,[9,11,18] the regions containing condensation appear as elongated structures nominally aligned in the streamwise direction. Because of the lack of condensation, it is not known if the elongated structures exist closer to the wall. The structures are less evident as the top of the boundary layer, and the more uniform condensation, is approached.

Removal of the flow conditioning elements (as was done for Fig. 10) has no noticeable effect on the elongated longitudinal structures in the plan views. That the elongated longitudinal structures survive the expansions and are present for such varied upstream conditions suggest they may be a robust feature of the compressible, turbulent boundary layer, although no comment can be made on their importance. The ensembles of plan views displaying the elongated longitudinal structures were averaged together to see if they

[12]Narasimha, R., and Viswanath, P. R., "Reverse Transition at an Expansion Corner in Supersonic Flow," *AIAA Journal*, Vol. 13, No. 5, 1975, pp. 693–695.

[13]Narasimha, R., and Sreenivasan, K. R., "Relaminarization in Highly Accelerated Turbulent Boundary Layers," *Journal of Fluid Mechanics*, Vol. 61, Pt. 3, 1973, pp. 417–447.

[14]Spina, E. F., Donovan, J. F., and Smits, A. J., "On the Structure of High-Reynolds-Number Supersonic Turbulent Boundary Layers," *Journal of Fluid Mechanics*, Vol. 222, 1991, pp. 293–327.

[15]Lee, S., Lele, S. K., and Moin, P., "Simulation of Spatially Evolving Turbulence and the Applicability of Taylor's Hypothesis in Compressible Flow," *Physics of Fluids A*, Vol. 4, No. 7, 1992, pp. 1521–1530.

[16]Robinson, S. K., "Coherent Motions in the Turbulent Boundary Layer," *Annual Review of Fluid Mechanics*, Vol. 23, 1991, pp. 601–639.

[17]Spina, E. F., and Smits, A. J., "Organized Structures in a Compressible, Turbulent Boundary Layer," *Journal of Fluid Mechanics*, Vol. 182, 1987, pp. 85–109.

[18]Samimy, M., Arnette, S. A., and Elliott, G. S., "Streamwise Structures in a Turbulent Supersonic Boundary Layer," *Physics of Fluids*, Vol. 6, No. 3, 1994, pp. 1081–1083.

[19]Samimy, M., Elliott, G. S., Glawe, D. D., Reeder, M. F., and Arnette, S. A., "Compressible Mixing Layers With and Without Particles," Ohio State Univ. Internal Report MEMS-92-101 Columbus, OH, Aug. 1992.

[20]Smith, M., Smits, A., and Miles, R., "Compressible Boundary-Layer Density Cross Sections by UV Rayleigh Scattering," *Optics Letters*, Vol. 14, No. 17, 1989, pp. 916–918.

[21]Miles, R. B., Lempert, W. R., and Forkey, J., "Instantaneous Velocity Fields and Background Suppression by Filtered Rayleigh Scattering," AIAA Paper 91-0357, Jan. 1991.

[22]Arnette, S. A., Samimy, M., and Elliott, G. S., "On Streamwise Vortices in High Reynolds Number Supersonic Axisymmetric Jets," *Physics of Fluids A*, Vol. 5, No. 1, 1993, pp. 187–202.

[23]Elliott, G. S., Samimy, M., and Arnette, S. A., "Study of Compressible Mixing Layers Using Filtered Rayleigh Scattering Based Visualizations," *AIAA Journal*, Vol. 30, No. 10, 1992, pp. 2567–2569.

[24]Miles, R. B., Forkey, J., and Lempert, W. R., "Filtered Rayleigh Scattering Measurements in Supersonic/Hypersonic Facilities," AIAA Paper 92-3894, July 1992.

[25]Elliott, G. S., Samimy, M., and Arnette, S. A., "Filtered Rayleigh Scattering Based Measurements in Compressible Mixing Layers," AIAA Paper 92-3543, July 1992.

[26]Elliott, G. S., Samimy, M., and Arnette, S. A., "Molecular Filter-Based Diagnostics in High Speed Flows," AIAA Paper 93-0512, Jan. 1993.

[27]Cogne, S., Forkey, J., Lempert, W., Miles, R. B., and Smits, A. J., "The Evolution of Large-Scale Structures in a Supersonic Turbulent Boundary Layer," *Proceedings of the Symposium on Transitional and Turbulent Compressible Flows*, American Society of Mechanical Engineers, Fluids Engineering Conference, 1993.

[28]Forkey, J., Cogne, S., Smits, A., Bogdonoff, S., Lempert, W. R., and Miles, R. B., "Time-Sequenced and Spectrally Filtered Rayleigh Imaging of Shock Wave and Boundary Layer Structure for Inlet Characterization," AIAA Paper 93-2300, June 1993.

[29]Elliott, G. S., Samimy, M., and Arnette, S. A., "The Evolution of Large Scale Structures in Compressible Mixing Layers," Ninth Turbulent Shear Flow Conference, Kyoto, Japan, Aug. 1993, Paper 19-4.

[30]Falco, R. E., "Coherent Motions in the Outer Region of Turbulent Boundary Layers," *Physics of Fluids*, Vol. 20, No. 10, Pt. 2, 1977, pp. S124–S132.

[31]Smith, M. W., and Smits, A. J., "Cinematic Visualization of Coherent Density Structures in a Supersonic Turbulent Boundary Layer," AIAA Paper 88-0500, Jan. 1988.

[32]Robinson, S. K., "Space-Time Correlation Measurements in a Compressible Turbulent Boundary Layer," AIAA Paper 86-1130, 1986.

[33]Wegener, P. P., and Mack, L. M., "Condensation in Supersonic and Hypersonic Wind Tunnels," *Advances in Applied Mechanics*, edited by H. L. Dryden and T. von Kármán, Academic, New York, Vol. 5, 1958, pp. 307–447.

[34]Laderman, A. J., and Demetriades, A., "Turbulent Shear Stresses in Compressible Boundary Layers," *AIAA Journal*, Vol. 17, No. 7, 1979, pp. 736–744.

[35]Kistler, A. L., "Fluctuation Measurements in a Supersonic Turbulent Boundary Layer," *Physics of Fluids*, Vol. 2, No. 3, 1959, pp. 290–296.
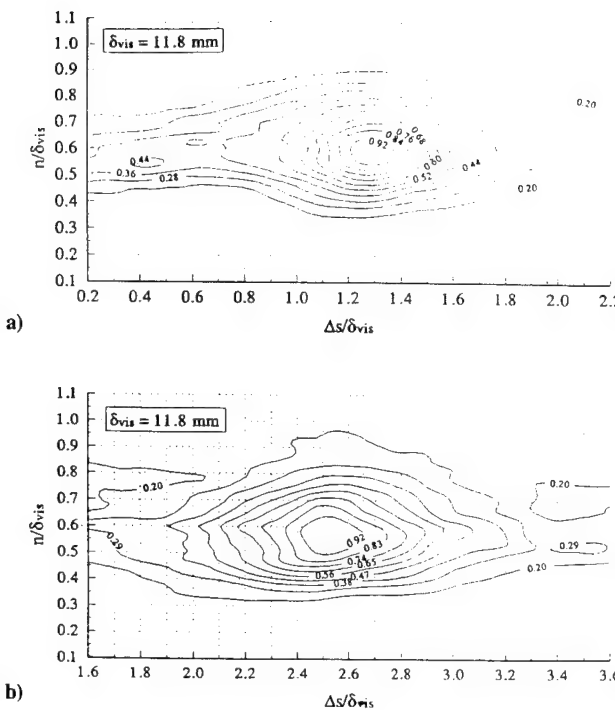
Fig. 13 Correlation fields calculated from ensembles of double-pulse images obtained in the flat plate boundary layer with a time delay of a) 25.0 μs and b) 50.0 μs.

Fig. 13b. The velocity obtained from the maximum correlation point, which occurs at $n/\delta_{vis} = 0.59$, is 595 ± 5 m/s.

To draw relevant comparisons, the delays employed downstream of the centered expansions were chosen so the structures would convect a similar distance. Accordingly, the 25.0 μs flat plate delay was scaled to 23.9 and 23.0 μs downstream of the 7-deg and 14-deg centered expansions, respectively, based on the ratio of freestream velocities across the expansions (obtained from a standard inviscid analysis). Downstream of the 7-deg centered expansion, the correlation fields are similar to those for the flat plate boundary layer. Delays of 16.0, 23.9, and 47.9 μs gave convection velocities of 590 ± 13, 620 ± 9, and 615 ± 5 m/s with the maximum correlation points at $n/\delta_{vis} = 0.73, 0.71$, and 0.71, all given respectively ($\delta_{vis} = 14.0$ mm).

That the maximum correlation point occurs at $n/\delta_{vis} = 0.6$–0.7 in the flat plate and 7-deg centered expansion boundary layers suggests the large-scale structures were mainly responsible for the correlations. Further, the derived convection velocities are reasonable. The unconditional nature of the correlations and modest sample sizes must be kept in mind when considering the importance of the actual velocity values. The differences between these convection velocities and those derived by Dawson et al.[10] from correlations of wall pressure fluctuations in these flows are too large to be accounted for by these sources of uncertainty. Clearly, the fluctuations responsible for Dawson et al.'s[10] correlations cannot be directly linked to the large-scale features responsible for the double-pulse correlations.

The correlation field for an ensemble with a time delay of 23.0 μs downstream of the 14-deg centered expansion (CO_2 condensation present) gave a convection velocity of 500 ± 10 m/s at $n/\delta_{vis} = 0.94$ ($\delta_{vis} = 22.3$ mm). The lack of identifiable large-scale features (Fig. 6c) resulted in the confinement of significant correlation levels to a thin region near the CO_2 condensation/no-condensation interface. The apparent deceleration across the 14-deg centered expansion runs counter to the acceleration detected by correlations of wall pressure fluctuations.[10] Again it appears the CO_2 condensation represents the boundary layer quite differently than the H_2O condensation. It is possible the CO_2 condensation occurs below the top edge of the velocity boundary layer, which could result in convection velocities much lower than the freestream velocity. Support for this idea comes from the fact that the boundary-layer thicknesses defined from the average intensity profiles (Fig. 9) are

very comparable downstream of the 7-deg and 14-deg centered expansions despite the fact that schlieren images show the 14-deg centered expansion boundary layer is much thicker. Mean velocity and turbulence LDV measurements to be acquired in these flow fields should allow further insight.

Conclusions

The effects of four expansion regions [centered and gradual ($R/\delta_0 \simeq 50$) 7-deg and 14-deg expansions] on a Mach 3 fully developed, compressible turbulent boundary layer were studied. Visualizations were acquired utilizing H_2O condensation present in the freestream and absent in the higher temperature boundary layer. Mean and rms intensity profiles confirm the condensation signal is most closely related to temperature. The occurrence of CO_2 condensation downstream of the 14-deg expansions made the visualizations difficult to interpret.

The elongated longitudinal structures shown previously to populate the flat plate boundary layer[18] were also present downstream of the expansion regions, both with and without the flow conditioning assembly installed, and were not noticeably different from those of the flat plate boundary layer. Small-scale motions in the incoming boundary layer appear to be quenched very quickly by the expansion regions. Large-scale structures experience an increase in scale across the expansion regions commensurate with the increase in boundary-layer thickness. This is indicated by a similar dimensionless extent of spatial correlations in the flat plate and 7-deg centered expanded boundary layers when normalized with local length scales. No strong differences between the centered and gradual expansions of the same total deflection were evident in the visualizations. Spatial correlations in the flat plate boundary layer suggest the large-scale structure angle is approximately 45 deg. Visualizations suggest the angle increases across the expansion, but spatial correlations downstream of the 7-deg centered expansion show this increase may be short lived. Convection velocities from double-pulse correlations are reasonable for the flat plate and 7-deg centered expansion boundary layers.

Acknowledgment

References

[1]Spina, E. F., Smits, A. J., and Robinson, S. K., "The Physics of Supersonic Turbulent Boundary Layers," *Annual Review of Fluid Mechanics*, Vol. 26, 1994, pp. 287–319.

[2]Bradshaw, P., "The Effect of Mean Compression or Dilatation on the Turbulence Structure of Supersonic Boundary Layers," *Journal of Fluid Mechanics*, Vol. 63, Pt. 3, 1974, pp. 449–464.

[3]Smits, A. J., and Wood, D. H., "The Response of Turbulent Boundary Layers to Sudden Perturbations," *Annual Review of Fluid Mechanics*, Vol. 17, 1985, pp. 321–358.

[4]Morkovin, M. V., "Effects of High Acceleration on a Turbulent Supersonic Shear Layer," Heat Transfer and Fluid Mechanics Inst., Stanford Univ., Stanford, CA, 1955.

[5]Thomann, H., "Effect of Streamwise Wall Curvature on Heat Transfer in a Turbulent Boundary Layer," *Journal of Fluid Mechanics*, Vol. 33, Pt. 2, 1968, pp. 283–292.

[6]Dussauge, J. P., and Gaviglio, J., "The Rapid Expansion of a Supersonic Turbulent Flow: Role of Bulk Dilatation," *Journal of Fluid Mechanics*, Vol. 174, 1987, pp. 81–112.

[7]Smith, D. R., and Smits, A. J., "The Rapid Expansion of a Turbulent Boundary Layer in a Supersonic Flow," *Theoretical Computational Fluid Dynamics*, Vol. 2, 1991, pp. 319–328.

[8]Johnson, A. W., "Laminarization and Retransition of Turbulent Boundary Layers in Supersonic Flow," Ph.D. Dissertation, Yale Univ., New Haven, CT, 1993.

[9]Arnette, S. A., Samimy, M., and Elliott, G. S., "The Effect of Expansion on the Large Scale Structure of a Compressible Turbulent Boundary Layer," AIAA Paper 93-2991, July 1993.

[10]Dawson, J. D., Samimy, M., and Arnette, S. A., "The Effects of Expansion on a Supersonic Boundary Layer: Surface Pressure Measurements," *AIAA Journal*, Vol. 32, No. 11, 1994, pp. 2169–2177.

[11]Arnette, S. A., Samimy, M., and Elliott, G. S., "Expansion Effects on Supersonic Boundary Layers," Ohio State Univ., Internal Report MEMS-94-101, Columbus, OH, Feb. 1994.

Appendix IV Arnette, S.A., Samimy, M., and Elliott, G.S., 1996, "Two-Component Filtered Planar Velocimetry Measurements in the Compressible Turbulent Boundary Layer," AIAA-96-0305.

AIAA-96-0305
Two-Component Filtered Planar Velocimetry in the
Compressible Turbulent Boundary Layer

Stephen A. Arnette, Mo Samimy, and Gregory S. Elliott
Department of Mechanical Engineering
The Ohio State University
206 West 18th Avenue
Columbus, OH 43210

34th Aerospace Sciences
Meeting & Exhibit
January 15-18, 1996 / Reno, NV

Two-Component Filtered Planar Velocimetry in the Compressible Turbulent Boundary Layer

Stephen A. Arnette[*], Mo Samimy[**], and Gregory S. Elliott[***]
Department of Mechanical Engineering
The Ohio State University
Columbus, Ohio 43210

Abstract

Filtered Planar Velocimetry (FPV) has been employed to obtain nonintrusive, instantaneous, planar measurements of streamwise and spanwise velocities in the compressible, turbulent boundary layer. Measurements were obtained in a fully-developed Mach 3 flat plate boundary layer and the nonequilibrium boundary layers obtained by subjecting the flat plate boundary layer to expansion corners of 7° and 14°. The FPV results were compared to measurements obtained with Laser Doppler Velocimetry. Although uncertainties associated with the FPV technique preclude detailed investigations of the boundary layer turbulence, mean velocity profiles measured with FPV and LDV exhibit very good agreement. As expected, near-zero spanwise velocities were measured in the two-dimensional flow field. The FPV technique provides much better near-wall resolution than LDV. FPV measurements were obtained to within 0.4 mm of the surface while LDV measurements could be acquired only to within approximately 2.0 mm of the surface.

Nomenclature

$\bar{i}$ Unit vector specifying the propagation direction of illuminating laser sheet.

$\underline{n}$ Normal distance above the boundary.

$\bar{o}$ Unit vector specifying the orientation of receiving optics.

P_{I2} Iodine vapor pressure in molecular filter.

P_{N2} Partial nitrogen pressure added to filter.

Re_θ Reynolds number based on momentum thickness.

s Streamwise distance along model surface from beginning of convex curvature.

T_{cell} Temperature of molecular filter.

T_{I2} Temperature of sidearm housing iodine crystals.

U_0 Mean velocity in the Mach 3 freestream.

U,V,W Streamwise, normal, and spanwise mean velocity components, respectively.

$\overline{V}$ Velocity vector.

x Horizontal distance from $(s,n) = (0,0)$.

y Vertical distance from $(s,n) = (0,0)$.

z Spanwise direction.

Δf Doppler shift.

δ_0 Flat plate boundary layer thickness just upstream of expansion corners (9.1 mm).

λ Wavelength of illuminating light.

θ Boundary layer momentum thickness.

ν Frequency.

Introduction

Our limited understanding of compressible turbulent boundary layers stems from both computational and experimental difficulties. The high Reynolds numbers associated with these flows remain an obstacle to computer

[*]   Engineer, Sverdrup Technology, 600 William Northern Blvd., P.O. Box 884, Tullahoma, TN 37388, Member AIAA

[**]   Professor, Associate AIAA Fellow

[***]   Assistant Professor, Dept. of Mechanical and Aerospace Engr., Rutgers Univ., Piscataway, NJ 08855, Member AIAA

simulation. Experimental difficulties stem from a lack of resolution, *both* spatial and temporal. An illustration of the spatial resolution required to fully resolve the near-wall region of the Mach 3 boundary layer of this study is provided by the fact that the mean velocity measured 0.35 mm above the surface ($n/\delta \approx 0.04$) is approximately 60% of the freestream velocity. As discussed by Spina and Smits [1987], fully resolving temporal variations near the wall of a compressible turbulent boundary layer requires a frequency response of at least $10\nu/u_*^2$ (approximately 25 MHz for this study). These requirements are well beyond the capabilities of established measurement techniques.

Given this discussion, there is a clear need for improved techniques for acquiring measurements in compressible turbulent boundary layers. In the work reported here, the Filtered Planar Velocimetry (FPV) employed successfully in obtaining one-component velocity measurements in the compressible mixing layer was extended to the measurement of two velocity components. Measurements were acquired in both equilibrium and perturbed compressible boundary layers.

During the course of this extended investigation, a fully-developed, Mach 3, turbulent boundary layer ($Re_\theta = 24700$) and the effects of four expansion regions on the boundary layer have been investigated. The expansions consist of centered expansions of 7° and 14° and gradual expansions (radius of curvature for the convex surface curvature is approximately 50δ) 7° and 14°. For the work reported here, only the centered expansions are considered.

A schematic of the interaction of the Mach 3 turbulent boundary layer with a centered expansion is depicted in Fig. 1. Within the expansion, the boundary layer encounters a favorable streamwise pressure gradient ($\partial p/\partial s < 0$ where s is the streamwise coordinate), a normal pressure gradient ($\partial p/\partial n > 0$ where n is the coordinate normal to the surface and increases away from the surface), and bulk dilatation ($\nabla \cdot \overline{V} > 0$, i.e. fluid elements undergo an increase in volume in the expansion). The combined effects of these perturbations give rise to a highly distorted boundary layer

downstream of the expansion. As discussed by Arnette et al. [1996], this flow field has been investigated relatively little.

Experimental Procedure

1. Introduction

Over the course of the extended investigation, several nonintrusive optical diagnostics have been employed. Flow visualizations were acquired with schlieren photography, Filtered Rayleigh Scattering (FRS), and double-pulsed Rayleigh scattering [Arnette et al., 1993, 1994a, 1994b, 1995]. Instantaneous velocity measurements were acquired with Laser Doppler Velocimetry (LDV) [Arnette et al., 1996]. Planar density measurements utilizing Planar Laser-Induced Fluorescence (PLIF) of seeded acetone were obtained with limited success [Arnette et al., 1994b]. In addition, the evolution of the boundary layer's mean velocity profile through the centered expansions was computed with the rotational method of characteristics [Arnette et al., 1996]. All results of the study have been compiled by Arnette [1995].

In the work presented here, planar measurements of instantaneous velocities have been acquired with Filtered Planar Velocimetry (FPV). The FPV technique was developed in our laboratory at The Ohio State University [Elliott et al., 1994a, 1994b]. In the present work, the FPV technique has been successfully extended to the measurement of two velocity components.

Over the course of the extended study, optical techniques were preferred over more classical probe-based techniques. In addition to eliminating flow interference problems, optical techniques offer the potential for improved spatial resolution relative to probe-based techniques. The size of a probe's sensing area effectively establishes a spatial scale threshold below which the probe is not effective. The spatial resolution associated with optical techniques can be increased almost limitlessly by changing the focus of the collecting optics.

Many optical techniques offer measurements in a two-dimensional image instead of at a single point. The cameras employed in this investigation possess a 578 x 384 pixel array. As a result, over 150,000 measurement locations are available in a single acquisition. That planar measurements allow the spatial structure of a turbulence field to be investigated is very significant. It is known that the various phenomena which occur in turbulent flows occur at different spatial scales. For instance, the entrainment of freestream fluid into a turbulent shear flow is achieved mainly by the largest turbulent eddies, while the dissipation of turbulent kinetic energy occurs at the smallest turbulent scales. Observations like these indicate that investigating the spatial structure of turbulence is important. This is quite different from the classical approach of investigating temporal variations at a single point in a field.

From the standpoint of frequency response, probe techniques currently enjoy a decided advantage over the optical techniques employed in this investigation, including FPV. Hot-wire or hot-film probes are employed to obtain measurements at frequencies of several hundred kilohertz. In the FPV measurements of this study, where a pulsed Nd:YAG laser was employed, the acquisition frequency was limited to the 10 Hz pulse frequency of the Nd:YAG laser. The framing rates of the employed ICCD cameras (about 2 Hz for a full-array image) was a further limitation. These measurement frequencies are obviously lower than would be desired. However, large samples of planar, instantaneous measurements were acquired. It should be mentioned that, in as much as Taylor's hypothesis holds, the possibility of converting planar measurements into single-point temporal variations exists.

It is significant that the limiting factors for the temporal resolution of the current measurements, framing rate and pulse frequency, are technology issues which will undoubtedly improve in the future. For example, our laboratory is currently in the process of acquiring an Nd:YAG laser with a pulse frequency of 100 kHz and an ICCD camera with a framing rate of several MHZ . As a result, it is likely that optical techniques similar to those of this study will become more widely employed in future investigations of compressible turbulence.

2. Flow Facility and Boundary Layer Models

The experiments were performed at the Aeronautical and Astronautical Research Laboratory at The Ohio State University. Two four-stage compressors supply air to the system, which has a storage capacity of 42.5 m^3 at pressures up to 16.4 MPa. Supply air is introduced to the stagnation chamber through an array of radial inlet holes. The stagnation chamber pressure is maintained to within ±1% of the set point. For these experiments, the stagnation pressure was 0.82 MPa (8.2 atm) and the stagnation temperature was nominally 280 K.

The employed supersonic wind tunnel is a blow-down facility which has been employed previously in a dual-stream configuration to investigate the compressible mixing layer. For the current investigation of turbulent boundary layers subjected to expansion regions, only the supersonic stream is utilized.

The boundary layer develops on the flat splitter plate (which separates the two streams of the compressible mixing layer) and the expansion models are fixed to a flat plate section which replaces the removable splitter plate tip. The converging-diverging nozzle profile is opposite the flat splitter plate in the top of the tunnel. As a result, the boundary layer develops on a flat plate from the stagnation chamber to the test section. The top surface of the splitter plate is at the lateral center of the test section, so that the incoming supersonic flow occupies a passage 152.4 mm wide by 76.2 mm high. After the expansion regions, the model surfaces diverge away from the expansion corner towards the bottom of the test section, which has a total cross section of 152.4 mm wide by 152.4 mm high. Thus only half of the test section is utilized at the onset of the expansion region.

The coordinate system to be used is presented in Fig. 1. The streamwise coordinate, s, is measured along the

2

surface of the expansion models. The origin (s = 0) occurs at the beginning of the expansion regions. The normal coordinate, n, is zero at the surface and everywhere normal to the surface. The (x,y) origin occurs at the surface at the beginning of the convex curvature.

In addition to the expansion models, a flat plate model was constructed. This was done to allow investigations of the non-perturbed boundary layer. With the expansion models installed, optical access to the incoming boundary layer is limited to approximately 3 cm. The flat plate model extends the incoming boundary layer through the length of the test section. Each side wall has an interchangeable window and blank panel which give a total possible viewing area of 450 mm in the streamwise direction and 80 mm in the normal direction. A window in the top wall was used to introduce the laser sheet.

Measurements acquired with Laser Doppler Velocimetry show the streamwise and normal turbulence intensities in the Mach 3 freestream to be less than 1.5% and 1.0%, respectively. The freestream velocity is nominally 600 m/s, but varies slightly from run to run with the stagnation temperature, which is measured. At the onset of the convex surface curvature associated with expansions, the boundary layer thickness ($\delta_{99\%}$) is 9.1 mm, the momentum thickness (θ) is 0.37 mm, and the Reynolds number based on momentum thickness (Re_θ) is 24700.

3. Basic Diagnostic Techniques

Upon installing a new model, schlieren images were acquired to insure no non-uniformities were present. Instantaneous schlieren images of the flat plate boundary layer, the passage of the boundary layer through the 7° centered expansion, and the passage of the boundary layer through the 14° centered expansion are presented in Figs. 2a, 2b, and 2c, respectively. As expected given the decrease in density sustained across an expansion, the boundary layer thickens across the expansions. The schlieren light source is a Xenon 437B Nanopulser which provides 5 mJ over a pulse duration of 10 ns, which effectively freezes the flow field. Spanwise and streamwise distributions of mean static pressures at the model surfaces were monitored with pressure taps in the models and a Scanivalve unit. Static pressure distributions have been presented elsewhere [Dawson et al., 1994, Arnette et al., 1994a, Arnette, 1995].

4. Laser Doppler Velocimetry

Laser Doppler Velocimetry (LDV) was employed to obtain measurements of streamwise and normal velocities in the incoming and perturbed boundary layers.

A TSI Model 9100-7 LDV system was used in conjunction with the blue (488 nm) and green (514.5 nm) beams of a Model 2020 Spectra Physics 5-watt Argon-ion laser. The beam pairs propagated through the test section in the spanwise direction at an orientation of 45° from both the normal and streamwise directions. All measurements were acquired in the spanwise center of the test section. This coupled with the convergence of the beams to form the measurement volume permitted measurements only to within about 2 mm of the surface. No frequency shifting was used. A 3.75X beam expander was used to reduce the size of the measurement volume, thereby improving the signal-to-noise ratio. Forward scattering was collected at an angle of 10° with the beam axis. Off-axis collection was used to help reduce the stray laser light seen by the photomultiplier tubes and to reduce the spanwise length of the measurement volume. The calculated ellipsoid measurement volume dimensions were 0.33 mm long in the spanwise direction and 0.13 mm in diameter at the e^{-2} intensity level.

Data was collected with TSI FIND software on a 486 personal computer. The photomultiplier tube outputs were filtered and processed with a Model IFA-750 digital burst correlator. For each point, 8192 measurements were collected at data rates of 5 to 10 kHz.

The flow was seeded with silicone oil particles less than 1 μm in diameter generated with a TSI Model 9306 six-jet atomizer. The particle-laden air stream was injected through the back wall of the stagnation chamber through an array of spanwise-aligned ports located approximately 10 mm above the flat plate on which the boundary layer formed. Injecting the particles through the rear wall of the stagnation chamber insured the seeding was not a source of boundary layer perturbation.

The LDV system was located on an automated optical table. For closed-loop positioning, the table was equipped with linear encoders having a resolution of 8000 steps/inch. Linear encoders were chosen over motor-mounted rotary encoders to ensure that any 'slop' in the table, if present, would not cause positioning errors. Data was collected only when the measurement volume was located within ± 0.001 mm of the desired position.

Since data were collected during runs of several minutes duration, the variation of the stagnation temperature (and hence the freestream velocity) was taken into account. The stagnation temperature was measured with an RTD to within ± 0.1 K throughout the duration of each run. The relationship of freestream velocity to stagnation temperature was established with LDV measurements. Once established, velocities measured at different points in the boundary layer could be normalized by the proper freestream velocity, i.e. the freestream velocity corresponding to the stagnation temperature at the time of the measurement.

5. Two-Component Filtered Planar Velocimetry

I. Introduction

Though Laser Doppler Velocimetry is a valuable, well-established technique for obtaining accurate measurements of instantaneous velocities, its most obvious shortcoming is that measurements are obtained only at a single point. Filtered Planar Velocimetry (FPV) was employed to obtain planar, instantaneous velocity measurements. Furthermore, FPV offers the potential for better near-wall resolution relative to LDV.

A Spectra Physics Model GCR-4 frequency-doubled Nd:YAG laser (532 nm) was used as the light source. When frequency-doubled, the Nd:YAG laser is capable of approximately 700 mJ/pulse. The laser has a pulse repetition rate of 10 Hz and a pulse duration of 9 ns. At the Mach 3 freestream velocity of 600 m/s, fluid convects only 5μm during the duration of a single pulse. As a result, the laser pulse is sufficiently short to 'freeze' the flow, yielding instantaneous measurements.

The laser is injection-seeded to produce narrow linewidth output (approximately 50 MHZ) and the center frequency of the Nd:YAG laser can be controlled. A course adjustment allows for a total tuning range in excess of 100 GHz. Fine adjustments are possible through a total range of approximately 40 GHz. The narrow linewidth and the ability to control the center frequency are very important in FPV and in Filtered Rayleigh Scattering (FRS), which was used extensively for flow visualization in this investigation [Arnette et al., 1993, 1994b, 1995 and Samimy et al., 1994].

The use of FRS to interrogate flow fields was originally proposed by Miles et al. [1991] and has been discussed elsewhere [Miles et al., 1992 and Elliott et al., 1992, 1993]. In the technique, an optical cell containing diatomic iodine vapor is used as a frequency-discriminating device and placed in front of the collecting lens. Iodine possesses electronic transitions that absorb the frequency-doubled 532 nm Nd:YAG radiation. The cumulative absorption of the iodine molecules forms a notch or band-reject filter in the transmission versus light frequency domain. For appropriate optical arrangements, light scattered by the flow or particles in the flow will possess a positive Doppler shift. The center frequency of the narrow linewidth, frequency-doubled Nd:YAG laser can be tuned such that the iodine vapor will absorb unwanted background reflections (which are at the laser frequency), while passing Doppler shifted scattering onto the camera.

When the collected scattering is the relatively weak molecular Rayleigh scattering from the actual flowing medium, it is difficult to absorb unshifted background reflections without also absorbing a large portion of the molecular scattering. This is because even in supersonic flows it is difficult to achieve Doppler shifts which are larger than the half-width of the Rayleigh scattering profile, at least for the case where collecting camera(s) are oriented nominally perpendicular to the illuminating laser sheet. This is discussed by Elliott et al. [1992]. For the case of scattering from particles which are insensitive to molecular motions, the linewidth of the scattering is simply that of the illuminating laser. As a result, background elimination with no signal attenuation is more easily accomplished.

For these reasons, small particles of condensed water which form during the expansion to Mach 3 were utilized in the FRS visualizations. The particle dimension is on the order of 50 nm. The condensate comes from the small amount of water vapor left in the supply air after being passed through the system's desiccant dryers. The estimated water content of the air is 2.9×10^{-5} kg H_2O/kg air. To put this value in perspective, the standard atmosphere contains 4.6×10^{-4} kg CO_2/kg air.

The condensed particles provide a scalar transport marker in the freestream. Water vapor in the boundary layer is superheated due to the higher static temperature and, as a result, condensation does not occur. Although there is no *a priori* reason to expect the bottom edge of the condensate to coincide with the edge of the velocity boundary layer, the boundary layer thickness derived from averages of instantaneous visualizations coincides with that derived from LDV measurements [Arnette 1995]. This indicates a good correspondence between the FRS visualizations and the velocity boundary layer.

Instantaneous FRS visualizations of the Mach 3 turbulent boundary layer are presented in Fig. 3. The large scale structure which dominates the outer portions of the boundary layer are evident in the images. Visualizations of the flow in the vicinity of the expansion corners, such as that of the 7° centered expansion in Fig. 3, allowed the effects of the expansion region on the large scale structures to be investigated.

The desire for more quantitative information than that afforded by FRS visualizations led to the development of FPV. FPV is similar to FRS in that both techniques are founded on the resonant absorption of Nd:YAG photons by diatomic iodine molecules.

In the past, FPV has been used to obtain instantaneous, planar measurements of one velocity component in supersonic jets [Elliott et al., 1993] and compressible, planar mixing layers [Elliott et al., 1994a, 1994b]. A detailed accounting of the FPV technique has been given by Elliott et al. [1994b]. In the present work, the technique was extended to measurements of two velocity components within the compressible boundary layer.

ii. Principle of Operation for Filtered Planar Velocimetry

As cited previously, light scattered by a moving particle or molecule contains a Doppler shift given by

$$\Delta f = \frac{1}{\lambda} \overline{V} \cdot (\overline{o} - \overline{i}) \qquad (1)$$

where Δf is the observed Doppler frequency shift, λ is the illuminating wavelength, $\overline{V}$ is the instantaneous vector velocity of the scattering particle, $\overline{o}$ is the outward unit vector in the direction of observation, and $\overline{i}$ is the unit vector along the illuminating light's direction of propagation. With this relationship, the velocity of a light-scattering particle can be determined if the Doppler shift present in the scattered light can be measured. This is the principle of operation for FPV.

As with FRS, diatomic iodine vapor is contained in an optical cell. The cells employed in this investigation, which are depicted schematically in Fig. 4, were 9 cm in diameter and 22 cm long. In FRS, the molecular iodine filter

eliminates unshifted background reflections. Accordingly, a Doppler or thermal broadened absorption profile in which absorption lines exhibit a rapid transition from near-zero to maximum transmission is required. In FPV, the molecular filter is used to measure the Doppler shift. To do this, the filter attenuates collected scattering an amount solely dependent on the frequency of the scattered light. For this reason, a profile possessing a more gradual transition from peak absorption to peak transmission is employed. Such a profile is generated with Lorentz or pressure broadening, as discussed further below.

The partial absorption of Doppler shifted scattering from small particles in the flow by a Lorentz broadened filter which occurs in FPV is illustrated schematically in Fig. 5. Changes in the velocity of the scattering particles change the magnitude of the observed Doppler shift, which results in a different transmission ratio through the filter. If the transmission ratio through the molecular filter can be determined, the frequency of the scattering can be obtained from the known absorption profile. Since the laser frequency is known, the Doppler shift is obtained by simple subtraction. With a known Doppler shift and information about the configuration, the velocity can be obtained with Eqn. 1.

In order to determine the transmission ratio through the filter, a measurement of the scattered intensity before and after the molecular filter is required. Since the absorption profile of the molecular filter is used to determine the Doppler shift from the transmission ratio, the absorption profile must be measured independently.

iii. Absorption Profile of the Molecular Filter

The shape of any absorption line is affected by three basic broadening processes [Mitchell and Zemansky (1934) and Elliott (1993)]: natural broadening due to the finite lifetime of the excited state, Doppler (temperature) broadening due to the random motion of the molecules, and Lorentz (pressure) broadening due to inter-molecular collisions. Although natural broadening is a function only of the composition of the absorbing molecule, Doppler and Lorentz broadening are functions of the thermodynamic state of the absorbing medium. At moderate temperatures and low pressures, the iodine absorption profile is primarily Doppler broadened with a Gaussian shape. However, when the absorption profile is dominated by Lorentz broadening, the sloping region near the edges of the absorption line (where the transmission varies from near-zero to a local maximum) occupies a much larger frequency range.

The frequency width of the sloping region at the edge of an absorption well limits the range of velocities which can be measured since outside this region the transmission through the filter is largely independent of frequency (Doppler shift). Although one could vary the observation angle to 'squeeze' a large range of velocities into a small range of Doppler shifts which fall within the sloping region at the edge of an absorption line, this has the undesired effect of degrading the resolution of the Doppler shift (and thus velocity) measurements and may require a very oblique

view of the illuminated flow field. An alternative method is to modify the shape of the absorption profile with Lorentz broadening, which was devised by Elliott [1993]. This provides a means of measuring a large range of velocities from any angle of observation. As in the mixing layer velocity measurements of Elliott et al. [1994a, 1994b], the iodine absorption profile was pressure broadened by introducing nitrogen to the cell.

The cell is prepared by inserting iodine crystals through the stopcock valve (Fig. 4) and evacuating the cell to low pressures. For the Doppler (temperature) broadened profiles employed in FRS visualizations, the cell contains only iodine. The amount of iodine which comes out into the diatomic vapor state increases with temperature. Specifically, the iodine vapor pressure is a function of the coldest point in the cell. This method of controlling the thermodynamic state of the absorbing medium has been employed by other investigators [Tellinghuisen (1973), Miles et al. (1992), and Elliott et al. (1993)].

The sidearm (Fig. 4) is made the coldest point in the cell. Its temperature, T_{I2}, is maintained by circulating constant-temperature water through the jacket surrounding the sidearm. The water temperature is maintained to within ± 0.1 K by a VWR circulation bath. To insure the sidearm is the coldest point in the cell, the rest of the cell is heated. This is done by wrapping the cell with resistance heating tape. The cell temperature, which is referred to as T_{cell}, is maintained to within ± 2 K with a variable transformer.

The addition of nitrogen gas to the filters was used to establish the Lorentz (pressure) broadened profiles. The nitrogen addition system is the same as that employed by Elliott [1993]. The pressure in the cell was measured to within ± 0.1 torr with an MKS baratron gage. So that the pressure being measured would be that only of the added nitrogen, all of the iodine vapor was first frozen out in the cold finger shown in Fig. 4, which is simply a second extension off of the main cell compartment similar to the sidearm. This was done by submerging the cold finger in a liquid acetone/dry ice slurry. After this was done, the stopcock valve on the cell was opened. The system was then pressurized with nitrogen by cracking the needle valve on the nitrogen supply. Once the nitrogen pressure was at the desired level, the stopcock valve on the cell was again closed. Before the pressure broadened profile could be acquired, several hours were allowed with T_{I2} and T_{cell} at their set points to allow the iodine/nitrogen mixture to achieve steady-state. This done, the sidearm valve was closed to seal off the iodine crystals. Once the sidearm valve was closed, it was necessary only to set T_{cell} to reestablish the desired absorption profile.

The system used to measure the absorption profiles of the molecular filter is identical to the system described by Elliott [1993] and Elliott et al. [1993, 1994a]. Further discussion is presented by Arnette [1995].

The portion of the Lorentz broadened profile used for the FPV measurements is presented in Fig. 6. Two filters were required for the measurement of two velocity

5

components. The cell conditions for the profiles were $P_{N2} = 20$ torr, $T_{I2} = 45.0$ °C, and $T_{cell} = 110.0$ °C. The small deviation between the profiles used for cameras 1 and 2 is probably due to slight cell nonuniformities. This does not adversely affect the FPV measurements. As long as the absorption profiles are known, the measured transmission ratio can be converted into a frequency (Doppler shift).

iv. Flow Seeding Issues

As cited previously, despite the relatively low temperatures of supersonic flows, the Rayleigh scattering from the molecules which comprise the flow is several GHZ in linewidth [Elliott et al., 1992]. This is wider than the iodine absorption wells used for suppression of 532 nm light. As a result, determining how much Doppler shift the Rayleigh scattering experiences via the deconvolution of the Rayleigh scattering from the absorption profile would be very difficult. The shape of the Rayleigh scattering spectrum is a strong function of thermodynamic properties [Elliott et al., 1992]. This is significant because the shape of the Rayleigh scattering spectrum is needed to determine the center frequency of the Rayleigh scattering from the measured transmission ratio.

Unfortunately, instantaneous planar measurements of enough properties to specify the local thermodynamic state are not currently possible. This situation may be remedied in the near future however. Substantial progress has been made in the measurement of instantaneous thermodynamic properties at a point with the Filtered Angularly-Resolved Rayleigh Scattering technique [Elliott and Samimy, 1995] and it seems entirely possible that the technique can be extended to planar measurements.

Because of these limitations, it was decided to seed the flow with scattering particles. If the scattering particles are insensitive to molecular motions, the linewidth of the particle scattering is simply that of the illuminating laser. When this is the case and a Lorentz broadenend profile is employed, the Doppler shifted scattering from the seeded particles can be confined to one side of an absorption well. In other words, the Doppler shifted scattering illustrated in Fig. 5 is confined between the local minimum and adjacent local maximum transmission points for the range of expected velocities. Determining the center frequency of the particle scattering, which is simply the sum of the laser frequency and the Doppler shift, then becomes very straightforward. First, the absorption profile must be known. Second, simultaneous images of the flow field are acquired - one with a camera which views the flow through a molecular filter and one with a camera which has no molecular filter. After this is done, dividing the filtered image by the non-filtered image yields the transmission ratio through the filter at each point in the flow. With the known transmission, the center frequency of the scattering can be obtained from the filter profile. Subtracting the laser frequency gives the Doppler shift at each point in the flow. Once this is known, obtaining the local velocity requires the solution of Eqn. 1, which is dependent only on the optical configuration.

The flow was seeded with acetone in the current experiments. Small liquid acetone droplets generated with a Spraying Systems Model LNND22 atomizing nozzle were injected into the stagnation chamber. Upon injection, the acetone evaporated. Upon expansion to supersonic speeds, the acetone condensed to form small particles. Although acetone condensation was a limiting factor in the planar laser induced fluorescence experiments [Arnette et al., 1994b, Arnette, 1995], it provided a very uniform seeding for the FPV experiments. Although no measurements of particle size were attempted, comparison of the scattered signal levels to previous experiments which utilized condensed water suggests the particle dimension was on the order of 50 nm.

In the PLIF experiments where acetone concentration was used as an indicator of air density, it was necessary that the acetone be thoroughly mixed with the tunnel supply air so that no false density variations would be detected [Arnette et al., 1994b]. As a result, the acetone was injected into air stream several meters ahead of the stagnation chamber. This is not a concern for FPV. Since the frequency-discriminated image is normalized by an unfiltered image, any adverse effects due to nonuniformities in particle concentration are eliminated. As a result, the acetone was seeded directly into the tunnel stagnation chamber, which is at a much lower pressure than the supply line upstream of the radial inlet plug at the stagnation chamber entrance. This allowed the injection system to be operated at lower pressures. One might also suspect that nonuniformities in illuminating intensity due to the Gaussian profile of the Nd:YAG laser beam might be incorrectly interpreted as variations in Doppler shift. Again, since variations are present in both the filtered and non-filtered images, the normalization eliminates any adverse effects.

v. Implementation of Filtered Planar Velocimetry for Boundary Layer Measurements

The frequency-doubled, injection-seeded Nd:YAG laser was used for illumination. Images were collected with computer-controlled Princeton Instruments 14-bit ICCD cameras. The cameras are thermoelectrically cooled to allow sensitivities on the order of 10 to 100 counts/photon. The laser provides an output for each pulse which is directed to each camera's pulse generator for synchronization. The 14-bit images are stored digitally on the controlling 486 personal computer. An image is not acquired until the previous image is stored in computer memory. This results in a framing rate of about 1 Hz for full array images. Parts of the array can be disabled or the array binned to form "superpixels" consisting of agglomerated groups of adjacent pixels to improve this rate if spatial resolution is not a concern. However, the laser pulse repetition rate of 10 Hz results in consecutive instantaneous images being totally uncorrelated.

In a basic FPV setup, two cameras are used to obtain images of an illuminated flow field. A molecular filter is placed in front of one camera, while the second acquires unfiltered images. Assuming the detectors to be identical, normalizing the filtered image by the unfiltered image gives

6

the transmission ratio at each pixel. As previously discussed, the transmission ratio is converted into a Doppler shift, which is converted into a velocity measurement.

Reflected laser light from the surfaces bounding the flow field can be a source of significant error. The laser frequency is typically tuned to near-zero transmission in the iodine absorption profile. If significant background reflections were present, they would be imaged by the non-filtered reference camera and almost fully eliminated from the image of the filtered camera. As a result, the intensity at a given pixel in the reference image would be artificially high, and the transmission ratio obtained in the ensuing normalization at that location would be artificially low. This would result in an artificially low Doppler shift measurement. Given the focus of this work on the flow just above a solid boundary, this issue is of prime importance.

When significant background reflections are present, corrective steps can be taken. Elliott et al. [1993, 1994a] successfully employed a sharp, Doppler broadened iodine filter in front of the reference camera to eliminate non-Doppler shifted scattering while passing all Doppler shifted scattering on to the camera. This took care of any adverse effects due to background reflections.

The boundary layer is a much more optically-challenging flow than the compressible mixing layer. While there are no solid surfaces near the mixing layer between two parallel freestreams, the boundary layer develops on a surface. The typical approach would be to bring the laser sheet downward into the boundary in the normal direction. This was done in previous PLIF and FRS experiments. In the PLIF experiments where ultraviolet light at 266 nm was used for illumination and visible light near 500 nm was collected, the inefficiency of the camera lens in the ultraviolet was sufficient to remove surface reflections. In the FRS visualizations, the iodine filter sharply attenuated the surface reflections but was not able to eliminate them entirely as the filter was saturated. As a result, the near-wall region had to be masked. Since the boundary layer was void of condensation (and thus scattering), this was acceptable. However, this was not an attractive option for the FPV experiments where it was hoped to measure velocities very near the solid surface.

For the FPV measurements, it was decided to avoid creating the surface reflections. This was done by illuminating the flow with a collimated laser sheet which propagated up the tunnel axis just above the solid surface. In order to form the upstream-propagating laser sheet, a prism had to be placed in the flow. A 12.7 mm wide section of a right angle prism with 50.8 mm faces was epoxied into a rectangular aluminum fixture which could be mounted at the downstream end of the boundary layer models. In order to protect the prism from particle impact, the prism was protected on the top and sides with replaceable 3.0 mm thick quartz windows, which were held in place by retaining clamps. The fixture proved quite sufficient, as the quartz windows were cracked only once during the FPV experiments. Photographs of the prism fixture mounted on

the flat plate boundary layer model and the 7° centered expansion model are presented in Fig. 7.

The redirection of the laser sheet up the tunnel axis is illustrated schematically in Fig. 8. The beam from the Nd:YAG laser was formed into a sheet with a cylindrical lens. A spherical lens was then placed such that its focal point coincided with the focal point of the cylindrical lens. This insured the sheet transmitted through the spherical lens was collimated (i.e. its width was constant). After passing through the spherical lens, the sheet passed into the tunnel and was turned upstream by the prism mounted in the test section, as illustrated in Fig. 8. The spherical lens was also placed such that the sheet waist occurred where the measurements were acquired. As a result, the sheet was only a fraction of a millimeter thick where the FPV measurements were obtained. This system allowed a collimated sheet which passed just above the solid surface to be formed without incurring significant surface reflections. As a result, no filter was used in front of the reference camera for the FPV measurements.

The system, which is illustrated schematically in Fig. 9, was configured to measure the streamwise (U) and spanwise (W) velocities (here, U and W are used to denote instantaneous velocities instead of mean values). There were two filtered cameras (one on each side of the tunnel) and one unfiltered camera (on the $z < 0$ side of the tunnel), all of which were at the same normal elevation as the laser sheet. As a result, the $\overline{o}$ and $\overline{i}$ unit vectors in Eqn. 1 had no components in the normal direction (neglecting the small normal component of $\overline{o}$ associated with the focussing of the image through the camera lens). For the configuration of Fig. 9, the Doppler shifts observed by camera 1 ($z > 0$ side of the tunnel) and camera 2 are

$$\Delta f_1 = \frac{1}{\lambda} \left(U \overline{e_x} + V \overline{e_y} + W \overline{e_z} \right) \bullet \left[(1 + \cos\theta_1) \overline{e_x} + \sin\theta_1 \overline{e_z} \right]$$
$$= \frac{1}{\lambda} \left[U (1 + \cos\theta_1) + W \sin\theta_1 \right] \tag{2}$$

and

$$\Delta f_2 = \frac{1}{\lambda} \left(U \overline{e_x} + V \overline{e_y} + W \overline{e_z} \right) \bullet \left[(1 + \cos\theta_2) \overline{e_x} - \sin\theta_2 \overline{e_z} \right]$$
$$= \frac{1}{\lambda} \left[U (1 + \cos\theta_2) - W \sin\theta_2 \right] \tag{3}$$

where Δf_i is the Doppler shifts present in the scattered light collected by camera I, θ_i is the angle between the x-axis and the axis of camera I, and subscripts 1 and 2 refer to cameras 1 and 2, respectively. After the Doppler shifts observed by Cameras 1 and 2 are known, obtaining U and W at each point becomes a simple matter of solving a two equation-two unknown system.

A photograph of Camera 2 as it was employed in the FPV measurements is presented in Fig. 10. The molecular filter (which is wrapped in insulating material with outer aluminum cladding) is in front of the camera. The variable transformer which powered the heat tape beneath the insulation and the RTD readout used to monitor T_{cell} are also in the picture. A photograph of the actual camera arrangement is presented in Fig. 11. As evident in the figure, cameras 1 and 2 were oriented essentially perpendicular to the laser sheet in the test section. If $\theta_1 = \theta_2 = 90°$, Eqns. 2 and 3 dictate that Camera 1 will observe a Doppler shift proportional to (U+W) and Camera 2 will observe a Doppler shift proportional to (U-W). The actual angular orientations of the cameras were measured for computing the velocities from the measured Doppler shifts.

Before filtered images could be normalized by reference images to obtain transmission ratios, several processing steps were required. First, the images obtained by camera 1 on the z < 0 side of the tunnel were flipped so that the flow was from left to right as in Camera 2 and the reference camera (Camera R). Then the images of the various cameras had to be aligned pixel-for-pixel. This was accomplished by acquiring images of a two-dimensional grid with all of the cameras. Since cameras were located on both sides of the wind tunnel, a two-dimensional grid was printed on an overhead transperancy and mounted in a frame. At the reference points on the grid, it was a simple matter to manually count the number of pixels the reference points in Cameras 2 and R needed to be shifted to align with Camera 1. At most pixels, no reference point was present and appropriate vertical and horizontal pixel shifts had to be calculated based on the known shifts at the four surrounding grid points.

Elliott et al. [1994a] used a two-dimensional linear interpolation. In the present study, this method was compared with a 'weighting' method. In the general case, a pixel is located between four reference points where the appropriate shifts are known. This situation is illustrated in Fig.12 where the appropriate shifts are desired at pixel A, the surrounding reference points are labeled 1, 2, 3, and 4, and the corresponding shifts at the reference points are denoted by ξ_1, ξ_2, ξ_3, and ξ_4. The shift at pixel A was then calculated as

$$\xi_A = \frac{\left(\dfrac{\Pi}{d_{A-1}}\right)\xi_1 + \left(\dfrac{\Pi}{d_{A-2}}\right)\xi_2 + \left(\dfrac{\Pi}{d_{A-3}}\right)\xi_3 + \left(\dfrac{\Pi}{d_{A-4}}\right)\xi_4}{\left(\dfrac{\Pi}{d_{A-1}}\right) + \left(\dfrac{\Pi}{d_{A-2}}\right) + \left(\dfrac{\Pi}{d_{A-3}}\right) + \left(\dfrac{\Pi}{d_{A-4}}\right)} \quad (4)$$

where $\Pi = d_{A-1} + d_{A-2} + d_{A-3} + d_{A-4}$ and d_{A-I} is the distance between point A and reference point I. To calculate the horizontal shifts at pixel A, the horizontal shifts at the reference points are substituted for the ξ_i's in Eqn. 4. To calculate the vertical shifts, the vertical shifts at the reference

points are substituted for the ξ_i's in Eqn. 4. The alignment mapping for the grid images of the three cameras is calculated with this equation. Then the same mapping is used to align the flow field images of the three cameras. This obviously required that the grid be placed in the plane of the laser sheet in the test section.

The alignment was performed with code written in Microsoft Fortran Powerstation and run on a 486 personal computer. Alignments performed with the standard two-dimensional linear interpolation and the weighted method displayed no noticeable differences. The weighted method was employed for the final alignments.

In order to obtain the correct transmission ratio from the image normalization, the filtered and unfiltered cameras must have the same response characteristics. Specifically, in the absence of any molecular filter, the cameras should yield the same count read-out at common points in aligned images. If this is the case, the normalization will isolate the effect of the molecular filter. Unfortunately, this is not generally true. The gain settings of the individual cameras can obviously lead to different numbers of counts being recorded by different cameras subjected to the same amount of light. Differences could also arise from the cameras' aperture settings.

Another cause for differences which is unrelated to the cameras' characteristics is the optical configuration. Since the three cameras are located at different locations around the test section, the angle from a scattering particle is different for the individual cameras. The polarization direction of the light sheet was normal to the plane defined by the three cameras. As a result, if the scattering fell within the Rayleigh regime, the three cameras would see the same amount of scattered light. However, the condensed particle scattering more likely fell somewhere between the Rayleigh and Mie scattering regimes. Thus it is likely that the scattered intensity varied at least mildly with observation angle, which could also give rise to different count read-outs for the different cameras.

In order to correct for these effects, images of the flow field were collected with the molecular filters removed. This was done just after the filtered FPV data was acquired so that everything was the same except for the removal of the molecular filters. The unfiltered calibration images allowed the question "When the reference camera (camera R) reads x counts at this pixel, how many counts would the filtered cameras 1 and 2 read at the pixels corresponding to the same spatial location were the molecular filters not in place?" to be answered. Once these values were obtained, dividing the number of counts recorded at each pixel in the filtered images by the number of counts which would have been read by the camera at that pixel were the filter not in place gave the transmission ratio through the molecular filter. After the transmission ratio was known, the frequency of the scattering was obtained from the measured absorption profile, the Doppler shift was obtained by subtracting the known laser frequency, and the streamwise and spanwise velocities were obtained by solving Eqns. 2 and 3.

8

A discussion of how the inter-camera calibration curves were established is in order. The employed Princeton Instruments cameras are linear devices (quoted nonlinearity of less than 2%), which is to say that for a fixed camera gain the number of counts recorded at a pixel is proportional to the number of incident photons. Accordingly, the number of counts recorded by cameras 1, 2, and R (with the molecular filters removed) can be expressed as,

$$I_1 = m_1 I_0 + b_1 \quad,$$
$$I_2 = m_2 (\alpha I_0) + b_2 \quad, \text{and} \qquad (5)$$
$$I_R = m_R (\beta I_0) + b_R \quad,$$

where I_1, I_2, and I_R are the number of counts recorded by cameras 1, 2, and R at pixel locations corresponding to the same spatial location, respectively, m_1, m_2, and m_R are the constants of proportionality between the change in incident intensity and the change in the number of recorded counts for the individual cameras, b_1, b_2, and b_R are the number of counts recorded by the cameras with zero incident light intensity, I_0 is the intensity incident on a pixel in camera 1, αI_0 is the intensity incident on a pixel in camera 2, and βI_0 is the intensity incident on a pixel in camera R. The incident intensity for cameras 2 and R has been modified by the constants α and β to include the possibility that angular variations in scattered intensity arise because of the angular dependence of Mie scattering.

Isolating I_0 in Eqns. 5 and combining gives

$$I_1 = \frac{m_1}{\beta m_R} I_R - \frac{m_1 b_R}{\beta m_R} \qquad (6)$$

or

$$I_1 = M_1 I_R + B_1 \qquad (7)$$

where $M_1 = \dfrac{m_1}{\beta m_R}$ and $B_1 = b_1 - \dfrac{m_1 b_R}{\beta m_R}$. Performing a similar procedure for camera 2 gives

$$I_2 = M_2 I_R + B_2 \quad. \qquad (8)$$

Thus, even though the scattering from the condensed acetone particles may not be classical Rayleigh scattering, a linear relationship exists between the number of counts recorded by cameras 1 and 2 (with the filters removed) and the number of counts recorded by camera R at pixels corresponding to the same spatial location.

For each set of FPV data, 300 images were acquired with the molecular filters removed. After aligning the images of the different cameras with the alignment code discussed previously, a linear regression was used to find M_1, M_2, B_1, and B_2. Instead of using a standard least squares regression to minimize $\sum (I_1 - I_R)^2$ [or $\sum (I_2 - I_R)^2$], a weighted least squares regression was used to minimize $\sum [(I_1 - I_R)/I_R]^2$ (or $\sum [(I_2 - I_R)/I_R]^2$). This is because if the deviation between Camera 1's unfiltered images and Camera R's images is spread over the entire 14-bit dynamic range of 0 to 16383, the deviation as a percent of the nominal value will by definition be smaller at the high end of the dynamic range. Minimizing the normalized residuals achieves the best inter-camera relationship over the entire dynamic range.

Initially, it was planned to calculate M_1, M_2, B_1, and B_2 for each pixel in the respective array. However, the values were found to not vary significantly over the array. As a result, single M and B values were calculated for each filtered camera to take advantage of a much larger sample size (188 pixels × 292 pixels in the array × 300 images). In the mean, this procedure was able to achieve excellent agreement between the unfiltered images obtained with the three cameras. The average deviation at individual pixels as a fraction of the reference camera read-out was found to be on the order of 0.1%, which was very encouraging for the ensuing mean velocity calculations. Instantaneously, the agreement was not as good. The standard deviation of the normalized inter-camera deviations was about 5% at all of the pixel locations, which translates directly into an uncertainty in the calculation of instantaneous velocities. That the standard deviation of the normalized inter-camera deviations was non-zero is probably an indication that the scattering is most correctly classified as Mie scattering and that the scattering condensed particles were not exactly spherical. Were this the case, the α and β in Eqns. 5-8 could vary slightly from image to image and the observed effect of finite instantaneous inter-camera deviations would result. By disqualifying pixels where one of the cameras recorded a much larger number of counts than the other cameras, it was insured that the finite instantaneous deviations were not a result of the spurious occurrences of large particles, which might be expected to scatter a much larger amount of light to one camera than the others.

It is worth noting here that an improvement can be made to the FPV system employed here to take care of the instantaneous inter-camera deviations. Meyers [1992] has employed a beam splitter placed in front of the molecular filters to obtain a reference image identical to the image that is passed through the molecular filter. For the sake of speeding up data acquisition and keeping a handle on the amount of collected data, the FPV data of this study was acquired with the Princeton Instruments camera array binned to 192 pixels × 288 pixels, although the full array is capable of obtaining images with 384 pixels × 576 pixels. One could conceivably split off an image before the molecular filter and

9

direct it to half of the camera array while collecting the image passed through the filter with the other half of the array, which was the approach adopted by McKenzie [1995] and Smith and Northam [1995] in systems similar to the FPV system of the current study. This would enable each camera to acquire its own reference image without any notable loss in spatial resolution, which would probably eliminate all of the problems associated with the inter-camera intensity alignment. This approach is currently being investigated in our laboratory at Ohio State University [Clancy et al., 1996].

For each set of FPV data, 750 images were acquired with the molecular filters in place before the 300 'calibration' images were acquired with the molecular filters removed. Once M_1, M_2, B_1, and B_2 had been acquired from the regression on the aligned, unfiltered images, the procedure for obtaining the instantaneous velocities went as follows. First, the count read-out at each pixel in an instantaneous reference camera image was used in conjunction with M_1 and B_1 (M_2 and B_2) to obtain the number of counts Camera 1 (Camera 2) would have recorded at the pixel corresponding to the same spatial location with the molecular filter removed, which is referred to as $I_{0,1}$ ($I_{0,2}$). Then the read-out obtained in the filtered image of Camera 1 (Camera 2) at that pixel was normalized by $I_{0,1}$ ($I_{0,2}$) to obtain the transmission ratio through the filter at that pixel. This transmission ratio was then compared to the appropriate filter profile to obtain the Doppler shift for the scattering collected by Camera 1 (or Camera 2). The Doppler shifts present in the collected scattering and the relevant angles from the configuration were then substituted into Eqns. 2 and 3 to obtain the instantaneous streamwise and spanwise velocities.

Results and Discussion

Planar, instantaneous measurements of streamwise and normal velocities were acquired with Filtered Planar Velocimetry (FPV). In the course of developing the technique, an error analysis indicated that velocity measurements acquired with the technique have an associated uncertainty of approximately ± 8.6% (details of the error analysis are given by Elliott [1993] and Elliott et al. [1994a]). As discussed previously, two-component LDV measurements could be acquired only to within 2 mm of the surface beneath the boundary layers. It was hoped that FPV would permit measurements closer to the surface.

1. Flat Plate Boundary Layer

The mean streamwise velocity image acquired in the flat plate boundary layer is presented in Fig. 13. The brightness level in the image is proportional to the magnitude of the streamwise velocity. Mean velocity profiles extracted from the mean velocity image are plotted in Fig. 14 along with the mean velocity profile obtained with LDV. For all of the profiles in Fig. 14, the normal coordinate has been nondimensionalized with local boundary layer thicknesses obtained from the LDV measurements. The agreement between the FPV and LDV measurements is very encouraging. Assuming the LDV measurements are an

accurate representation of the true velocity profile, dashed curves have been added at ± 8% of the LDV profile to give an indication of the accuracy of the FPV measurements. The FPV profile falls well within the ± 8% boundaries, suggesting the computed uncertainty of ± 8.6% is quite conservative with respect to mean velocity measurements.

Another important point that should be made in conjunction with Fig. 14 is the large improvement in near-wall resolution obtained with FPV relative to LDV. The measurements were obtained with a spatial resolution of about 0.35 mm/pixel and seemingly good velocity measurements were obtained at the first pixel above the surface in the images. If the temperature is assumed to be $1.85T_{freestream}$ at this normal elevation (value measured by Smits [1990] in a Mach 2.8 turbulent boundary layer), the velocity of 0.6 U_0 (approximately 360 m/s) gives a Mach number of about 1.3 at this location. Thus it appears that the sonic line occurs beneath n = 0.35 mm (n/δ_0 = 0.04) in the flat plate boundary layer of the current study.

Since the average spanwise velocity was essentially zero everywhere in the measurement plane (magnitudes of less than 3% of the freestream velocity everywhere in the image), the average spanwise velocity image is not presented. This result confirms that the tunnel flow is highly two-dimensional. Given the decision to measure two velocity components (which required the acquisition of a third Princeton Instruments ICCD camera system), it would have been most desirable to measure the streamwise and normal velocities. The employed optical configuration was totally insensitive to velocities in the normal direction. Unfortunately, there was no easily achievable optical configuration which would have been sensitive to the streamwise and normal velocities without being sensitive to the spanwise velocity. This situation could be rectified by measuring all three velocity components. The only method to measure all three velocity components with three cameras is to acquire both filtered and reference images with each camera, as discussed in the Experimental Procedure chapter [Clancy et al., 1996].

In examining the average velocity image of Fig. 13, there are lines parallel to the surface where the velocity measurements display small-amplitude discontinuities. It should be recalled that the prism which directs the illuminating laser sheet up the tunnel axis is located within the supersonic flow field.

In the instantaneous images, the shock waves and recirculation zone in front of the prism give rise to small discontinuities in the intensity distribution of the illuminating laser sheet. This is due to the large density variations (and therefore index of refraction variations) associated with the shock system. When a portion of the laser sheet encounters changes in index of refraction, the light is refracted away from its incoming direction of propagation. The net result of these local refractions is a sheet containing regions of increased and decreased intensity compared to the Gaussian sheet which enters the tunnel. Similar results were obtained by Fourguette et al. [1995] in passing a laser sheet through a

jet with an index of refraction significantly different than the ambient fluid.

Since these effects are present in the images of all three cameras, the velocity measurements should not be adversely affected. However, the discontinuities appear as thin striations with a width of only a fraction of a millimeter (of no more than a single pixel in amplitude). Since the sheet discontinuities occur over such a small spatial scale, it is possible that the algorithm to align the images of the different cameras is not accurate enough to result in the striations exactly coinciding in the aligned images. In fact, qualitative observation of the aligned images shows that the striations exhibit a small amount of spatial jitter about their true location (of no more than 1 pixel in amplitude) after the alignment process. This small amount of misalignment would also be present for the case of a uniform sheet distribution, but would not be as significant a problem because there would be essentially negligible differences in the illuminating intensity at adjacent pixels. However, for the distorted sheet of the current experiments, significant uncertainties might result.

The striations change position from image to image because of the unsteady nature of the recirculation zone, which generates significant shock wave jitter. In the mean velocity image of Fig. 13, horizontal discontinuities are present at only a few normal elevations. This suggests that only the mean sheet discontinuities due to the mean presence of the shock wave and recirculation zone have a noticeable effect on the mean velocity measurements. If this is the cause of the discrepancy, it is significant to note that this is an image alignment problem that can probably be eliminated with more accurate alignment algorithms. If the images were perfectly aligned, the technique would not encounter problems with the sheet discontinuities.

This discussion of uncertainties induced by aero-optic effects is tempered by the observation that horizontal discontinuities are not present in the mean velocity images obtained downstream of the centered expansion regions, which are presented below. The profile of the standard deviation of the measured streamwise velocity fluctuations in the flat plate boundary layer is presented in Fig. 15. Unfortunately, there is a significant deviation between the results obtained with FPV and LDV. The standard deviation is approximately 5% of the mean velocity everywhere except very near the surface. It appears that the uncertainties associated with the instantaneous FPV measurements precludes the resolution of the turbulent velocity fluctuations. This is a consequence of the uncertainties with the FPV technique (discussed in detail by Elliott et al. [1994b]) and the uncertainties in the employed normalization procedure (recall that pixel read-outs in the aligned, unfiltered images displayed a standard deviation of about 5%). This is a clear illustration of the work that remains before FPV will be a quantitatively reliable technique for the turbulence investigations.

2. Boundary Layer Downstream of the 7° Centered Expansion

The mean streamwise velocity images obtained downstream of the 7° centered expansion corner are presented in Fig. 16. As was the case for the measurements in the flat plate boundary layer, the mean spanwise velocity was essentially zero everywhere in the images, confirming that the tunnel flow remains two-dimensional downstream of the expansion.

At the locations where LDV measurements were acquired, velocity profiles were extracted from the FPV average velocity images of Fig. 16 for comparison. The LDV and FPV velocity profiles obtained at $s/\delta_0 = 1.5$ and 2.8 are presented in Fig. 17. At $s/\delta_0 = 1.5$, the agreement between the two profiles is quite good, with maximum deviations of well less than 5% of the freestream velocity. At $s/\delta_0 = 2.8$ there is a region which displays deviations on the order of 5% of the mean velocity. Although these deviations are noticeable, they are still well within the previously cited uncertainty of $\pm 8.6\%$. Profiles obtained at $s/\delta_0 = 5.6$ and 8.4 are presented in Fig. 18 (no LDV profiles were acquired at $s/\delta_0 = 5.6$). The profiles display excellent agreement at $s/\delta_0 = 8.4$. Profiles obtained at $s/\delta_0 = 14.0$ and 19.2 are presented in Fig. 19. Again, the agreement between the FPV and LDV results is good.

If one looks at the bottom of the FPV profiles, the effect of the expansions on the mean velocity of the near-wall region can be investigated. Between $s/\delta_0 = 1.5$ and 2.8, there is an acceleration of about $0.05U_0$. Between $s/\delta_0 = 2.8$ and 5.6 there is further acceleration near the wall, even though these locations are well downstream of the expansion corner, indicating the flow may not respond immediately to the expansion region in the portion of the boundary layer where viscous effects are significant. This behavior represents a significant departure from the inviscid method of characteristics computations where the velocity profile is frozen downstream of the expansion.

Between $s/\delta_0 = 5.6$ and 8.4 (Fig. 18), the FPV measurement nearest the surface experiences a deceleration of approximately $0.03U_0$, indicating that the retarding effect of the surface is beginning to dominate the region near the wall. Between both $s/\delta_0 = 8.4$ (Fig. 18) and 14.0 (Fig. 19) and $s/\delta_0 = 14.0$ and 19.2 (Fig. 19), the velocity nearest the wall continually decreases. The value nearest the surface at $s/\delta_0 = 19.2$ is still about 10% higher than that measured just above the surface in the flat plate boundary layer. It appears that the near-wall mean velocity has not fully recovered its equilibrium value at $s/\delta_0 = 19.2$.

Profiles of the standard deviation of the streamwise velocity fluctuations obtained with LDV and FPV at $s/\delta_0 = 1.5$ and 19.2 are presented in Fig. 20. Similar to the FPV measurements in the incoming boundary layer, the measurement uncertainties give rise to significant freestream fluctuations. Although this was deduced from the comparison to the turbulence profiles measured with LDV in the incoming boundary layer, the perseverance of the freestream fluctuation levels in the FPV profiles across the

expansion region further confirms that they originate from measurement uncertainties since turbulent velocity fluctuations should decrease across the expansion region.

3. Boundary Layer Downstream of the 14° Centered Expansion

The average streamwise velocity obtained downstream of the 14° centered expansion is presented in Fig. 21. As with the other measurements, the average spanwise velocity was again less than 3% of the freestream velocity everywhere in the measurement plane, indicating the tunnel flow was highly two-dimensional. The low velocity region in the bottom right of the measurement region is the recirculation zone in front of the prism assembly. Because of the relatively short length of the 14° centered expansion model, the face of the prism assembly was only about $19\delta_0$ downstream of the expansion corner. This left very little streamwise distance downstream of the corner where the boundary layer was unaffected by the shock waves and recirculation zone in front of the prism assembly.

Profiles obtained at $s/\delta_0 = 1.5$ and 2.8 from the FPV and LDV measurements are presented in Fig. 22. Although there is good agreement away from the surface, significant deviations between the FPV and LDV measurements are present for $n/\delta_0 < 0.5$ at $s/\delta_0 = 1.5$ and $n/\delta_0 = 1.0$ at $s/\delta_0 = 2.8$. If the problem was primarily associated with the inability of the LDV seed particles to respond quickly enough to the expansion, the LDV measurements would be expected to be less than the FPV measurements, which is not the case. The velocities measured with FPV appear to be too low. This might be a result of surface reflections. Although it was intended to pass the collimated laser sheet along the surface of the models, it is possible that it was either not perfectly collimated or directed slightly into the surface (or both). Since there is no means to eliminate reflected light from the reference image, reflections would give rise to an artificially low velocity measurement, as discussed in the Experimental Procedure section. However, the normal extent of the deviations is larger than would be expected if reflections were encountered only near the surface.

It might also be possible that the shock system in front of the prism assembly is affecting the flow field at $s/\delta_0 = 1.5$ and 2.8. If this were true, the FPV velocity measurements would be expected to be lower than the LDV measurements, as is the case in Fig. 22. The standard deviation of the streamwise velocity fluctuations measured with FPV and LDV is presented in Fig. 23. As with the other FPV measurements, the measurement uncertainties preclude any detailed consideration of the turbulent velocity fluctuations based on the FPV results.

Conclusion

Planar, instantaneous velocity measurements were obtained with Filtered Planar Velocimetry (FPV), a nonintrusive diagnostic developed in our laboratory at The Ohio State University [Elliott et al., 1994a, 1994b]. In the current work, the FPV technique was extended to the measurement of two velocity components (streamwise and spanwise). Measurements were acquired in a Mach 3, fully-developed turbulent boundary layer and in the same boundary layer downstream of 7° and 14° expansions.

The FPV measurements offered a large improvement in near-wall resolution relative to that obtainable with LDV. LDV permitted measurements only to within about 2 mm of the boundary while FPV permitted measurements to within 0.4 mm of the boundary.

Unfortunately, the uncertainties associated with the instantaneous FPV measurements are of the same order as the turbulent velocity fluctuation levels in the boundary layers. Fortunately, these measurement uncertainties should be reduced in the future with technique improvements through advances in laser technology and technique refinements. Nevertheless, the current uncertainty levels precluded detailed investigations of the boundary layer turbulence based on the FPV results.

Despite the inability to investigate the turbulent velocity fluctuations, the mean velocities obtained with FPV in both the flat plate boundary layer and the boundary layer downstream of the 7° centered expansion exhibit very good agreement with the LDV measurements. Further, the average spanwise velocities measured with FPV were essentially zero, confirming that the flow upstream and downstream of the expansion regions is two-dimensional. Although some discrepancies exist between the LDV and FPV results obtained near the boundary downstream of the 14° centered expansion, all indications are that FPV is potentially an extremely valuable tool for investigations of compressible turbulence in that instantaneous, planar measurements of multiple velocity components are possible.

References

Anderson, J.D., 1990, Modern Compressible Flow with Historical Perspective, McGraw-Hill, New York, NY.

Arnette, S.A., Samimy, M., and Elliott, G.S., 1993, "The Effect of Expansion on the Large Scale Structure of a Compressible Turbulent Boundary Layer," AIAA-93-2991.

Arnette, S.A., Samimy, M., and Elliott, G.S., 1994a, "Expansion Effects on Supersonic Boundary Layers," Ohio State University Internal Report MEMS-94- 101.

Arnette, S.A., Samimy, M., and Elliott, G.S., 1994b, "The Effect of Expansion on Large Scale Structure Evolution in a Compressible Turbulent Boundary Layer," AIAA-94-2228.

Arnette, S.A., Samimy, M., and Elliott, G.S., 1995, "Structure of Supersonic Turbulent Boundary Layer After Expansion Regions," AIAA J., 33: 430- 438.

Arnette, S.A., Samimy, M., and Elliott, G.S., 1996, "The Effects of Expansions on the Turbulence Structure of a Compressible Boundary Layer," AIAA-96-0656.

Arnette, S.A., 1995, "The Effects of Expansion Regions on Supersonic Turbulent Boundary Layers," Ph.D. Dissertation, Dept. of Mechanical Engineering, The Ohio State University, Columbus, Ohio.

Clancy, P., Kim, J.-H., and Samimy, M., 1996, "Filtered Planar Velocimetry in High Speed Flows," to be presented at the 27th AIAA Fluid Dynamics Conference.

Dawson, J.D.Samimy, M., and Arnette, S.A., 1994, "The Effects of Expansion on a Supersonic Boundary Layer: Surface Pressure Measurements ", AIAA J.,.32: 2169-2177.

Elliott, G.S., Samimy, M., and Arnette, S.A., 1992, "Filtered Rayleigh Scattering Based Measurements in Compressible Mixing Layers," AIAA-92-3543.

Elliott, G.S., 1993, "A Study of Compressible Mixing Layers Using Laser Based Diagnostic Techniques," Ph.D. Dissertation, Department of Mechanical Engineering, The Ohio State University.

Elliott, G.S., Samimy, M., and Arnette, S.A., 1993, "Molecular Filter-Based Diagnostics in High Speed Flows ," AIAA-93-0512.

Elliott, G.S., Samimy, M., and Arnette, S.A., 1994a, "Details of a Molecular Filter-Based Velocimetry Technique," AIAA-94-0490.

Elliott, G.S., Samimy, M., and Arnette, S.A., 1994b, "A Molecular Filter Based Velocimetry Technique for High Speed Flows," Experiments in Fluids, 18: 107-118.

Elliott, G.S. and Samimy, M., 1995, "Simultaneous Measurement of Velocity and Thermodynamic Quantities Using a Molecular Filter Based Technique," 10th Symposium on Turbulent Shear Flows, Pennsylvania State University (to appear in AIAA J., 1996).

Fourguette, D.C., Dimotakis, P.E., and Ching, W.K., 1995, "Index-of-Refraction Imaging and Aero-Optics Effects in a Fully-Developed Axisymmetric Turbulent Jet," AIAA-95-1980.

McKenzie, R.L., 1995, "Measurement Capabilities of Planar Doppler Velocimetry Using Pulsed Lasers," AIAA-95-0297.

Meyers, J.F., 1992, "Doppler Global Velocimetry: The Next Generation?" AIAA-92-3897.

Miles, R.B., Lempert, W.R., and Forkey, J., 1991, "Instantaneous Velocity Fields and Background Suppression by Filtered Rayleigh Scattering," AIAA- 91-0357.

Miles, R.B., Forkey, J.,and Lempert, W.R., 1992, "Filtered Rayleigh Scattering Measurements in Supersonic/Hypersonic Facilities," AIAA-92-3894.

Mitchell, A.C.G. and Zemansky, M.W., 1934, Resonance Radiation and Excited Atoms, Cambridge University Press, London, England.

Samimy, M., Arnette, S.A., and Elliott, G.S., 1994, "Streamwise Structures in a High Reynolds Number Supersonic Boundary Layer," Physics of Fluids, 6: 1081-1083.

Smith, M.W., and Northam, G.B., 1995, "Application of Absorption Filter-Planar Doppler Velocimetry to Sonic and Supersonic Jets," AIAA-95-0299.

Smits, A.J., 1990, "New Developments in Understanding Supersonic Turbulent Boundary Layers," 12th Symposium on Turbulence, Rolla, Missouri.

Spina, E.F. and Smits, A.J., 1987, "Organized Structures in a Compressible, Turbulent Boundary Layer," J. of Fluid Mech., 182: 85-109.

Tellinghuisen, J., 1978, "Intensity Factors for the I_2 B-X Band System," J. of Quantitative Spectroscopy and Radiative Transfer, 19: 149-161.
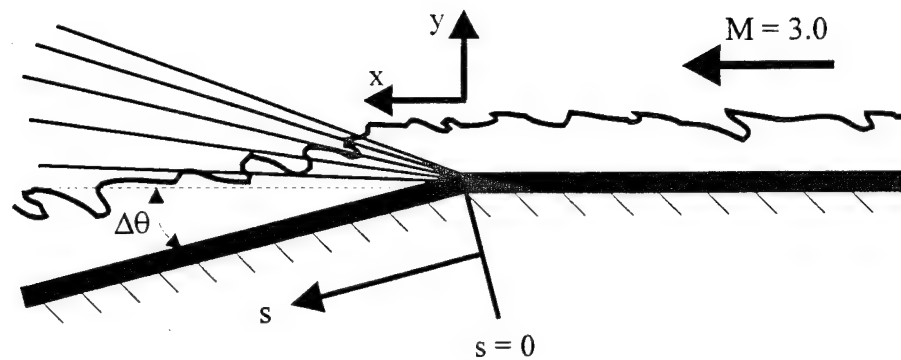
Figure 1. Schematic of the boundary layer passing through the centered expansions. There are two centered expansion ($\Delta\theta = 7°$ and $14°$).The (x,y) origin is on the surface at the corner. The n coordinate is zero at the surface and everywhere normal to the surface.
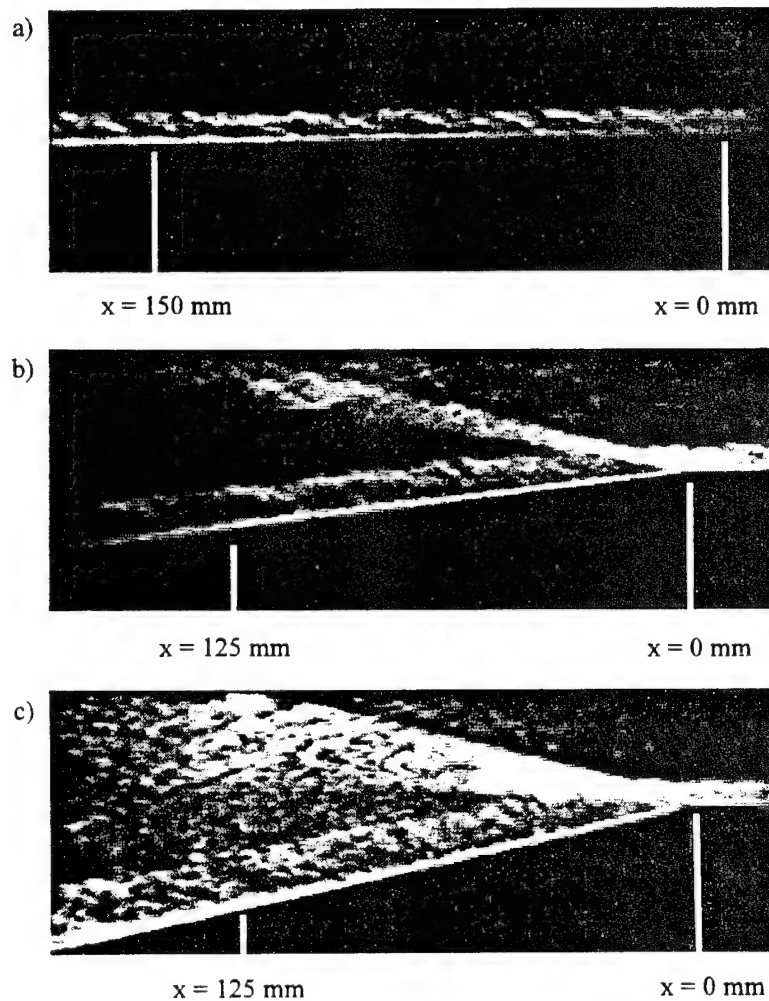

Figure 2. Instantaneous schlieren images of the a) flat plate, b) $7°$ centered expansion, and c) $14°$ centered expansion boundary layers.

14

a)

b)

s = 135 mm   s = 75 mm

c)

d)

s = 80 mm   s = 0 mm
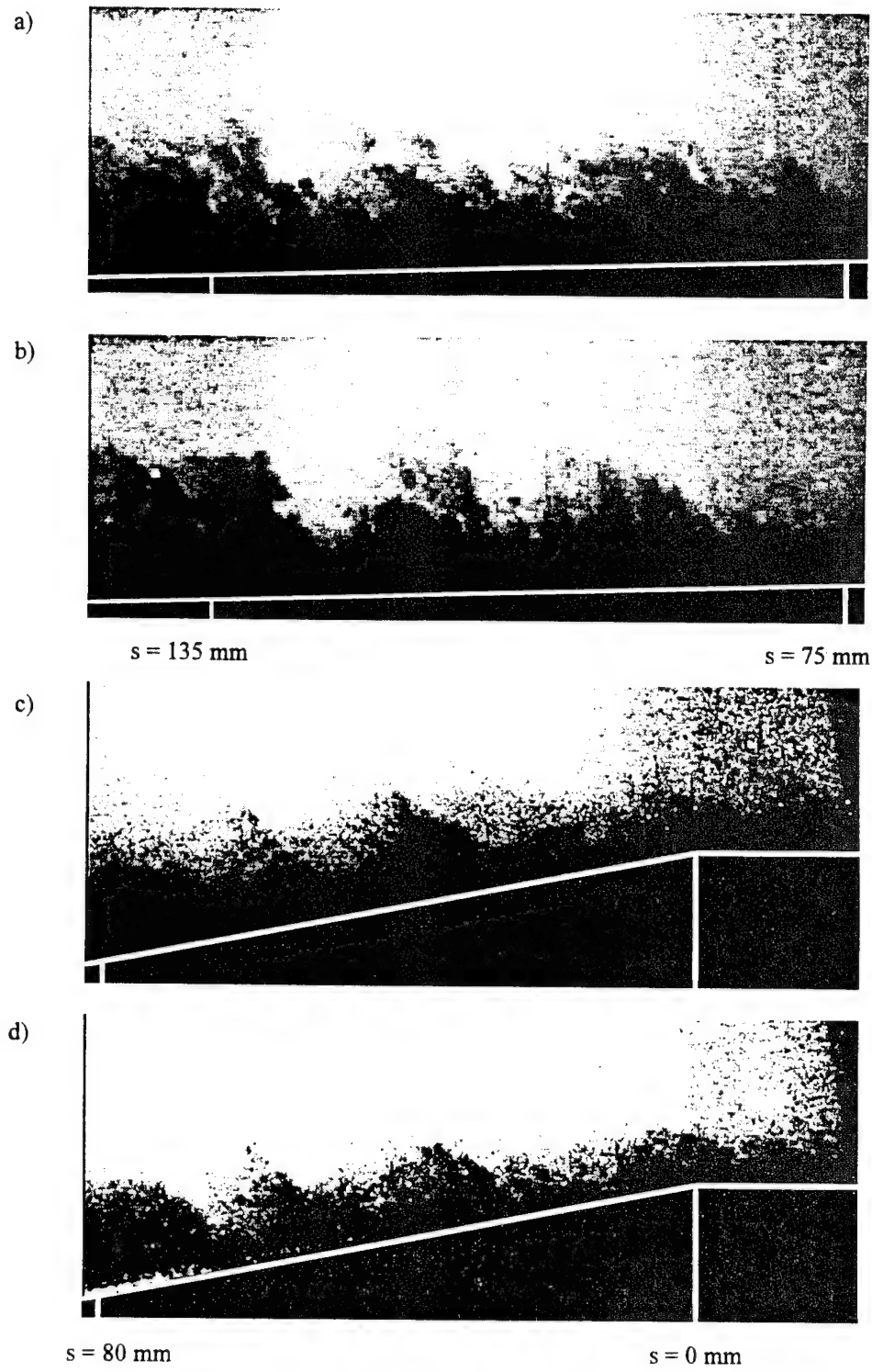
Figure 3. Instantaneous FRS visualizations of the Mach 3 flat plate boundary layer (a and b) and the boundary layer in the vicinity of the $7°$ centered expansion (c and d). The added white lines indicate the position of the model surface.

15
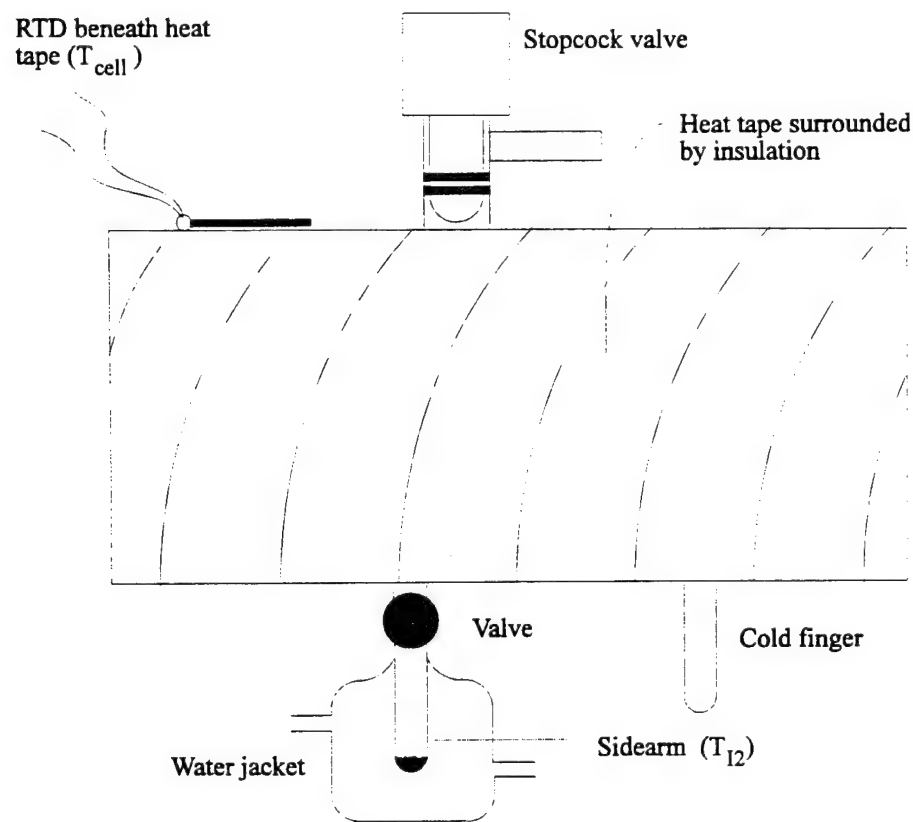
Figure 4. Schematic of the iodine cell (molecular filter).
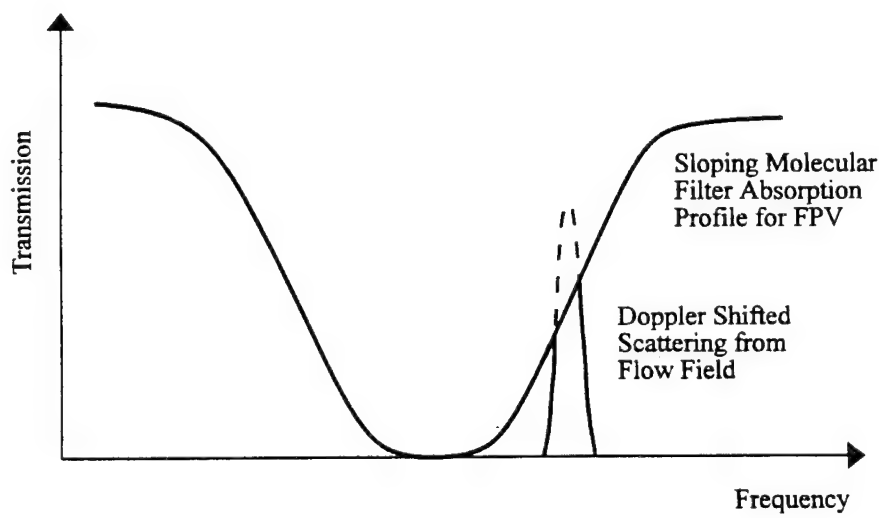
Figure 5. Schematic of partial filter attenuation used in Filtered Planar Velocimetry.

16
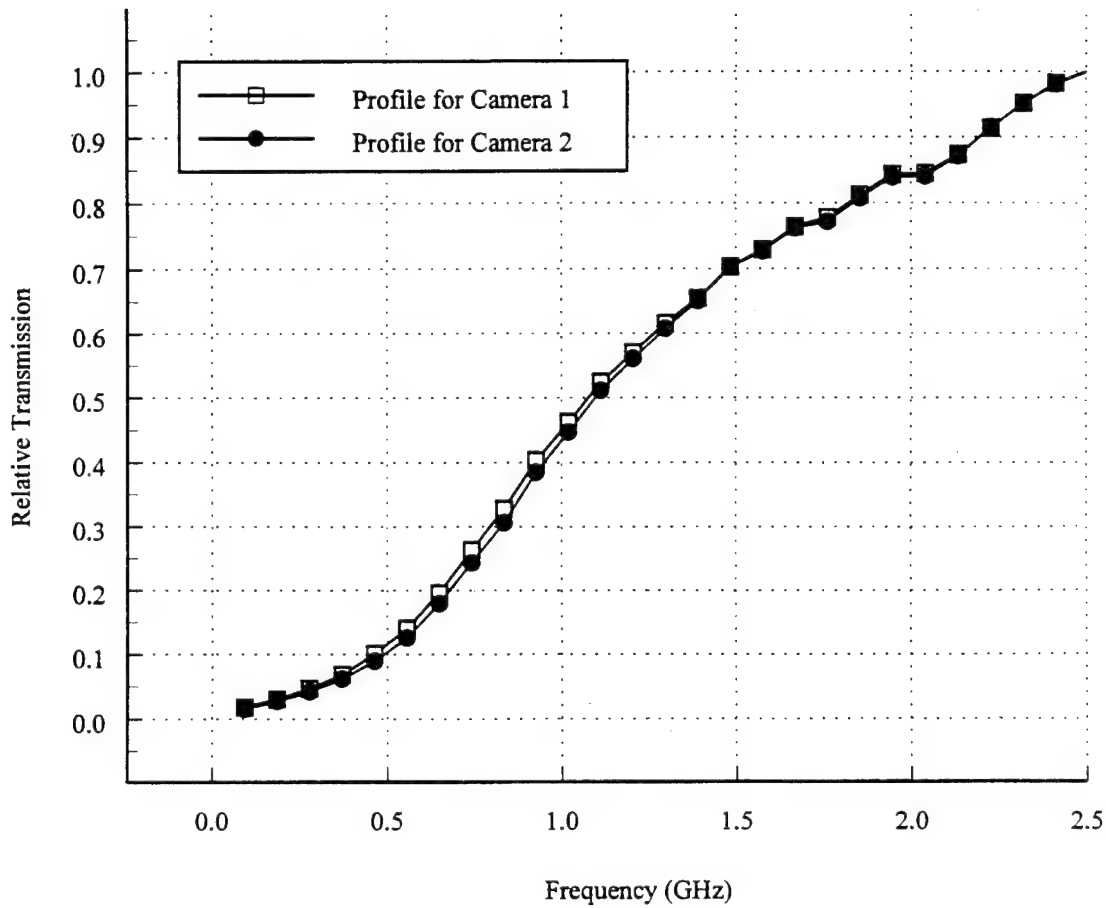
Figure 6. Filter profiles employed for the Filtered Planar Velocimetry measurements.
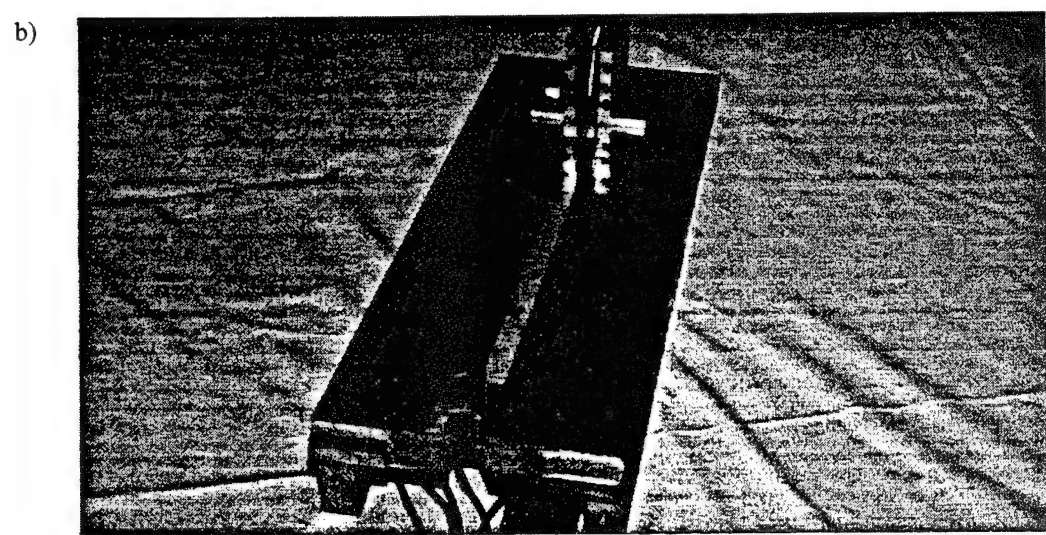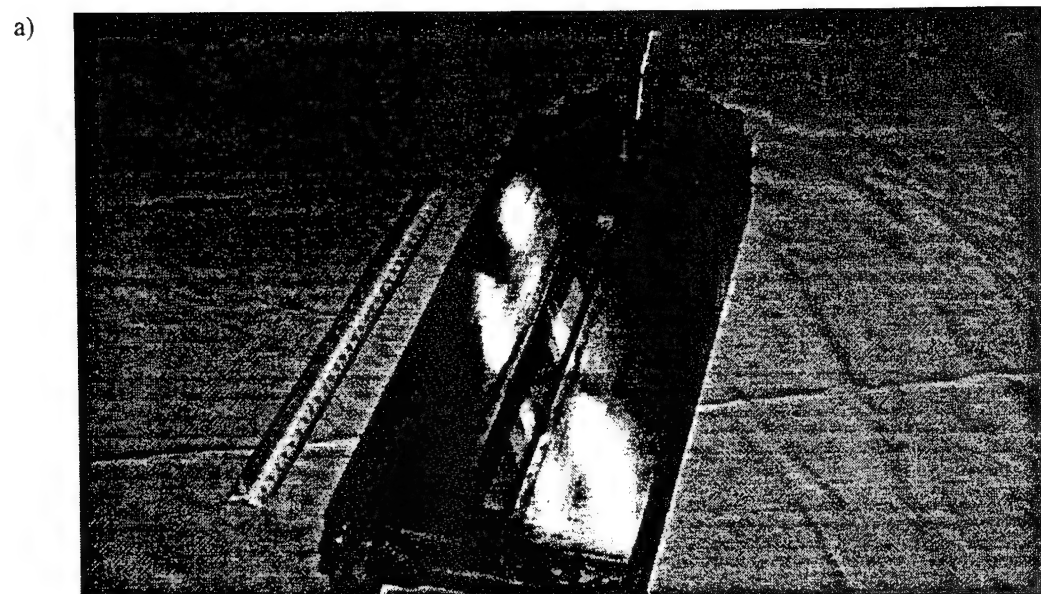
Figure 7. Photographs of the prism assembly used in the FPV measurements mounted on the flat plat model (a) and the 7° centered expansion model (b).
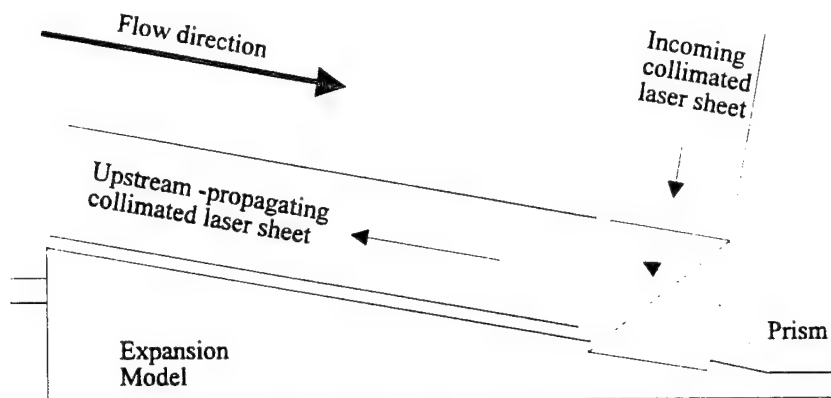
Figure 8. Schematic of the redirection of the collimated sheet by the prism mounted in the tunnel.
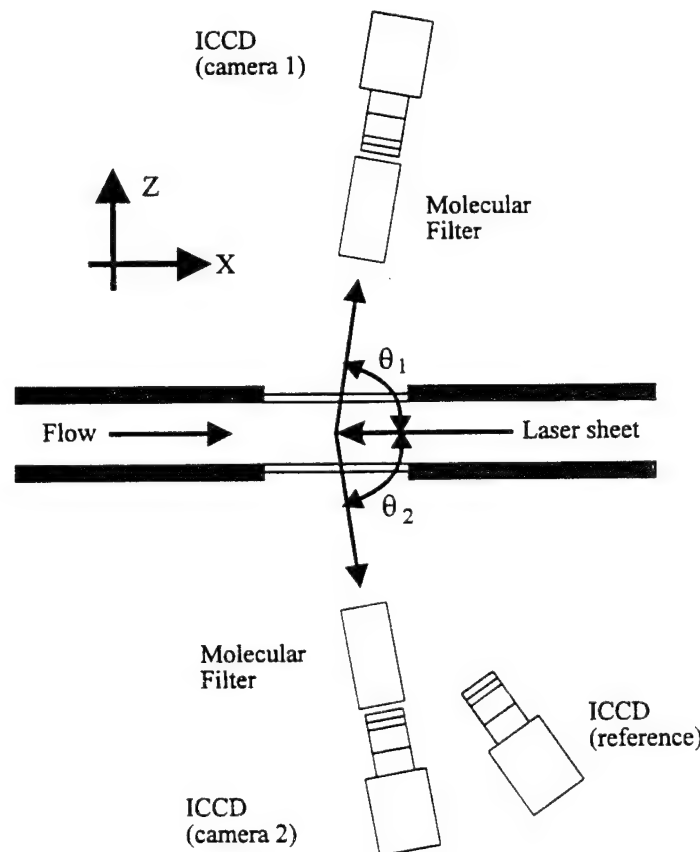
Figure 9. Top view of the optical arrangement for the two-component Filtered Planar Velocimetry measurements.
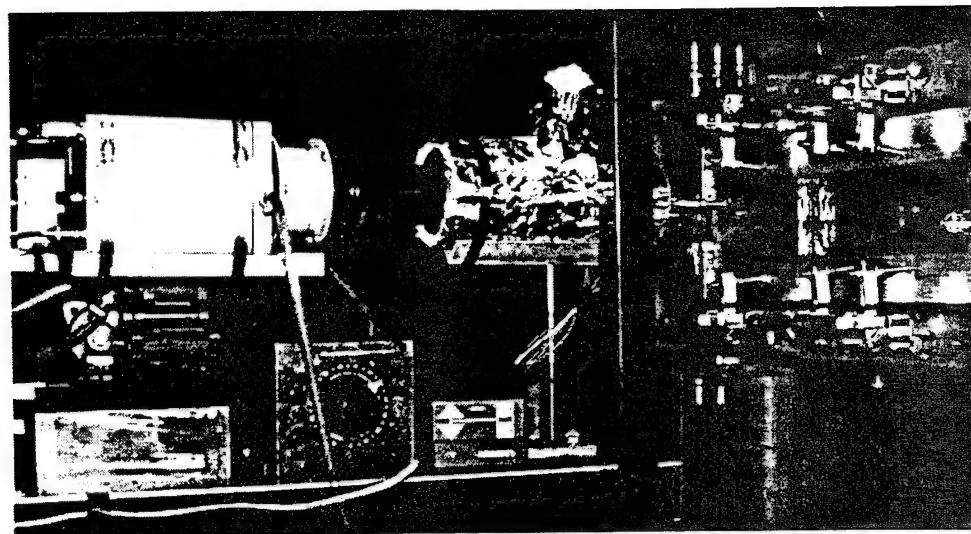
Figure 10. Arrangement of the molecular filter and ICCD camera for the Filtered Planar Velocimetry measurements.
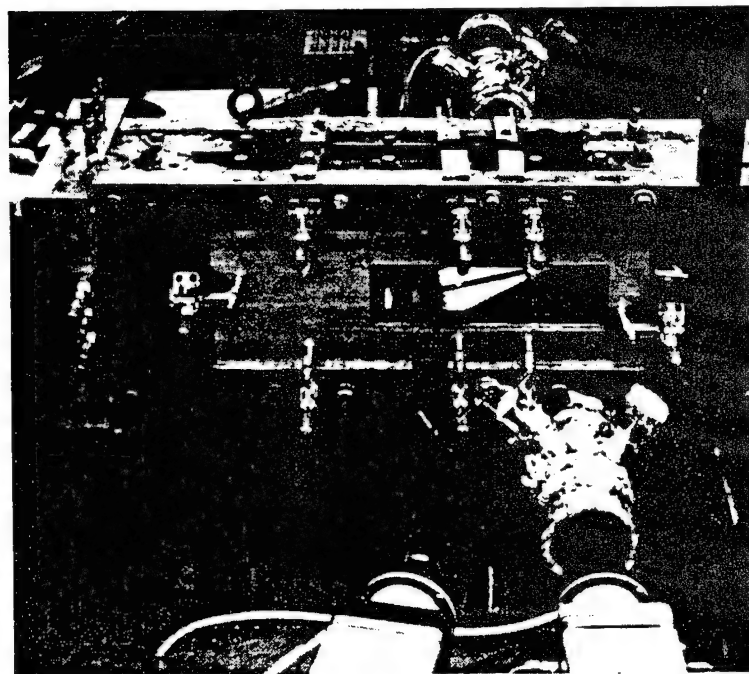
Figure 11. Arrangement for the three cameras used in the Filtered Planar Velocimetry measurements.

20
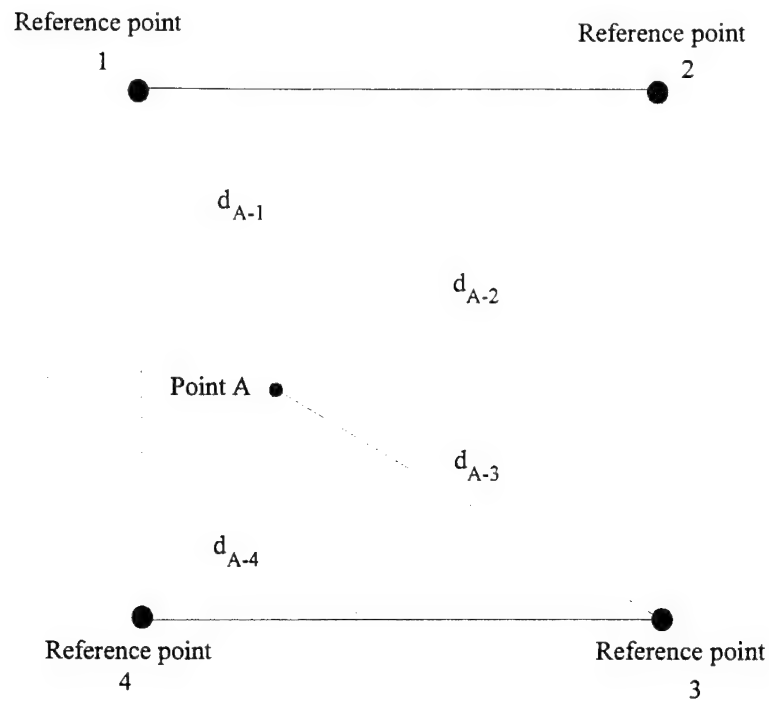
Figure 12. Schematic for the calculation of the horizontal and vertical shifts needed to align the images of the various cameras.

s = 80 mm   s = 0 mm
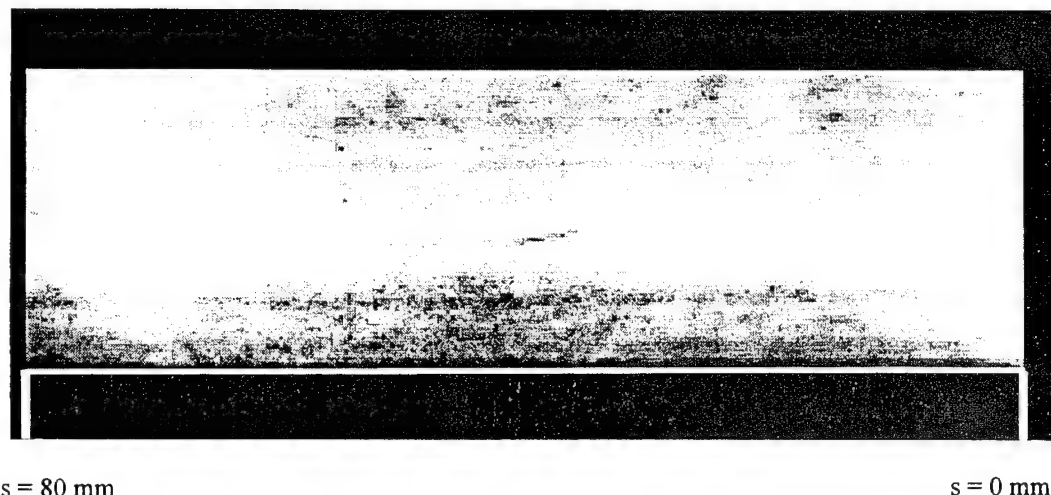
Figure 13. Average streamwise velocity image of the flat plate boundary layer obtained with Filtered Planar Velocimetry.

21
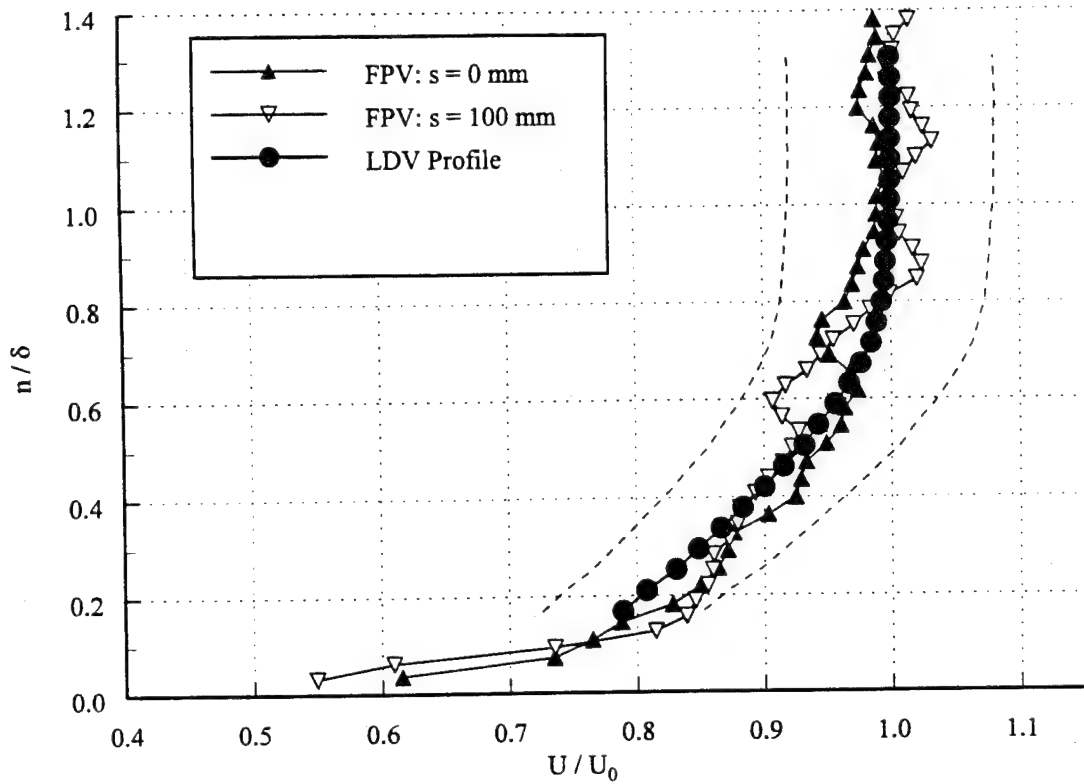
Figure 14. Mean velocity profiles obtained with FPV and LDV in the flat plate boundary layer.
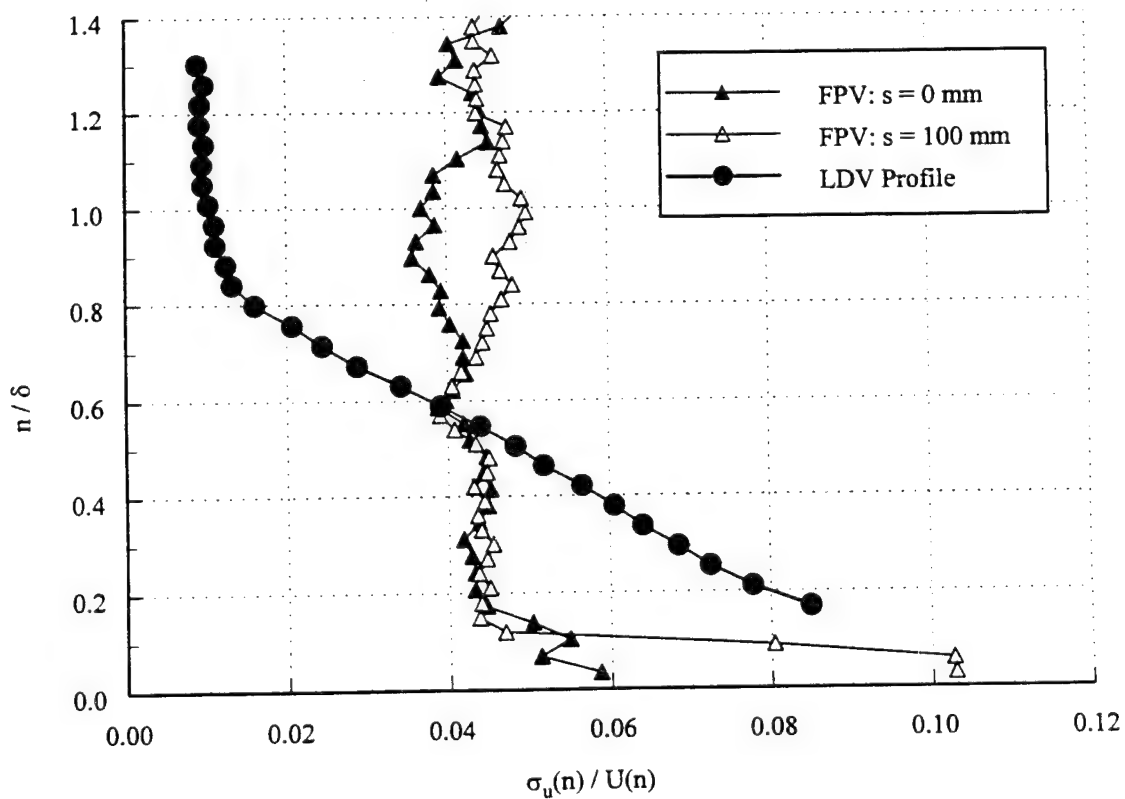
Figure 15. Streamwise turbulence profiles obtained with FPV and LDV in the flat plate boundary layer.

22

a)
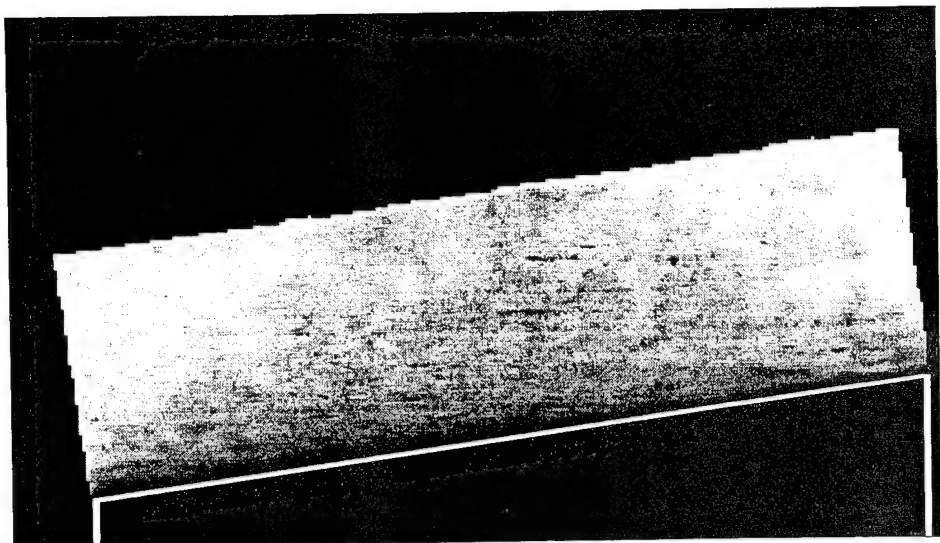
s = 95 mm   s = 5 mm

b)
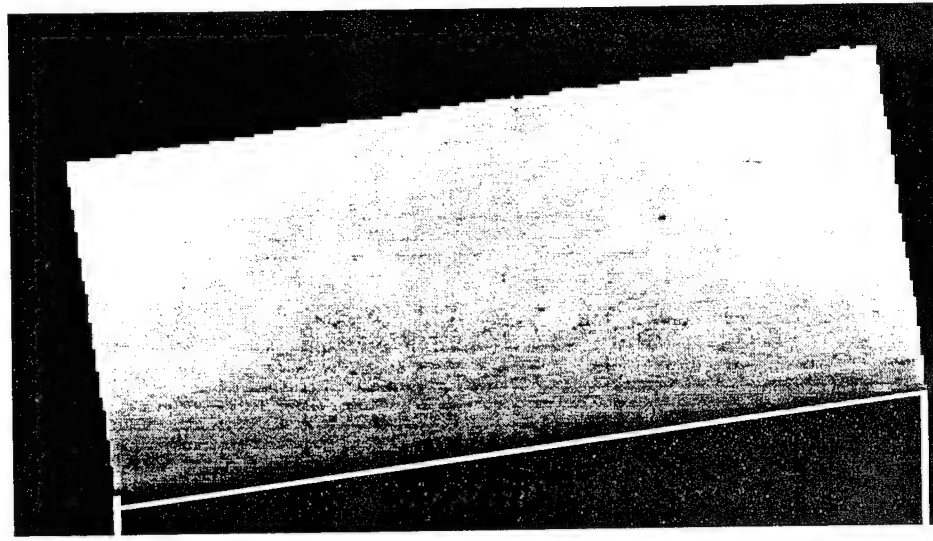
s = 220 mm   s = 125 mm

Figure 16. Average streamwise velocity images obtained with Filtered Planar Velocimetry at two streamwise locations downstream of the 7° centered expansion.
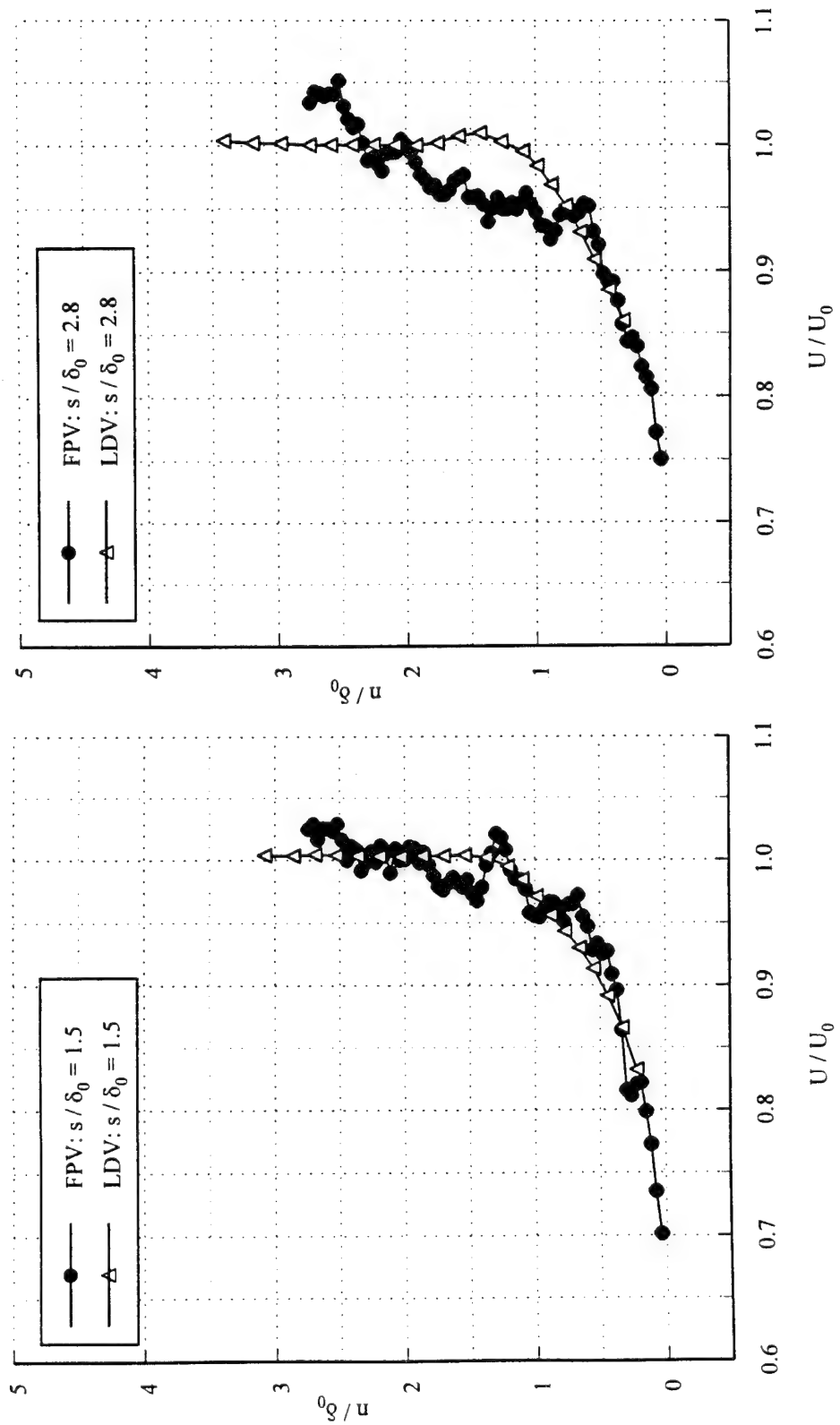
23

Figure 17. Mean velocity profiles obtained downstream of the 7 degree centered expansion at $s / \delta_0 = 1.5$ and 2.8 with FPV and LDV.
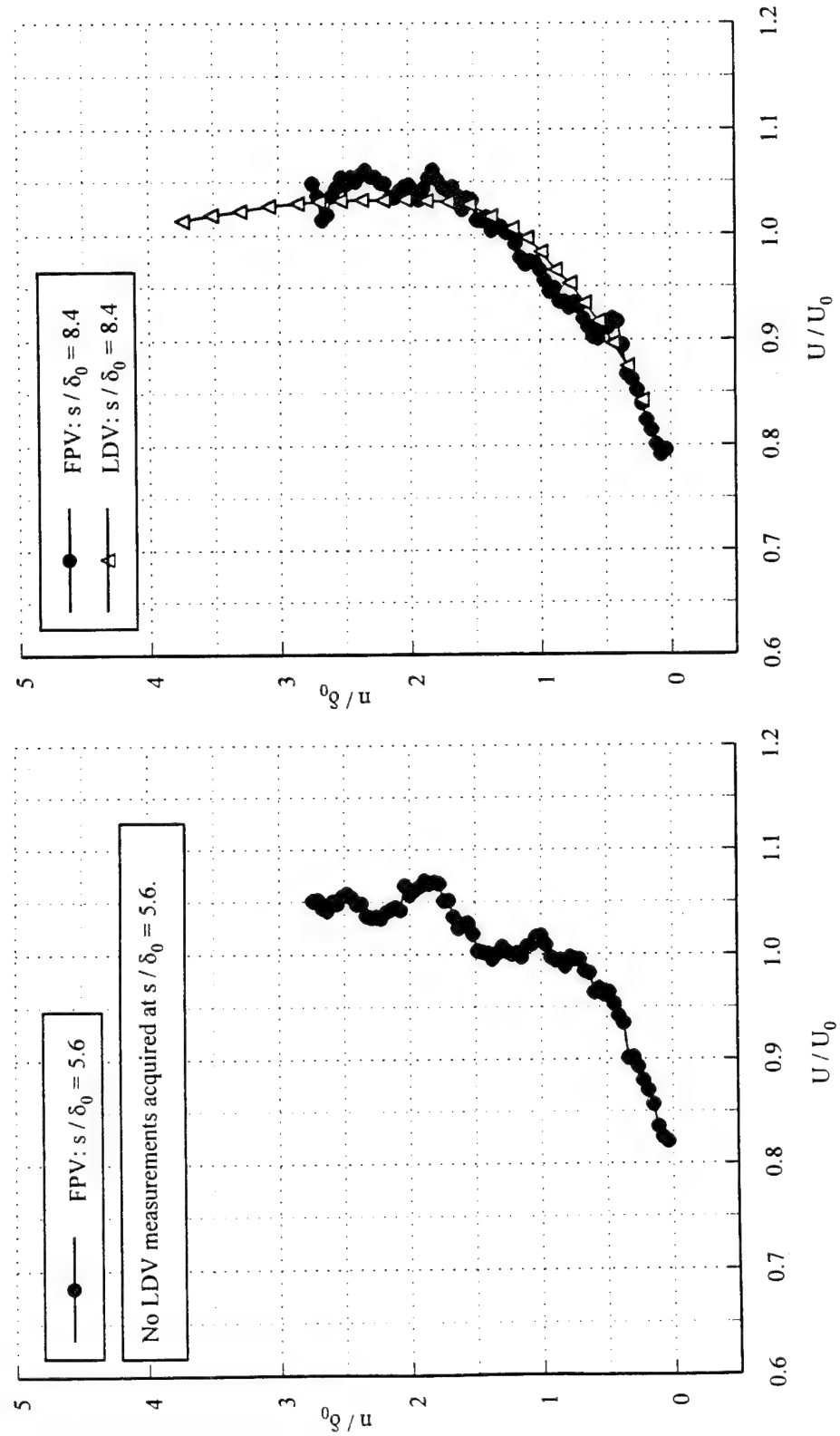
Figure 18. Mean velocity profiles obtained downstream of the 7 degree centered expansion at $s / \delta_0 = 5.6$ and 8.4 with LDV and FPV.

25
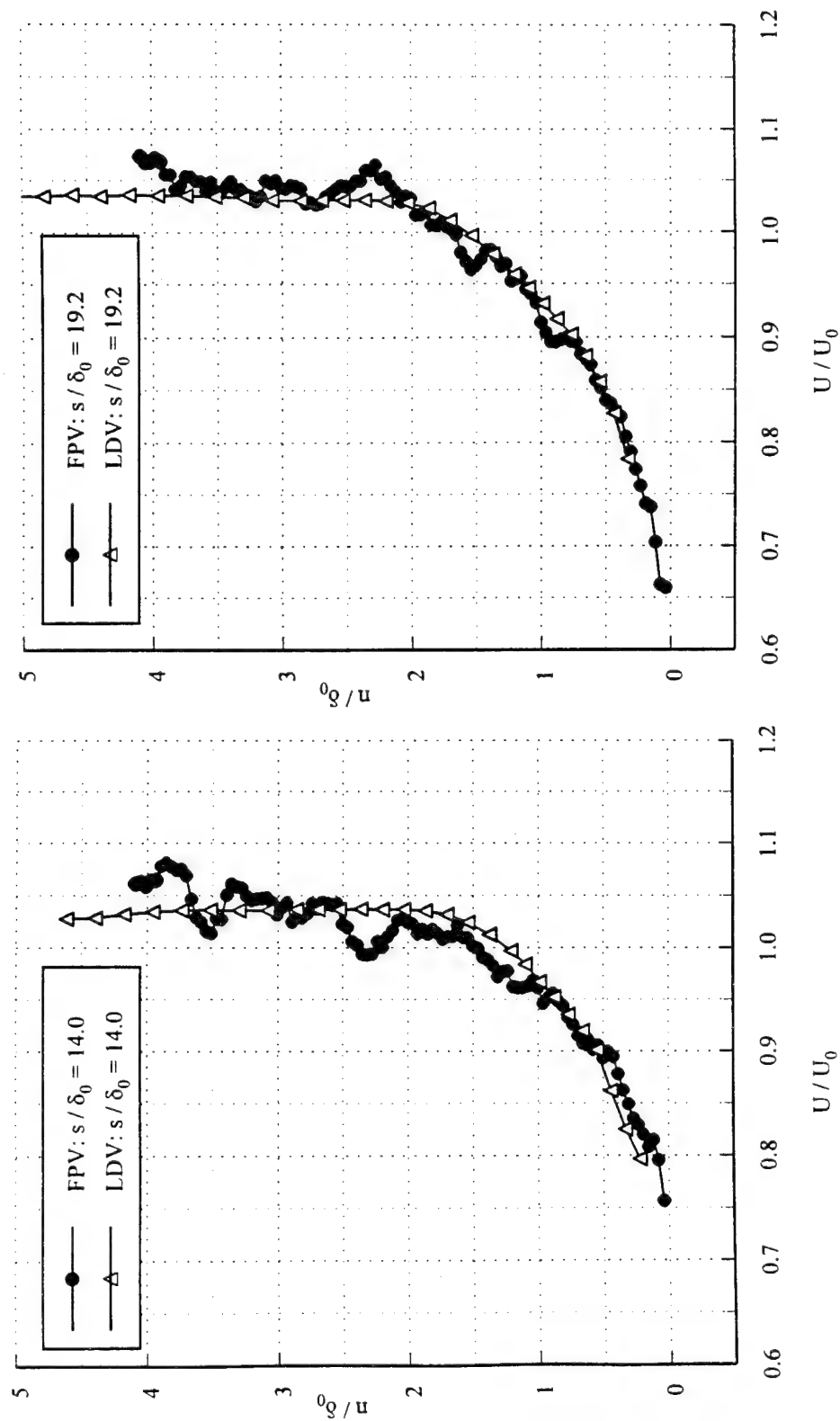
Figure 19. Mean velocity profiles obtained downstream of the 7 degree centered expansion at s / δ₀ = 14.0 and 19.2 with LDV and FPV.

26
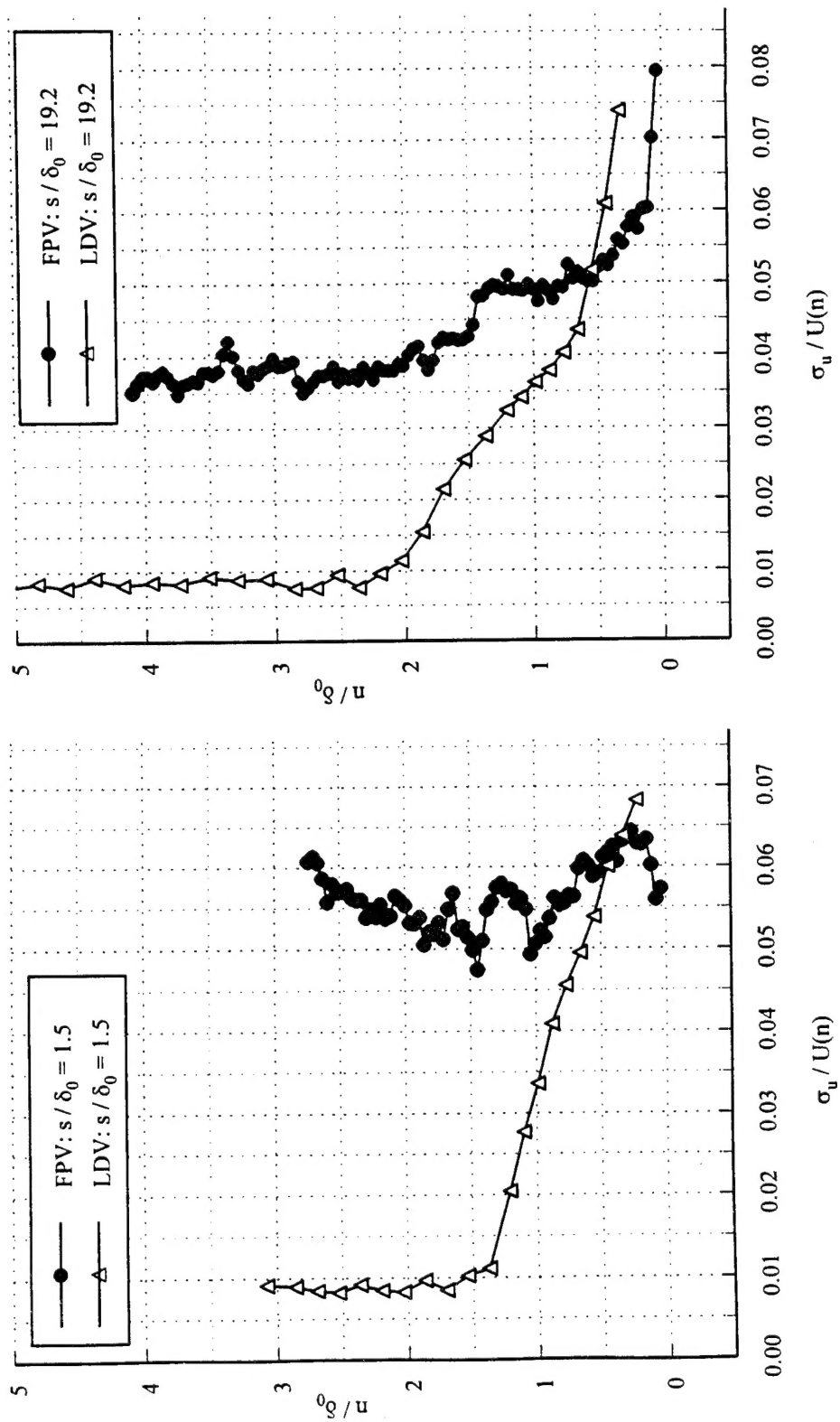
Figure 20. Streamwise turbulence profiles obtained downstream of the 7 degree centered expansion at $s/\delta_0 = 1.5$ and 19.2 with LDV and FPV.

s = 90 mm   s = 2 mm
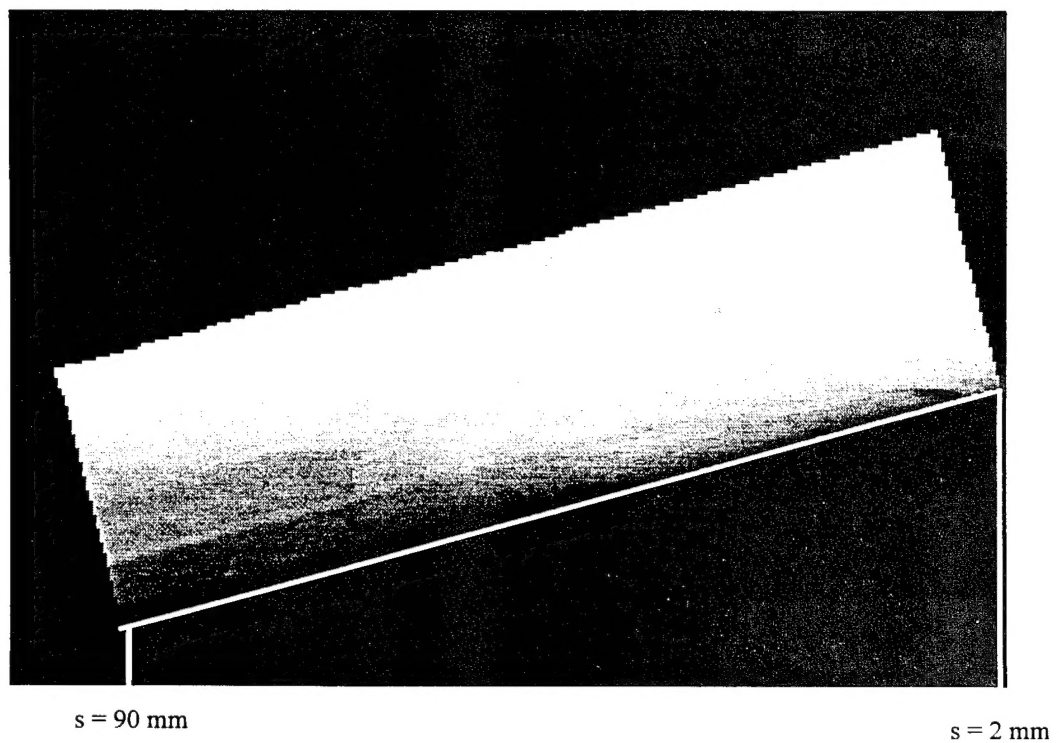
Figure 21. Average streamwise velocity image obtained with Filtered Planar Velocimetry downstream of the 14° centered expansion.
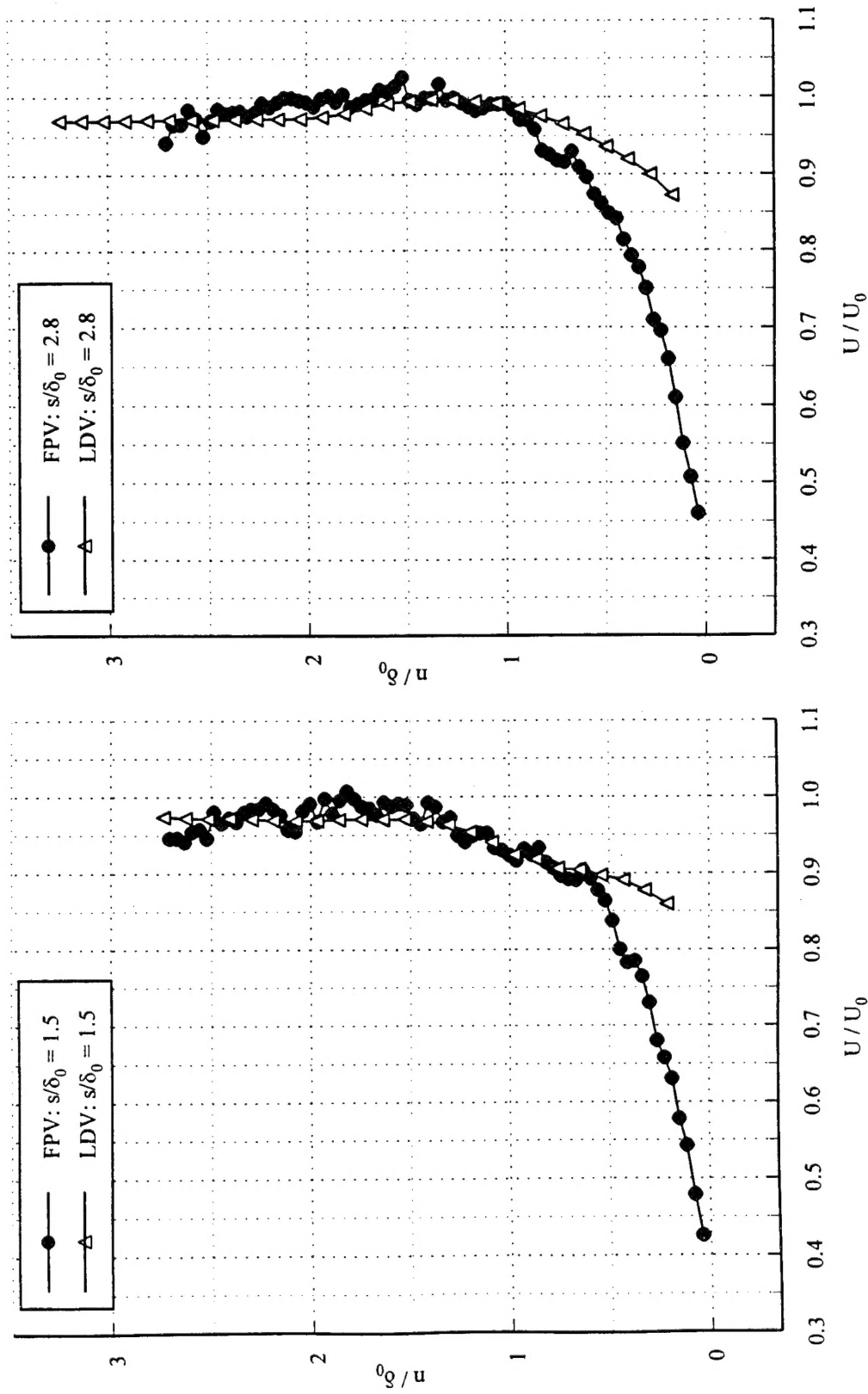
Figure 22. Mean velocity profiles obtained downstream of the 14 degree centered expansion at $s\delta_0 = 1.5$ and 2.8 with LDV and FPV.
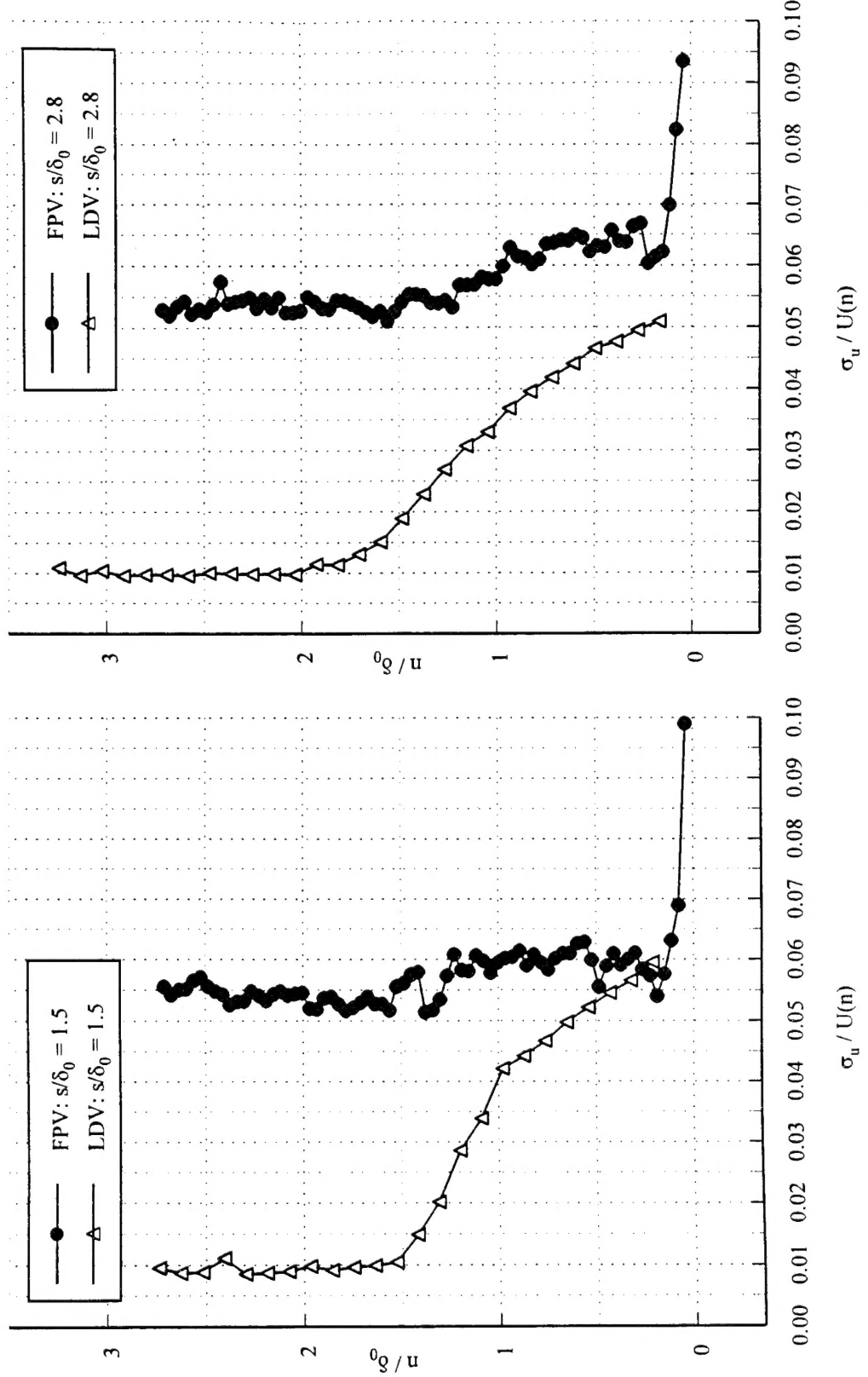
Figure 23. Streamwise turbulence profiles obtained downstream of the 14 degree centered expansion at $s\delta_0 = 1.5$ and 2.8 with LDV and FPV.